P
2 mil

FINAL REPORT

MARINER JUPITER/SATURN INFRARED INSTRUMENTATION STUDY

JPL Contract No. 953304

Prepared For - Jet Propulsion Laboratory
California Institute of Technology
4800 Oak Grove Drive
Pasadena, California 91103

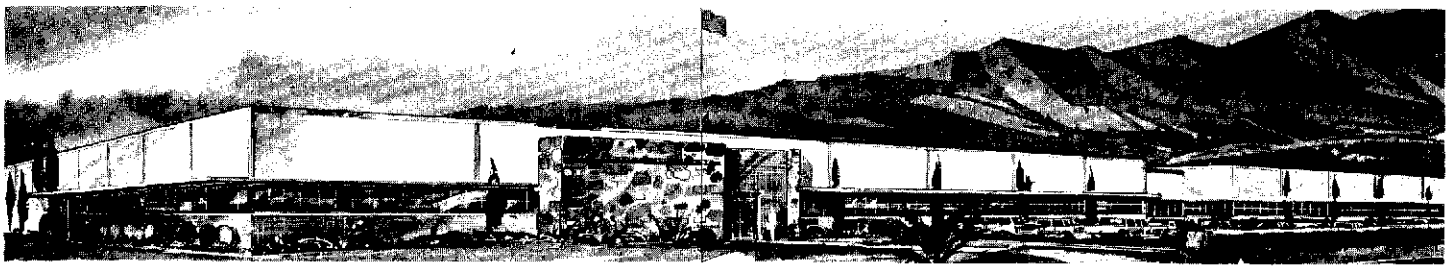

SANTA BARBARA RESEARCH CENTER

A Subsidiary of Hughes Aircraft Company

SBRC

SANTA BARBARA RESEARCH CENTER

A Subsidiary of Hughes Aircraft Company

75 COROMAR DRIVE • GOLETA, CALIFORNIA

FINAL REPORT

MARINER JUPITER/SATURN INFRARED INSTRUMENTATION STUDY

JPL Contract No. 953304

for

Jet Propulsion Laboratory
California Institute of Technology
4800 Oak Grove Drive
Pasadena, California 91103

25 July 1972

CONTENTS

CONTENTS (Cont)

CONTENTS (Cont)

ILLUSTRATIONS

ILLUSTRATIONS (Cont)

ILLUSTRATIONS (Cont)

TABLES

TABLES (Cont)

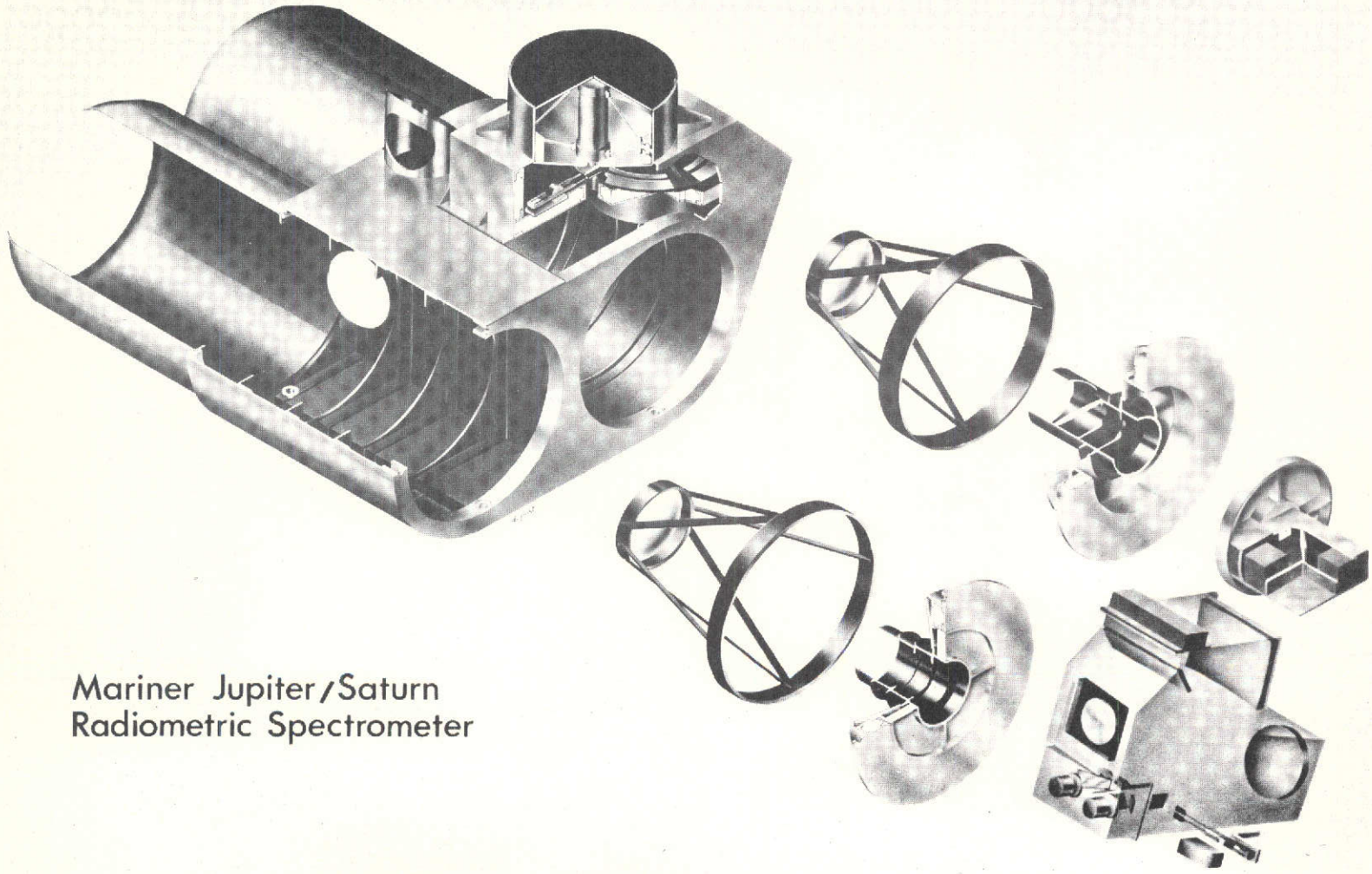

Mariner Jupiter/Saturn
Radiometric Spectrometer

Frontispiece

Section 1
INTRODUCTION

The Mariner Jupiter/Saturn Infrared Instrumentation conceptual design study was conducted to determine in detail the physical and operational characteristics of the instrumentation necessary to satisfy the Experiment Science Requirements.[1]

This report is the result of several iterations with the Science Team and many interactions with individual members of the team. As a result of these interchanges, both the science requirements and the concept of the instrumentation have changed from that originally outlined in the Team Proposal.[2] The changes made to the hardware, however, have been directed toward better performance, lighter weight, and higher reliability.

The thrust of this study has been directed toward the design of an instrument using as many proven concepts as possible; that is,the design and performance are considered to be current state of the art. Many design features are taken from current SBRC developments such as the Mariner, Pioneer 10, Viking Orbiter radiometers and the Nimbus D (SIRS) spectrometer. Design of the radiation cooler parallels the SBRC VISSR[3] development.

The instrument resulting from this study is extraordinarily light in weight owing to the use of stressed skin structure, honeycomb panels, and replicated optics. Similarly, the electronics design makes extensive use of hybrid circuits and repairable cordwood packaging, much of this a product of the Viking Orbiter Infrared Thermal Mapper development.

---

[1] The Experiment Science Requirements, formulated by the Infrared Science Team, are contained in Appendix A.

[2] Proposal for Participation in Mission Definition for Grand Tour Missions to the Outer Solar System - Infrared Experiments Team - Jet Propulsion Laboratory - January 1971.

[3] VISSR - Visible Infrared Spin-Scan Radiometer, developed for NASA by SBRC.

Section 1
INTRODUCTION

The Mariner Jupiter/Saturn Infrared Instrumentation conceptual design study was conducted to determine in detail the physical and operational characteristics of the instrumentation necessary to satisfy the Experiment Science Requirements.[1]

This report is the result of several iterations with the Science Team and many interactions with individual members of the team. As a result of these interchanges, both the science requirements and the concept of the instrumentation have changed from that originally outlined in the Team Proposal.[2] The changes made to the hardware, however, have been directed toward better performance, lighter weight, and higher reliability.

The thrust of this study has been directed toward the design of an instrument using as many proven concepts as possible; that is,the design and performance are considered to be current state of the art. Many design features are taken from current SBRC developments such as the Mariner, Pioneer 10, Viking Orbiter radiometers and the Nimbus D (SIRS) spectrometer. Design of the radiation cooler parallels the SBRC VISSR[3] development.

The instrument resulting from this study is extraordinarily light in weight owing to the use of stressed skin structure, honeycomb panels, and replicated optics. Similarly, the electronics design makes extensive use of hybrid circuits and repairable cordwood packaging, much of this a product of the Viking Orbiter Infrared Thermal Mapper development.

---

[1] The Experiment Science Requirements, formulated by the Infrared Science Team, are contained in Appendix A.

[2] Proposal for Participation in Mission Definition for Grand Tour Missions to the Outer Solar System - Infrared Experiments Team - Jet Propulsion Laboratory - January 1971.

[3] VISSR - Visible Infrared Spin-Scan Radiometer, developed for NASA by SBRC.

Section 2
GENERAL DESCRIPTION

INFRARED INSTRUMENTATION

The instrument presently envisioned and described in this report consists of two identical 6-inch diameter f/3.5 telescopes contained in a common monocoque structure as shown in the isometric cutaway drawing, Figure 2-1. Primary and secondary mirrors, and, in fact, many other mirrors in the system are made by replicating the reflective optical surface on an aluminum backed epoxy surface. Aluminum used as the reflecting surface is first evaporated on the master and is then parted with the mirror. SiO_2 is then used to protect the optical surface. In the figure, the left hand "A" telescope is used for the ten long-wavelength radiometric channels. Eight of the ten are associated with the fixed grating spectrometer and are divided into two redundant groups of four. Corresponding detectors in each group cover the same spectral band and all detectors in each group are spatially coincident, but the two groups view different spatial areas. The spectral bands covered by the grating spectrometer are:

25 to 27.8 μm
30.8 to 34.4 μm
35.7 to 38.4 μm

In addition to these channels, three broadband channels operate at 14 to 24 μm, 16 to 35 μm and 40 to 55 μm. Reststrahlen reflection properties of crystals are used to define the spectral bands. Two reflections of LiF are used for the 17- to 35-μm band and three reflections of single-crystal CdSe for the 40- to 55-μm band.

The arrangement of instantaneous fields of view (IFOV) of these channels is shown in Figure 2-2.

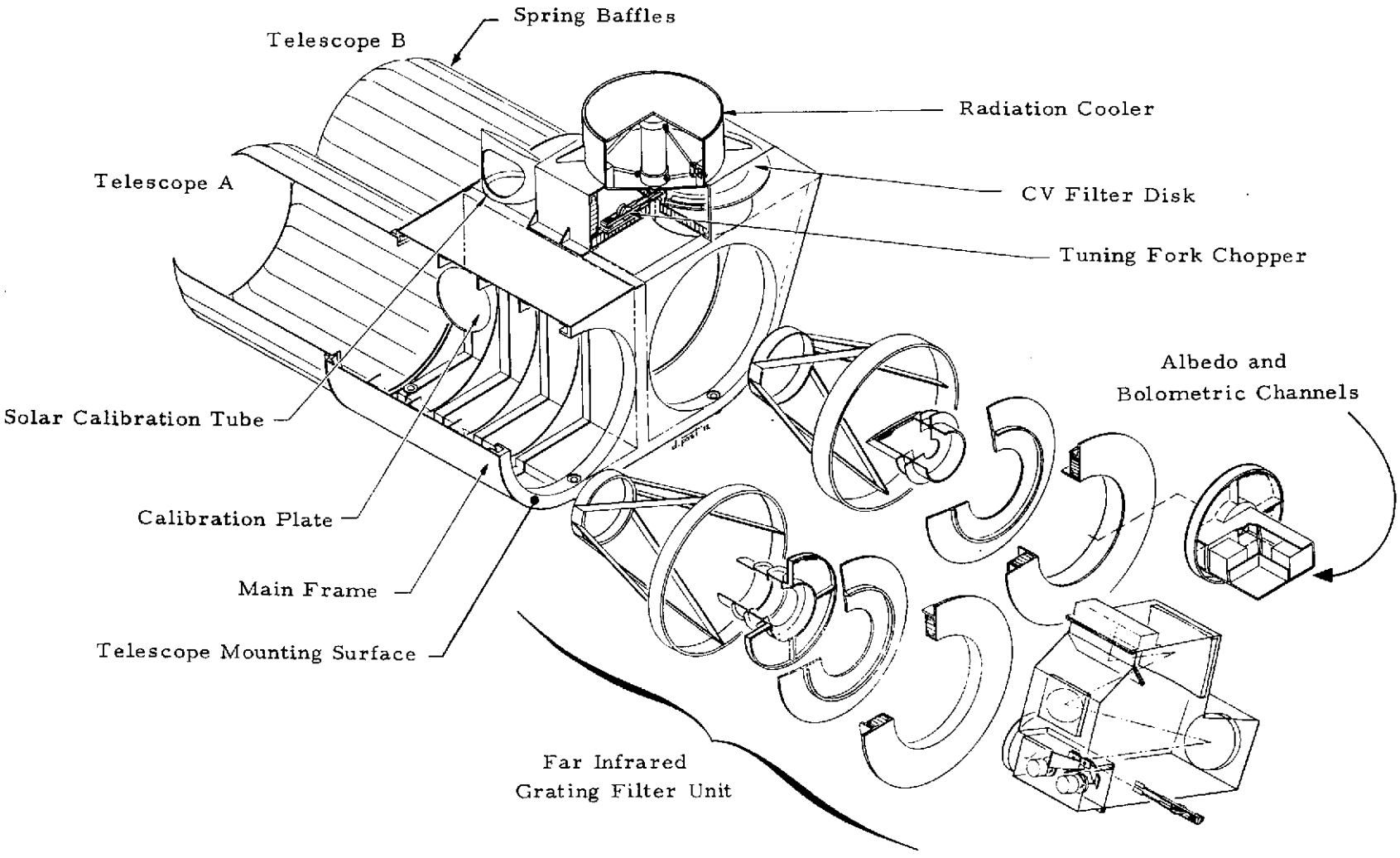

Figure 2-1. Mariner Jupiter/Saturn Radiometric Spectrometer

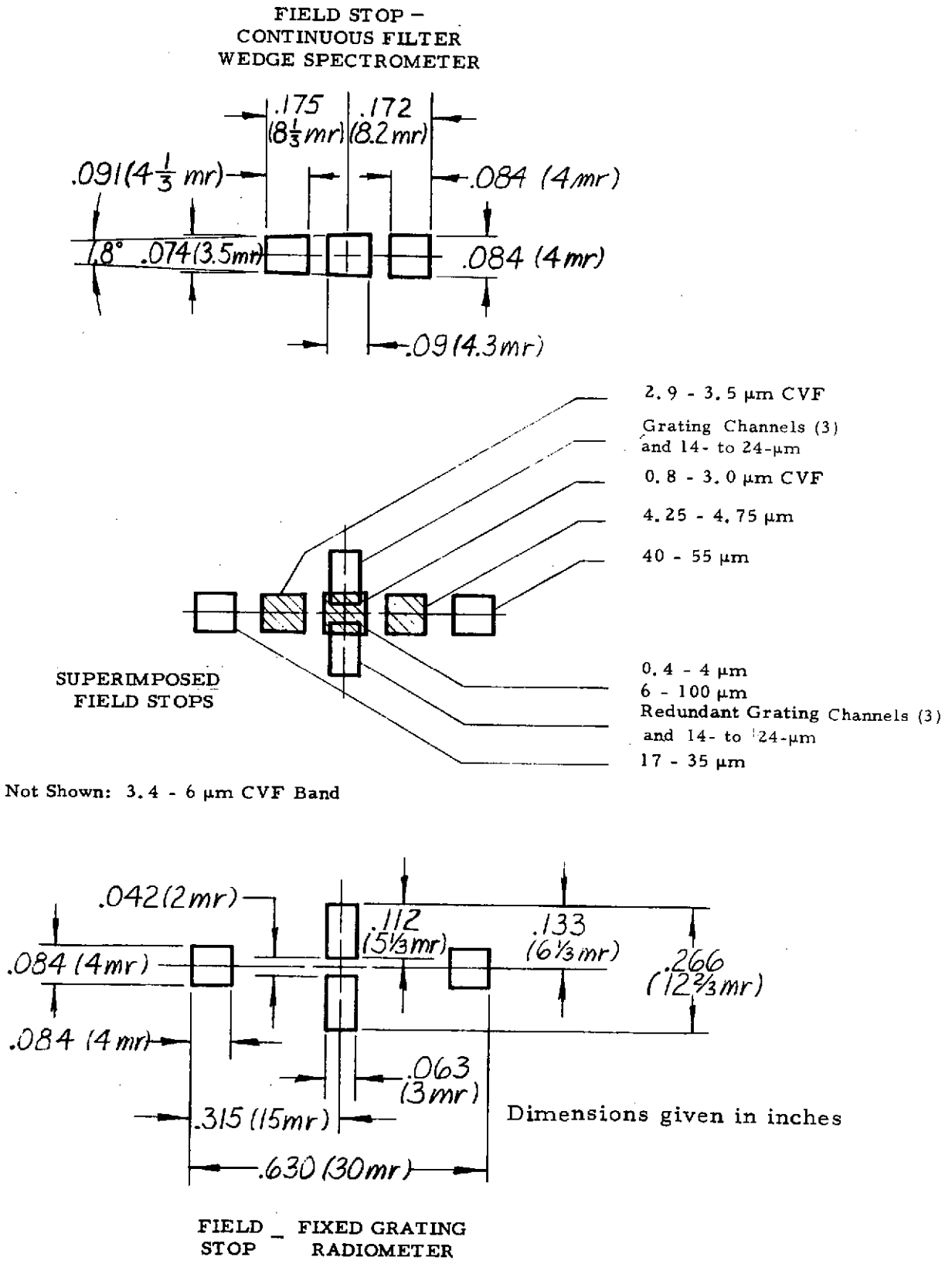

Figure 2-2. Arrangement of Fields of View and Field Stops

An optical schematic diagram of the long-wavelength channels is shown in Figure 2-3. For a detailed discussion of the optical design, refer to the Optics section (Section 4).

A resonant fork chopper operating at 10 Hz chops the radiation at the focal plane, the dimensions of which are also shown in Figure 2-2. The chopper blades are made from MgO which is transparent below 8.5 μm. Good short-wavelength rejection is provided since the radiation below 8.5 μm is not chopped.

Pyroelectric detectors are used for all the long-wavelength channels. Triglycine sulfate (TGS) appears to be the best candidate from the point of view of detectivity, but other types, namely lithium tantalate ($LiTaO_3$), triglycine selenide (TGSe), and lead titanate ($PbTiO_3$) offer advantages of lower dependence of detectivity on temperature, higher resistance to humidity, and better mechanical properties.

Evaporated thermopiles have also been considered for the grating channels but the system signal-to-noise ratios (SNRs) would be about a factor of three lower than the pyroelectric detectors despite the fact that a chopper would not be required. Refer to Sections 3 and 5 for a detailed discussion.

The box at the rear of the telescope contains the grating and all of the optical elements, detectors, and hybrid preamplifiers for the channels described.

The second or "B" telescope, boresighted with and identical to the first, is used for the short-wavelength channels. These include:

- 0.8 to 3.0 μm immersed PbS at 180°K
- 3.0 to 3.5 μm immersed PbSe at 180°K
- 3.4 to 6.0 μm HgCdTe at 180°K

  } Circular Variable Filter (CVF) Spectrometer

- 4.25 to 4.75 μm immersed PbSe at 180°K, fixed filter mounted next to the edge of the CVF wheel

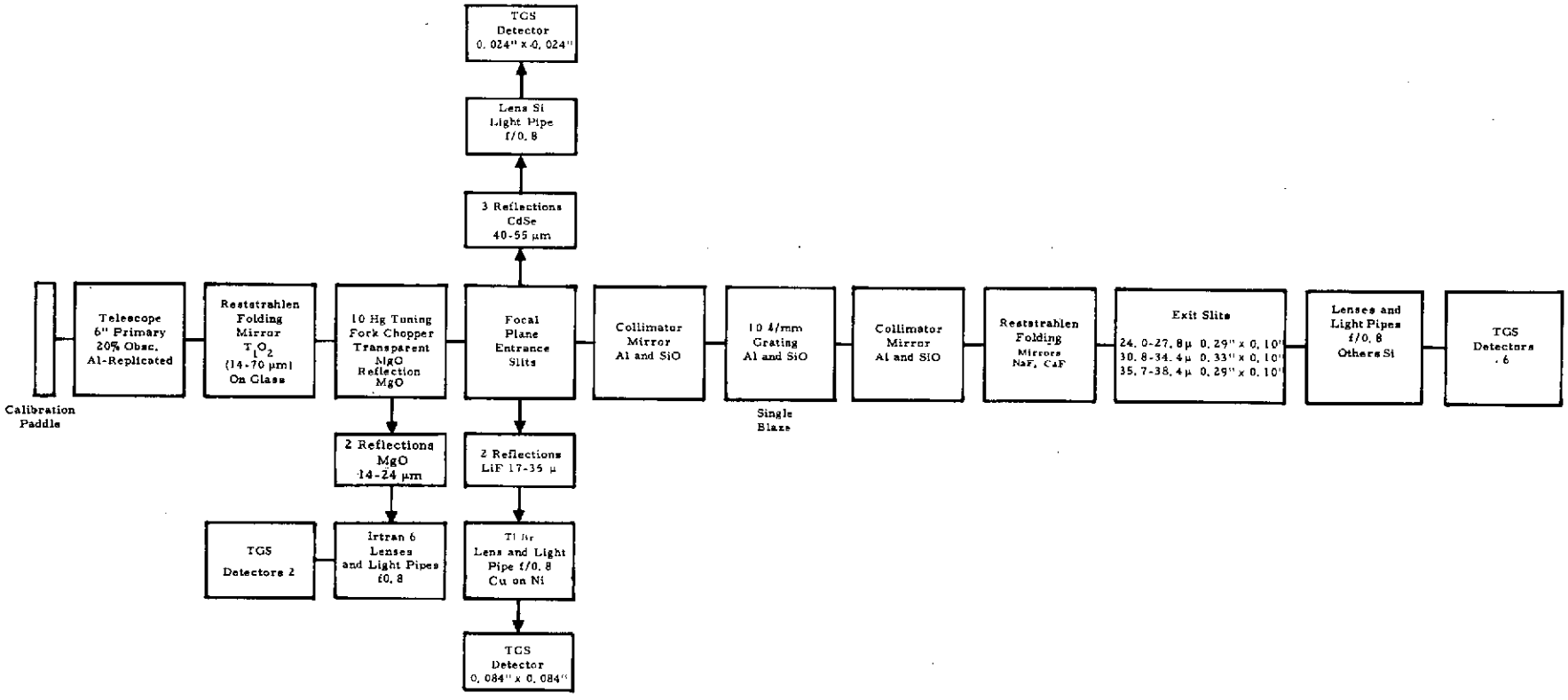

Figure 2-3. Optical Schematic Diagram for Telescope A

0.4 to 4.0 μm thermopile albedo channel

6 to 100 μm thermopile bolometric channel.

An optical schematic diagram for the "B" telescope is shown in Figure 2-4 (refer also to Figure 6-1, Optical-Mechanical Schematic). A diagonal mirror placed between the primary and secondary mirrors and occupying 75% of the optical bundle area provides energy for the filter wheel spectrometer. The remaining 25% of the energy passes through the telescope to the 0.4- to 4.0-μm albedo and 6- to 100-μm bolometric channels which individually are separated by a dichromatic beam splitter.

Field of view orientation for telescope "B" is also shown in Figure 2-2. The fields of view of the CVF and grating instruments are shown 90° out of coincidence. This reflects the present mechanical arrangement but it can be corrected in the final instrument by re-arranging the detectors on the cold finger or by rotating the CVF assembly 90°.

The FOVs for the 3.4- to 6.0-μm CVF band and the 4.25- to 4.75-μm fixed-filter channel are spatially separate from the other channels and each other. The annular CVF segment for the 3.5- to 6.0-μm band (not shown in Figure 2-2) occupies a position on the wheel closer to the center and a HgCdTe detector is used. Chopping at 500 Hz is provided for all cooled channels by means of a resonant fork chopper which operates close to the focal plane.

Details of the CVF spectrometer system can be seen in Figure 2-5. Positioning and sequencing of the CVF wheel are provided by a stepping motor driving the wheel directly at 1.8° per step. Two 1.8° steps and dwell times are used for each 2% spectral element for bands 1, 2, and 3. One step per element is used for bands 4 and 5. Spectral coverage on the CVF wheel cannot be continuous over the entire band from 0.8 to 3.5 μm but must be broken into separate bands because of the manufacturing process. Spectral coverage of the bands and the number of 2% resolution elements per band are given in Table 2-1.

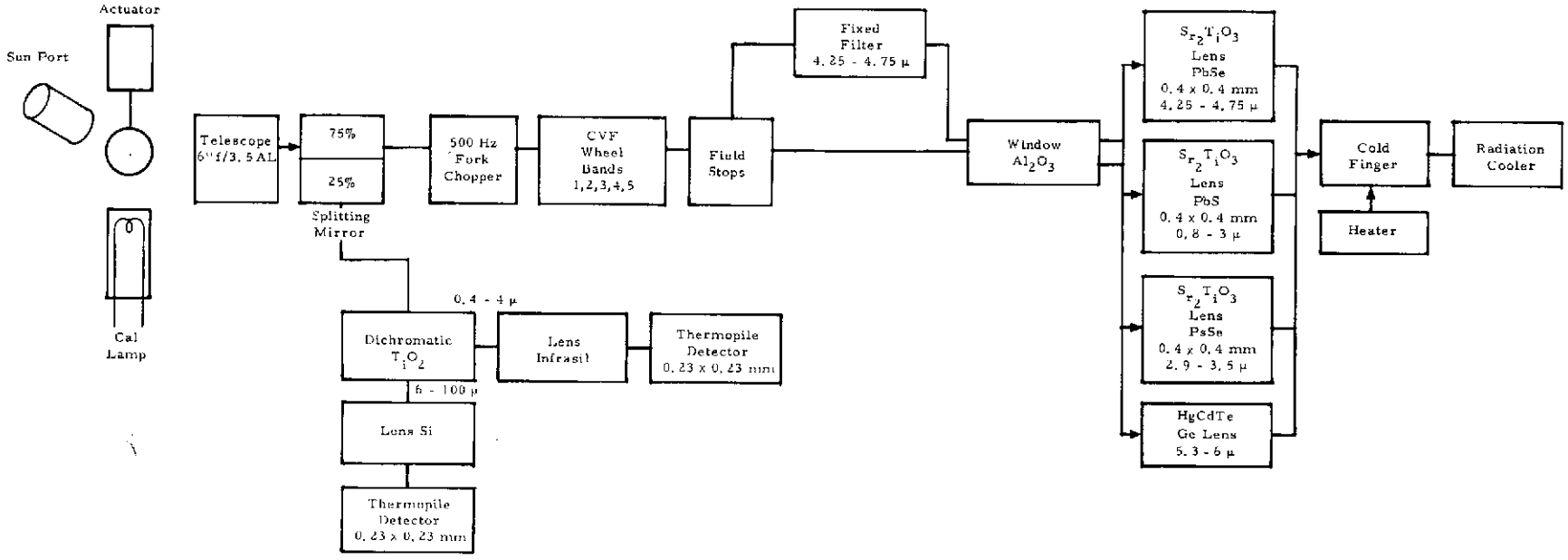

Figure 2-4. Optical Schematic Diagram for Telescope B

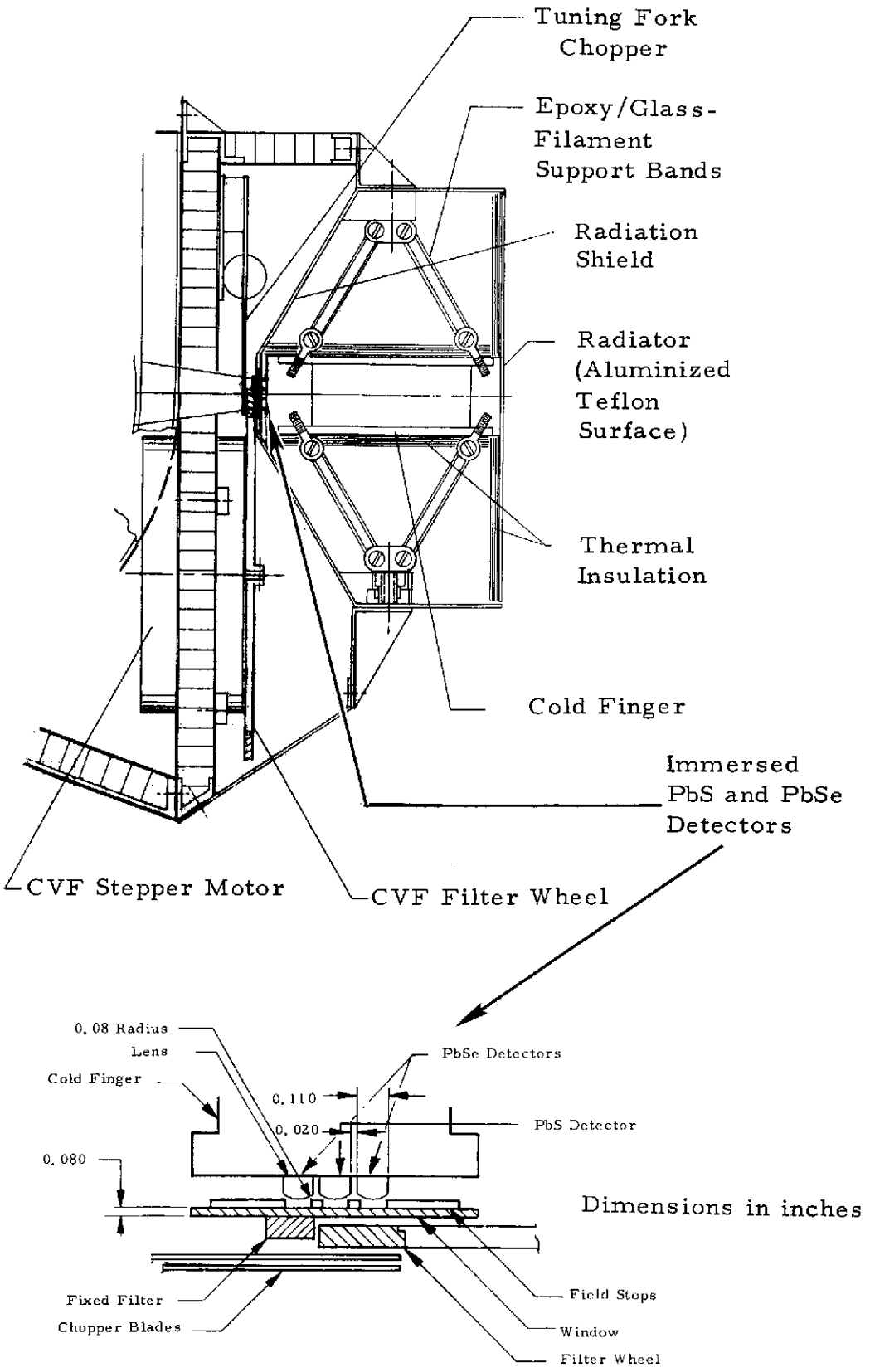

Figure 2-5. CVF Spectrometer Detail Layout

From Table 2-1 it can be seen that for bands 1, 2, and 3 the maximum angular velocity of the wheel is 18 deg/sec or 0.1 sec/step. For bands 4 or 5,[1] the longer dwell time slows the wheel down to 0.36 deg/sec or 10 sec/step. Therefore, a spectrum including bands 1, 2, 3, and 4 would require 114 seconds but inclusion of band 5 would increase the time per spectrum to 304 seconds.[1]

Table 2-1. CVF Wheel Considerations

Band (μm)	Rotation (deg)	2% Resolution Elements (Per Band)	Dwell Time Per 2% Element (sec)	Total Dwell Time (sec)
1 0.8 - 1.3	91.5	25	0.2	5.0
2 1.25 - 2.45	125.5	34	0.2	6.8
3 2.35 - 3.0	47	13	0.2	2.6
4 2.9 - 3.5	36	10	10	100
5 3.4 - 6.0	104	29	10	290

Total rotation not including the 3.4- to 6-μm band = 281°
Total resolution elements including the 3.4- to 6-μm band = 111

An inner annulus of the CVF wheel contains an optical position encoder which is used for angular position readout. Mechanical detenting of the stepping motor is unnecessary except at the stowed position where an opaque segment of the wheel covers the field stops.

Both the PbS and PbSe detectors are immersed on the backs of strontium titanate hyperhemispherical lenses which in turn are mounted side by side on the end of the radiation cooler cold finger. Cooling to 180°K is provided by a simple single-stage cooler which incorporates several features used in other SBRC cooler designs. Both the 5-inch diameter radiating surface and the tubular cold finger are supported by epoxy impregnated continuous filament glass fiber bands. Optical alignment of the system is maintained at operating temperature by the mechanical tolerances of the system. A heater

[1] Data from bands 4 and 5 can be taken simultaneously since separate detectors are used.

element on the cold finger is used to periodically boil off condensibles which could otherwise degrade performance. Contaminants entering the telescope aperture are prevented from depositing on the detectors by a sapphire window. Contaminants entering from the cooler end will tend to deposit on cold parts of the cooler before reaching the detectors. The cooler is capable of temperatures below 180°K so the heating element is also used to keep the detector temperature constant during the mission.

INFLIGHT CALIBRATION

Three types of inflight calibration are provided for the system: 1) short-wavelength solar calibration, 2) long-wavelength blackbody calibration, and 3) a filament lamp for the short wavelength and 3- to 6-μm regions. Each telescope contains an elliptically-shaped paddle which is driven by a common 45° stepper motor. The paddle surfaces, when aligned normal to the optical axis, obscure approximately 10% of the aperture area. When in this position and with the instrument viewing space, the black high-emissivity surface will radiate sufficient energy to calibrate the long-wavelength channels and the bolometric channel. The amount of energy radiated is known by monitoring the temperature of the paddle. When the paddles are rotated 135° from the normal position and the scan platform is aligned to a fixed position relative to the sun, solar energy is diffusely reflected from the back of the paddle in Telescope B which has a sand-blasted aluminum finish. When not in use, the paddle is aligned parallel to the optical axis of the telescope and is in line with one of the secondary mirror supports. This type of calibration, while not ideal since the aperture is not filled, is fail-safe in the sense that even if the paddle actuator fails in the calibrate position, a loss of less than 10% in sensitivity will occur. Because the aperture of Telescope B is shared by the spectrometer and thermopile channels, the paddle is positioned to overlap the two systems in the area ratio of 75% for the spectrometer and 25% for the albedo and bolometric channels.

The telescope apertures are protected by the folding flower-petal type closures shown in Figure 2-1. In the relaxed state, the petals are straight

because they are curved across their narrow dimension (much like a steel measuring tape), and an extension of the telescope baffle is thus formed. Before launch and until the spacecraft is past the asteroid belt, the petals are held closed by a dacron string. A burn wire is used to melt the dacron string and open the petals.

SYSTEM OPERATION

Operation of the system can be understood by referring to the block diagram of Figure 2-6. Control of all system functions including several operational modes is by the spacecraft Flight Data Subsystem (FDS). All data from the channels are analog and are therefore converted to pulse width data by the A/PW converter before transfer to the FDS. The A/PW converter is actually a part of the FDS which is carried in the instrument.

Consider the long-wavelength telescope A system. The channels in this system measure radiance in a radiometric sense; therefore, they must be referenced to a known source which is, in this case, space. In the Mariner radiometers, this was done approximately once per minute by a mirror internal to the instrument. However, in this case the size and weight of such a mirror precludes this approach. Instead, the scan platform must be scanned off the planet. Because of the impact of this approach on other instruments on the scan platform, the views to space will be less frequent, probably separated by at least 30 minutes or more.

The sequence of operation begins with the instrument viewing space. At this time, the dc restore circuit in each channel is clamped to zero and the memory capacitors are charged to a voltage proportional to the sum of the electrical and thermal offsets in the system. At the end of this interval, which could be several seconds depending on the restore time-constant, the switch is opened and a calibration is performed before the scan platform is returned to the planet viewing position.

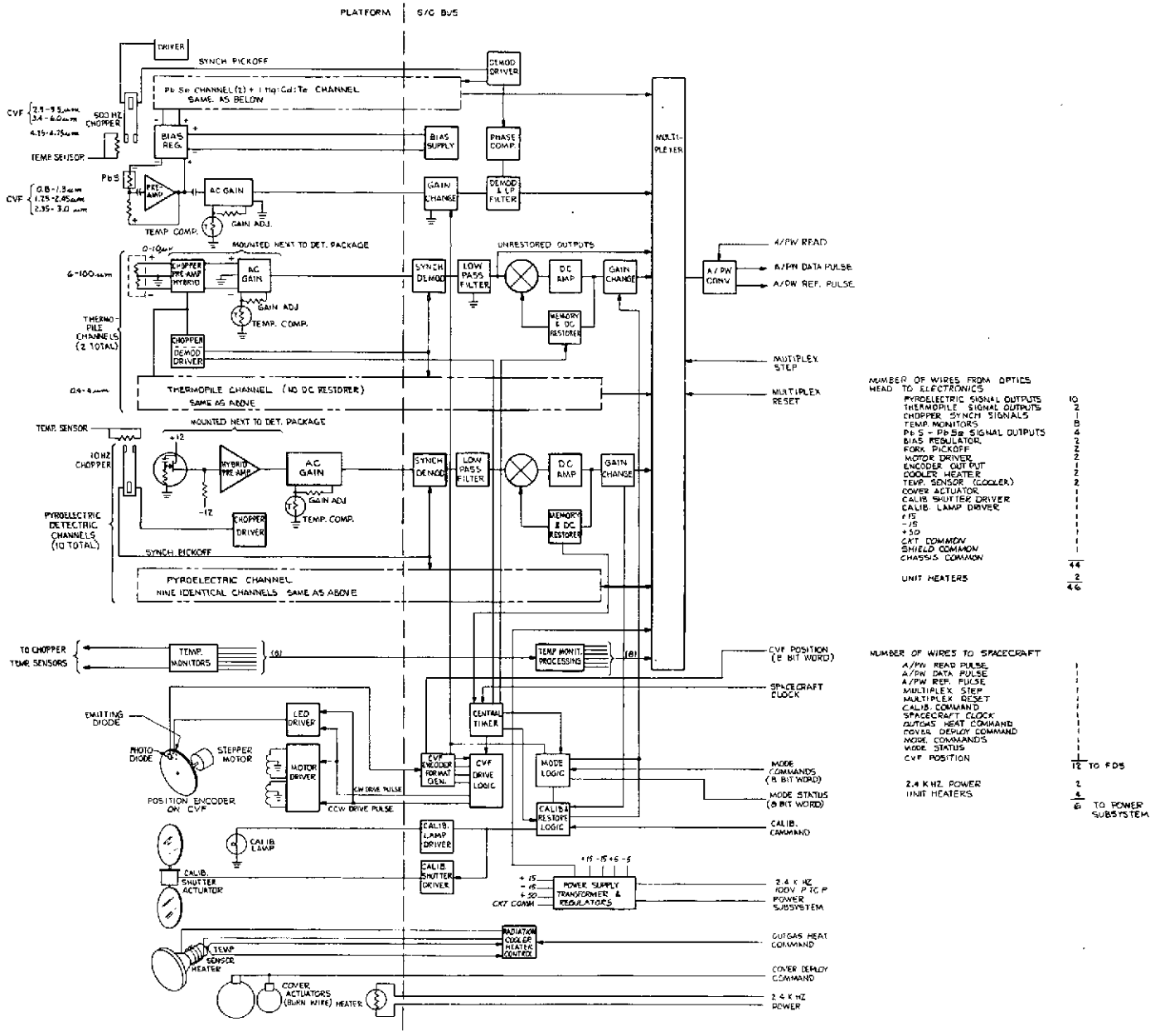

Figure 2-6. System Block Diagram

SBRC

Because the memory capacitor is connected to a high-impedance FET network, it produces an equivalent time constant of several hours. Thus, when viewing the scene or the calibration paddle, the output of the system is the difference between the scene signal plus the offset signal and the previously stored offset signal. In this way, the output is proportional only to scene radiance; self-emittance and electrical offset effects are removed.

In this system where extremely long "hold" times may be required, an alternate dc restorer technique involving an analog-to-digital converter and memory register could be used.

The purpose of the dc restorer system, besides establishing a zero radiance point, is to preserve dynamic range; that is, system offsets are removed which would otherwise require a larger dynamic range. The digitization accuracy of the system is thus improved since each digitization level corresponds to a smaller radiance increment.

All 10 pyroelectric detector channels are identical except for gain settings. Signal is produced by chopping the field defining apertures (field stops) at the focal plane simultaneously at 10 Hz. Each detector is provided with a load resistor of approximately 5×10^{11} ohms and an extremely low-leakage FET source-follower which are internal to the detector package. AC gain for the system is provided by integrated hybrid operational amplifiers. Monotonic temperature dependence of the TGS detectors is compensated for by a thermistor network in the feedback loop of one operational amplifier. The thermistor is actually located in the detector housing where it is in good thermal contact with the detector. A sync pickoff from the fork chopper provides drive to the synchronous demodulator to produce a dc output to a fourth order Bessel low-pass filter with linear phase. For the same 3-db information bandwidth, it can be shown that a true integrator will allow only slightly more noise to pass than a low-pass filter, and the integrator has the advantage of independence of readings (the integrator is dumped after each reading). However, in this case, for

a given dwell time the equivalent noise bandwidth of a low-pass filter can be much less than for a true integrator (see Systems Design section). The dwell time necessary to produce a satisfactory SNR for this system is 10 seconds. In this time the planet, either Jupiter or Saturn, has rotated the equivalent of one-half the 4-mr FOV. Therefore, at one planet radius there is 50% spatial smear in the samples regardless of the type of filter used, ignoring spacecraft motion.

Signals from the 17- to 35-μm, and 40- to 55-μm channels are processed in exactly the same manner as the grating spectrometer. The data sequence for the instrument is shown in Figure 2-7.

The calibrate sequence immediately follows the restore sequence while the instrument is viewing space. Slews of 30° on and off the planet are assumed to be sufficient to get a clean view of space and are at the high rate of 1°/sec. Settling time of 40 sec is used only when slewing back to the planet. The entire space restore/calibrate sequence requires from 2 to 6 minutes depending on how many CVF spectral elements are calibrated. During the time that the scan platform is slewing, housekeeping data are multiplexed to the FDS. These data consist of eleven unrestored analog outputs which are used to monitor the magnitude of offsets in the channels, eight temperature sensor outputs and five power supply voltage monitor outputs.

Gain of the channels can be changed to preserve dynamic range during the mission by means of the mode command interface. The mode status line verifies the commanded mode to the FDS.

Operation of the CVF, albedo and bolometric channels is similar to that described.

For the CVF channels, the 500-Hz resonant fork chopper chops both field stop apertures which are adjacent in the telescope "B" focal plane. In this system it is unnecessary to dc restore since the offsets due to thermal gradients are expected to be small. However, obtaining a spectrum when viewing space will provide an absolute zero for the system. Space must be viewed

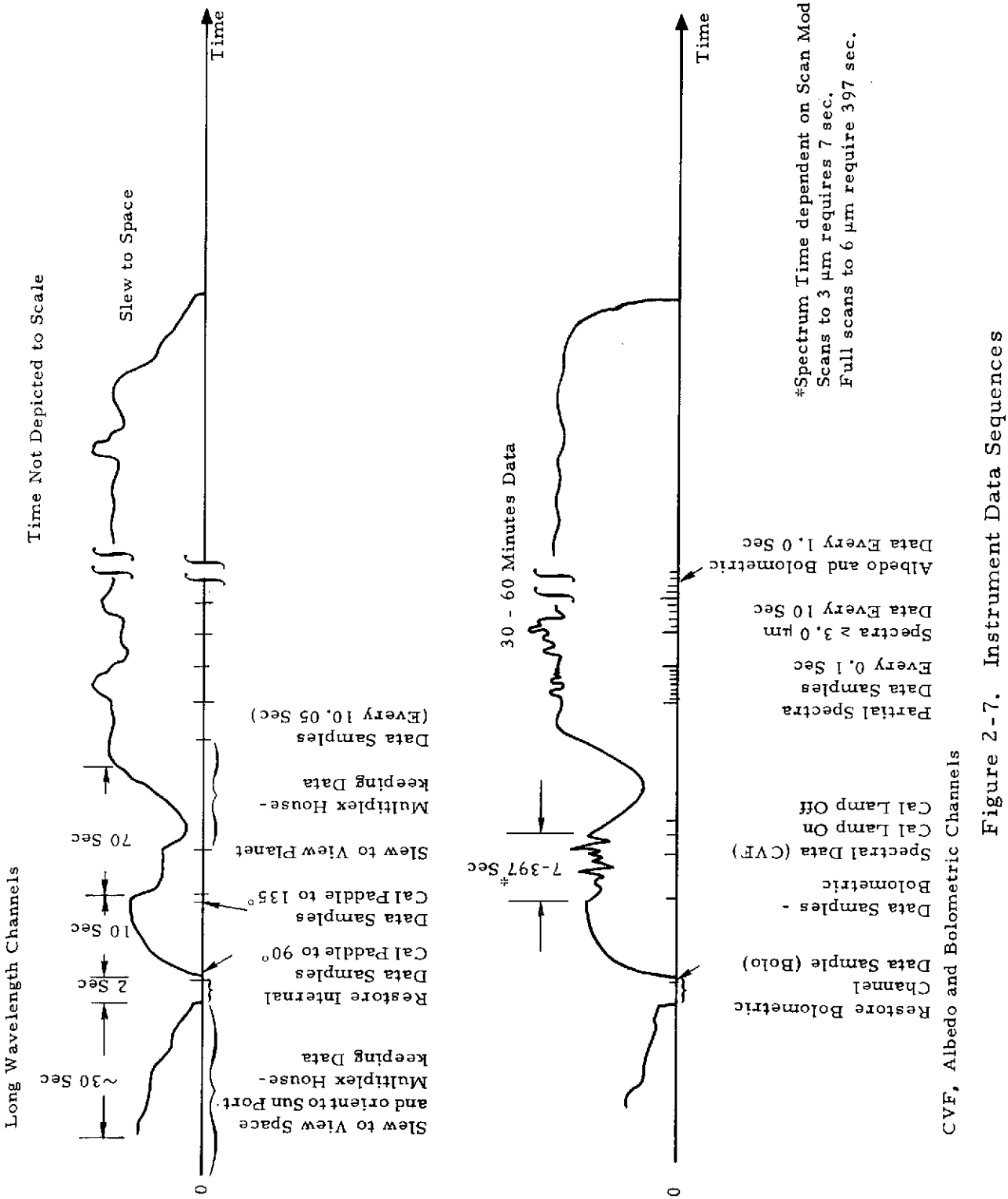

Figure 2-7. Instrument Data Sequences

when calibrating the channels. This can be done simultaneously with the long-wavelength channels. DC restoration is used for the 4.25- to 4.75-μm channel, however.

Although the PbS and PbSe detectors are mounted on a temperature-controlled cold finger, temperature compensation is provided to give less temperature dependent operation. Phase compensation is required to account for phase delay in the detector (primarily PbS chopped at 500 Hz) and in the amplifiers.

The SNR is sufficiently high that a simple low-pass filter is sufficient for CVF bands 1, 2, and 3 for which the dwell time is 0.1 sec (see Table 2-1). Bands 4 and 5 require 10 seconds per spectral resolution element, and the dwell time per spectrum could be as high as 304 seconds.

The albedo and bolometric channels which use evaporated thermopile detectors do not require optical chopping since they operate at dc with no 1/f noise. Instead, chopping is done electrically at the detector output so that the preamplifier can operate above the 1/f noise region. The chopper also acts as a voltage doubler which raises the detector signal and noise with respect to the preamplifier noise. DC restoration is used only for the 6- to 100-μm channel. Dwell time for these channels is 1 sec.

The inflight solar diffuser will provide sufficient energy for the 0.4- to 4.0-μm channel and the CVF channels out to 2.9 μm. Beyond 3.0 μm, however, a filament lamp will be used as a check-of-calibration. As with the other channels, this calibration must be done while viewing space.

Short-wavelength system data sequences are also shown in Figure 2-7. The sequences shown operate simultaneously using a common A/PW converter. That is, the grating channels, 6- to 100-μm, 0.4- to 4.0-μm, 2.9- to 3.5-μm CVF and 3.4- to 6-μm CVF channels are sampled on 4.25-msec centers (the cycle time of the A/PW converter). Bands 1, 2, and 3 of the CVF are sampled at 0.1-sec intervals between the 10-sec samples.

DESIGN SUMMARY

Instrument Type:	Fixed grating spectro-radiometer, filter wheel spectrometer, and fixed filter channels.	
Spectral Range:		
Telescope A	25-27.8 μm (2 channel) 30.8-34.4 (2-channel) 35.7-38.4 (2-channel)	Fixed grating spectrometer
	14-24 (2-channel)	Reflecting chopper
	17-35 (1-channel) 40-55 (1-channel)	Reststrahlen filters
Telescope B_1	0.8-1.3 μm, CVF Band, $\Delta\lambda$ = 2% 1.25-2.45, CVF Band, $\Delta\lambda$ = 2% 2.35-3.0, CVF Band, $\Delta\lambda$ = 2% 2.9-3.5, CVF Band, $\Delta\lambda$ = 2% 3.5-6.0, CVF Band, $\Delta\lambda$ = 2%	Filter wheel spectrometer
	4.25-4.75, Fixed interference filter	
Telescope B_2	0.4-4μm Fixed filter (InfraSil) 6-100 Fixed filter (dichromatic)	
Fields of View:	All are 4 x 4 mrad except those for the grating spectrometer which are 3 x 5.3 mrad. Arrangement of FOVs in object space is shown in Figure 2-2.	
Optics:		
Telescope A:	6-inch diameter, f/3.5 Ritchey-Chrétien replicated on aluminum	
Telescope B:	6-inch diameter, f/3.5 Ritchey-Chrétien identical to Telescope "A". Aperture is shared so that 75% of the clear aperture area is reflected to the CVF spectrometer and 25% passes straight through to the albedo and bolometric channels.	
Spectrometer, Fixed Grating, Telescope A	Off-plane Czerny-Turner grating is single blazed, 10 lines/mm.	
Spectrometer, Continuously Variable Filter (CVF)	Filter wheel has five separate annular CVF segments, each having 2% spectral resolution. Four segments are at one radius, fifth is at smaller radius.	
Detectors:		
Telescope A:	Pyroelectric (TGS) all ten channels. Detectors are mounted at the end of reflecting light pipes.	

Telescope B: PbS immersed on strontium titanate lens for CVF bands 0.8 through 3.0 μm.

PbSe immersed on strontium titanate lens for CVF bands 2.9 through 3.5 μm and fixed 4.25- to 4.75-μm channels.

HgCdTe for 3.4 through 6.0 μm CVF band (if used).

Thermopile 0.4- to 4.0-μm channel and 6- to 100-μm channel.

Total Detectors: 16, including HgCdTe option

Detector Cooling: 5-inch diameter, single-stage radiator, thermostatically controlled to 180°K

In-Flight Calibration: Long-wavelength channels: emitting blackbody paddle.

Short-wavelength channels: 0.8 through 3.0 μm uses solar diffuser on back of paddle; 2.9 through 6.0 μm channel uses a filament lamp located on secondary.

Systems and Electronics:

Dwell Time: 10 sec, Equivalent Noise Bandwidth, $\Delta f = 0.0288$ Hz all TGS channels, and CVF bands 2.9 through 3.5 μm, 3.4 through 6.0 μm, and 4.25 through 4.75 μm.

1 sec, $\Delta f = 0.288$ Hz, 0.4 through 4.0 μm and 6.0 through 100 μm.

0.1 sec, $\Delta f = 2.88$ Hz, CVF bands 0.8 through 1.3 μm, 1.25 through 2.45 μm, and 2.35 through 3.0 μm.

Signal to Noise Ratios: Telescope A, Long-Wavelength Channels

Band/Channel (μm)	Jupiter		Saturn		Dwell Time (Sec)
	SNR	NEDT (°C)	SNR	NEDT (°C)	
1) 14.0-24.0	5900	0.005	1050	0.01	10
2) 25.0-27.8	875	0.04	250	0.06	10
3) 30.8-34.4	677	0.06	234	0.09	10
4) 35.7-38.4	443	0.15	175	0.13	10
5) 17.0-35.0	11,500	0.003	845	0.005	10
6) 40.0-55.0	1,520	0.04	625	0.04	10

Signal to Noise Ratios: Telescope B, CVF Spectrometer, Albedo and Bolometric Channels

Band/Channel (μm)		SNR (Jupiter)		SNR (Saturn)		Dwell Time (Sec)
		Short	Long	Short	Long	
CVF 1)	0.8-1.3	2540	1550	825	516	0.1
CVF 2)	1.25-2.45	2580	785	850	264	0.1
CVF 3)	2.35-3.0	2160	1200	575	364	0.1
CVF 4)	2.9-3.5	280	201	86	66	10.0
CVF 5)	3.4-6.0	353	73	112	22	10.0
Fixed Filter	4.25-4.75	1070		355		10.0
Albedo	0.4-4.0	2900		925		1.0
Bolo.	6.0-100.0	966		330		1.0

Data Bit Rate: Maximum rate = 221 BPS, when CVF wheel is on bands 1, 2, or 3 at 10 bits/sample.

Low Rate = 31 BPS when CVF wheel is on bands 4 or 5 at 10 bits/sample.

Housekeeping Data Rate: 11 channels unrestored planet data and 8 temperature and voltage measurements. Data rate included above.

Operating Temperature Range: -40°C to 0°C

System Accuracy: See Tables 11-2 and 11-4.

Weight: 23.5 lb, including electronics

Section 3

SYSTEM DESIGN AND PERFORMANCE

TELESCOPE A: FIXED GRATING SPECTROMETER AND RESTSTRAHLEN CHANNELS

The signal-to-noise ratios (SNRs) for the long-wavelength channels are given by:

$$SNR = \frac{N_{\Delta\lambda} A_o \Omega \tau_o}{C\ (NEP)\ (\Delta f)^{1/2}}$$

where $N_{\Delta\lambda}$ = Planet radiance (watts-cm^{-2}-ster^{-1}) in the spectral interval. Spectral radiance curves for planets are given in Figure 3-1.

$A_o = 0.8\pi r^2 = 145$ (cm)^2 for 6-inch diameter telescope 20% obscured by secondary mirror and supports.

$\Omega = 4 \times 4$ mrad $= 1.6 \times 10^{-5}$ steradian, solid angle of view.

τ_o = Optical transmittance of system. Values for each channel are given in Table 3-1.

$C = 2.45$, chopping factor for resonant fork chopper.

NEP = Noise equivalent power [watts-(Hz)$^{-1/2}$] for TGS detectors; values for each channel given in Table 3-1.

$\Delta f = 0.0288$ Hz for 10-sec dwell time

Determination of the equivalent noise bandwidth, Δf, is based on the optimum use of a low-pass filter. It is assumed that during the dwell time, T, the output of the filter will rise to 67% of final value in response to a step input. This is a conservative assumption because in practice even the steepest temperature gradients to be encountered will produce ramp outputs as the finite FOV is slewed on and off the planet limbs. Also, temperature

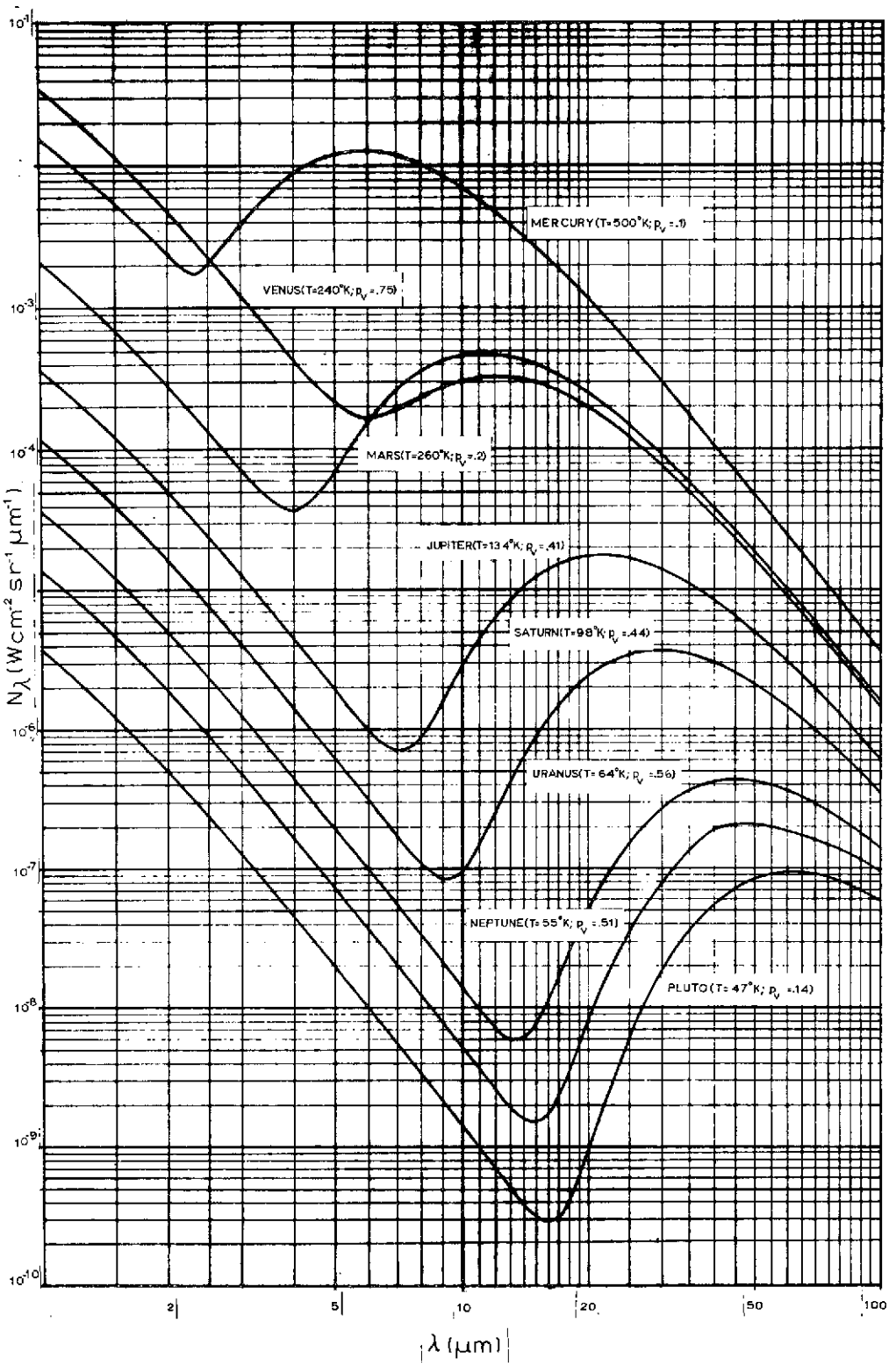

Figure 3-1. Spectral Radiance of the Planets

gradients in the scene would not be expected to encompass more than a fraction of the system dynamic range in one dwell time. Therefore, the error to be expected would be much less than 10%, depending on the nature of the temperature structure.

Table 3-1. Telescope A Optical Transmittance and Detector Parameters

Channel (μm)	Transmittance (%)							TGS Detectors	
	Primary/ Secondary	Reststrahlen Folding Mirror	Spectrometer Mirrors (2)	Grating	Reststrahlen Folding Mirror	Detector Lens	τ_o (%)	Size (mm x mm)	NEP watts/$\sqrt{Hz}$
14.0-24.0	94	75	94	--	70	80	37	0.61 x 0.61	4.6×10^{-11}
25.0-27.8	94	70	94	81	84	75	31.5	0.61 x 1.73	8.00×10^{-11}
30.8-34.4	94	80	94	80	90	70	35.6	0.61 x 2.0	8.75×10^{-11}
35.7-38.4	94	80	94	71	91	52	23.6	0.61 x 1.73	7.8×10^{-11}
17.0-35.0	94	70	--	--	65	80	35.0	0.61 x 0.61	4.6×10^{-11}
40.0-55.0	94	70	--	--	42	52	14.5	0.61 x 0.61	4.6×10^{-11}

For a two-section RC filter with the above properties,

$$T/\tau = 2.3$$

where $\tau = RC$

The equivalent noise bandwidth is given by

$$\Delta f = \frac{\pi}{4} f_{3\ db} = \frac{\pi}{4} \times \frac{1}{2\pi\tau}$$

For T = 0.1 sec, Δf = 2.88 Hz
T = 1.0 sec, Δf = 0.288 Hz
T = 10 sec, Δf = 0.0288 Hz

For a true integrator with the same dwell time, the noise bandwidth would be

$$\Delta f_{TI} \cong \frac{1}{2T}$$

and the equivalent noise bandwidth would be a factor of 1.74 higher.

Other low-pass filter designs are better for this application than the 2-pole RC type described above. For example, a fourth order Bessel filter with linear phase would give a smaller noise bandwidth for the same rise time requirements and would also give the lowest distortion. In this sense, distortion means the rms of the difference between the output and input waveform of the filter with a fixed delay and the output normalized to the input. [1] For ramp inputs, therefore, the output would be a more faithful reproduction of the input, except for a delay, than would be the case for other types of filters.

Performance of radiometric systems is frequently described by the value of NEΔT, where:

$$NE\Delta T = W\left(\frac{dW}{dT}\right)^{-1} (SNR)^{-1}_{T,\,\Delta\lambda}$$

W = Radiant emittance for a given scene temperature T and wavelength interval $\Delta\lambda$

$\frac{dW}{dT}$ = Slope of W versus T curve for a given temperature T

SNR = Signal-to-noise ratio of the system at scene temperature T

NEΔT is the incremental change in scene temperature required to produce a change in signal equal to the rms noise. In this system, NEΔT has no direct relevance because the channels are used for temperature sounding and H:He determination. NEΔT is useful when considering the calibration, however, because it is an indication of the temperature resolution capability of the system. Values for SNR and NEΔT are given in Table 3-2.

---

[1] Tavares, S.E., A comparison of Integration and Low-Pass Filtering, IEEE Transactions on Instrumentation and Measurements, Vol. IM-15, No. 1-2, March-June 1966.

Table 3-2. SNR and NEΔT Values for Long Wavelength Channels, Telescope A

Band (μm)	Jupiter			Saturn		
	NΔλ (watts-cm^{-2}-st^{-1})	SNR	NEΔT (°C)	NΔλ (watts-cm^{-2}-st^{-1})	SNR	NEΔT (°C)
14.0-24.0	1.32×10^{-4}	5900	0.005	2.36×10^{-5}	1050	0.01
25.0-27.8	4.00×10^{-5}	875	0.04	1.14×10^{-5}	250	0.06
30.8-34.4	4.16×10^{-5}	677	0.06	1.44×10^{-5}	234	0.09
35.7-38.4	2.63×10^{-5}	443	0.15	1.04×10^{-5}	175	0.13
17.0-35.0	2.72×10^{-4}	11,500	0.003	2.00×10^{-5}	845	0.005
40.0-55.0	8.67×10^{-5}	1520	0.04	3.56×10^{-5}	625	0.04

TELESCOPE B: CVF WHEEL SPECTROMETER, ALBEDO AND BOLOMETRIC CHANNEL PERFORMANCE

The aperture of the B telescope is shared so that 75% of the available area is reflected by a folding mirror into the CVF spectrometer, and 25% passes through the Cassegrainian focus to the albedo and bolometric channels.

For the CVF spectrometer the signal-to-noise ratio is given by:

$$SNR = \frac{A_o \, \Omega}{C \, (A_d)^{1/2} \, (\Delta f)^{1/2}} \, N_{\Delta\lambda} \, \tau_o \, D^*$$

where $A_o = 0.8\pi r^2 \, (0.75) = 110 \, (cm)^2$ for the 6-inch diameter telescope 20% obscured

$\Omega = 4 \times 4$ mrad $= 1.6 \times 10^{-5}$ steradian, solid angle of view

$C = 2.45$, degradation factor due to chopping

A_d = Area of detector in $(cm)^2$. In the CVF system the detector images the entrance aperture. Therefore, since 75% of the aperture is used by the system, the detector is smaller than would be the case for full aperture but is irregularly shaped. Assuming a focal ratio of f/0.75 in the immersion lens the detector area is

$$A_d \, (CVF) = 1.57 \times 10^{-3} \, (cm)^2$$

For the albedo and bolometric channels the detector is still smaller since only a segment of the aperture comprising 25% of the area is used.

$$A_d\ (a, b) = 0.522 \times 10^{-3}\ (cm)^2$$

Δf = 2.88 Hz, for T = 0.1 sec, bands 1, 2, 3

= 0.288 Hz, for T = 1.0 sec, fixed filter

= 0.0288 Hz, for T = 10 sec, bands 4, 5

$N_{\Delta\lambda}$ = Radiance within the 2% spectral interval of the CVF wheel or within the total spectral band of the albedo or bolometric channels, (watts-cm^{-2}-ster^{-1}). See Table 3-5.

τ_o = Optical transmittance. See Table 3-3.

Table 3-3. Optical Transmittances, CVF Spectrometer

	Band (μm)	Pri*Sec *Fold (%)	CVF (%)	Immersion Lens (%)	τ_o (%)
1	0.8-1.3	86	20	70	12.0
2	1.25-2.45	86	20	70	12.0
3	2.35-3.0	86	40	70	22.4
4	2.9-3.5	86	40	70	22.4
5	3.4-6.0	86	40	70	22.4
*	4.25-4.75	86	60	70	36.0

*With Fixed Filter

D* = Detectivity of detectors (cm-Hz$^{1/2}$-watt^{-1}). Values for each band are given in Table 3-4.

Table 3-4. Detector D* Summary, Cooled to 180 - 190°K

Band (μm)	Detector Type[1]	Published D*	Correction Factors		Corrected D* cm-Hz$^{1/2}$-watt^{-1}
			Chop[2] at 500 Hz	Cold Shield[3] f/1	
0.8-1.3	PbS	2.9×10^{11}	0.67	1.6	3.1×10^{11}
1.25-2.45	PbS	5.0×10^{11}	0.67	1.6	5.3×10^{11}
2.35-3.0	PbS	6.0×10^{11}	0.67	1.6	6.4×10^{11}
2.9-3.5	PbSe	1.25×10^{10}	0.75	1.6	1.5×10^{10}
3.4-6.0	HgCdTe	3.16×10^{10}	0.67	1.6	3.4×10^{10}
4.25-4.75	PbSe	1.5×10^{10}	0.75	1.6	1.85×10^{10}

1. PbS and PbSe are immersed on strontium titanate hyperhemispheres. The equivalent focal ratio at the detector is assumed to be f/0.75. Immersion is not possible with HgCdTe. In this case, a separate field lens is used giving a focal ratio at the detector of f/1.
2. Chopper frequency is as low as possible considering degradation of PbSe D*. Lower frequencies allow better PbS D* and more efficient chopper operation.
3. Typical values given. Actual values will vary.

Table 3-5 summarizes the signal-to-noise ratios attainable with the CVF Spectrometer.

Table 3-5. CVF Spectrometer Signal-to-Noise Ratio Summary

Band (μm)	N (Jupiter) watt-cm^{-2}-st^{-1} (130°K)		SNR (Jupiter)		N (Saturn) watt-cm^{-2}-st^{-1} (100°K)		SNR (Saturn)		Dwell Time (Sec)
	Short	Long	Short	Long	Short	Long	Short	Long	
0.8-1.3	6.4×10^{-6}	3.9×10^{-6}	2540	1550	2.08×10^{-6}	1.3×10^{-6}	825	516	0.1
1.25-2.45	3.8×10^{-6}	1.15×10^{-6}	2580	785	1.25×10^{-6}	3.9×10^{-7}	850	264	0.1
2.35-3.0	1.41×10^{-6}	7.8×10^{-7}	2160	1200	3.76×10^{-7}	2.4×10^{-7}	575	364	0.1
2.9-3.5	7.8×10^{-7}	5.6×10^{-7}	280	201	2.4×10^{-7}	1.82×10^{-7}	86	66	10.0
3.4-6.0	5.78×10^{-7}	1.2×10^{-7}	353	73	1.84×10^{-7}	3.6×10^{-8}	112	21.9	10.0
4.25-4.75	1.5×10^{-6}		1070		5×10^{-7}		355		10.0

CHANNEL PERFORMANCE; 0.4- to 4.0-μm ALBEDO, 6- to 100-μm BOLOMETRIC

Evaporated antimony-bismuth thin-film thermopile detectors are used for these two channels. Optical chopping is unnecessary because the detectors operate at zero frequency and produce no 1/f noise. The output of each thermopiles is electrically chopped at 1 kHz, however, so that the preamplifier can operate out of the 1/f region. Synchronous demodulation and low-pass filtering is used to produce the required bandpass around the chopping frequency.

Signal-to-noise ratios achieved with these channels is given by:

$$SNR = \frac{N_{\Delta\lambda} A_o \Omega \tau_o}{\gamma (NEP) (\Delta f)^{1/2}}$$

where: $N_{\Delta\lambda}$ = Radiance within the spectral band (watts-cm^{-2}-ster^{-1}), See Table 3-7.

A_o = $0.8\pi r (0.25) - 36.8$ cm^2

Ω = $4 \times 10^{-3} \times 4 \times 10^{-3} = 1.6 \times 10^{-5}$ ster

τ_o = Optical transmittance, see Table 3-6

γ = 1.5, degradation factor to account for preamp noise[2]

NEP = Detector noise equivalent power, (watts/$\sqrt{Hz}$), see Table 3-7

Δf = 0.288 Hz dwell time for both channels in 1 sec.

Signal-to-noise values are summarized in Table 3-7.

Table 3-6. Optical Transmittances 0.4- to 4.0-μm and 6- to 100-μm Channels

Band (μm)	Pri*Sec (%)	Dichromatic (%)	Field Lens (%)	τ_o (%)
0.4-4.0	90	85	90	69
6-100	90	70	50	31

[2]Thermopile systems tend to be preamplifier limited since the detectors are low impedance (5-15 Kohm) and produce only Johnson noise.

Table 3-7. Signal-to-Noise Performance 0.4- to 4.0-μm and 6- to 100-μm Channels

Band (μm)	$N_{\Delta\lambda}$ (Jupiter) (w-cm^{-2}-st^{-1})	$N_{\Delta\lambda}$ (Saturn) (w-cm^{-2}-st^{-1})	Detector[a] NEP watts/$\sqrt{Hz}$	SNR	
				Jupiter	Saturn
0.4-4.0	5.47×10^{-4}	1.74×10^{-4}	9.5×10^{-11}	2900	925
6-100	4.86×10^{-4}	1.66×10^{-4}	1.14×10^{-10}	966	330

a. Measured D* for SBRC thermopile detectors is:

$D^* = 2.4 \times 10^8$ cm $(Hz)^{1/2}$-watt^{-1}, 0.022×0.022 cm^2 area, 600°C blackbody

and $D^* = 2.0 \times 10^8$ cm $(Hz)^{1/2}$-watt^{-1}, $\lambda \geq 6\mu m$

For detectors having $A_d = 0.522 \times 10^{-3}$ $(cm)^2$ NEP is given by the expression:

$$NEP = \frac{\sqrt{A_d}}{D^*}$$

LONG-WAVELENGTH CALIBRATION

As previously described, each of the two telescopes is provided with a rotatable paddle mounted in the telescope. When rotated normal to the optical axis a portion of the aperture is filled with emitted energy from the paddle. During the calibration interval the telescope must view space so that the only energy input to the system is from the paddle.

The object of the analysis is to determine the optimum size for the paddle and to determine the output of each channel expressed as a fraction of its dynamic range.

From the thermal analysis* it was determined that the paddles would be at a temperature in the range 213 °K to 253 °K. Since both of these temperature extremes will produce blackbody radiance, if the aperture were filled, of greater than full scale for most channels, a fraction of the aperture was selected. Assuming a value of 10% the output values shown in Table 3-8 were calculated.

Table 3-8. Channel Outputs from Inflight Blackbody Calibration

Band (μm)	Calibration Paddle Temperature Extremes (°K)	Radiance From 10% Paddle ($W\text{-}cm^{-2}\text{-}st$)	Full Scale Radiance From Planet Model ($W\text{-}cm^{-2}\text{-}st^{-1}$)		Fraction of Full Scale[a] Output Produced By Calibration Paddle
			Jupiter	Saturn	
14.0-24.0	213 253	1.41×10^{-4} 2.58×10^{-4}	1.32×10^{-4}	2.36×10^{-5}	107 195
25.0-27.8	213 253	2.20×10^{-5} 3.66×10^{-5}	4.00×10^{-5}	1.14×10^{-5}	55 92
30.8-34.4	213 253	1.70×10^{-5} 2.42×10^{-5}	4.16×10^{-5}	1.44×10^{-5}	41 58
35.7-38.4	213 253	0.85×10^{-5} 1.32×10^{-5}	2.63×10^{-5}	1.04×10^{-5}	32 50
17.0-35.0	213 253	1.49×10^{-4} 2.55×10^{-4}	2.72×10^{-4}	2.00×10^{-5}	55 94
40.0-55.0	213 253	6.85×10^{-5} 9.68×10^{-5}	8.67×10^{-5}	3.65×10^{-5}	79 112
6-100	213 253	3.65×10^{-4} 7.17×10^{-4}	4.86×10^{-4}	1.66×10^{-4}	19 37
0.4-4.0	213 253	1.48×10^{-8} 2.71×10^{-7}	5.47×10^{-4}	1.74×10^{-4}	0.0007 0.012

[a]The stated value assumes that full scale is fixed for Jupiter Radiance.

*See the Thermal Analysis Section

For the 6- to 100-μm and 0.4- to 4.0-μm cases only 25% of the paddle area is used in the calculation because the paddle area is shared between the two systems using Telescope B. Table 3-8 shows clearly that this type of calibration is suitable for the long-wavelength channels and is satisfactory for the 6- to 100-μm bolometric channel, but that it is totally inadequate for the albedo channel. The following section treats the case using the solar diffuser backside of the calibration paddle for the short-wavelength channels.

SHORT-WAVELENGTH CALIBRATION

The short-wavelength calibration of the CVF spectrometer channels and the albedo channel is accomplished by positioning the paddle at the 135° position. This allows sunlight coming through the sun tube to reflect diffusely from the paddle on the side facing the telescope. The surface is prepared by sandblasting the aluminum. Roughened aluminum plate has a scattering property approximating a Lambertian scatterer. The effective reflectance of this material is on the order of 70%. Therefore, the output would be approximately equal to

$$V_o = K \frac{A_s}{A_t} \frac{\rho_s}{\rho_p} B(\lambda)$$

where the ratio $\frac{A_s}{A_t}$ is the fraction of the aperture obscured by the paddle which in this case is 7-1/2%. $\frac{\rho_s}{\rho_p}$ is the ratio of the paddle reflectance to the planet albedo which is equal approximately to $\frac{0.7}{0.4}$ $B(\lambda)$ is the wavelength dependence of reflectance. Therefore, the output would be roughly 10% of full scale if full scale were set for Jupiter. If the gain were set for Saturn, the same fraction would apply.

This calibration approach will work for all the channels out to the 2.35- to 3.0-μm CVF channels, but will not work for the 2.9- to 3.5-μm and the 3.4- to 6.0-μm CVF channels because the thermal output of the scatter plate is too low. For these channels a filament lamp calibrator will be used. The lamp provided with a sapphire window will be mounted behind the secondary mirror. Sufficient

power is available from a very small filament to give adequate signal-to-noise ratio (SNR) in all channels as is shown by the calculations below. In fact the radiating area of the filament need only be 1/4-mm square to give ample SNR even at the 6-μm end of band 5. The lamp is turned on only during the calibration interval when the system is viewing space. Also, since the filament temperature is selected to give a wavelength spectral peak at 1.4 μm, the calibration lamp can be used in lieu of solar calibration in the event it is inconvenient to move the spacecraft scan platform to view the sun.

Consider the worst case; namely, the 6-μm end of band 5 where the sensitivity is lowest.

A filament temperature of 2000°K is selected to give a spectral peak at 1.4 μm; at this temperature the lamp life is expected to be in excess of 100,000 hours. The SNR of the system viewing space with the lamp on is given by:

$$SNR = \frac{A_a A_c}{L^2 C (A_d)^{1/2} (\Delta f)^{1/2}} N_{\Delta\lambda} \tau_o D^* = 320$$

where A_a = Area of field stop = 3.48×10^{-2} cm^2

A_c = Area of radiating source = 0.25×0.25 mm^2 = 6.25×10^{-4} cm^2

A_d = Detector area = 1.57×10^{-3} cm^2

L = Distance between source and detector field stop $\cong$ 20 cm

τ_o = Optical transmittance = 0.224

Δf = 0.0288 Hz

D^* = 3.4×10^{10} cm-Hz$^{1/2}$-watt^{-1} HgCdTe

$N_{\Delta\lambda}$ = Radiance of filament at 6μm = 1.3×10^{-2} watts-cm^{-2}-ster^{-1}

C = 2.45 chopping factor

The SNR achieved is about equal to the full scale Jupiter signal for this channel. Even greater SNRs will be obtained for the shorter wavelength channels.

The power radiated by the filament, assuming both sides radiate equally, is:

$$P = 90 \text{ watts/cm} \times 12.5 \times 10^{-4}\text{cm}^{-2} = 0.112 \text{ watt}$$

Taking into account conductive and other lamp losses, the lamp power would be approximately 0.5 to 1.0 watt.

One difficulty with this approach is that the filament represents essentially a point source at the telescope entrance aperture and thus is imaged on the detector as a point. Therefore, if response non-uniformities develop in the detector they may not be picked up. This problem could be helped by filling as much of the dead spot area in the secondary as possible with either an integrating sphere or lens. If this were done approximately 25% of the detector would be illuminated. Thus, there would be less chance of saturating the detectors and lower lamp power would be required.

Section 4
OPTICAL SYSTEM DESIGN

GENERAL OPTICAL DESCRIPTION

The optical system has been designed to satisfy the scientific requirements of spectral, time, and spatial simultaneity of the data. Figure 2-1 shows the optical arrangement of the two telescope systems. The two telescopes are boresighted in object-space to produce the orientation of FOVs shown in Figure 2-2. All the FOVs see the scene simultaneously although the sample rates and dwell times of individual channels differ. Also, the CVF spectrometer produces a spectral scan so that all spectral elements do not view the scene simultaneously. Spectral simultaneity is accomplished, however, in the grating radiometer in which one pair of entrance slits is used for four spectral channels. There is spatial simultaneity in the sense that, with the exception of the 17- to 35-μm, 40-to 55-μm, and 4.25- to 4.75-μm bands, the channel fields of view are coincident in object space.

The telescope aperture areas are divided among the spectral channels in a manner consistent with the signal-to-noise requirements. In Telescope A the entire aperture is used for the grating radiometer system. The other two long-wavelength channels, while using the same aperture, do not share a common FOV. In Telescope B, 75% of the available aperture is used for the CVF spectrometer; the remaining 25% is used for the albedo and bolometric channels. In this case, all of these channels, with the exception of the 4.25- to 4.75-μm channel, have a common FOV. The CVF spectrometer in Telescope B is a folded system because the radiation cooler is best designed for end-looking cooled detectors. The radiation cooler must look at cold space during system operation which is in the direction normal to the telescope axis.

TELESCOPE - OPTICAL DESIGN

The telescopes are the Ritchey-Chrétien variation of the Cassegrainian family. The aperture is 6 inches in diameter, the focal ratio is f/3.50.

Because of the multiple FOVs it is necessary to have correction over a 2° diameter field angle. This is achievable using the hyperboloid-hyperboloid system. The optical parameters for the telescope are shown in Table 4-1. Figures 4-1, 4-2, 4-3 show the image quality for a point 0.3° off-axis. These geometric aberrations are smaller than can be expected using replicated mirrors where the blur circle for a point source owing to fabrication in perfections is expected to be 0.8 mr, or 0.016-inch diameter. The computed design shows a 0.0005 inch diameter blur circle.

Table 4-1. Optical Design Parameters

Aperture Diameter	6.0 in.
Focal Length	21.0 in.
f/No.	3.5
Field Coverage	2.0°
Elemental Field of View	4 X 4 mr
Primary Mirror, basic radius	18.0000 in.
Secondary Mirror, basic radius	12.5219 in.
Primary to Secondary Spacing	5.425 in.
Secondary to Image Spacing	8.333 in.

OPTICAL REQUIREMENTS - GRATING RADIOMETER

The planets Jupiter and Saturn will be observed in the following spectral intervals (Table 4-2) at medium spatial resolution. It is desirable to make the observations simultaneously and coincidentally. A wavelength tolerance of ±10% on the first four channels is assumed. The FOV for these channels is determined by energy considerations, but the two broad channels are more flexible because of their width.

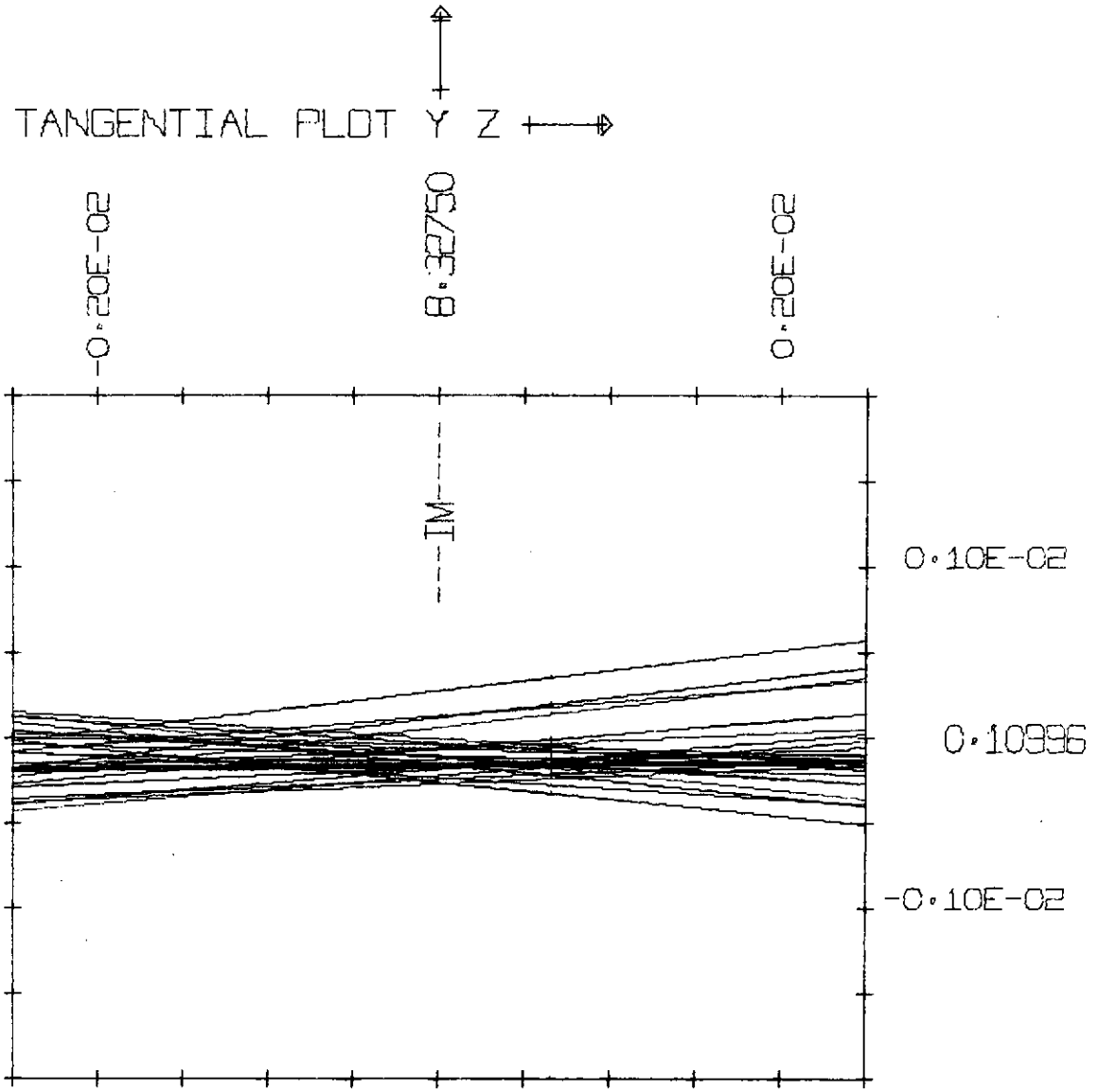

Figure 4-1. Tangential Plot

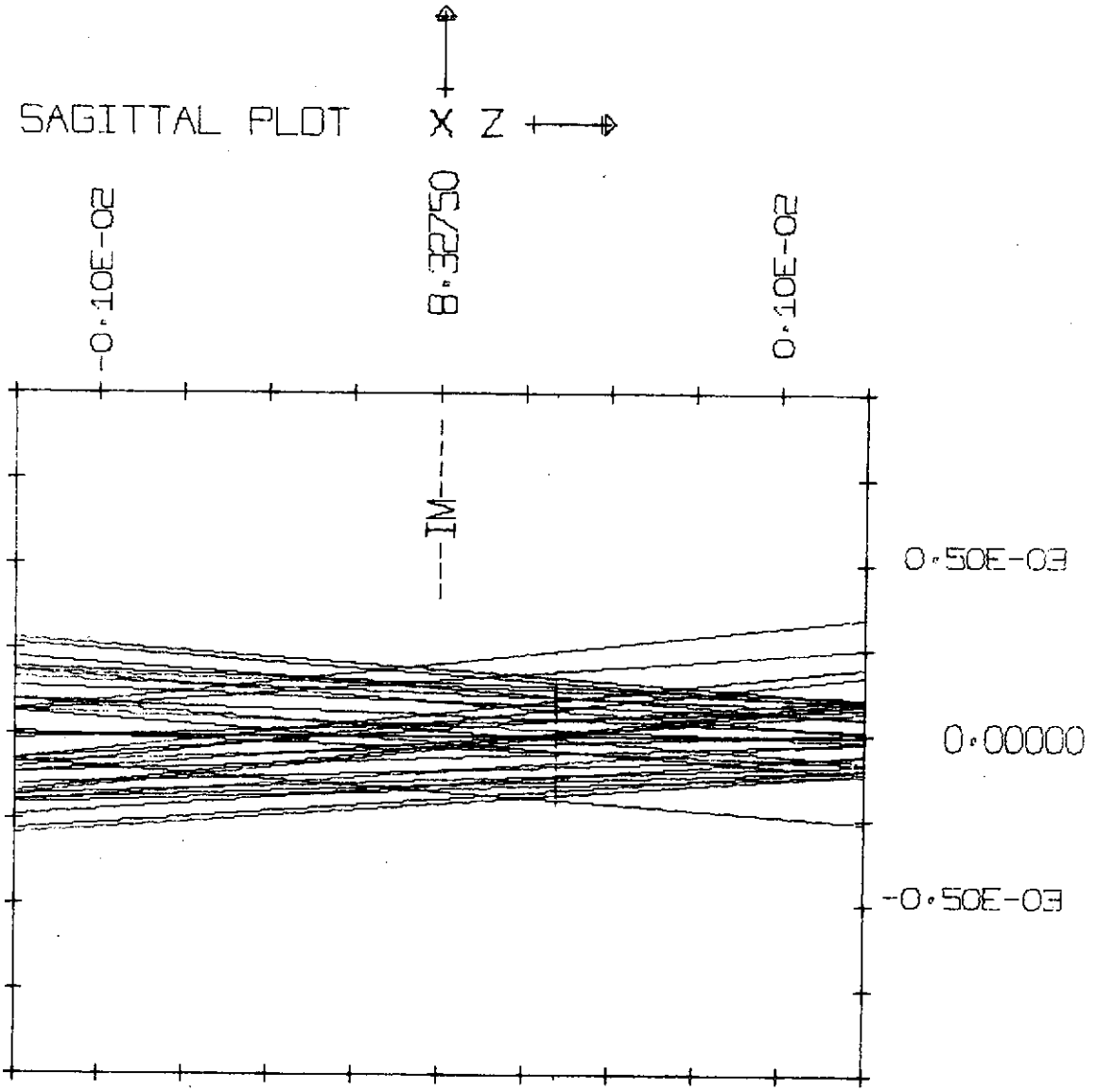

Figure 4-2. Sagittal Plot

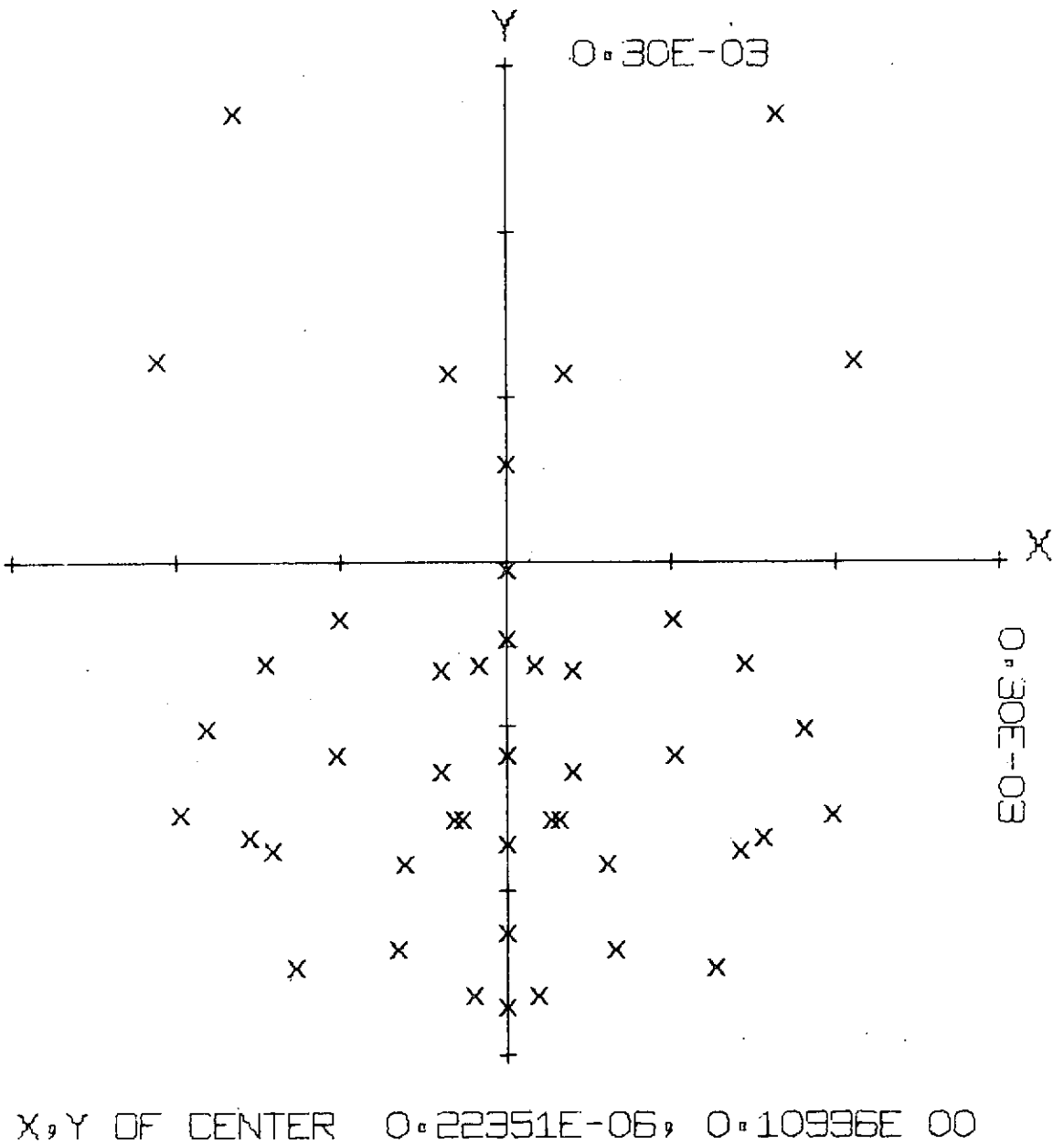

Figure 4-3. Spot Diagram

Table 4-2. Spectral Intervals

Half Response Wavelength (μm)	Wave Number (cm^{-1})
14.0-24.0	417-714
25.0-27.8	360-400
30.8-34.4	291-325
35.7-38.4	260-279
~14 (17) - 35	
~40 - ~55	

Spectral Bandpass Isolation

Isolation of these spectral intervals is a major problem. While each of the six standard techniques (Yamada, reststrahlen, interference multilayers, metal mesh, multiplex type spectrometer, and grating spectrometer) for filtering has its own particular difficulties, five can be quickly eliminated from consideration for the desired application.

The requirements for wavelength isolation are that: 1) the in-band transmission be greater than 60%, 2) the rejection (especially between 1.2 and 14 μm) be sufficient to ensure that the integrated out-of-band signal is $<1\%$ of the in-band signal, 3) the cutoff and cut-on slopes be steep, 4) the filters be durable to the environment and to handling, 5) they can be realized without a major advance in technical feasibility, and 6) they be priced within reason. In addition, 7) simultaneous observations of a single area on the planet are essential for the most meaningful interpretations of the data.

The available techniques are briefly evaluated in the following.

Yamada (Yoshinaga[1])* filters cannot be made narrow enough for the present pass-bands, and the transition from stop-band to pass-band is a gradual one.

*A list of References for this section is presented at the end of this section.

A set of narrow-band reststrahlen reflection filters was devised using II-V and III-V[2] compound semiconductors. These can satisfy all the requirements with the exception of the simultaneity. Because the out-of-band reflectivity is typically 10% to 20%, three reflections are required to reduce it to an acceptable level. The filters are consequently not compact. Except for the semiconductor reststrahlen materials a technique using interference is required to give steep slopes.

Multilayer (thin-film) interference bandpass filters[3] can be constructed up to about 30 μm. However, the thickness of an individual layer is so great (e.g. $\lambda/4$ at 28 μm for $n = 2.2$ is 3.2 μm) that shear and compressional stresses develop in the stack. The multilayer is consequently sensitive to mechanical and environmental forces. The paucity of thin-film materials suitable for the far infrared, which can be combined to give an index ratio > 3 thereby reducing the number of layers to nearly 10 also sheds a discouraging light on this technique. For those filters which can be constructed, $T_{max} \leq 0.40$. Such filters all violate the remainder of the stated requirements with the possible exception of (2), the blocking.

Analogous Fabry-Perot and double half-wave filters can be constructed using capacitive (low-pass) grids and/or inductive (high-pass) metallic meshes as the reflecting stacks.[3, 4, 5, 6, 7, 8] This approach has successfully filled the need for selective filtering at wavelengths greater than 50 μm. In principle, efficient band-pass filters could be made for shorter wavelengths. In practice, severe problems are encountered in obtaining the required optical tolerances using mechanical techniques. As the frequency of the radiation is increased, the ohmic losses due to surface currents increase because the conductance of metals decreases.

The inductive mesh consists of square holes in a thin metal film; the capacitive mesh is the complementary structure. The former is self-supporting, the latter requires a supporting substrate. Thus there will be dielectric losses in the substrate because of the concentration of electrical

field energy in the gaps between the metal squares. These losses also increase with increasing frequency. Absorption losses in suitable substrate materials for the region below 50 μm also reduce efficiencies. Polypropylene and polyethylene films have less absorption than Mylar; however they are softer and it is more difficult to obtain the required flatness tolerances.

When a plane electromagnetic wave is incident normal to a metallic mesh surface, currents and charges are produced which in turn are the sources of E and M fields. For the case when the mesh constant "g" is less than the wavelength, no diffraction orders are propagated. The scattered fields give rise to zero order transmitted and reflected waves of equal amplitude. Behind the mesh the scattered and incident wave superpose to give a total transmitted wave. Both the transmitted and the reflected wave depend on the ratio a/g where "a" is the width of the metal bar in a mesh and the width of the open space in a grid, "g" equals the width of the bar plus the width of the square (street width plus block width). Thus the transmission and reflection of a lossless mesh at normal incidence is

$$T = \frac{4g^2 \left[\log_e \left(\frac{g}{2\pi a}\right)\right]^2}{\lambda^2 + 4g^2 \left[\log_e \left(\frac{g}{2\pi a}\right)\right]^2}$$

$$R = 1 - T$$

Rather than the Fabry-Perot design which gives 1% to 2% bandwidths and an Airy transmission characteristic, a bandwidth near 10% having a square shape and greater attenuation is of more interest. The simplest is the double halfwave design which consists of three reflectors separated by two spacers. The order desired for operation is determined by the spacer thickness, but multiple order transmission peaks are also present. As the order number is decreased to the 8th order, the bandpass width increases and the tolerances on the spacer flatness, parallelism, and thickness be-become tighter by the factor "q."

The finesse[7] of a bandpass filter is determined in part by the flatness of the spacer and can be written

$$\frac{\Delta\lambda}{\delta\lambda} = \frac{m}{2}$$

where $\Delta\lambda$ = free spectral range

$\delta\lambda$ = half-width

m = flatness factor

For example, if the plates are flat to λ/m, the finesse cannot exceed $m/2$. Thus, if the spacers are flat to within 1.5 μm for a filter at λ = 30 μm, the finesse is limited to 10, which corresponds to a 10% filter width. For a single mesh this requires $g/\lambda = 1.2$ or g = 36 μm for λ = 30 μm.

The characteristic impedance and the sharpness of the transition from pass to stop band depend on the ratio a/g. It is desirable to have "a" = 0.1g.

The spacing "s" of the grids in a filter is chosen so that

$$s = \frac{\lambda}{2} \doteq 15\ \mu m$$

for a Fabry-Perot etalon. The spacers must be flat and plane parallel to 1 μm as shown above. Such thin fragile spacers are best made from stainless steel for handling and polishing reasons. The passband is obviously temperature dependent since the $\lambda_{peak} = 2s$.

As an improvement on the resonant cavity types described above, Ulrich[8] has devised resonant grids. In this type the open spaces are not square but cross shaped. At low frequencies, $g << \lambda$ the transmission can be represented as a constant inductance shunting an equivalent transmission line. At higher frequencies the representation is a capacitance in parallel with a constant inductance. The transmission peak $g/\lambda = 0.5$ is then the resonance of the LC circuit (for the mesh it was = 0.85). Distorting the square of the metal meshes discussed previously into a cross brings the opposite sides of the hole closer together, thus increasing the capacitance.

The effect is a reduction of the resonance frequency to a value far below the onset of diffraction, thus the resonance can now be used directly for filtering, without disturbance by diffraction. A single such grid is thus a fair filter in itself. The finesse is of course improved if more grids are used in combination, however, variation in their spacing are now not critical. The dependence of the resonant wavelength on the geometry of the crosses and spaces, which solely determine the characteristics of the bandpass, are not quantitatively known. A major advantage of this type of filter is the absence of higher order bands near 2 and 3 times the fundamental passband frequency. It is not known how narrow a bandpass can be achieved.

The preceding discussion shows that it is possible to design efficient ($T \sim 60\%$) bandpass filters in the region of interest. The only limits are those of construction, namely the grid constant and open space widths, and the flatness and the parallelism of the spacers. For the present application a development program would be required. Furthermore, discrete filters contradict the requirement of observational simultaneity.

Another method for obtaining spectral selection is by means of a Fourier or Hadamard transform spectrometer using, for example, a Michelson interferometer. Briefly, the advantages of the Fourier transform instrument versus the proposed grating instrument result because of the throughput and multiplex gains. Those of the proposed instrument accrue from the simultaneity of measurement, lower data rate requirement and redundancy provided by the use of several dual detectors.

The basic optical system (Michelson interferometer) of the Fourier spectrometer can be made significantly smaller (throughput gain) than the proposed grating instrument for similar resolving power. However, the need for an end-mirror drive system for the interferometer reduces this advantage. Due to the multiplex advantage of the Fourier transform spectrometer, a single detector can provide similar or greater spectral coverage than the multichannel instrument. The use of a sufficient number of detectors

in the proposed instrument to provide the desired spectral data essentially nullifies this advantage. Also, the multichannel grating instrument has the decided advantage for this experiment of providing simultaneous spatial and spectral measurements. Thus, the interaction of the relative spacecraft and planet motion and planet rotation is sufficiently small that with the proposed instrument such effects will have a negligible effect on the experiment results. With a Fourier transform spectrometer (or for that matter with a Hadamard transform spectrometer which has similar advantages and disadvantages) such interaction can have the effect of "mixing" the spatial and spectral information with a consequent loss of spectroradiometric accuracy. Only the use of a very high interferogram scan rate (with the probable necessity of summing interferograms to attain adequate SNR) can this disadvantage be eliminated. The data rate requirement would also be significantly increased with either transform type instrument. Finally, the use of multiple detectors provides a measure of redundancy so desirable for an extended mission such as MJS.

The section below considers the problems associated with operating the 14- to 24-μm channel on the grating and carries the design through on this basis. It is concluded, however, that a superior approach is to separate the 14- to 24-μm channel from the grating using a reflective chopper and reststrahlen filters and to optimize the grating for the remaining three long wavelength channels. These modifications are discussed beginning on page 4-32.

OPTICAL SYSTEM - LONG WAVELENGTH CHANNELS

The beam from the f/3.50, 6-inch aperture telescope is folded with a selective reflector which reflects 14 to 70 μm with an efficiency of 70% to 80% and $\lambda < 13\mu m$ with an efficiency 10% to 20%. This rejection is required because of the large out-of-band radiance and higher order sensitivity of the grating spectrometer.

The TiO_2 reststrahlen coating is the most efficient filter which provides good reduction of higher order radiation. Further reduction will be obtained by using a Schott neutral absorbing glass as the substrate. Thus scattering from the second surface is eliminated.

Selective specularity is another method for attenuating shorter wavelengths. This is achieved by roughening a surface in such a way that it is diffuse at short wavelengths and specular at long. A surface roughness dimension $\lambda/2$ will scatter wavelengths $\leq\lambda$. However, control of the statistical distribution of roughness dimension to be within a narrow range is very difficult. Consequently, in practice the transition from diffuse to specular properties as wavelength is changed is very gradual. Radiation which is scattering in uncontrollable directions is also cause for concern. An unpredictable amount of practical study would be required to perfect a reproducible procedure for particular spectral ranges.

Following the folding mirror are the focal plane field apertures for the low and the medium spectral resolution channels.

Low Spectral Resolution Channels

Isolation of the bands 17 to 35 μm and 40 to 55 μm is achieved by means of a combination of reststrahlen reflectors and absorbing windows. The 4-mr square fields are located at 9 mr from either edge of the grating fields.

The 17- to 35-μm band is isolated with two reststrahlen reflections from LiF crystal combined with the TiO_2 reflection which cuts on at 14 μm. The cutoff near 36 μm is defined by absorption in the TℓBr lens combined with the reduced reflectivity of LiF above 35 μm. Since TℓBr will solarize in short-wavelength radiation, it will be necessary to protect the lens from exposure to UV during handling, or to coat it with an infrared-transmitting, UV-absorbing material. The reststrahlen mirrors are mounted with their planes of reflection perpendicular in order to reduce the short-wavelength response to negligible values. Figure 4-4 shows the predicted throughput for this and the 40- to 55-μm band. The effect of crossed reflection planes is not shown.

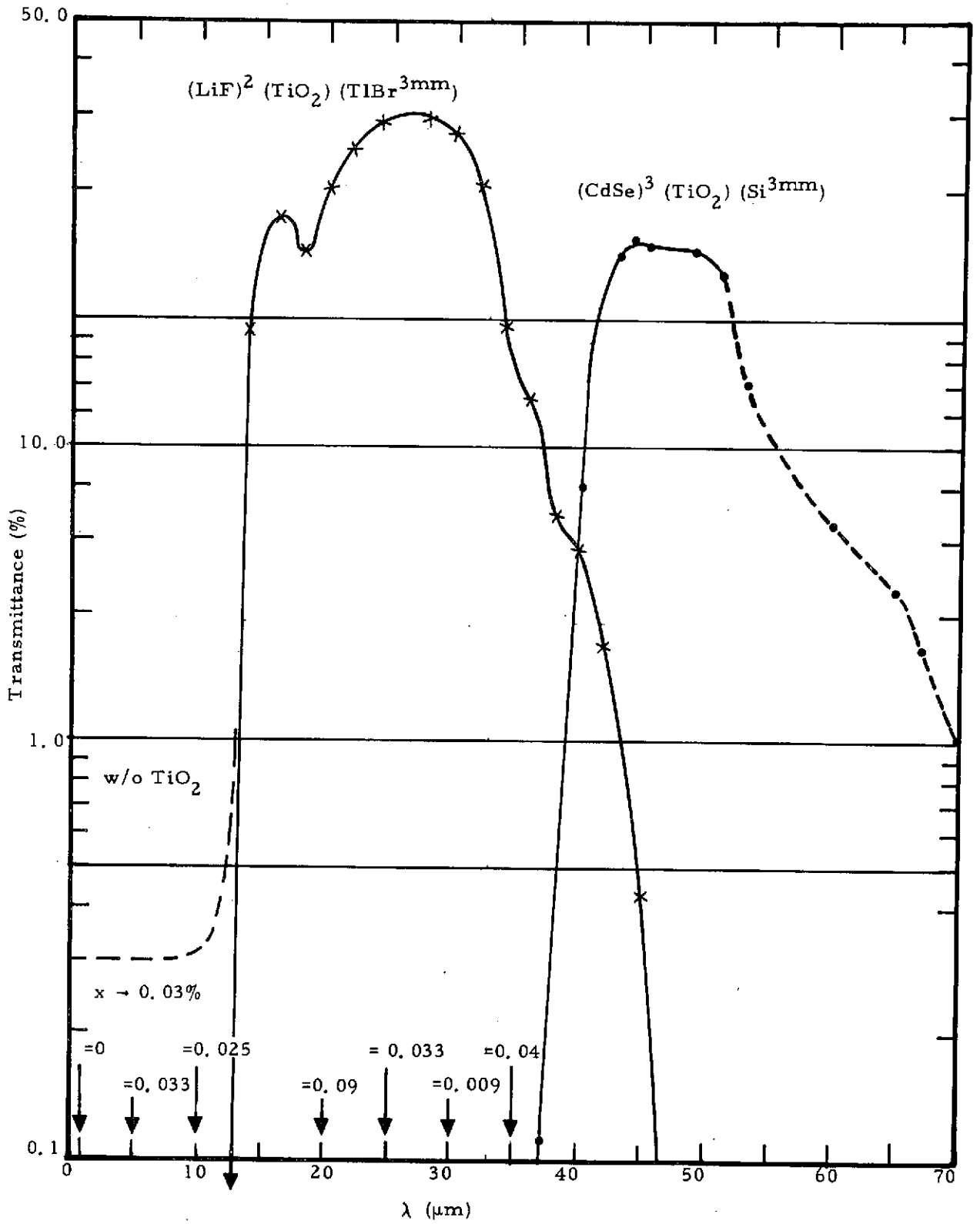

Figure 4-4. Transmittances of Low Resolution Channels

The 40- to 55-μm reststrahlen mirrors are CdSe doped so as to shorten the short-wavelength cut-on to 40 μm.[10] It will be necessary to scatter the short wavelengths to further reduce their intensity. This effect is not shown.

Medium Spectral Resolution Channels

Simultaneous and spatially coincident isolation of the wavelength bands between 14 and 38.4 μm is achieved with a fixed diffraction grating and multiple detectors. The grating is mounted in an unequally spaced, off-plane (Czerny-Turner) arrangement (Figure 4-5). Two 3-mr by 5.33-mr entrance apertures (telescope focal plane apertures) separated by 2 mr are imaged at the spectrometer exit plane, where a dual set of detectors and associated imaging optics (detector lens) and condensing (light funnel) optics are located. The relay (collimating) and condensing arms of the spectrometer are made unequal for the purpose of minifying the images of the entrance apertures (by the factor 2/3) and consequently minimizing the detector areas.

The mirrors are off-axis paraboloids tipped at angles such that the incident and emergent rays are symmetrical. The axis of the relay (collimating) mirror passes through the center of the entrance aperture; the axis of the condensing mirror passes through the exit aperture for the center wavelength. The off-plane mounting eliminates the possibility for dispersed radiation falling on the grating. This is a serious and difficult to detect source of unwanted radiation for in-plane systems. Since all of the elements are also out-of-line with each other in the unequal arm configuration this is an efficient way to prevent the propagation of unwanted energy through the system.

The relay mirror forms an image of the telescope exit aperture on the grating. The condensing mirror forms images of the spectrometer entrance aperture in a continuous band of wavelengths. The bandpasses of interest are isolated with a perforated mask at the exit image plane. Each detector lens images the grating on a detector. Thus variations in the spatial distribution of radiance in the scene will not interact with any spatial sensitivity contours

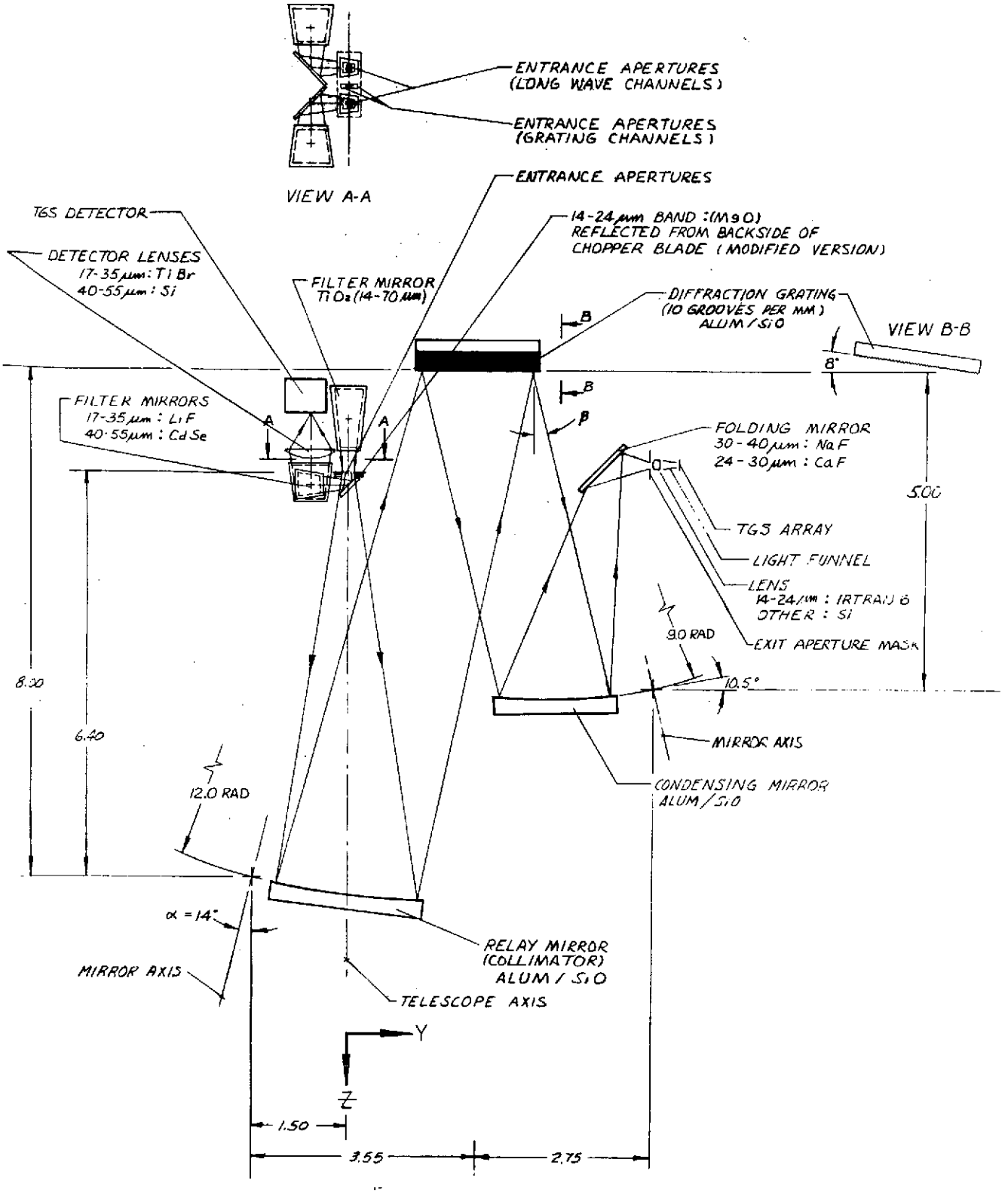

Figure 4-5. Grating Radiometer Optical Schematic

that might exist in the detector. The radiation is further scrambled by the light funnel.

The grating can be used in the m= -1 order only because radiation of wavelengths greater than 28 μm will occur with high efficiency at the same emergent angle (β) as wavelengths in the 14- to 24-μm band. Thus, filtering which will reject wavelengths greater than 28 μm is required for the shortest bandpass. The efficiency of the grating as a function of wavelength is considered below. When this efficiency is multiplied by the radiance distribution of Jupiter or Saturn we find that a rejection ratio of 10:1 is required to reduce the second order signal to a negligible level. This filtering is achieved by using the reststrahlen reflection band of MgO. The folding mirror just preceding the detector package for the 14- to 24-μm band is a plate of MgO. Further reduction of 28 μm is produced by the Irtran-6 lens which transmits only to 31 μm. The throughput of the combination is shown in Figure 4-6. The longer wavelength bands require no order filtering, but the detector mirror associated with them reflects 0.7 to 0.8 for $\lambda > 15$ μm and 0.15 for $\lambda < 14$ μm. This reflection combined with a similiar coating on the folding mirror in the telescope beam reflects $\sim 0.06\%$ for $\lambda < 13$ μm.

Alternatively, the final fold before the detectors can be eliminated if a bandpass transmitting filter for 14 to 24 μm is applied to the Irtran-6 lens. The best transmission that can be expected is shown as the dashed curve in Figure 4-6. The rejection for such a filter will be $\sim 0.1\%$, but this is not a deciding factor. The coating cost would be $\sim \$3000$ per lot, a factor of 10 to 20 times the cost of the MgO mirror and not nearly as durable or efficient. Furthermore, it would be desirable to reduce the $\lambda < 14$ μm response for the other channels by using another TiO_2 reflection. This folded geometry also serves to obscure the detector from direct scattering of stray light by the grating and relay mirrors. For these reasons we recommend the folding geometry for the detector package and MgO reststrahlen for the order filtering.

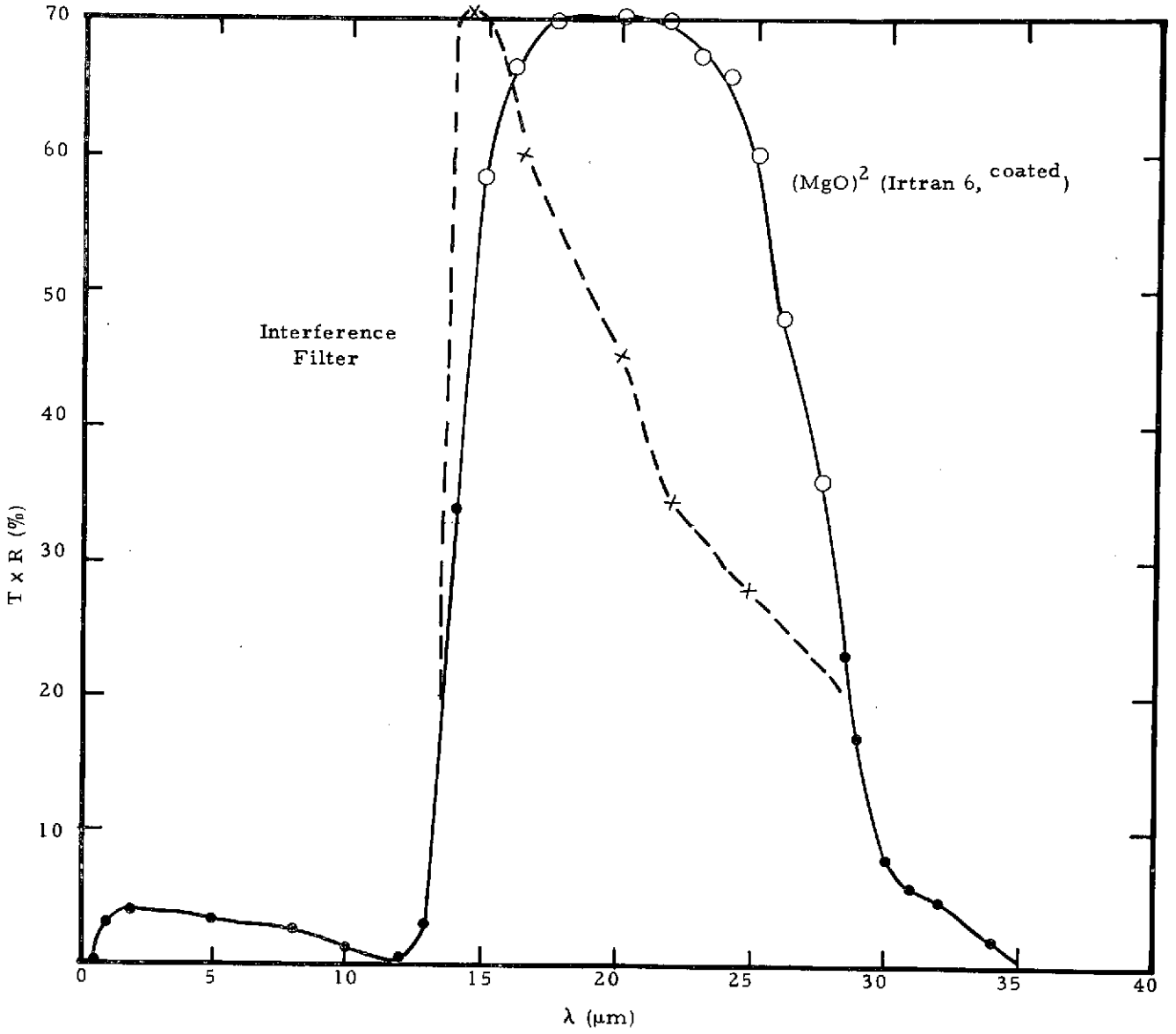

Figure 4-6. Order Filter for the 14- to 24-μm Band

The detector lenses and detector are mounted in close proximity at the opposite ends of gold-coated light funnels whose purpose is to condense the light bundle further. The final f/No. of the bundles will be approximately f/0.8 or smaller.

The most severe problem associated with using a diffraction grating for wavelength isolation for the proposed application is that of maintaining adequate efficiency in one order over the large span of wavelengths. No data are available from the suppliers concerning the spectral efficiency of a grating similiar to the discussed design for the spectral region >15 μm. The Measurements were made at SBRC on the original-type grating used for the Nimbus D Satellite Infrared Spectrometer (SIRS). The ruling was 26.93 g/mm, blazed at 45.6 μm and used (in four orders) to cover 11 to 36 μm. The M=1 order half-efficiency bandwidth was 17 μm; the quarter efficiency bandwidth was 30 μm. The peak efficiency for the best grating measured was 90 ± 5% for p- and s- polarization.

Communications with Perkin-Elmer Corp., and Dr. E. Loewen of Bausch and Lomb suggest that a 10g/mm ruling would have similiar m=1 order characteristics. Considerations regarding the expected energy distribution for the four bands, and especially within the 14- to 24-μm band where the radiance can change by the factor 5 (Saturn), 2 (Jupiter) between wavelength extremes, reveal an efficiency problem for the two extreme bands (Figure 4-7). If the grating is blazed near 18 μm the efficiency distribution will be uniform within the 14- to 24-μm band, but the SNR will be very low in the 35.7- to 38.4-μm band. If the blaze is shifted to, say 30 μm, the efficiency in the long-wavelength channel will be nearly doubled, but the great slope within the 14- to 24-μm band will produce a spike profile in the spectral transmittance for this band. The situation would be improved if the 14- to 24-μm band could be narrowed and the 35.7- to 38.4-μm band widened.

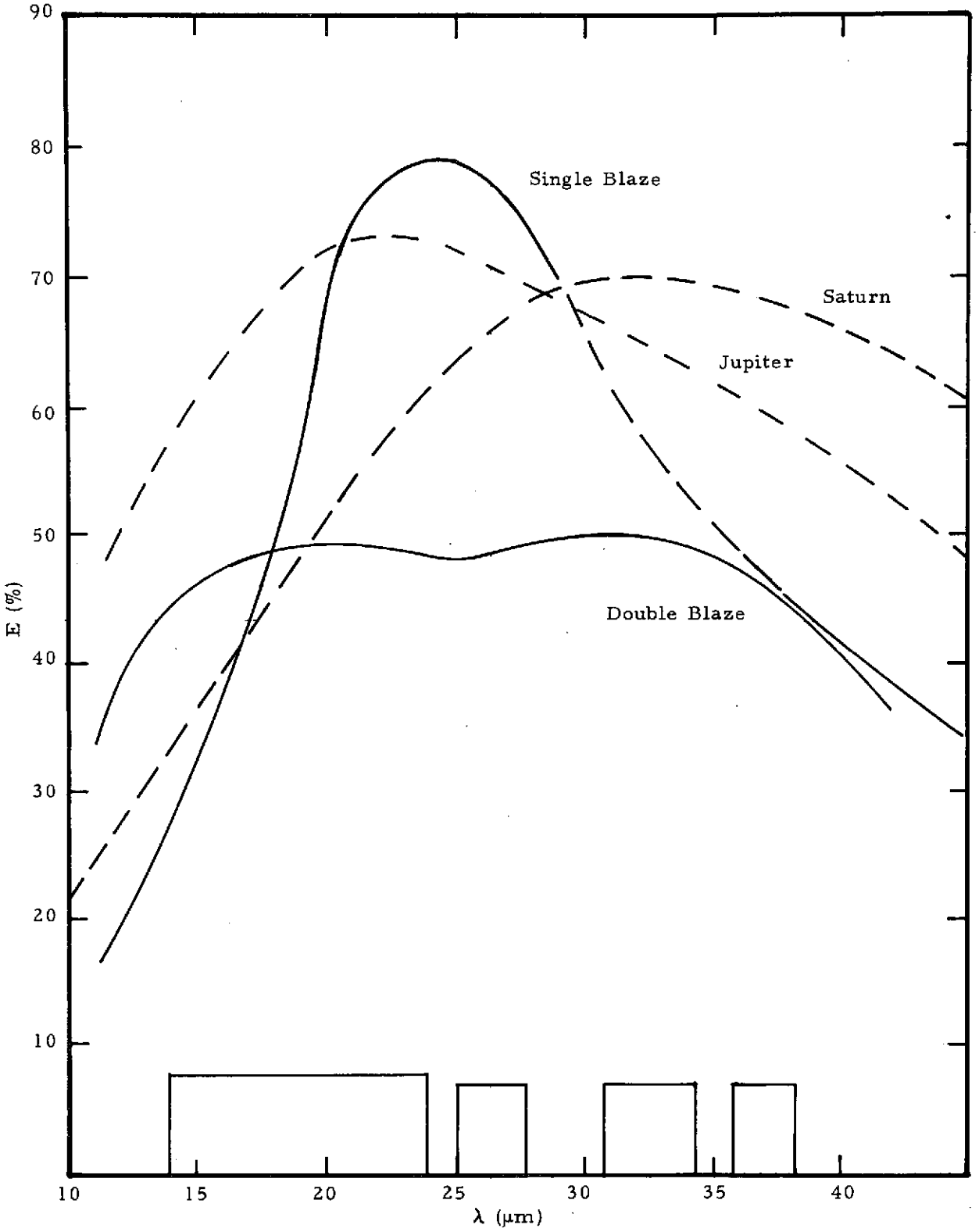

Figure 4-7. Predicted Efficiency of a 10g/mm Grating Blazed at 20 μm Compared with a Double-Blazed Ruling

An alternative solution is to use a double blazed ruling where each groove includes two blaze angles. Thereby the two blaze curves sum to give a flat efficiency curve over a broader region. The disadvantage is that only roughly half of the area of each groove contributes at a single groove angle. Thus, the peak efficiency is automatically reduced (see Figure 4-7). The approach eventually decided upon in the system appears later in this section.

Grating Specification

The grating equation for an off-plane mounting is

$$m\lambda = a \cos \gamma \, (\sin \alpha + \sin \beta).$$

where m = order number,

a = the ruling spacing

γ = off-plane angle,

α = angle of incidence referenced to the grating normal

β = angle of diffraction. β is negative for rays emerging at angles on the opposite side of the normal from α.

The angular dispersion is given by

$$\frac{d\beta}{d\lambda} = \frac{-m}{a \cos \gamma \cos \beta}$$

The wavelength of the blaze (or the blaze angle) is determined from

$$\sin \phi = \frac{-m}{2 \, a \cos \gamma \cos \alpha}$$

The design and ray tracing of the spectrometer was accomplished using the Paraxial Optical System Design program on the SBRC General Automation 18/30 Computing System. That program has the capability of handling tilted and decentered elements and diffraction gratings; however a program which can automatically optimize such a system does not exist. Consequently, many iterations were required to optimize all the wavelengths simultaneously. The resulting image quality is discussed further.

The specifications of the spectrometer are given in Table 4-3.

Table 4-3. Spectrometer Specifications

Grating	
Ruling Spacing, α	100.0 μm (10 grooves/mm)
Diffraction order m	-1.
Blaze Wavelength	20 μm
Blaze Angle, ϕ_B	5.8°
Clear Aperture	43 mm diameter
Spectrometer	
Dispersion, $d\beta/d\lambda$	0.0104 μm^{-1} at 25.8 μm
Off-plane Angle, γ	14.0°
Incidence Angle, α	8.0°
Exit Plane Scale (= $d\beta/d\lambda$ x f.l. coll. mirror)	1.2 mm/μm at 25.8 μm
Material	Aluminum with SiO coating

Spectrometer Aberrations

Because of the large angles of incidence and emergence, the relatively high speeds of the spectrometer arms (both of which result from the compact design), and the large entrance apertures, the images at the exit plane will normally be blurred by comatic and astigmatic aberration. In the present design this blur is minimized by using off-axis paraboloids for the relay and condensing mirrors. Figure 4-8 shows the image of a point on the edge of the telescope exit pupil, as rays from that point traverse the top of one entrance aperture, the axial point between the apertures, and the bottom of the second entrance aperture. The wavelength is 27.8 μm, and the scale is 10 times. The blur average diameter is 0.01 inch and results from residual astigmatism.

As a comparison, the smallest achievable blur for the corresponding aperture points for 10-mr apertures and a 12-inch diameter f/3.30 telescope is shown in Figure 4-9. The blur diameter is 10 times larger. Furthermore, the best foci for the other wavelengths in that design occur on an image plane which has a radius of curvature of 6 inches and a tilt angle of 9°. In the present system a flat focal plane is perfectly adequate.

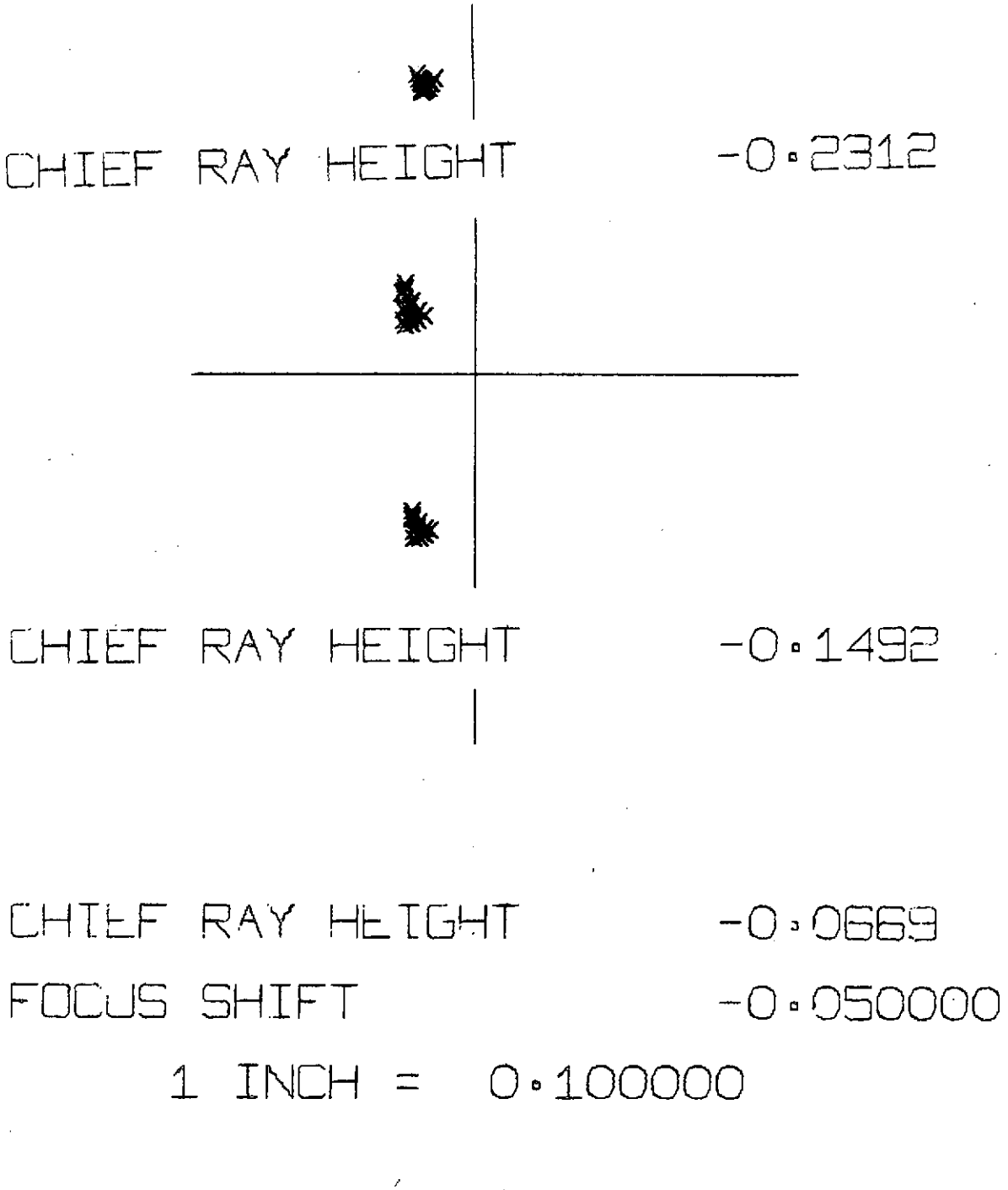

Figure 4-8. Spot Diagram at Spectrometer Exit Plane for Rays from 5.3 x 3 mr, f/3.5, 6 in. diameter Telescope. λ = 27.8 μm Top, Middle and Bottom of Entrance Field (see text).

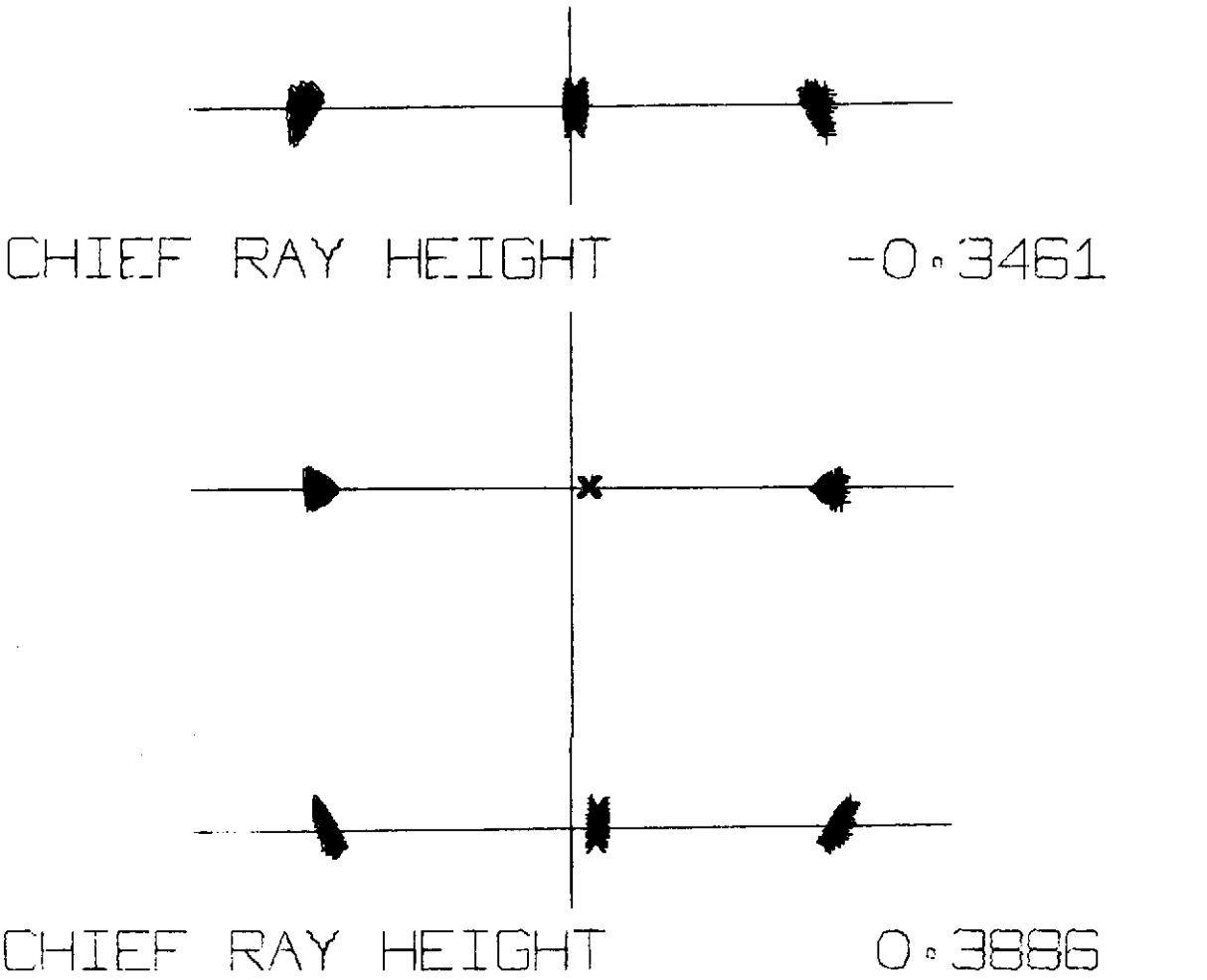

Figure 4-9. Spot Diagram for 10 x 10 mr, f/3.3, 12 in. Aperture
λ = 27.8 μm Top, Middle and Bottom of Field

The exit aperture dimensions that can be expected with the optical configuration and focal plane arrangement under discussion (f/3.50, 6 inch diameter telescope), two (rectangular fields 3 X 5.33 mr in size fields, etc.) are shown in Figure 4-10. The slight rotation of the images is characteristic of the off-plane mounting. It was necessary to adopt rectangular fields to eliminate the overlap between adjacent bands. Some residual effect is evident in Figure 4-10. This shape also reduces the aspect ratio for the detectors.

Another form of grating aberration is the difference in reflection coefficients between radiation polarized parallel to and perpendicular to the plane of reflection. No quantitative data for a comparable ruling is available, but the grating suppliers predict that coarse ruling (spacing 2.5 to 7 times the wavelength) should exhibit polarization to a relatively small degree.

A characteristic peculiar to diffraction gratings is the Wood anomalies.[11] These appear as dark bands when radiation is missing from a diffracted beam and appears in the zero order, or bright bands when radiation from the zero order appears in the diffracted beam. These anomalies are sensitive to the state of polarization: S anomalies occur for radiation whose electric vector is perpendicular to the grooves, P anomalies appear for the parallel vector.

The P anomalies are strongest in deeply grooved gratings and are absent at wavelengths greater than the groove depth. The S anomalies, however, are stronger at longer wavelengths. Wood's anomalies occur at wavelengths for which radiation at the same λ is diffracted in some order so as to graze the surface of the ruling. They occur nearly coincident with the Rayleigh wavelengths λ_R which are wavelengths which diffract at an angle of $\pm 90°$. Thus anomalies[11] occur at

$$\lambda_R = \frac{a}{m} \sin \gamma \, (\sin \alpha \pm \sin 90°)$$

The + sign is associated with +m and - with -m.

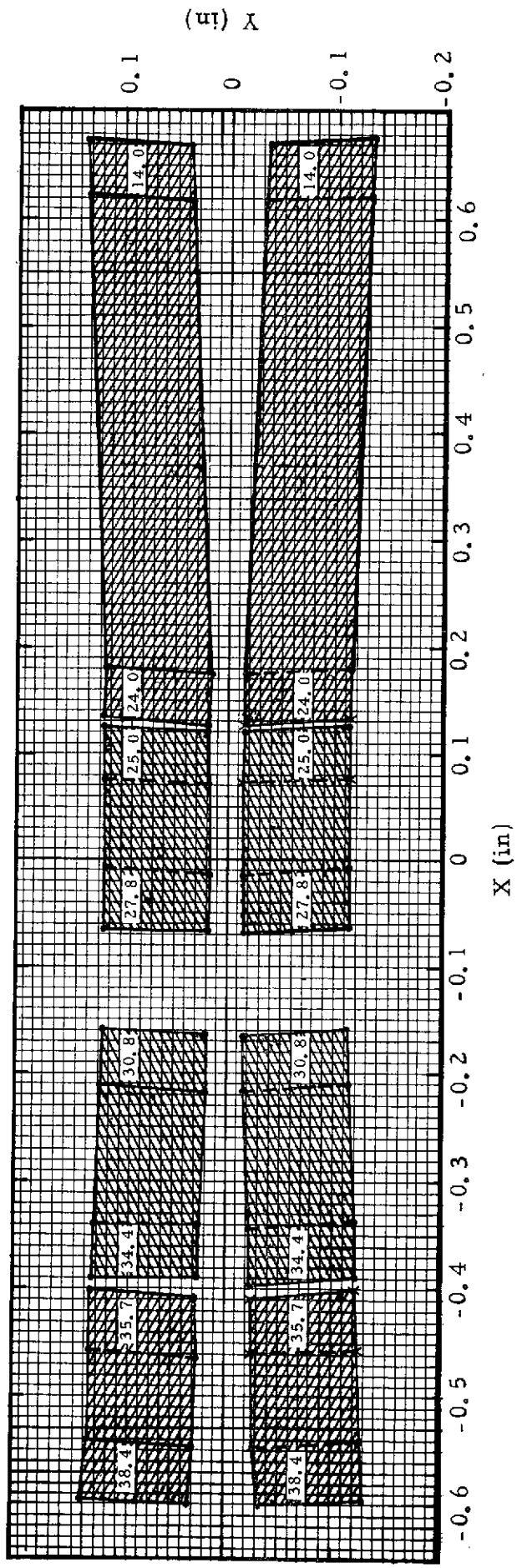

Figure 4-10. Exit Plane Aperture Configuration

For the grating proposed, a = 100 μm, α = 7.5°, γ = 14°, λ blaze ~ 20 μm, and λ_R for various orders are shown in Figure 4-11. These were calculated using an SBRC computer program which was developed for the Satellite Infrared Spectrometer (SIRS) project. For the nominal spectrometer parameters given above, a minimum number of possibly interfering anomalies appear in the long-wavelength bands, and it is not possible to eliminate or reduce the number of anomalies that might possibly appear in the 14- to 24-μm band.

In terms of scattered light and resolving power, there is no advantage to using replicated rulings at these wavelengths. However, the cost savings and reproducibility available with replicated rulings speak strongly in favor of them. The epoxies used for replication are reported to be reliable for extended use in high vacuum over temperatures ranging from +40°C to -20°C. Only a small line of epoxy is actually exposed to the environment. Assembly and alignment problems are also mitigated if identical rulings are used for multiple units.

SPECTRAL SLIT FUNCTIONS

Reference to Figure 4-10 reveals that the images at the spectrometer exit plane consist of an image of the entrance aperture in each wavelength contained in the bandpass plus the width due to linear dispersion. For the bands of interest the exit apertures have the dimensions given in Table 4-4.

Table 4-4. Exit Aperture Dimensions

Band (μm)	X (in.)	Y (in.)
14.0-24.0	0.55	0.10
25.0-27.8	0.29	0.10
30.8-34.4	0.33	0.10
35.7-38.4	0.29	0.10

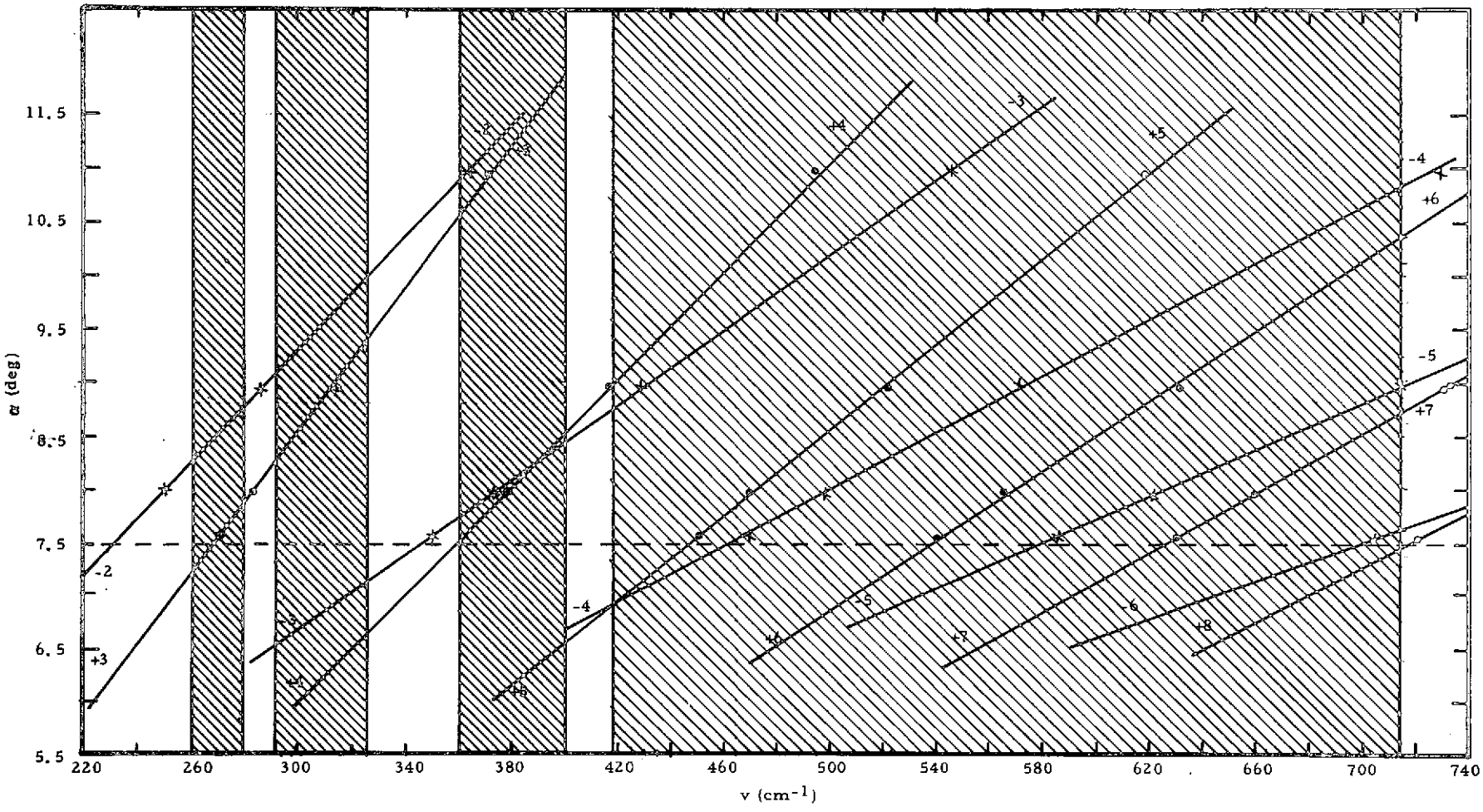

Figure 4-11. Predicted Rayleigh Wavelengths (Wood's Anomalies) for Various Grating Angles of Incidence (α) and Diffraction Orders -6 to +8. The Nominal Design α is 7.5 Degrees

Since the entrance aperture has a width of 0.063 inch, it is evident that convolution of the entrance and exit apertures will give trapezoidal functions. If it is assumed that the transmission through both of the apertures is

$$t(x) = \begin{cases} 1 & 1/2\ (-w_x) \leq x \leq 1/2\ (+w_x) \\ 0 & \text{otherwise} \end{cases}$$

where w_x is the aperture width, then the spectral slit functions will be represented by the shapes shown in Figure 4-12. For these wide slits Fraunhofer and Fresnel diffraction are negligible, as is the image blur of a point due to geometrical aberrations. Actual transmission functions will change the relative amplitudes and slopes of the spectral slit functions.

Spectrometer Materials

The materials are given in Figure 4-5.

Optical Tolerances

The computer program previously mentioned was used to determine the sensitivities of the optical efficiency and wavelength accuracy to spacing changes and tilts of the mirrors and grating.

In general, because of the inherent low resolution, the throughput efficiency (image blur size) has low sensitivity, and the resolution and wavelength accuracy are insensitive to relatively large spacing changes. In particular, it was found that an axial shift of 0.050 inch in the focusing of the condensing mirror causes an increase of 0.015 inch in the diameter of the blur circle for the image of a point. Since this is only 5% of the width of the narrowest slit, the resulting light loss would be insignificant.

If the grating is rotated 0.2° from its nominal position about the X-axis i.e., a change in the off-plane angle $\gamma = -0.20°$, a signal loss of 20% and a wavelength shift of 0.02 μm is produced. If the α angle (angle of incidence) is changed by -0.20°, a wavelength shift of 0.4 μm and no change in signal level is produced. Small rotations of the relay mirror will produce negligible changes. Rotation of the condensing mirror by -0.20° shifts λ by 0.024 μm,

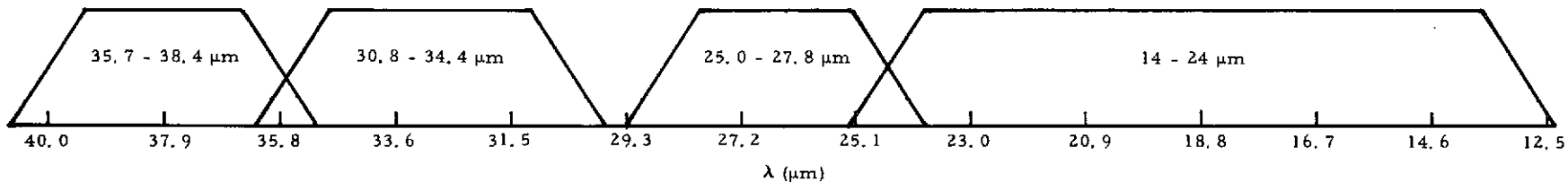

Figure 4-12. Spectral Slit Shape for Grating Spectrometer

but causes an image shift in the Y-direction by 0.020 inch producing a light loss of 20%. If the grating is ruled in aluminum and experiences a -100°C temperature change, the spacing will change by -1 μm causing a wavelength shift longward amounting to 0.36 μm. Tilting the folding mirror before the detectors by ~0.2° about the Y-axis will cause a wavelength shift of approximately 0.1 μm.

Thus, the spacings of the elements need not be held to tight tolerances, consequently aluminum mountings can be used. However, stresses or vibrations which might cause rotations in the elements, especially the grating, must be minimized. Furthermore, it would be desirable to rule the grating in beryllium (which would give a wavelength shift of 0.18 μm per 100°C) or perhaps titanium (0.12 μm/100°C). Glass would be best of all, however, it is heavier, and a ruling as course as 10 grooves/mm will have to be cut into the solid substrate rather than burnished into an aluminum coating.

OUT-OF-BAND RESPONSE

Since the grating channels will have sensitivity to all radiation for $\lambda > 1.2\mu m$, it is important to effectively attenuate the response to the higher order radiation that overlaps the desired first order radiation at the exit plane. Using a program developed at SBRC for the SIRS spectrometer, the contributions for all higher orders up to the silicon cutoff due to reflected solar radiation and blackbody radiation were computed.

For these calculations the following assumptions were made: 1) grating blaze wavelength of 22 μm; 2) Jupiter and Saturn radiances equivalent to blackbody temperatures of 134°K and 98°K respectively; 3) solar irradiance with spectral distribution of 5800°K blackbody; and 4) planet albedos of unity. It was also assumed that the higher order grating efficiency was never less than 5% even where extrapolated first order data would suggest that this should be true.

In summary then, the calculated results shown in Table 4-5 can be considered to be a worst case estimate of the out-of-band contributions. The filtering data shown in the table include the grating and TiO_2 folding mirror for the three lower wavenumber channels and with the addition of an MgO order filter for the highest wavenumber channel.

Table 4-5. Contributions of Higher Orders to Spectrometer Channels for Scattered Sunlight and Planet Emission[a]

Channel ν (cm^{-1})	Order Number (m)	Transmittance[b]	Jupiter			Saturn		
			Scattered Sunlight	134°K Blackbody	Out-of-band In-band	Scattered Sunlight	98°K Blackbody	Out-of-band In-band
260-279	1	0.30	-	1.00	-	-	1.00	-
520-558	2	0.04	nil	0.12	0.12	nil	0.05	0.05
etc.	3	0.01	↓	0.01	0.01	↓	0.002	0.002
	4-37	0.005	0.53	nil	0.53	0.45	nil	
Out-of-band Total →			0.53	0.13	0.66	0.45	0.05	0.50
291-325	1	0.42	-	1.00	-	-	1.00	-
582-650	2	0.09	nil	0.15	0.15	nil	0.05	0.05
etc.	3	0.008	↓	0.003	0.003	↓	nil	nil
	4-31	0.005	0.26	nil	0.26	0.25	↓	0.25
Out-of-band Total →			0.26	0.15	0.41	0.25	0.05	0.30
360-400	1	0.52	-	1.00	-	-	1.00	-
720-800	2	0.19	nil	0.13	0.13	nil	0.03	0.03
etc.	3	0.03	↓	0.002	0.002	↓	nil	nil
	4	0.02	↓	nil	nil	↓	↓	↓
	5-25	0.005	0.16	↓	0.16	0.19	↓	0.19
Out-of-band Total			0.16	0.13	0.29	0.19	0.03	0.22
417-714	1	0.32	-	1.00	-	-	1.00	-
834-1428	2	0.0002	nil	0.0002	0.0002	nil	nil	nil
etc.	3-22	0.0002	0.008	nil	0.008	0.01	↓	0.01
Out-of-band Total →			0.008	0.0002	0.008	0.01	nil	0.01

[a] Scattered sunlight assumed to have spectral distribution of 5800°K blackbody with planetary albedos = 1; in-band planetary radiance of Jupiter and Saturn assumed given by 134° and 98°K blackbodies, respectively; and grating blaze wavelength chosen at 22 μm. Effect of addition of selective chopper is discussed in text, but for clarity is not included in table.

[b] Transmittances include grating efficiency and TiO_2 folding mirror. (Note that initial design did not provide for reststrahlen order filters; proposed modifications include use of such order filters and effect is included in later table.)

From the tabulated results it is apparent that the order filter for the short-wavelength channel is effective at reducing the adjacent order contributions. However, the longest wavelength channels will require order filters to

reduce the second and third orders to acceptable levels. The scattered sunlight components contributed by the higher orders near the silicon cutoff wavelength obviously need to be reduced. This can be achieved either by means of additional order filtering as mentioned above and/or a selective chopper.

The use of a selective chopper which is transparent to $\lambda < 14$ μm but opaque otherwise allows maximum in-band modulation efficiencies to be maintained and permits the out-of-band signal to be effectively reduced. Among the possible materials for such a selective chopper blade are (See Figure 4-13):

Material	Thickness for T = .50 at 13 μm
Barium Fluoride	3 mm
Lead Fluoride	2.5
Sodium Fluoride	2

Since the crystal transmits 95% (89% for PbF2), the radiation at $\lambda < 10$ μm would be rejected by the factor 20 (9 for PbF2) by the modulation process. The radiation between 10 and 15 μm is reduced by a lesser factor because of the non-square shape of the absorption curve for the crystal materials. The residual out-of-band response can be further reduced by appropriate compensation of the crystal chopper. This can be done by blocking the "open" portion of the chopping cycle by an amount corresponding to the short-wavelength reflectance of the crystal chopper.

PROPOSED MODIFICATION AND EFFECT ON OPTICAL PERFORMANCE

As a consequence of the wide spectral coverage (14 to 38 μm) the grating efficiency necessarily would be fairly low for the longest wavelength grating channel. If the 14- to 25μm wavelength channel is separated from the longest three grating channels by a reflective chopper, the grating efficiency can be more nearly optimized. With this approach the measurement simultaneity is retained for all four channels. Selecting the blaze wavelength at

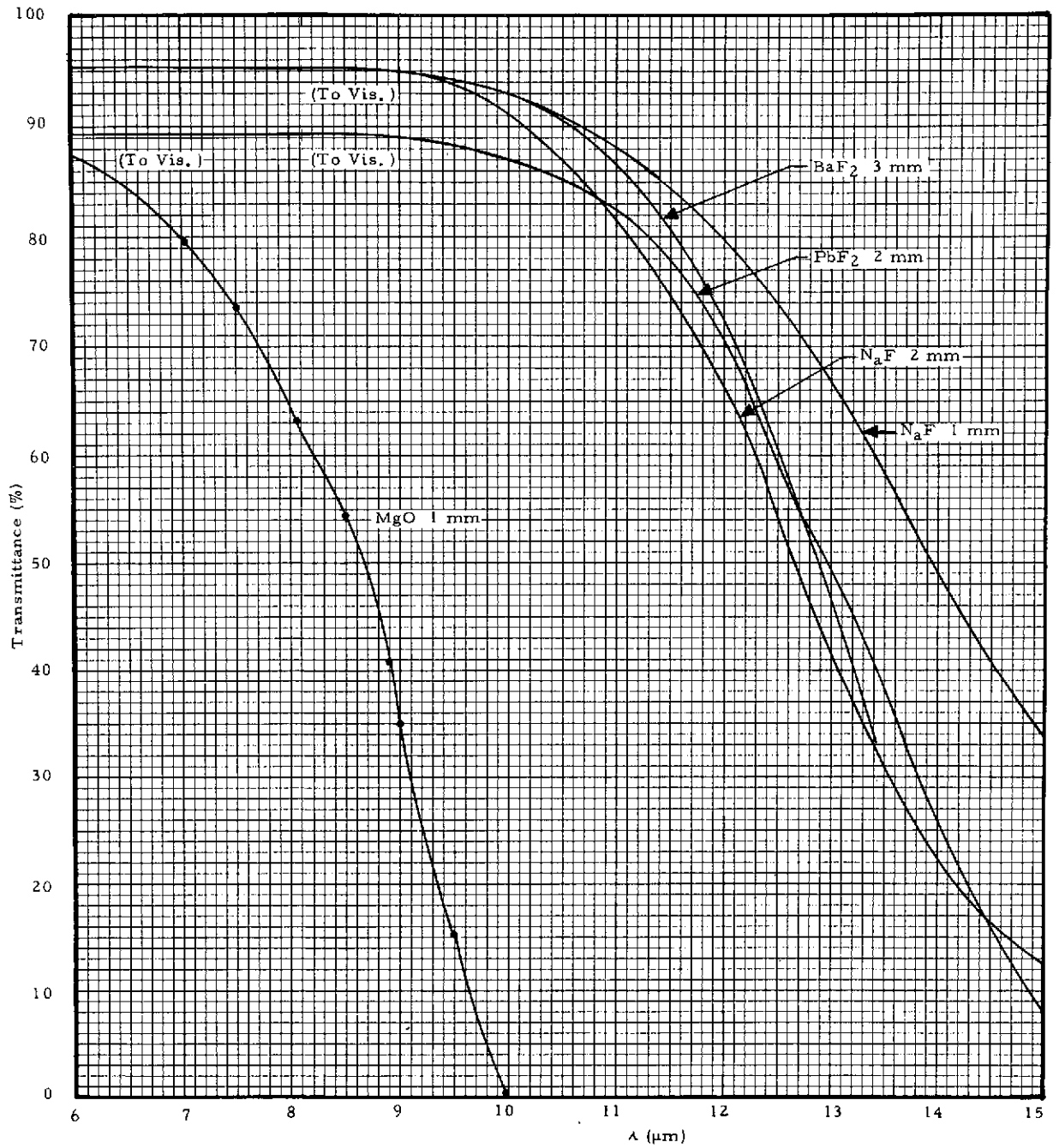

Figure 4-13. Selective Chopper Materials

31 μm results in approximately a factor of two increase in the grating efficiency in the longest wavelength channel and significant increases in the other two. This choice also retains the off-blaze condition for these channels to give efficient rejection of the high order grating orders. If the reflective chopper element is MgO then it can also serve as a selective chopper for all four channels.

The out-of-band response with the proposed modifications is given in Table 4-6. The tabulated values include the effect of the addition of reststrahlen

Table 4-6. Contributions of Higher Orders to Spectrometer Channels for Scattered Sunlight and Planet Emission with Proposed Modifications[a]

Channel ν (cm^{-1})	Order Number (m)	Transmittance[b]	Jupiter			Saturn		
			Scattered Sunlight	134°K Blackbody	Out-of-band / In-band	Scattered Sunlight	98°K Blackbody	Out-of-band / In-band
260-279	1	0.52	-	1.000	--	--	1.000	-
520-558	2	0.004	nil	0.007	0.007	nil	0.003	0.003
etc	3	0.001	nil	0.001	0.001	nil	nil	nil
↓	4-37	0.0002	0.01	nil	0.01	0.008	nil	0.008
Out-of-band Total →			0.01	0.008	0.018	0.008	0.003	0.011
291-325	1	0.58	-	1.000	-	-	1.000	-
582-650	2	0.005	nil	0.006	0.006	nil	0.002	0.002
etc.	3-5	0.002	0.0001	0.001	0.001	↓	nil	nil
↓	6-8	0.001	0.0003	nil	0.0003		↓	nil
	9-31	0.0002	0.008	nil	0.008	0.007		0.007
Out-of-band Total →			0.008	0.007	0.015	0.008	0.002	0.010
360-400	1	0.48	-	1.000	-	-	1.000	-
↓	2	0.003	nil	0.002	0.002	nil	0.0004	0.0004
	3-4	0.002	0.0001	nil	nil	↓	nil	nil
	5-6	0.001	0.0002	↓	↓		↓	↓
	7	0.0005	0.0001					
	8-25	0.0002	0.006		0.006	0.007		0.007
Out-of-band Total →			0.007	0.002	0.009	0.008	0.0004	0.008
400-700	In-band	0.44	-	1.000	-	-	1.000	-
Out-of-band Total →			0.0001	nil	0.0001	0.0002	nil	0.0002

[a] Scattered sunlight assumed to have spectral distribution of 5800°K blackbody with planetary albedos = 1; in-band planetary radiance of Jupiter and Saturn assumed given by 134° and 98°K blackbodies, respectively; and grating blaze wavelength chosen at 31 μm. The effect of a selective/reflective chopper is discussed separately in the text.

[b] Transmittances include grating efficiency, TiO_2 folding mirror reststrahlen order filters of NaF for longest wavelength channel and CaF_2 for other two grating channels, and three MgO reststrahlen reflections and an Irtran-6 detector lens for the 400- to 700-cm^{-1} channel.

order filters for the three grating channels; NaF for the longest wavelength channel and CaF_2 for the other two. The calculations for the shortest wavelength channel (400-700 cm^{-1}) assume two additional MgO reststrahlen reflections in addition to that from the chopper blade. The effect of the use of the MgO selective chopper has not been included in the table. Such a chopper would reduce the tabulated out-of-band contributions in all four channels from wavelengths shorter than 6 to 7 μm by a factor of nearly eight. While the calculated out-of-band response for the shortest wavelength channel assumed three MgO reststrahlen reflections, the use of two such reflections including one from the selective chopper should give adequate rejection with an increase in in-band transmittance and a slight broadening of the channel spectral width.

CVF INSTRUMENTATION AND TELESCOPE B

The CVF spectrometer is designed around the current state-of-the-art filter wheel (continuously variable bandpass) produced by Optical Coating Laboratories, Inc., of Santa Rosa, Ca. To save weight, the filter segments are of minimum size and mounted (bonded) in a custom filter-wheel frame (See Figure 4-14).

Specific MJS design requirements for the filter wheel spectrometer are:

1. 2% bandwidth of center wavelength for four broad spectral ranges.
2. Spectral Ranges (μm)
   - 0.8 to 1.3
   - 1.25 to 2.45
   - 2.35 to 3.0
   - 2.9 to 3.5
   - 3.4 to 6.0
3. Each 2% wide spectral element must be contained within one IFOV of the telescope having a solid angle equivalent to 4 X 4 mr.
4. The CVF must have unique 2% spectral bands for each 3.6° of rotation which corresponds to two 1.8° steps of the drive motor.

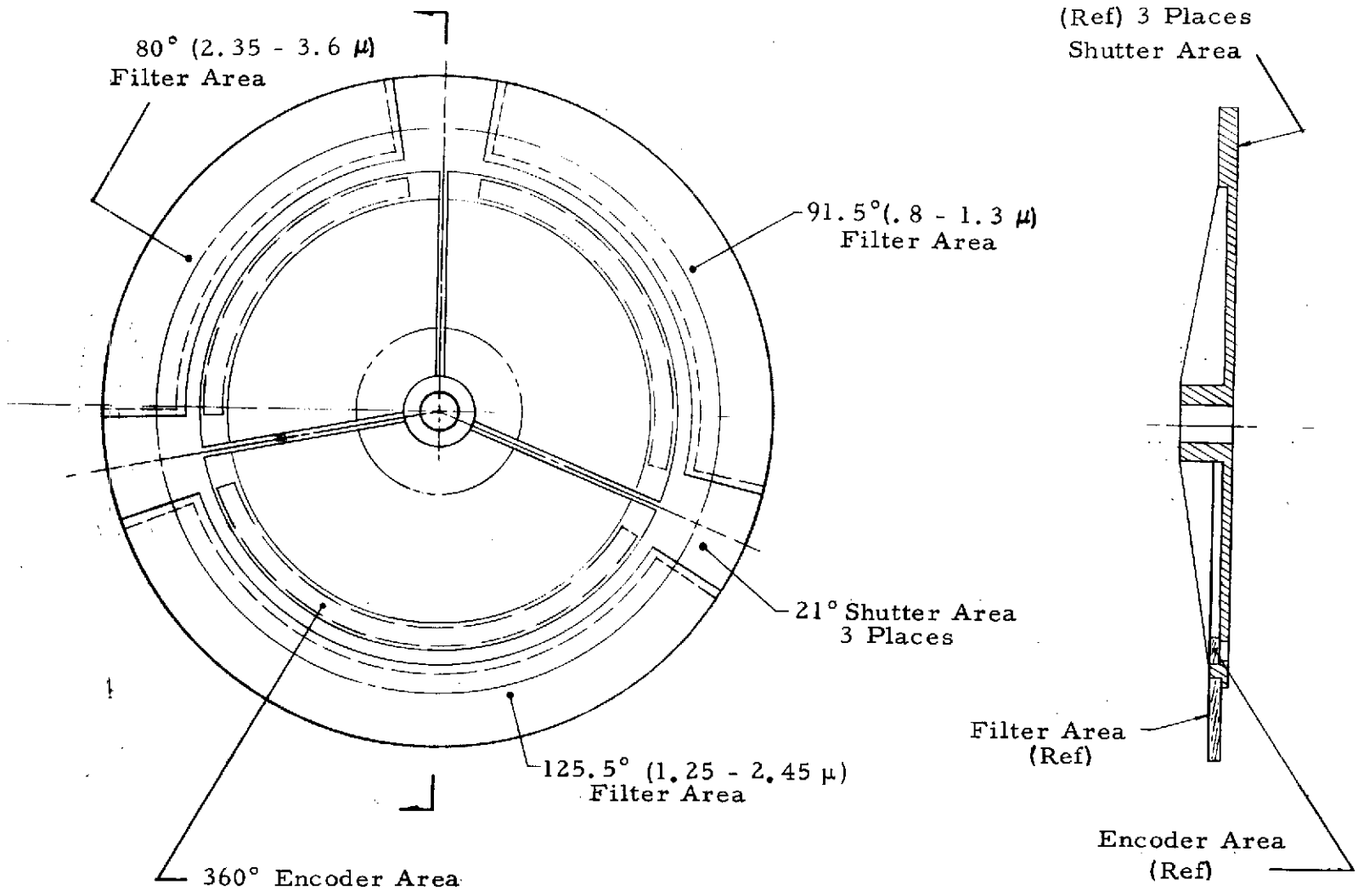

Figure 4-14. CVF Wheel Mounting for Circular Filter Segments

5. The IFOV must be shaped with a wedge angle of the sides of 3.6° to provide the best band-pass edge, and be configured close to a truncated square so that the immersion lens diameter may be small, and still capture all corner rays from the FOV.
6. The field stop must be as close as possible to the CVF wheel so that the spectral resolution element is sharply defined. The chopper blades must also be placed close to the field stop to produce an efficient chopping waveform and to keep the chopper small.
7. The FOVs for the PbS and the two PbSe channels must be as close together (in a line suitable for modulation) as mounting and optical parameters permit.
8. A common 0.030-inch thick sapphire window must be located over the cooled immersed detectors for use in laboratory test configurations and to prevent condensation of contaminants on the detector immersion lenses.
9. A 4.25 to 4.75 μm channel (also immersed PbSe) must share the same chopper as the CVF wheel.

Figure 2-5 illustrates the design solution. The 4.25- to 4.75-μm channel FOV, which is in line with the CVF PbS spectrometer and the PbSe detector channels FOVs (bands 1 through 4), continuously operates behind a fixed bandpass filter located at the edge of the filter wheel. This channel, using an immersed PbSe detector, shares the same radiation cooled-cold finger, sapphire window, and vibrating fork chopper.

The PbS and PbSe detectors immersed on strontium titanate immersion lenses (hyperhemispheres) are located close to the field stops which are deposited on the sapphire window. The immersion lenses image the telescope entrance aperture on the detector sensitive areas. The fixed PbSe, 4.25- to 4.75-μm channel, located at the edge of the filter wheel utilizes the same optical configuration as the CVF channels except that the bandpass filter is deposited on the sapphire window within the field stop area. Figure 2-5 shows schematically a cemented filter substrate instead of the direct deposition on the window. The direct deposition of the 4.25- to 4.75-μm filter allows for better baffling against crosstalk between channels.

The desired design feature of an added spectral range of 3.4 to 6.0 μm using 2% wide spectral elements in series with the other spectral bands was not feasible in the above CVF wheel design because of the limitation of 3.6° elements within 360°; i.e., a total of 100 elements. Consequently the CVF segment covering 3.4 to 6.0 μm can only be placed in parallel with the shorter wavelength filter segments, and closer to the center of the filter wheel. The HgCdTe detector and field lens required for this spectral range will also be located closer to the center. The germanium field lens images the entrance aperture on the detector. Figure 2-5 shows the lightweight, metal mounted filter segments, the CVF, field stop, chopper, and detector assembly, but does not show the HgCdTe channel. The design of a longer tuning fork chopper to modulate all four FOVs was not covered in this study.

The maximum chopped aperture available in a standard American Time resonant fork chopper configuration at 600 Hz is 0.120 inch. The FOVs can be shaped to stay within this limit, without loss of the solid angle of 16×10^{-6} steradians. The chopping frequency of 500 Hz designed for the 0.120-inch width aperture is a good compromise for the PbS and PbSe detectors. (Wider chopping apertures would necessitate lower chopping frequencies for the same power.

Chopper location with respect to the CVF wheel: Space limitations dictate that the drive motor for the CVF wheel and the chopper actuator be on opposite sides.

An encoder pattern is deposited on a circular zone substrate bonded to the CVF filter wheel assembly on the inside edge of the CVF filter substrate. An encoder source and pickup assembly picks off the the position of the filter wheel which is converted to an exact spectral bandpass by reference to the wavelength calibration data.

Dichromatic Filter (in Telescope B)

Division of wavelengths 6 to 70 μm and 0.4 to 4.0 μm is accomplished by means of a design developed by SBRC in cooperation with an outside coating laboratory. It consists of a multilayer stack which extends the reflection

region of a reststrahlen coating from 14 to 6 μm. A first attempt in the construction of this filter showed encouraging optical results, but stresses in the relatively thick layers and poor adhesion to the sapphire substrate caused the multilayer to flake. Work is continuing, using other substrate materials and processes.

The selective reflector used to fold the telescope beam before the grating entrance is coated with TiO_2 to take advantage of its high reststrahlen reflection efficiency. This coating also partially rejects radiation $\lambda < 13$ μm. While the rejection is not as great as that found for bulk TiO_2 (namely 5 to 10% reflectance), the coating does not display the multiple phonon absorption bands at 22 and 24 μm that occur with bulk material. Also, the maximum size available for TiO_2 crystal is 22 mm in diameter. It is believed that the average reflectance can be raised to 70-80% by making the coating thicker. This improvement is intimately associated with the dichromatic development in progress.

Replicated Mirrors for Telescopes A and B

The two 6-inch diameter, F/3.5 telescopes are of identical Ritchey Chretien design except for the utilization of the image surfaces, and for the internal folding of the B telescope to the side. (See Figures 2-1 and 2-2.)

The mirror blanks are machined from aluminum, 0.050 inch thick for the primary mirror, and 0.040 inch thick for the secondary mirror. After suitable stress relieving and surface preparation, the optical surfaces and coatings are replicated on to the aluminum blanks. The coatings and epoxy have a combined thickness in the range of 0.001 to 0.003 inch. The extremely thin layer of epoxy forming the basic optical surface makes the thermal expansion mismatch between materials an insignificant factor.

The selection of thin-layer replication on aluminum backings was made to obtain lightweight mirrors which have the advantages of high thermal conductivity (low thermal gradients) of aluminum. The lightweight (thin) mirror blank is feasible when the blank does not have to withstand the normal

loads of optical fabrication. Consequently, the aluminum backings need only be thick enough to support their own weight. The aspheric figures for the primary and secondary mirrors are transferred from a glass master, which has been coated with a release agent, the overcoating (SiO), aluminum, and the layer of epoxy which is bonded to the metal substrate. The aluminum substrate is machined to within 0.001 inch of the final optical figure, so that the replicated layer of epoxy may be thin (0.001 to 0.003 inch). The glass master is separated from the overcoating layer of SiO with the aid of a release agent originally deposited on the glass master.

The Sisyphus optical system on the Pioneer 10 Spacecraft has an 8-inch diameter reflective optical system with replicated-aluminum mirrors-which has about 1.5-mr image blur at F/1.0. Mr. Harro Wahl, who fabricated the 8-inch diameter F/1 replicated telescopes for Pioneer 10 reports the following data:

> "Practical data were obtained by putting an 8-inch F:1 telescope made from 0.060-inch aluminum through the following tests:
>
> | | |
> |---|---|
> | Vibration: | Up to 40g peak sinusoidal to 100 kHz
$15g^2$ g^2/Hz random to 2,000 kHz |
> | Thermal Vacuum: | +120°F to -365°F at 10^{-5} torr |
> | Mechanical Shock: | 50g |
> | Thermal Shock: | Dropping of the entire assembly at 130°F into LN_2 |
>
> No mechanical or optical damage was observed even after repeated cycling. The optical resolution was maintained during the temperature change from +120°F to -365°F."

Mirror Durability

A current data sheet from Harro Wahl of Replica Optics Inc., lists the following under the heading, "Durability":

> "Replica mirrors pass the following Military Specifications:
> MIL-M-1350 B paragraph 4.4.6 and 4.4.7 MIL-C-675A
> MIL-STD-810 B, method 503, procedure 1
> Aluminum-backed lightweight replica mirrors have been

cycled between 100°C and LN_2 temperatures, without physical or optical damage to the structure. Spherical replica mirrors on pyrex backings with better than a 10th wave accuracy have been checked over a period of 10 years; no degradation of the optical figure has been observed to date. Replica diffraction gratings have been in continuous use for over 20 years in commercially built spectrophotometers."

The primary and secondary mirrors of the proposed Ritchey Chretien design are both mounted with space qualified, low modulus bonding materials. The bonding materials will be filled to provide good thermal conduction paths between the mounts and the mirror. The maximum change in mirror spacings and figure (curvature) due to thermal environment has been calculated to have the combined net effect of changing the back focus (image plane location) by 0.003 inch. (See Thermal Analysis Section.) The depth of focus of the F/3.5 telescope for a usable blur of 0.016-mr maximum (0.8 mr) is approximately 0.040 inch.

The depth of focus, otherwise known as the axial position tolerance of the image surface in relation to the field stop, is not critical. The telescope may be focussed for the optimum value at the middle of the operational temperature range, assuming the mirrors and spider temperature calculated for the space thermal environment. (See the Thermal Analysis Section for the analysis showing predicted temperatures for the telescope components.)

Alignment of the two telescope axes to within 1.0 mr may be accomplished by using conventional shimming and field-stop adjustment techniques.

Alternate Design Considerations for Primary Mirrors

The 6-inch diameter telescope primary mirrors were not considered candidates for honeycomb backed, sandwich type substrates because the rigidity of the thin aluminum backings is sufficient for the MJS application. During one phase of the design study consideration was given to the need for a 12-inch diameter telescope for the grating spectrometer. Honeycomb mirror structure was recommended for a lightweight primary mirror design using a replicated optical surface. The mechanical design section of this

report covers the description of the fluxless brazed aluminum honeycomb which is proposed for other portions of the instrument structure. The honeycomb described is basically the same as considered for the 12-inch diameter primary mirror. The aluminum skin on the concave surface was to be machined to within 0.001 inch from the final optical figure, which was also within 0.001 inch deviation from a sphere. Figure 4-15 shows the mirror configuration. An aluminum honeycomb backed 12-inch diameter concave mirror with a replicated optical surface has never been fabricated according to information available to this date, although large plane mirrors have been made. Consequently, if the 12-inch diameter telescope were to be proposed for MJS, SBRC would recommend that a feasibility-hardware development program be initiated.

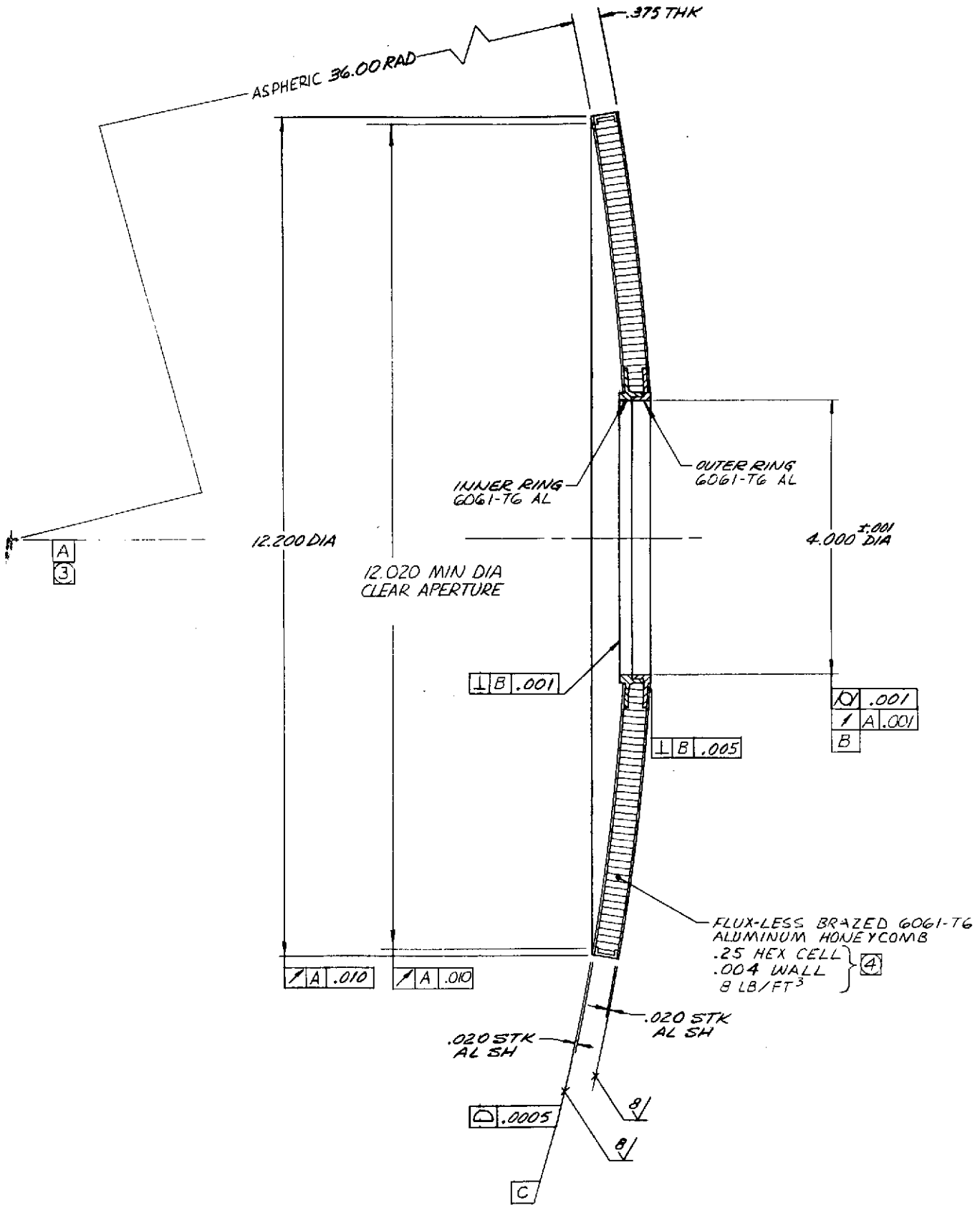

Figure 4-15. 12-inch Diameter Honeycomb Backed Primary Mirror

REFERENCES

1. Y. Yamada, A. Mitsuishi and H. Yoshinaga, J. O. S. A. 52 17, (1962).
2. G. Picus, E. Burstein, B. W. Henris and M. Hass, J. Phys. Chem. Solids 8, 282 (1959).
3. S. D. Smith and J. S. Seeley, Multilayer Filters for the Region 0.8 to 100 microns. Final Scientific Report. Contract AF 61 (052)-835, (1968).
4. R. Ulrich, Infrared Physics 7, 65 (1967), Ibid p. 37.
5. R. D. Rawcliff and C. M. Randall, Appl. Opt. 6, 1353 (1967).
6. G. D. Holah and S. C. Smith, Interference Filters for Wavelengths Greater than 40 μm, Joint Confer. in IR Tech., U. Reading 21-23 Sept., 1971, p. 143-154.
7. R. Ulrich, T. J. Bridges, M. A. Pollack, Appl. Opt. 9, 2511 (1968).
8. R. Ulrich, Appl. Opt. Opt. 7, 1987 (1968).
9. Karl Dieter Moller and Water G. Rothschild, Far Infrared Spectroscopy (John Wiley & Sons New York, 1971).
10. Piper and Marple, J. Appl. Phys. 32, 2237 (1961).
11. (Ref: James E. Steward and William S. Gallaway, Appl. Opt. 1, 421 (1962); a more recent theory is given in S. Jovicevic and S. Sesnic, J. O. S. A. 62, 865 (1972); a theory which is capable of predicting intensities as well as positions is given in C. Harvey Palmer and Howard W. LeBrun, Appl. Opt. 11, 907 (1972). This paper attributes the anomalous behavior to multiple diffraction within a single groove.)

Section 5
DETECTOR CONSIDERATIONS

Five types of detectors are required for the MJS Inrared Instrument because of requirements of sensitivity and broad spectral coverage. Table 5-1 summarizes the detector types, usage and typical performance. See also Table 3-4.

Table 5-1. Detector Summary

Wavelength (μm)	Detector Type	Cooling (°K)	Chop. Freq. (Hz)	D^* (cm-Hz$^{\frac{1}{2}}$-W^{-1})	NEP (Watts/$\sqrt{Hz}$)	Size (mm x mm)
14.0-24.0	TGS	None	10	$1.32 \times 10^{+9}$	4.6×10^{-11}	0.61 x 0.61
25.0-27.8	TGS	None	10	1.28×10^{9}	8.0×10^{-11}	0.61 x 1.73
30.8-34.4	TGS	None	10	1.24×10^{9}	8.75×10^{-11}	0.61 x 2.0
35.7-38.4	TGS	None	10	1.32×10^{9}	7.8×10^{-11}	0.61 x 1.73
17.0-35.0	TGS	None	10	$1.32 \times 10^{+9}$	4.6×10^{-11}	0.61 x 0.61
40.0-55.0	TGS	None	10	$1.32 \times 10^{+9}$	4.6×10^{-11}	0.61 x 0.61
0.8 -3.0	PbS	180°	500	3.6×10^{11}	1.1×10^{-13}	0.395 x 0.395
2.9 -3.5	PbSe	180°	500	1.5×10^{10}	2.6×10^{-12}	0.395 x 0.395
3.4 -6.0	HgCdTe	180°	500	3.4×10^{10}	1.2×10^{-12}	0.395 x 0.395
4.25-4.75	PbSe	180°	500	1.85×10^{10}	2.1×10^{-12}	0.395 x 0.395
0.4 -4.0	Thermopile	None	None	2.4×10^{8}	9.5×10^{-11}	0.228 x 0.228
6.0 -100	Thermopile	None	None	2.0×10^{8}	1.14×10^{-10}	0.228 x 0.228

THERMAL DETECTORS

Long-wavelength operation and limited detector cooling capabilities require the use of thermal detectors. Of the three generally available types, namely thermistor bolometers, thermopiles, and pyroelectric detectors, thermistor bolometers were rejected out-of-hand owing to poorer performance than the other two. The NEP for thermistors is higher than for TGS detectors. Also, thermistor bolometers require higher chopping frequencies; they have inherent 1/f noise and they require bias supplies which themselves can have significant 1/f current noise. Furthermore, owing to large bias voltages, thermistor bolometers tend to be microphonic. Therefore, in applications where mechanical vibrations are involved, these detectors tend to be noisy.

Of the two remaining types, evaporated antimony-bismuth thermopiles were first considered for use in the long-wavelength channels primarily because of SBRC's experience with them. SBRC-developed thermopiles have been used successfully in a number of past projects; namely, Mariner '69, '71 and Pioneer-10 radiometers. These systems took advantage of the fact that thermopiles do not require chopping and can operate at dc; that is, no 1/f noise is associated with thermopiles, only Johnson noise. Electronically chopping the output minimized 1/f noise contribution from the preamplifier. In addition, by using a full-wave chopper voltage doubling, which doubled both the detector signal and the noise, provided a system which was less preamplifier-noise limited than would otherwise be the case. A third development involving thermopiles was to center-tap them; that is, provide the same number of junctions on one side of the center-tap as the other and operate the detector into a differential input preamplifier. This provided common mode rejection of chopping spikes, RFI, and other noise effects.

In spite of these advantages, after reviewing the available detector types and performance, it became clear that pyroelectric detectors, in particular, triglycine sulphate (TGS) was a superior detector in terms of detectivity. The device acts as a capacitor; hence, the responsivity of the

device is inversely proportional to frequency. Since the device does not operate at zero frequency, chopping is required. This is a particular disadvantage because of the chopping losses involved (a factor of 2.45), and also the power, weight, and reliability problems associated with the chopper. However, in this case, a factor of approximately 10 improvement in detectivity is possible with pyroelectric detectors as compared to thermopiles and hence the advantages override the previously mentioned disadvantages.

Performance of various types of pyroelectric detectors are discussed in detail in a later section of this report.

THERMOPILE STUDY

As a part of this study thermopiles were examined with two basic goals in mind. The first was to determine an optimum blacking material to be used with thermopiles and the second was to design a thermopile with a large sensitive area. During the early phases of the study it was thought necessary to have large area thermopiles for the grating instrument (about 6 X 10 mm). This is about an order of magnitude larger area than has previously been made, and problems with scaling the NEP with the square root of the area were anticipated. Also, fabrication techniques needed to be examined.

Blacking Materials

A schematic of a typical evaporated bismuth antimony thermopile is shown in Figure 5-1. The collector is a gold evaporation which, for previous detectors, has been covered with a form of bismuth oxide. Reflectance measurements of the black made prior to this study show the unabsorbed radiation, i.e., total reflectance, to be in the order of 50 to 60% over the range of interest.

Figure 5-2 shows the spectral dependence of absorptance of the bismuth oxide black used for typical SBRC thermopile detectors. As can be seen the absorptance is down to about 50% beyond 25 μm where operation of the grating instrument is required. The study therefore attempted to find a better

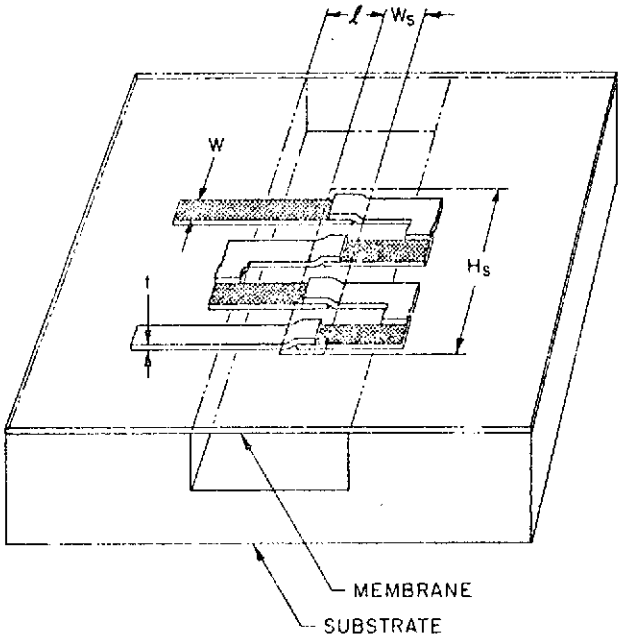

Figure 5-1. Evaporated-Thermopile Schematic

blacking material which would have higher and more uniform absorption at long wavelengths. The hoped-for improvement could reasonably only be a factor of about 1.5.

Materials selected had to be applicable through a defining area of a mask onto a thin film (less than 2000Å). Preferably, the materials should be nonconductive so as not to short out adjacent couples. Table 5-2 shows the materials selected.

The two paints, Cat-a-Lac Black and 3M Velvet Black, were applied with an airbrush through a mask. The third coating was several evaporated interference layers to optimize the absorptance at long wavelength. Performance with these three coatings was to be compared with thermopile No. 23 (Table 5-2) which had the best electrical characteristics of the conventional configuration. Where a thermopile number indicates two blackings, the bismuth oxide was applied, tested, and then removed. The comparative coating was then applied. In cases where the sensitive area was poorly defined (those with paint), all electrical characteristics were normalized to

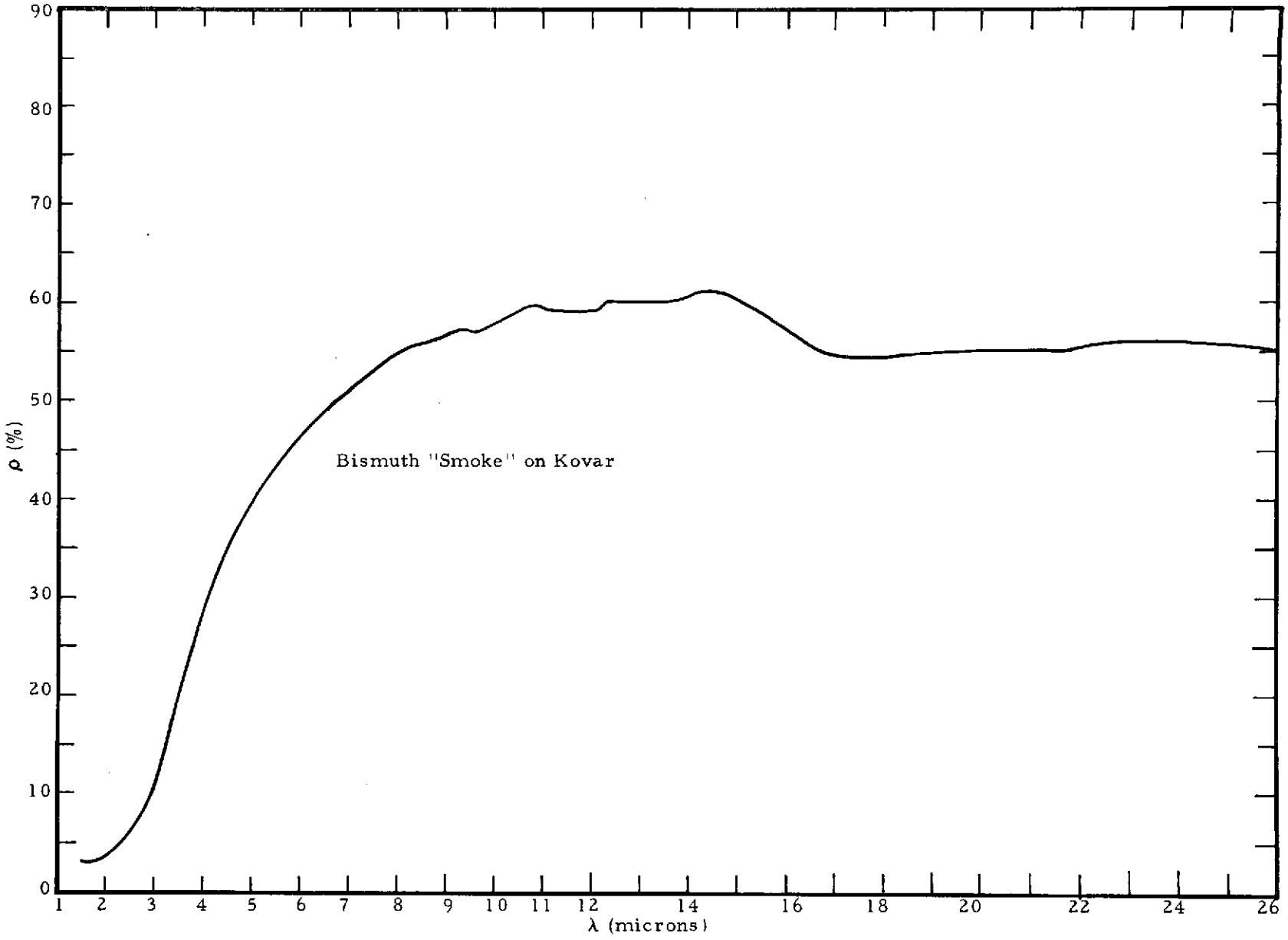

Figure 5-2. Total Reflectance of Bismuth Oxide on Kovar

Table 5-2. Comparative Tests of Various Materials for Use as Thermopile Collectors

Thermopile No.	Blacking Material	Blacking Thickness (inches)	Z (KΩ)	R (V/W)	τ (sec)	Response (μV)			Long-Wavelength Degradation Factor		Responsivity (1) (V/W)	
						Wide Band	MVM Filter	14 μm Filter	MVM Filter	14 μm Filter	MVM Filter	14 μm Filter
23	Bismuth Oxide	0.0007 or <	9.8	288	0.072	620	130	24.5	4.8	25.3	60	11.5
1	Bismuth Oxide	0.0007 or <	8.2	230	0.074	480	94	21.0	5.1	22.8	45	10.0
1	Cat-A-Lac	0.0015	8.2	350	1.2	820	142	29.0	5.1	28.3	68	12.0
2	Cat-A-Lac	0.0015	8.5	305	1.1	680	125	25.0	5.5	27.3	55	11.0
13	Bismuth Oxide	0.0007 or <	8.5	288	0.080	640	94	26.0	6.8	24.8	42	11.6
13	3M Velvet	0.0004	8.9	354	0.6	800	182	27.0	4.4	29.3	80	12.0
28	Bi/Ge/ZnS Evaporation	(2)	11.2	221	0.3	550	100	27.5	5.5	20.0	55	11.0

Test Conditions:
1) Blackbody at 600°C
2) Source aperture area = 0.332 cm^2
3) Detector sensitive area = 1.83×10^{-3} cm^2
4) Test package equipped with 0.020-inch thick uncoated Si window
5) All electrical measurements in vacuum
6) MVM Filter: Irtran-2 with 7.5- to 14-μm coating
7) 14-μm Filter: KRS-5 with ~14.5 μm to KRS-5 cutoff

Notes: (1) Not corrected for optical losses
(2) Bi 0.5 μm
Ge 3.1 μm
ZnS 2.3 μm

the area indicated. In the wide-band measurements the paints gave an average of 25% increase in responsivity. The bismuth/germanium/zinc sulfide response was down about 10%. In the 7.5- to 14-μm wavelength region the paints gave an average 15% increase in responsivity with the bismuth/germanium/zinc sulfide response down slightly over 20%. In the 14.5-μm-plus region all the investigated coatings gave about a 15% increase in responsivity. The error in measurement not taken into account in the preceding percentages was around 10%. All improvements, however, were from a general raising of the signal level. The degradation factor (Ratio $\frac{\text{Response wide-band}}{\text{Response @ 714.5 } \mu\text{m}}$) is as great or greater with the new blacks than with the bismuth oxide. Therefore, the responsivity improvement was small.

Table 5-2 also shows the effect of the new coatings on time constants. In the case of the paint, the time constant was increased from less than 100 msec to about 1 second. Therefore, in terms of figure of merit, the performance with these new materials was really no better than the original bismuth black primarily because of thermal loading of the collector area with the heavy paint.

Figure 5-3 shows photomicrographs of a typical detector, in this case the MVM'73 detector, with various blacks applied. In photo A, the conventional bismuth black was applied and the regularity and well-defined active area of the detector are clearly better than in any other detectors, particularly those with paint. The detector with the bismuth/germanium/zinc sulfide evaporations is uniform due to the fact it was evaporated through a mask, but since the material is conductive it was necessary to evaporate the black on individual couples to eliminate conductance between the couples.

SAMPLE DETECTOR

Originally, the grating spectrometer design (12-inch diameter, 10 x 10 mr FOV) required a large area detector (1 X 10 mm). A detector of this size had not previously been fabricated at SBRC and it was felt that problems might be encountered. Accordingly, one thermopile was fabricated with a sensitive area of 6 X 1 mm (see Figure 5-4). Wide-band measurements of the thermopile in vacuum were Z = 6.5 Kohms, R = 12 volts/watt, τ = 130 msec. Performance of larger detectors can be inferred from these data because additional junctions can be added to the detector. At the time the detector was designed it was assumed that access to the antimony bismuth bars would be limited to one side of the detector owing to the presence of the adjacent redundant detector. It was later determined that this was not the case, that bars could be brought in to both sides of the sensitive area. Nevertheless, the performance indicated is based on this earlier concept. Responsivity at 12 volts/watt is quite low and the profile (Figure 5-5) was taken to determine the cause of the low responsivity. The sag in the profile indicates that of the collected thermal energy only a small portion is conducted by the antimony bismuth bars to the cold sink. The major portion is evidently dissipated in the aluminum oxide film or is radiated to the surrounding environment. The problem here is that the gold evaporation of the collecting gold was not scaled up appropriately as the area of the detector was increased. However, some question exists as to whether the practical limitation by evaporating these bars approximately 15 times thicker would be exceeded.

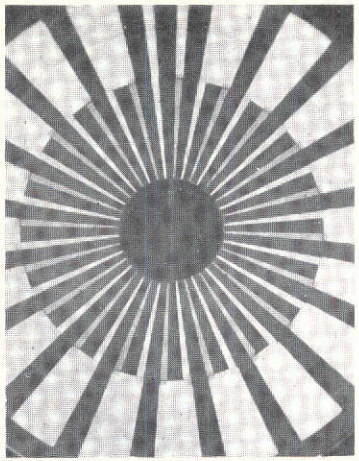

Typical Bi Black

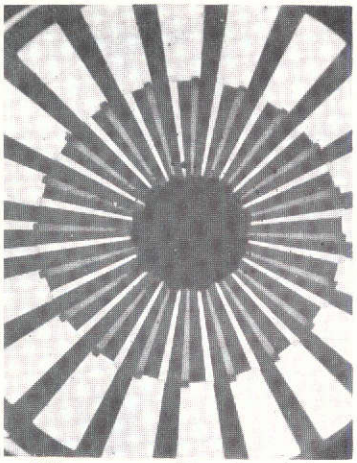

Thermopile 2 with
Cat-a-Lac Black

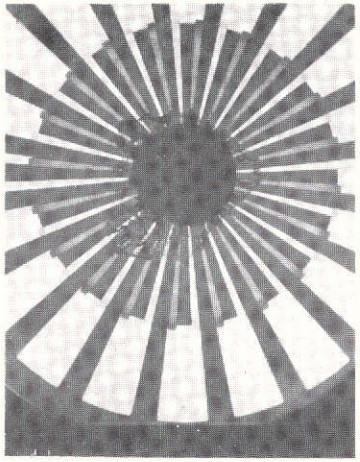

Thermopile 1 with
Cat-a-Lac Black

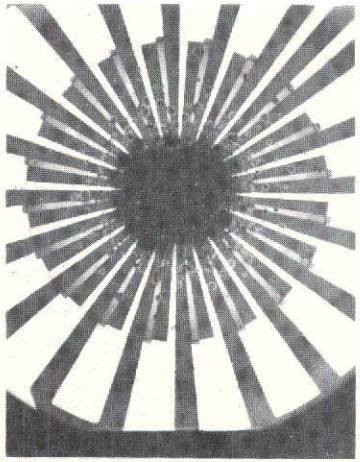

Thermopile 13 with
3M Velvet Black

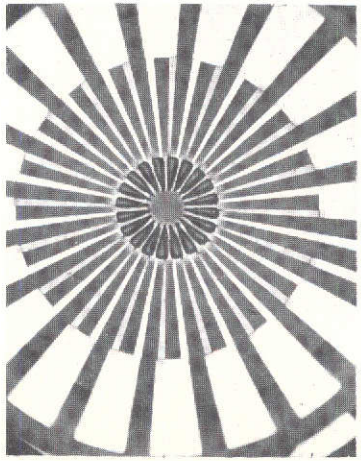

Bi/Ge/ZnS Black
Thermopile 28

Figure 5-3. Photomicrographs of MVM'73 Thermopile with Various Black Absorbers

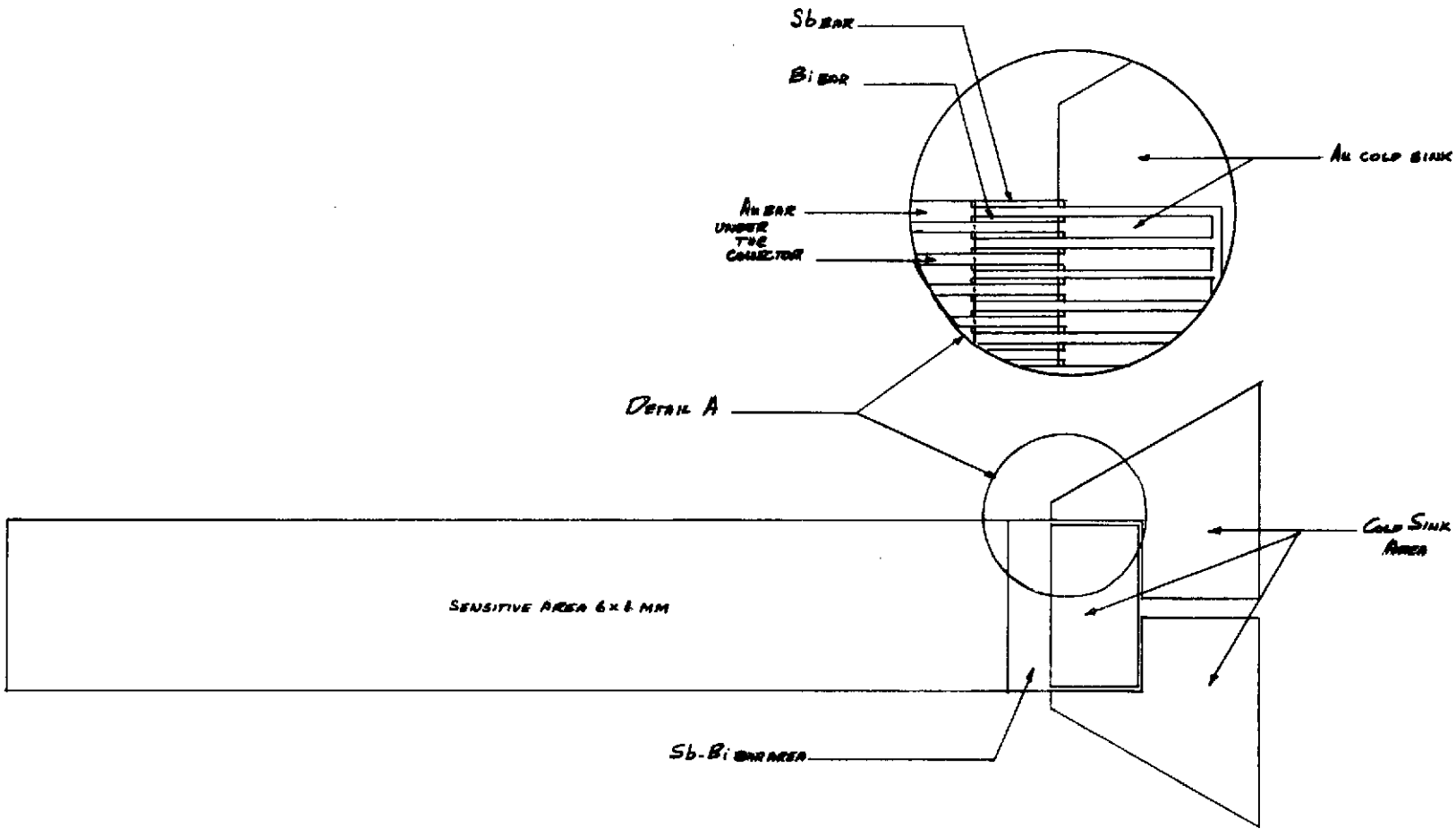

Figure 5-4. Sample Thermopile Layout

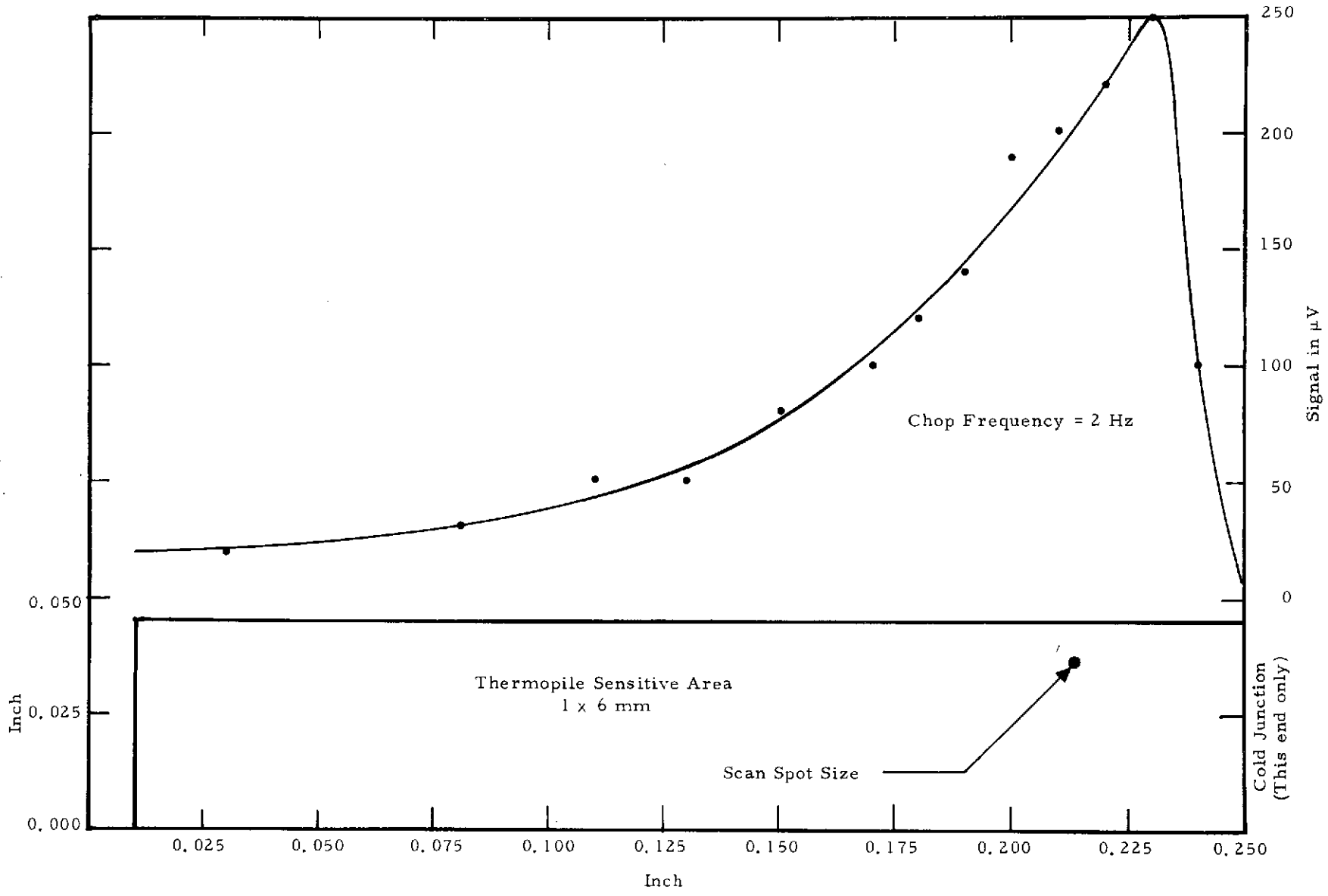

Figure 5-5. Thermopile Profile

SBRC

The study of thermopiles was terminated at this point because available data for TGS detectors indicated considerably better performance was available. Nevertheless, thermopile detectors are used in the 0.4- to 4.0-μm and the 6.0- to 100-μm channels because satisfactory performance is possible without chopping. Performance indicated for thermopile detectors is based on data taken during the Viking IRTM Critical Components Study,[1] and NEP values were scaled from the square root of the area of the detectors studied in the reference study. It can be shown that the NEP for small size thermopiles is proportional to the square root of the area.

PYROELECTRIC DETECTORS

Thermal detectors sense radiation by the temperature rise produced in an absorbing receiver. This temperature rise is generally converted to an electrical signal by making the absorber of some material which exhibits a strong thermoelectric effect. In the case of thermopile detectors it is the Seebeck effect that is used to generate the detector signal and in the case of the pyroelectric detectors it is the pyroelectric effect.

When an electrostatic field is placed across any dielectric, it becomes electrically polarized to a degree determined by its dielectric constant. For most materials this polarization disappears when the field is removed, but in certain classes of crystals a strong residual polarization remains. These crystals are called ferroelectric by analogy with residual magnetism in ferromagnetic materials even though they generally contain no ferrous metals. The surface charge by this polarization is soon neutralized by leakage but in some ferroelectrics the residual polarization is strongly sensitive to temperature. When the temperature is changed the consequent change in residual polarization causes a new charge to appear, which will be positive or negative depending on the direction of the temperature change. Such temperature-sensitive ferroelectrics are called pyroelectrics and their pyroelectric coefficient is defined as the temperature derivative of the polarization (dP/dT).

The pyroelectric detector is electrically a capacitor and therefore produces no signal for constant radiance inputs. As a result a chopper is required with the use of these detectors. General properties of the pyroelectric detector are as follows:

1. Being a thermal detector it is uniformly sensitive over a wide spectral range. Generally, most pyroelectric materials are highly absorbing beyond the region of 1 to 3 μm and therefore for long-wavelength applications require no blacking. The electrodes normally are placed on the detector faces rather than the edges which permits flexibility in detector shape. The electrode facing the incident radiation is normally a very thin nichrome or nickel coating which is mostly transparent to the incident radiation which is absorbed in the crystal.
2. No cryogenics are required.
3. There is no requirement for a quiet, highly regulated bias supply.
4. Present state-of-the-art limitation on size is about 0.25 x 0.25 mm due to fabrication difficulties and degradation of performance caused by stray capacitance.
5. Detectors larger than approximately 5.0 x 5.0 mm are difficult to fabricate because of the possibility of fracturing in the thin crystal, although large detectors can be fabricated by building up the area using a number of smaller detectors.
6. Ferroelectrics lose all polarization if the temperature exceeds the limit known as the Curie point. For TGS the Curie point is 49°C and the responsivity degrades rapidly above 45°C. The detector is not damaged permanently if the Curie point is exceeded but must be repolarized. This can be done automatically by circuitry integral to the detector. The Curie point in TGS can be raised by a process called deuteration which can be done during the aqueous growth of the crystal. Some of the hydrogen atoms in the crystal are replaced by deuterium atoms. This process also increases the degree of polarization of the crystal; hence, increases the responsivity. Another process is the irradiation of the crystal which in effect "locks in" the polarization. When this is done the detector does not require repolarizing when the Curie point is exceeded; once the polarization is done it need not be done again. Alanine doping of the TGS is another method for "locking-in" the polarization.
7. The TGS material is humidity-sensitive and must be protected from humidity during fabrication and test. This is generally accomplished by packaging the detector in a detector cell with a transparent window and filling the detector package with an inert

gas, generally krypton, or it can be evacuated. The detectivity is the same in either case except at low chop frequencies below 10 Hz where the thermal time constant can be affected.

Responsivity of the TGS detector as a function of ambient temperature is shown in Figure 5-6. In the voltage mode maximum responsivity occurs near 25 °C and falls off as the temperature is increased or decreased. This figure shows that at a temperature of 250 °K (-23 °C), probably the lowest operating temperature the system will see, the responsivity for TGS is down about 20% from the value at about 25 °C. However, in some instances the FET noise is also reduced at low temperatures so that the equivalent NEP does not suffer as much degradation as appears in the figure. This is particularly true with detector configurations where the largest noise contribution is FET current noise. In the voltage mode the voltage responsivity of the detector is proportional to the pyroelectric coefficient divided by the dielectric constant of the material, both of which are temperature dependent in the same way. In the current mode, however, in which the detector operates into a short circuit, the responsivity is proportional only to the pyroelectric coefficient so that the temperature dependence is much stronger. In general this connection is not used.

Calculations that describe the TGS performance in other portions of this report were done assuming 25 °C ambient temperature. At the actual operating temperatures of the system, a factor of almost 2 higher NEP would be realized. Therefore, in all probability the detector package will be temperature controlled in the vicinity of 25 °C to achieve maximum performance. The storage temperature of the TGS is between -40 °C and 100 °C. However, the detector should not be subjected to thermal shocks exceeding 2 °C per minute due to the possibility of fracturing the crystal.

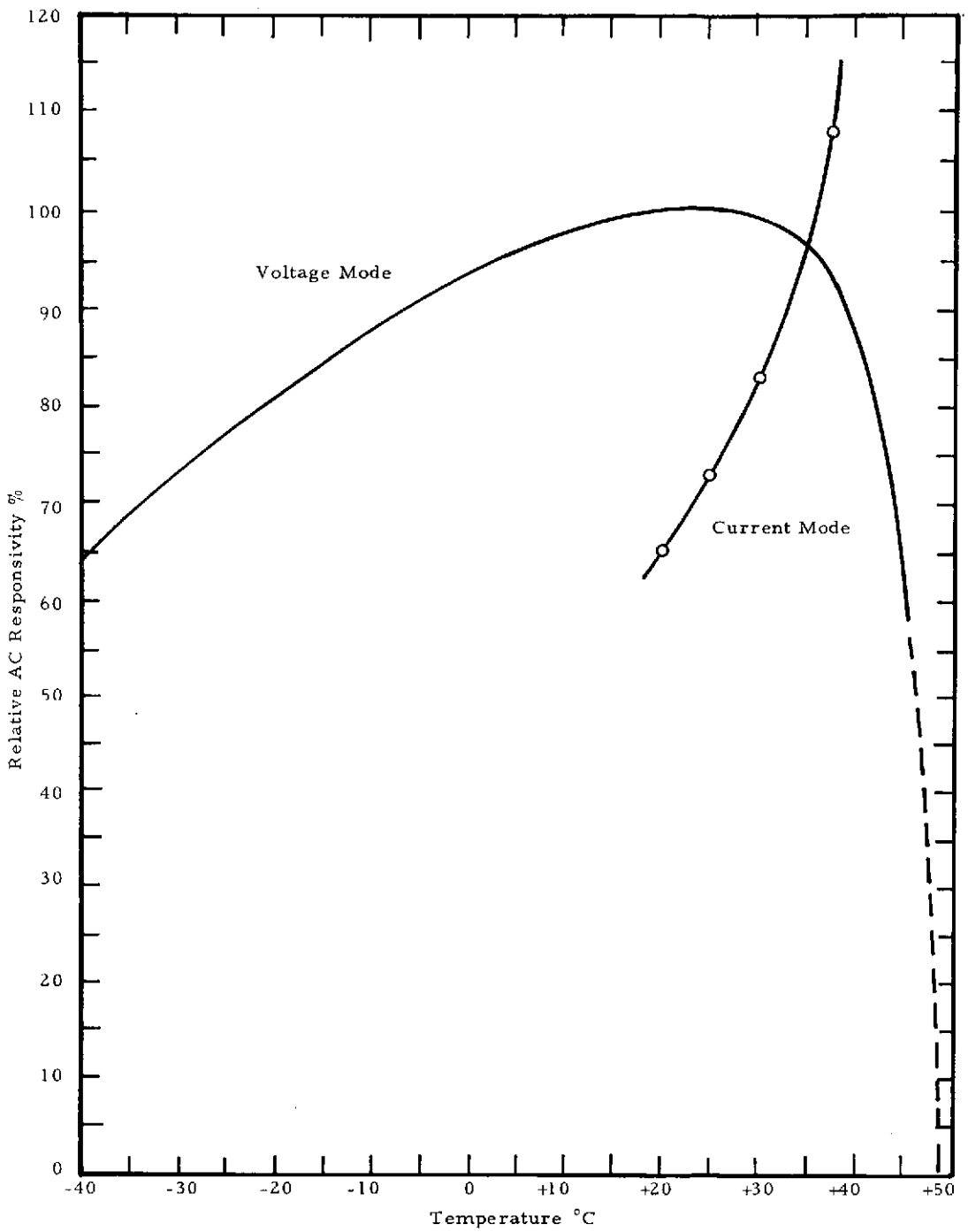

Figure 5-6. Responsivity of TGS Detector as a Function of Ambient Temperature

Pyroelectric detectors are readily fabricated in array form. The low thermal diffusivity of TGS permits arrays to be fabricated on a common crystal without appreciable thermal crosstalk. Such construction is simpler than one using separate crystals for each element and is directly applicable to the fabrication of the eight-detector array for the grating instrument. The array package uses a condensing lens and light pipe assembly over each of the eight detectors. The light pipe is fabricated by electrodepositing nickel over a mandrel and then flame-depositing copper over the nickel to achieve the desired thickness for strength and rigidity. Light pipes of this type have been fabricated by Hughes Aircraft Co. and Barnes Engineering Company for other applications. The detector is then placed as close as possible (0.002 to 0.003 inch) to the exit end of the light pipe.

Calculation of detector NEP involves the root-mean-square of the noise contributions from five sources: Johnson noise in the dc load resistor, Johnson noise due to the dc dielectric loss of the detector (loss tangent), amplifier noise voltage, amplifier current noise, and noise from thermal fluctuations of the crystal. It has been found[2] that these noise sources have relative significance depending on the frequency of operation, detector area and thickness, and the particular FET used for the first amplifier stage. Thus, a material figure-of-merit based on only one parameter such as the pyroelectric coefficient can be misleading. NEP values for state-of-the-art detectors have been improved within the last year owing to developments in the input stage FET transistor. The best available transistor apparently is the TI E1600 FET produced in England.

In general, however, the noise, responsivity, and D* dependence with frequency is shown typically in Figure 5-7 for a 0.5 x 0.5 mm detector. From the figure it is clear that both the responsivity and the noise decrease are approximately as 1/f and consequently D* value remains relatively constant out to high frequencies. However, peak D* occurs at low frequencies in the vicinity of 10 to 20 Hz where the chop frequency for this system has been selected. State-of-the-art performance for TGS obtained from both Barnes

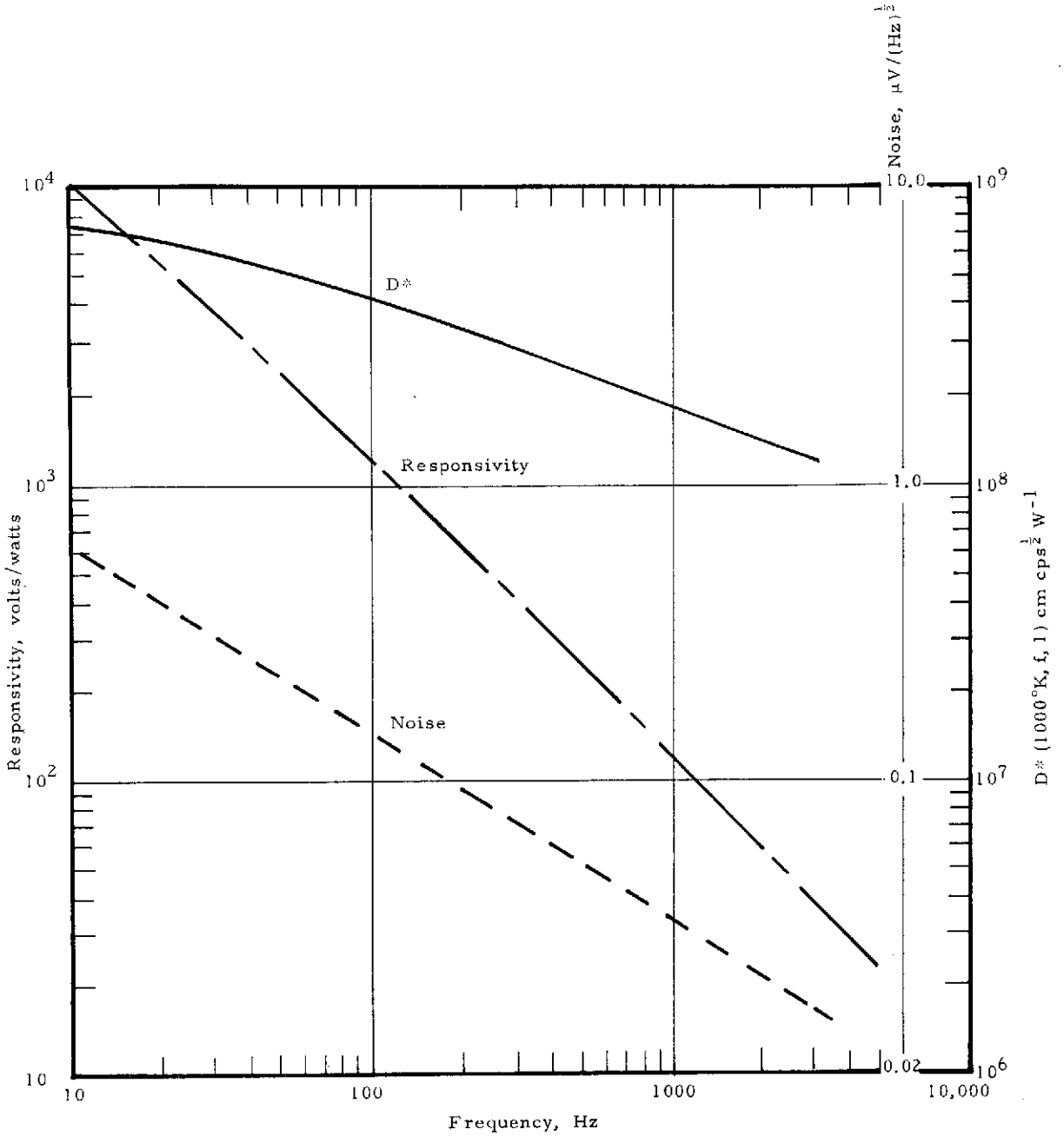

Figure 5-7. Performance of a Typical 0.5 × 0.5 mm Pyroelectric Detector

Engineering Co. and Mullard Ltd. in England is shown in Table 5-3 and it is this data that is used for system calculations in Sections 2 and 3 of this report.

Table 5-3. TGS Detector Data (Barnes Engineering Co. and Mullard Ltd.)

Manufacturer	Size (mm x mm)	NEP (Watts/$\sqrt{Hz}$ x 10^{-10})	Comments
Barnes (S. Weiner)	0.52 x 5.2	1.8	Chop at 15 Hz 25°C
	0.52 x 1.78	1.2	
	0.52 x 2.14	1.3	
			Hz °C
Mullard (D. Charlton)	3.0 x 9.0	3.5	15 25
	3.0 x 3.0	2.5	15 25
	0.5 x 5.0	1.8 Typ	10 25
		2.5 Max	10 25
	0.5 x 2.0	1.0 Typ	10 25
		2.0 Max	10 25
	0.5 x 1.75	0.8 Typ	10 25
		1.7 Max	10 25

Window losses are not included in above NEP values.

Current Developments in Pyroelectric Detectors

There is considerable interest in developing new ferroelectric materials for use in low level detectors and for development of fast nanosecond detectors.[2,3]

New materials currently being examined are variations of TGS, namely, deuterated TGS (DTGS), irradiated TGS, and alanine-doped TGS (ATGS). The modifications to the basic TGS tend to raise the Curie point and to provide locked-in polarization. For ATGS Lock[4] claims a D* of 2×10^9 cm $Hz^{\frac{1}{2}}$-watt^{-1} for a 0.5 x 0.5 mm detector below 10 Hz. Another material, lead titanate ($PbTiO_3$) appears to have several advantages over TGS. Because

the crystal is grown from a melt rather than aqueous solution the material is much less humidity-sensitive than TGS. In addition, it has a much higher Curie point. As a result, the responsivity dependence on temperature is much lower than for TGS which operates very close to its Curie temperature. Yamaka, et al., [5, 6] claims a D* value of 8×10^8 cm $Hz^{\frac{1}{2}}w^{-1}$ at 10 Hz at 500°K blackbody. However, there seems to be some question as to the validity of this claim. [7]

Performance of $LiTaO_3$, $LiNbO_3$, $SrBaNb_2O_6$, and TGS have been investigated by Byer and Roundy, [2] and comparative values of NEP as a function of frequency are shown in Figure 5-8. All of the crystals used to produce this data are $1 \times 1 \times 0.03$ mm. Both the $LiNbO_3$ and $LiTaO_3$ are current noise-limited while the $SrBaNb_2O_6$ and TGS are loss tangent noise-limited, and a reduction in crystal thickness from 30 to 10 μm reduces the NEP for $LiTaO_3$ and $LiNbO_3$ by a factor of three by reducing the NEP for $SrBaNb_2O_6$ and TGS by $\sqrt{3}$.

The more favorable mechanical and hydroscopic properties of $LiTaO_3$ compared to TGS may favor the use of thinner $LiTaO_3$ elements in pyroelectric detectors. In Figure 5-8 the NEP was calculated using rms value of all five noise contributions. However, the data show that at 10 Hz the TGS detector is still superior to other materials, and, indeed, the Byer and Roundy data for TGS compare almost identically with that of both Barnes and Mullard.

Considerable development activity is currently in progress to develop room temperature pyroelectric detectors using nonhydroscopic materials and performance better than that quoted can be expected within the next year or two.

A conceptual drawing of the pyroelectric detector array with light pipes is shown in Figure 5-9.

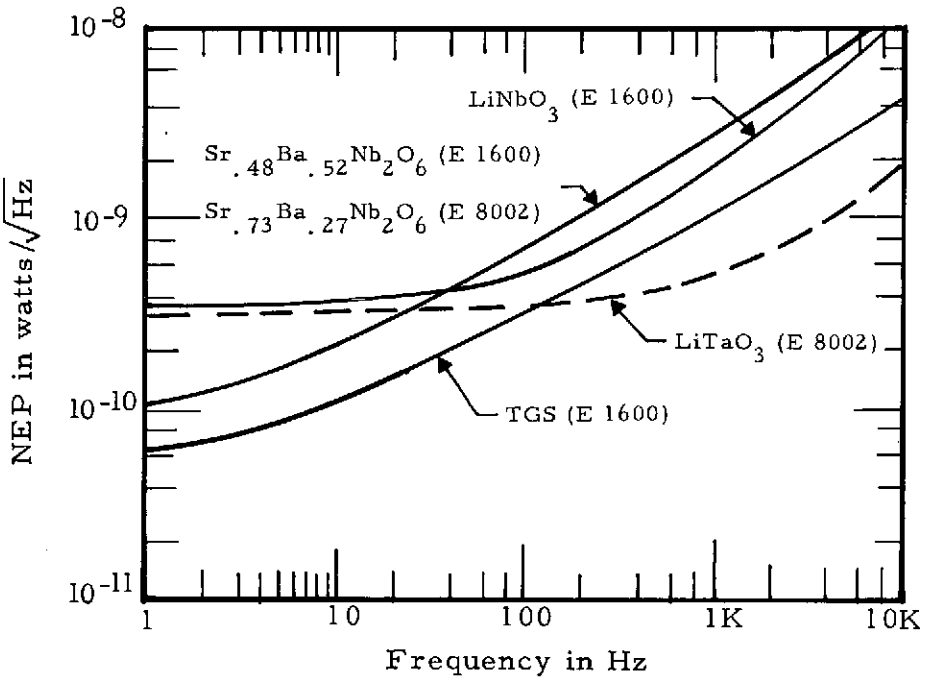

Figure 5-8. NEP_{RMS} of Five Materials versus Frequency for Specified FET

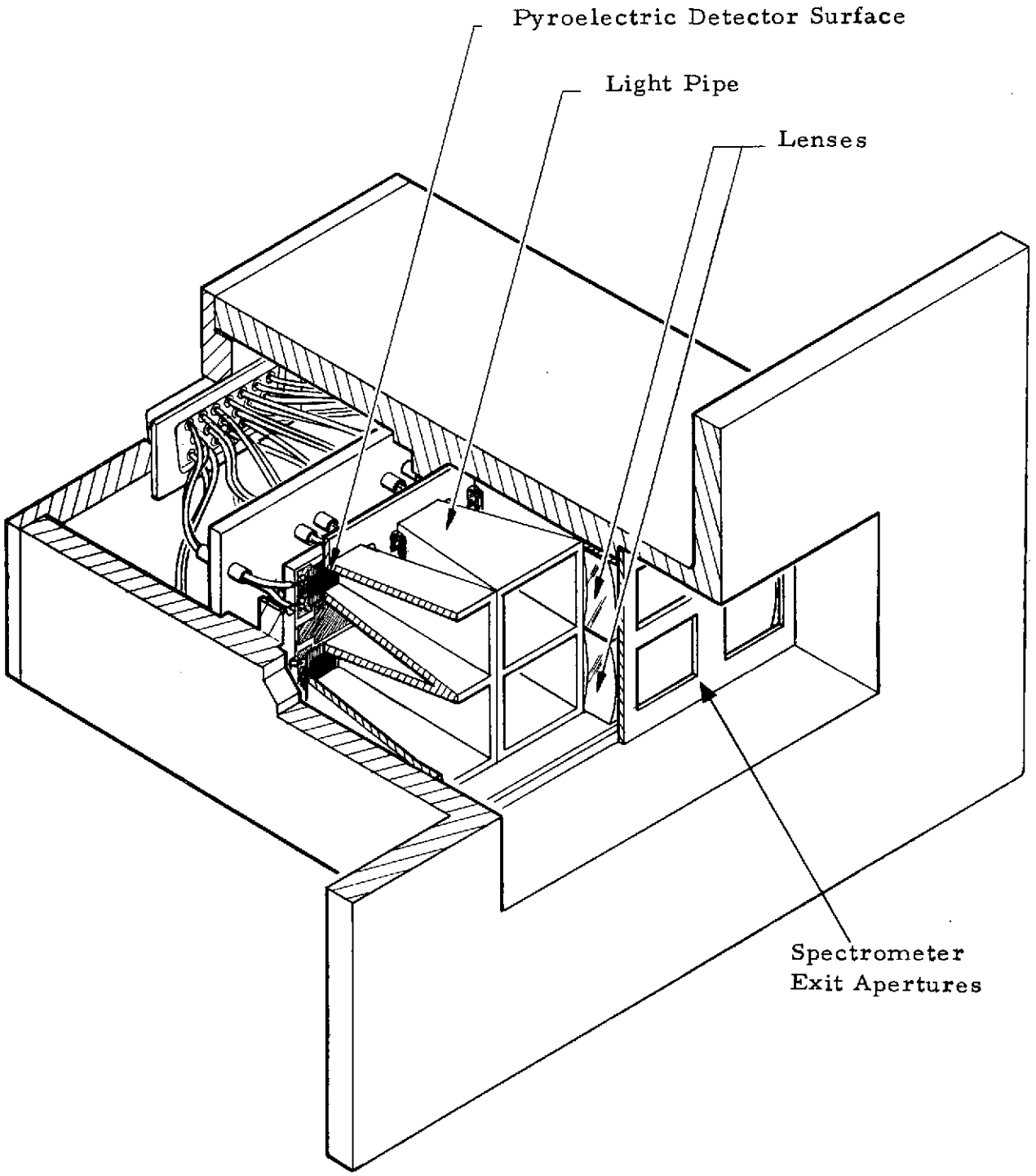

Figure 5-9. Pyroelectric Detector Package

PHOTOCONDUCTORS

Three types of photoconductor detectors have been selected to cover the spectral range from 0.8 to 6 μm. The three detectors, PbS, PbSe, and HgCdTe, are mounted on the end of the radiation cooler cold finger; all operate at 180°K. Figure 5-10 shows detectivity versus wavelength for various detectors at 194°K. The circles represent Honeywell data on HgCdTe, the triangles are for Texas Instruments HgCdTe, and the line extending from the triangles is an extrapolation of D* out to 6 μm which is the longest wavelength of interest. Also shown on the curve are values of detectivity for PbS, PbSe, indium arsenide (InAs), and indium antimonide (InSb) at specific wavelengths.

Referring to the Texas Instruments data for HgCdTe, detectivity is peaked at 4.3 μm and is chopped at 700 Hz which gives a D* equal to 5.5×10^{10} cm-Hz$^{\frac{1}{2}}$-w^{-1}. Correcting for a chopping frequency of 500 Hz gives a D* value equal to 2.13×10^{10} cm-Hz$^{\frac{1}{2}}$-w^{-1}. Correcting for the cold stop at f/3.5 gives an improvement of perhaps 1.5 to 2. A value of 3.4×10^{10} cm-Hz$^{\frac{1}{2}}$-w^{-1} was used for the systems calculations. The D* values and the correction factors used to obtain them are shown in Table 3-4. Curves showing detectivity as a function of wavelength for PbS and PbSe are shown in Figures 5-11 and 5-12 which were used as the basis for these calculations. Background limited performance was assumed.

Referring again to Figure 5-10, HgCdTe would be superior to PbSe; however, PbSe can be immersed on the back of the strontium titanate hyperhemisphere whereas HgCdTe cannot. Therefore, when this improvement factor for PbSe is taken into account, it becomes better than HgCdTe.

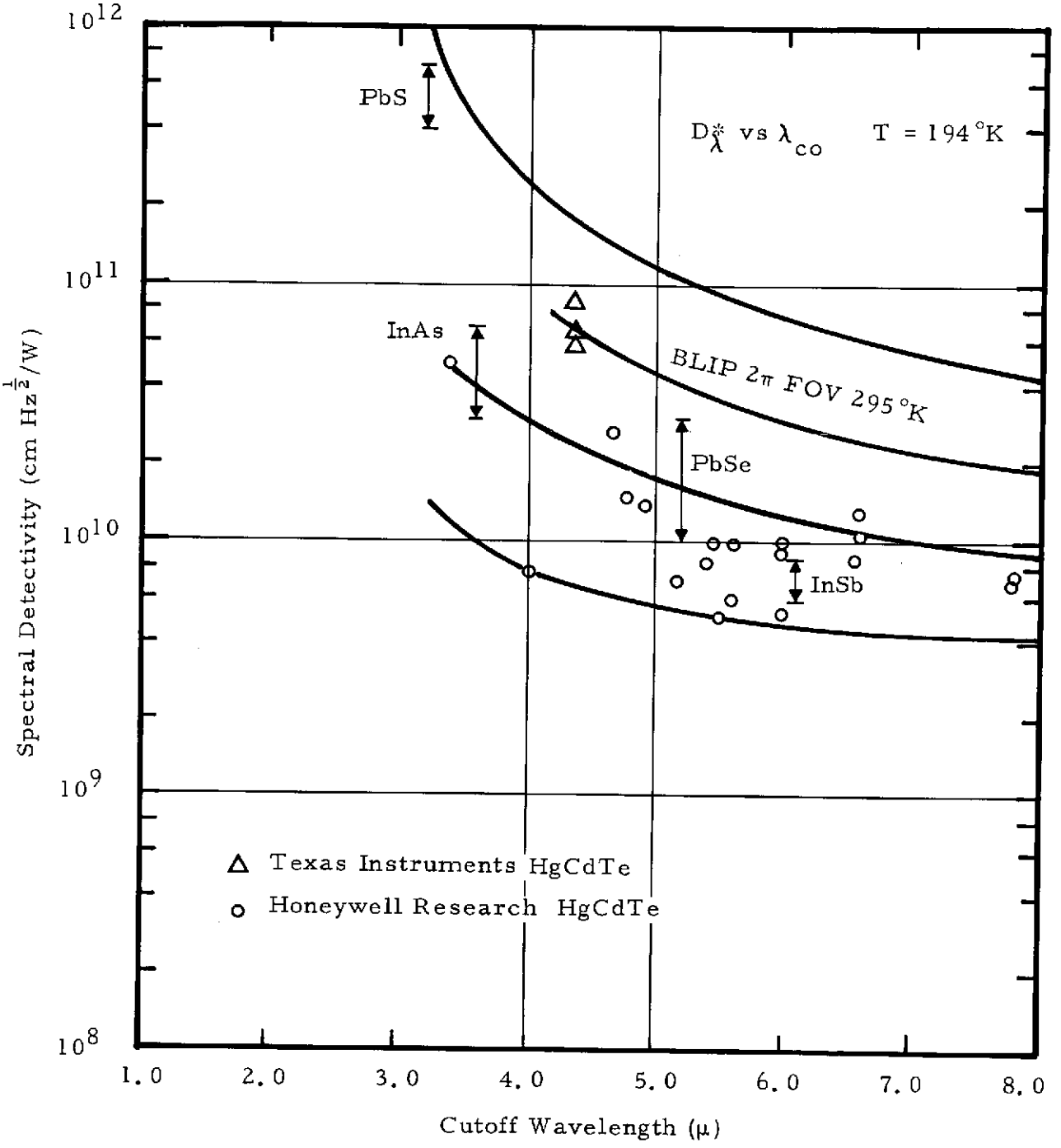

Figure 5-10. Detectivity vs Wavelength for Various Detectors at 194 °K

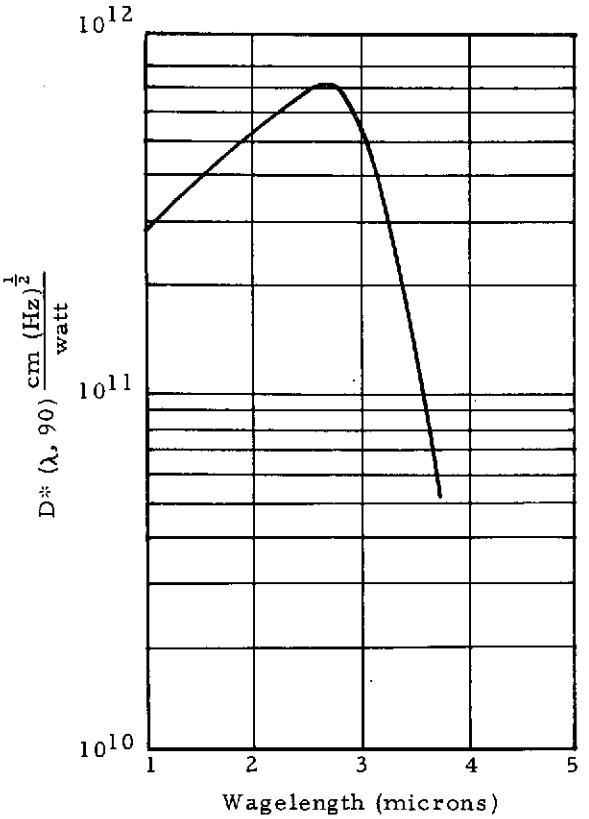

Figure 5-11. Spectral Detectivity for PbS at 193°K

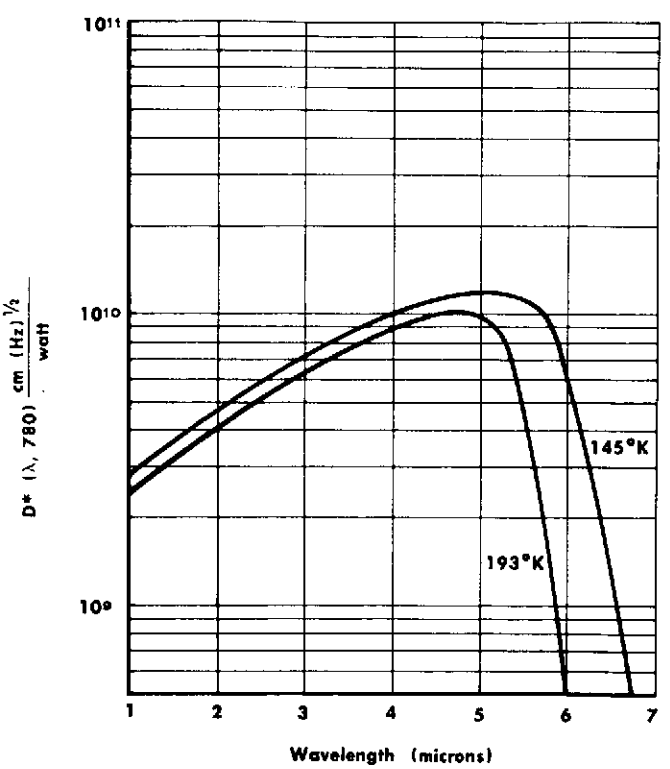

Figure 5-12. Spectral Detectivities for PbSe

CALCULATIONS FOR BACKGROUND FLUX FOR PbSe DETECTORS

Background flux on the detector consists of contributions from the following sources: 1) the scene - 130 °K Jupiter, 100 °K Saturn; 2) telescope - temperature assumed to be 250 °K; 3) sky background - assumed to be zero in this case.

CALCULATION OF BACKGROUND PHOTON FLUX FOR THE PbSe DETECTORS

Jupiter at 2.9 μm gives photon radiance of

$$Q_J = 2.42 \times 10^{14} \text{ photons - sec}^{-1} \text{ - cm}^{-2} \text{ - ster}^{-1}$$

at the detector

$$H_J = \frac{Q_J A_o \Omega \tau_o}{C}$$

Where quantities have previously been defined

$$H_J = \frac{2.42 \times 10^{14} \times 110 \times 1.6 \times 10^{-5} \times 0.224}{2.45} = 3.9 \times 10^{10} \text{ photons-sec}^{-1}$$

Assuming that the detector operates at f/1, the background flux from the telescope will be:

> The detector views the back of the filter wheel (at 250 °K or warmer) at f/1 through the immersion lens which is coated to transmit only between 2.8 and 4.8 μm. Except for the small amount it transmits in this region the filter wheel is opaque.

Therefore, the photon radiance is

$$Q_F = 3 \times 10^{14} \text{ photons - sec}^{-1} \text{ - cm}^{-2} \text{ - ster}^{-1}$$

$$H_F = Q_F A_d \Omega$$

where $\Omega = 0.857$ ster

$$H_F = 3 \times 10^{14} \times 1.57 \times 10^{-3} \times 8.57 \times 10^{-1} = 4 \times 10^{11} \text{ photons-sec}^{-1}$$

The background photon flux outside the f/1 beam coming from the 180°K cold shield is:

$$Q_B = 1.96 \times 10^{12} \text{ photons - sec}^{-1} \text{ - cm}^{-2} \text{ - ster}^{-1}$$

$$H_B = 1.96 \times 10^{12} \times 5.42 \times 1.57 \times 10^{-3} = 1.7 \times 10^{10} \text{ photon-sec}^{-1}$$

Total photon flux contributions are therefore:

1. From Jupiter, 3.9×10^{10} photons-sec^{-1}
2. From inside f/1, 4×10^{11} photons-sec^{-1}
3. From outside f/1, 1.7×10^{10} photons-sec^{-1}

Therefore, the detector is clearly background limited by at least a factor of 10 at Jupiter and of course more at Saturn. Therefore, detector parameters will not vary substantially as a function of scene radiance.

REFERENCES

1. JPL Contract No. 953089, Final Report, published 11 February 1972.
2. Byer, R. L. and Roundy, C. B., Practical Considerations for Low NEP Pyroelectric Detectors, Stanford University, to be published.
3. Weiner, Seymour, Beerman, Henry P., and Schwarz, Frank, Development of Improved Pyroelectric Detectors, Barnes Engineering Co., Inc., 29 February 1972. Technical Report for period November 1971 through February 1972 prepared for Goddard Space Flight Center. BEC2064QR2.
4. Lock, P. J., Appl. Phys. Letters, 19, 390, (1971).
5. Yamaka, Eiso, $PbTiO_3$ (an internal report of Matsushita Research Institute Tokyo, Inc.).
6. Yamaka, Eiso, $PbTiO_3$ Pyroelectric Detectors, Letters to the Editor, Infrared Physics, 1971, Vol. 11, pp 247-248.
7. Schwarz, Frank, Claims of High Detectivity for $PbTiO_3$ Pyroelectric Detectors, Barnes Engineering Co., 9 May 1972. Memo.

Section 6
MECHANICAL DESIGN

DESIGN PHILOSOPHY

To achieve an optimum trade-off between weight and design requirements, the design approach used has been to minimize payload weights (detectors and optical components) thereby pyramiding weight savings in the structure required for support of these components.

DESIGN CONFIGURATION

Optical Configuration

The optical schematic shown in Figure 6-1 consists of a spectrometer and several radiometric channels using separate 6-inch diameter Cassegrainian telescopes, boresighted and aligned for coincident FOVs. Optical requirements are discussed elsewhere in the report.

Functional Configuration

Other than support structure, both telescope systems require choppers at the telescope field stops, deployable telescope aperture covers, and calibration blades. In addition, the "Continuous Filter Wedge Spectrometer" requires a stepper drive motor for the CV filter disk and a radiation cooler for its detectors.

Overall Configuration

A detailed design layout is shown in Figure 6-2. Figure 6-3 is an exploded-view isometric of this detail layout. Figure 6-4 shows the external size, mounting holes and external FOV requirements. A weight summary will be found on page 6-17 for the design in Figure 6-2.

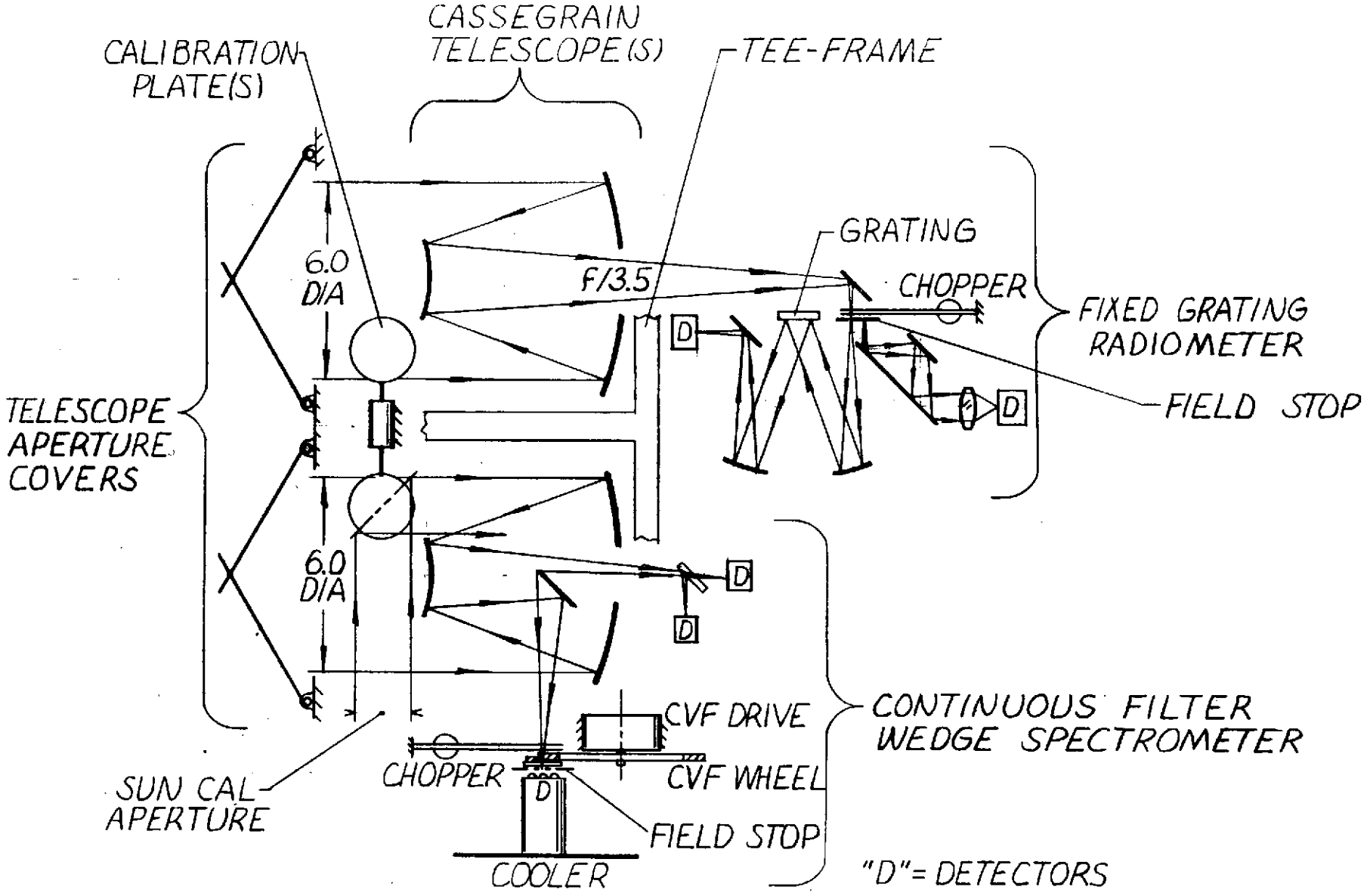

Figure 6-1. Opto-Mechanical Schematic

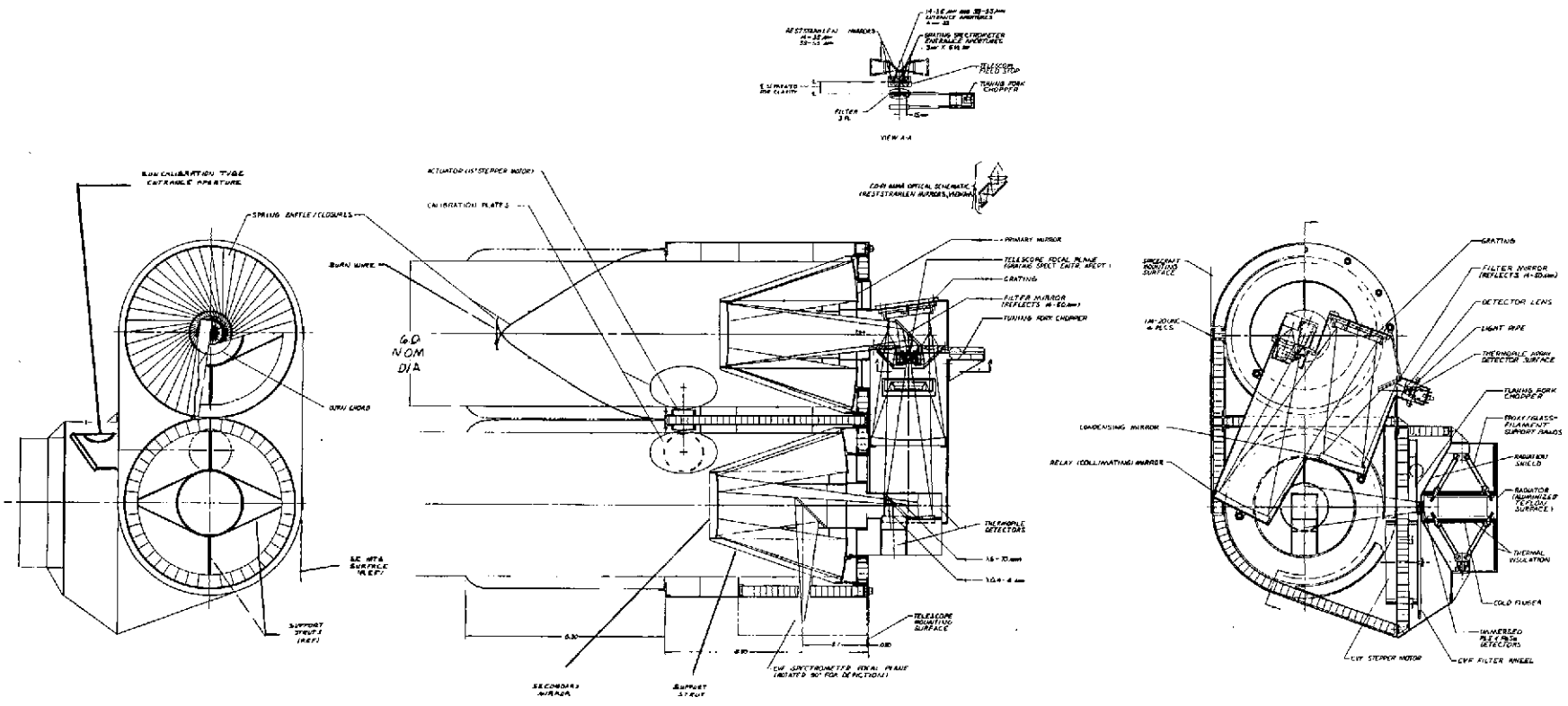

Figure 6-2. Radiometric Spectrometer Detail Layout

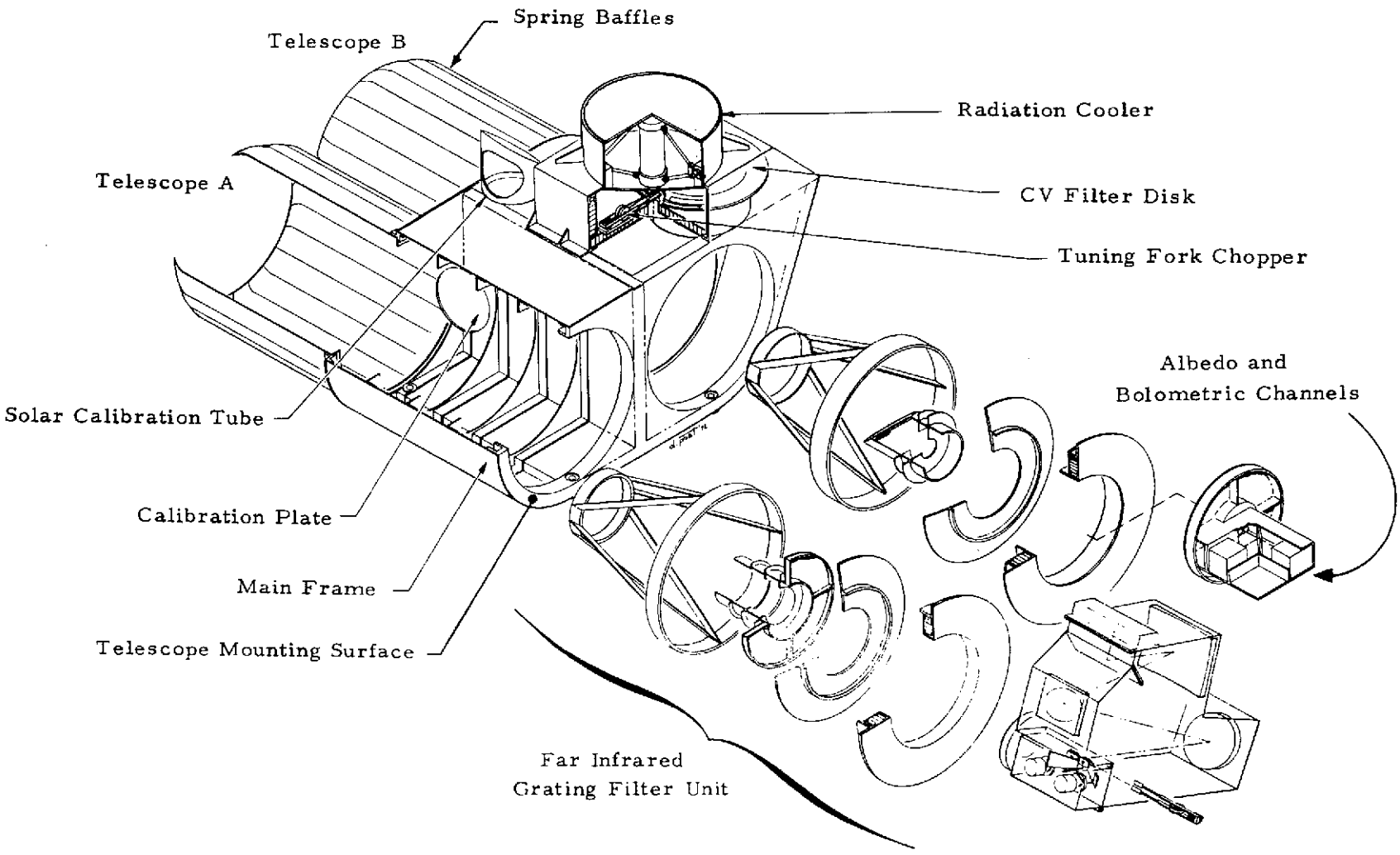

Figure 6-3. Mariner Jupiter/Saturn Radiometric Spectrometer

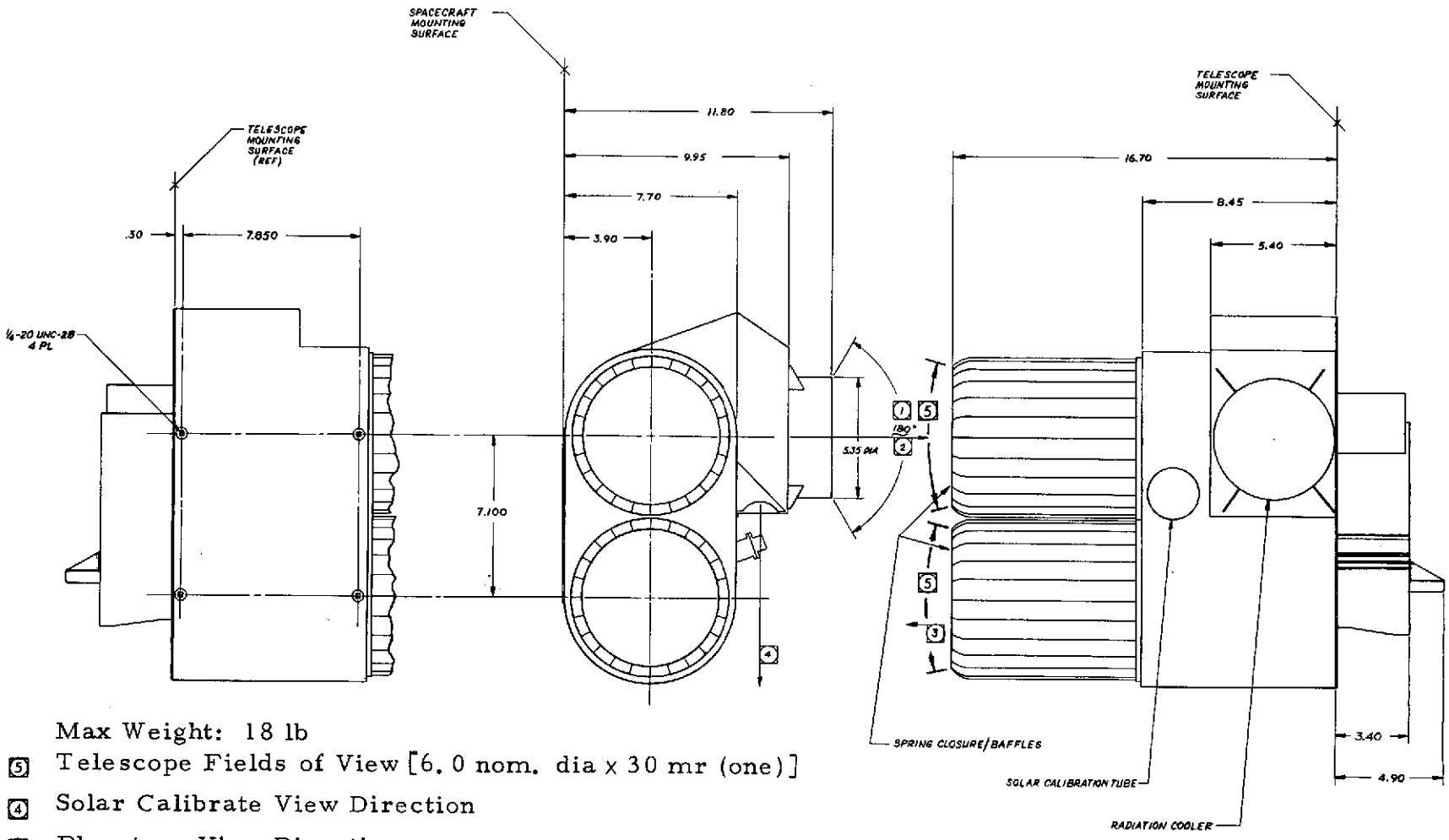

Max Weight: 18 lb

[5] Telescope Fields of View [6.0 nom. dia x 30 mr (one)]

[4] Solar Calibrate View Direction

[3] Planetary View Direction

[2] Deep Space View Direction

[1] Radiation Cooler Field of View

Figure 6-4. Mariner Jupiter/Saturn Radiometric Spectrometer Configuration Drawing

DESIGN CONSIDERATIONS

Environmental Considerations

Vibrational Considerations - As the vibrational environment has not yet been defined, the design has been configured so as to achieve high natural frequencies in support structures (i.e., use of monocoque construction and honeycomb sandwich panels to achieve high stiffness to weight ratios). Past experience has shown that a good assumption to follow in design of spacecraft instrument payloads has been to maintain natural frequencies of support structures above 200 Hz.

Thermal Considerations - A thermal analysis was performed on the detailed layout (Figure 6-2) and appears in Section 7. Preliminary results had indicated that the principal path of heat transfer would be by radiation to space through the two telescope apertures (i.e., along the telescope axes) with heat sources mounted either directly on the main frame or in the aft optics (behind the telescope's primary mirrors).

Interface of the telescope with the aft optics and main frame had to minimize conductive heat transfer into the primary and secondary mirrors, yet maximize the radiation heat transfer into the main frame cavity. This was accomplished by decoupling the secondary mirror from the main frame and using the telescope central baffles as radiating heat sinks for the aft optics heat sources. The telescope design is described in Section 4.

STRUCTURAL CONSIDERATIONS

Material Comparison

For a given design configuration, the theory of models can be used to derive weight parameters based on dimensional stability between optical elements. The weight ratio between any two structures of different materials but equivalent dimensional stability will be directly proportional to the ratio of their respective weight parameters. *

Support Structure Performance Criteria	Weight Parameter*
1 - Stiffness designed (equivalent natural frequencies and static deflections)	$\sqrt{\frac{\rho^3\lambda}{E}}$
2 - Stress Design (maximum bending stress = PEL)**	$\frac{\rho}{\sqrt{PEL}}$
3 - Design for thermal stability (equivalent thermal expansion)	$\frac{\rho\alpha}{k}$

where ρ = Density

E = Modulus of elasticity

λ = 1 - (Poisson's ratio)^2

α = Coefficient of thermal expansion

k = Thermal conductivity

**PEL = Precision Elastic Limit

---

* Derivation assumes variable wall thickness wherein,

$$\frac{(\text{Structure Weight})_{\text{Material A}}}{(\text{Structure Weight})_{\text{Material B}}} = \frac{(\text{Weight Parameter})_{\text{Material A}}}{(\text{Weight Parameter})_{\text{Material B}}}$$

** Precision elastic limit or microyield strength is defined as the stress at which one micro inch per inch of plastic strain occurs. By comparison, the conventional yield strength definition (0.2% offset) is defined as the stress at which two thousand micro inch per inch of plastic strain occurs.

Property values listed in Table 6-1 were used to calculate weight parameters for several low-density structural materials. Weight ratios were then calculated for each material with respect to an all beryllium structure and the results tabulated in Table 6-2. Beryllium is generally considered the optimum material for minimum weight, precision optical structures.

The aluminum honeycomb sandwich material, by virtue of its very low effective density, showed the greatest promise of weight savings in meeting structural load requirements. However, thermal stability requirements appeared as a potential problem area in sandwich construction and particular attention would have to be paid to application of thermal control techniques to realize this potential weight savings.

Material and Processes

Weight savings has been the primary factor in choice of materials and construction techniques.

The basic material selected for use throughout the unit is aluminum, primarily because it readily lends itself to lightweight sandwich construction techniques. Its only disadvantage,* high thermal expansion, can be compensated for in the design by careful application of thermal control techniques to minimize thermal gradients between optical elements. Thus, gross overall temperature changes from assembly room temperature will merely result in an overall change in scale with no effect on optical performance.

The use of bonded construction techniques in the main frame permits the fabrication of a main honeycomb sandwich tee-frame "backbone" that is also integral with a sheet metal skin and rib housing (i.e., monocoque construction). All materials would be of optimum mechnical properties (strength and stability) prior to joining, with the tee-frame providing the majority of the frame's strength and stability.

*Advantages of aluminum are high thermal conductivity, high specific heat, and moderately high specific strength and specific stiffness.

Table 6-1. Structural Materials Property Values

Properties[1]	Honeycomb[2] Sandwich (6061-T6 Al)	6061-T6 Alum	7075-T6 Alum	HK31A-H24 Mag	HM21A-T8 Mag	Beryllium 4% BeO
ρ lb/in^3	0.0098	0.098	0.101	0.065	0.064	0.066
E x 10^6 psi	10.0	10.0	10.4	6.4	6.4	42.5
μ Poisson's Ratio	0.34	0.34	0.34	0.33	0.33	0.03
$\lambda = 1 - \mu^2$	0.8844	0.8844	0.8844	0.8911	0.8911	0.9991
K $\frac{\text{BTU-FT}}{\text{HR FT}^2\ ^\circ\text{F}}$	9.9	99.0	70.0	66.0	79.0	87.0
$\alpha \frac{\text{Micro Inch}}{\text{Inch}\ ^\circ\text{F}}$	13.0	13.0	13.1	16.0	16.0	6.4
[3]PEL x 10^3 psi	12.0	12.0	40.0	12.0	12.0	8.0

[1]Material properties taken from Materials Engineering and Machine Design reference magazines.

[2]Previous HAC experience has shown that AVCO's fluxless brazed aluminum honeycomb sandwich material can be considered as dimensionally stable as other solid, low residual stress aluminum sheet and plate.

[3]PEL values taken from ASTIA Report No. AD 144130.

Table 6-2. Weight Ratios with Respect to Beryllium (4% BeO) For Specified Structural Material

Performance Criteria	Weight Parameter	Honeycomb Sandwich (6061-T6 Al)	6061-T6 Alum	7075-T6 Alum	HK31A-H34 Mag	HM21A-T8 Mag	Beryllium 4% BeO
Equivalent Natural Frequencies	$\sqrt{\frac{\rho^3\lambda}{E}}$	0.11	3.6	3.8	2.5	2.4	1
Equal Strength	$\frac{\rho}{\sqrt{PEL}}$	0.12	1.2	0.68	0.80	0.79	1
Equal Thermal Stability	$\frac{\rho\alpha}{k}$	2.6	2.6	3.8	3.2	2.6	1

The honeycomb core used in the tee-frame and the telescope base plates is constructed of 4 mil (0.004 inch) thick 6061-T6 aluminum foil, perforated and ultrasonically welded* into a 1/4 inch hex cell. The face sheets are typically 0.020 inch 6951-T6 aluminum clad with 2 to 5 mils fluxless braze material (approximately 93% Al and 7% SiO). The core, face sheets and end closures would be joined in the following special fluxless brazing process developed by AVCO Corporation's aerospace structures division.

Aluminum Fluxless Brazing - The fluxless brazing method for aluminum alloys is similar to that used for brazing the large complex stainless-steel honeycomb sandwich structures of the XB-70 aircraft. Special chemical reagents are used to remove the naturally formed oxide film from aluminum surfaces so that atomic diffusion between the braze filler metal and base metal can occur. The aluminum parts and preforms of the braze filler metal are carefully prefitted, under clean environmental conditions. The gap tolerance between the structural parts is 0.0 to 0.003 inch. However, wider tolerances may be permissible, depending on the properties and processing characteristics of the braze filler metal.

The prefitted parts are then installed in a chemically cleaned metal envelope equipped with provisions for attaching pressure, vacuum and purge lines. The envelope is sealed and slightly pressurized to permit leak detection.

The leakproof, sealed assembly is placed between the platens of an Avcoramic brazing unit (see Figure 6-5). Suitable pressure is applied to ensure intimate contact of the parts. After all air is purged from the assembly, the brazing cycle begins. The temperature-pressure-time relationship used depends on the alloys being brazed, and the configuration of the assembly.

---

*Currently, AVCO is developing a method for fluxless brazing of the core material to remove the restrictions on core size and depth, imposed by ultrasonic tool limitations.

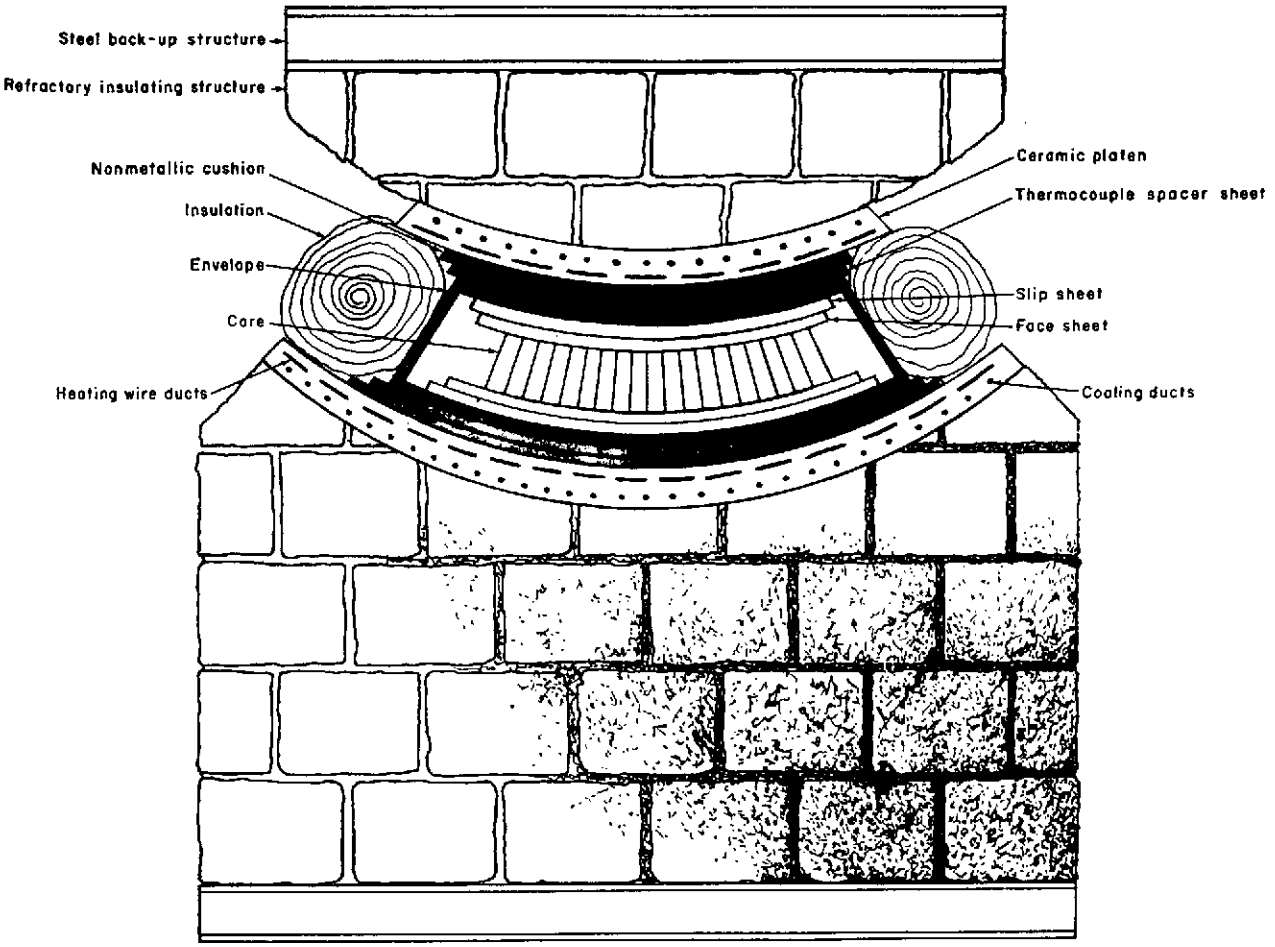

Figure 6-5. Fluxless Brazing Fixture

Brazing unit, shown in cross section, provides several important advantages, including: 1) variable heating rates over a wide temperature range with uniform temperature control; 2) controllable uniform cooling rates; 3) built-in dimensional control - platen surfaces are used to provide accurate references for assembly surfaces; 4) heating, brazing and cooling are performed without disturbing the assembly, ensuring greater dimensional accuracy and more economical processing; 5) zoned heat flux provides additional heat in local areas for panels varying greatly in mass cross sections; and 6) accurate temperature control permits brazing close to the melting range of the parent metal alloys.

Because commercial filler metals for brazing aluminum alloys melt at temperatures close to the melting temperatures of the aluminum alloys, it is vitally important that brazing temperatures be uniform throughout the assembly. It is standard practice to hold temperatures within ±10°F of nominal, but ±5°F is possible with small assemblies.

The brazing pressures are critical because of the relatively low strength of aluminum at the brazing temperatures used. Only slight pressure is required if fit-up operations are performed with meticulous care. The brazing cycle should be as short as possible to prevent undesirable diffusion between the filler metal and the aluminum. After brazing, the assembly is cooled uniformly to prevent distortion from thermal stresses.

Current research is aimed at developing rapid cooling methods for the solution heat treatment of complex aluminum alloy brazed structures. Methods have already been developed for solution treating at the end of the cycle which can significantly enhance the potential of the fluxless brazing process.

DETAIL DESIGN CONSIDERATIONS

General Construction

Due to the relatively moderate precision required of the optical system (4-mr resolution) it was felt that the greatest weight savings could be realized by going to an all-aluminum telescope housing that would utilize aluminum honeycomb sandwich material in a tee-frame configuration as the backbone of a bonded frame of monocoque construction*. Such a structure would have sufficient strength-to-weight ratio to permit a design in which individual optical subassemblies could be separately assembled and aligned prior to installation onto the main frame for subsequent final alignment. Such a design would permit parallel fabrication, assembly, and test of individual subassemblies and flexibility in incorporation of design changes, especially in the later stages of assembly.

*In this type of construction the chassis (sandwich panel tee-frame) and body (ribs and outer skin) are an integral bonded assembly.

Main Frame Assembly - General Description

Two separate 1/2-inch thick optics base plate rings fabricated by fluxless brazing of aluminum honeycomb are bolted directly to the telescope mounting surface of the main frame. These two base plate rings carry the telescopes mounted on one side, and the aft optics subassemblies mounted on the other. In Figure 6-3 these two subassemblies comprise the Fixed Grating Radiometer and the Continuous Filter Wedge Spectrometer. The outer boss diameters and mounting flanges of the honeycomb base plates are used for registration during assembly and alignment. On mating with the two holes bored in the main frame telescope mounting surface the base plates would be rotated on these diameters to obtain coincident telescope FOVs. The radiation cooler, circular variable filter disk with its 1.8° stepper motor drive, and a 600-Hz tuning-fork-chopper are assembled and aligned within a separable housing which bolts to the top surface of the main frame.

The calibration paddles are attached to the output shafts of a double ended, 45° stepper motor mounted in the central wall of the tee-frame so as to align the calibration plates within the obscuration shadow of one of the telescope's secondary mirror support struts when not in use. At one 45° position, the back side of one calibration plate acts as a scattering surface for directing solar energy from the solar calibration tube into the CVF Spectrometer telescope aperture.

During the two-year journey to Jupiter the telescope entrance apertures will be closed by two unique dual-purpose* spring closure-and-baffle systems extending from the forward end of the main frame telescope housing. These assemblies each comprise 44 1/2-inch wide spring steel fingers 0.005 thick and dished to automatically form a continuous circular telescope baffle tube when released. To form an aperture cover, these fingers are folded into an overlapping flower petal arrangement for an iris-closure effect, and held in place by an outgassed dacron string. Internal surfaces would be black chrome-plated for maximum absorption with minimum particle generation during the

*The dual usage design approach is intended as a weight savings.

closure release affected by a melt wire concept similar to that used on the ALSEP* Solar Wind Spectrometer. The ALSEP package used a spring-loaded aperture cover which was released by burning through the hold-down dacron string with two Nichrome wire filaments supplies with 1/2 amps at 3 volts.

Telescopes

Optical Elements - The two 6-inch Cassegrainian telescopes use identical replicated optical elements (primary and secondary mirrors). The replication process is described elsewhere in the report. Functionally, it is a method for reproducing a mirror surface from a precision optical master by use of an epoxy substrate coated onto an aluminum mirror blank. (Aluminum's coefficient of thermal expansion would be compatible with that of the epoxy for any gross temperature changes.)

For the primary mirror, a dinner plate configuration is the most efficient use of material, as the mounting ring on the back side effectively provides a fixed edge for two concentric, cantilevered, circular plates of relatively short span. The optimum positioning of the ring is at approximately 0.7 of the mirror outside radius.[1]

Support Structure - The primary mirror is spot bonded three places to the inner ring of the optics base plate after being positioned and held in place by special tooling. The secondary mirror is also positioned and spot bonded inside a circular aluminum ring which is part of a brazed aluminum frame consisting of six 0.2-inch wide by 0.050-inch thick struts connecting two concentric cylindrical rings so as to form a truss structure of conical shape between the two rings. (Adjacent struts form triangular frames with ring segments as the third member.) Struts on opposing sides of the truss form 4-bar linkages with the rings as parallel links. Small deflections of the secondary mirror ring will result in the secondary mirror rotating about its center of curvature with resulting negligible effects on optical performance of the telescope assembly. The truss structure is bonded directly to the primary

[1] Chin, D., "Mirror Mount Design," Applied Optics, 3, 895 (1964).

*Apollo Lunar Solar Experiment Package

mirror support (optics base plate). Although the aft optics subassemblies are mounted on the optics base plates and use the telescope central baffles for a heat sink (radiating directly into the main frame cavity), heat loads into the optics base plates are minimized by using spoked wheels to locate the central baffles with respect to the primary mirrors.

Far Infrared Grating Filter Unit

This unit is shown as an aft optics subassembly in Figures 6-2 and 6-3. Basically, it comprises two optical systems using the same telescope and tuning-fork chopper (see Figure 6-1). The fixed grating assembly will be similar to one used successfully on the SIRS-B program as follows:

Grating Assembly* - The TiF_6 glass grating must be positioned accurately and retain this position during the launch and use environments. Stresses caused by differential thermal expansion must be avoided. Figure 6-6 shows the grating assembly. The grating is spot bonded to an accurately machined beryllium adapter plate which serves as the mechanical register and as a thermal adapter between the aluminum frame and TiF_6 glass grating. The kinematic pin and slot arrangement in the backing plate absorbs the differential expansion and provides the accurate positioning. The grating-adapter plate combination is held to the aluminum frame by means of a three-piece aluminum assembly and strategically placed pads made of Mylar and Viton rubber. The mount is designed so that the grating, adapter plate, and housing parts are one integral assembly. When mounted in the frame, the distortion forces are dampened by the pads while the adapter plate maintains position. A cover, part of the assembly, protects the critically ruled surface of the grating and is not removed until the assembly is safely mounted on the grating frame.

The mirrors and detector package for the grating channels will be shimmed for alignment and bonded in place within an all-aluminum frame

*This design approach has been proven out in actual space flight hardware. (Ref: NASA Nimbus D, SIRS-B program)

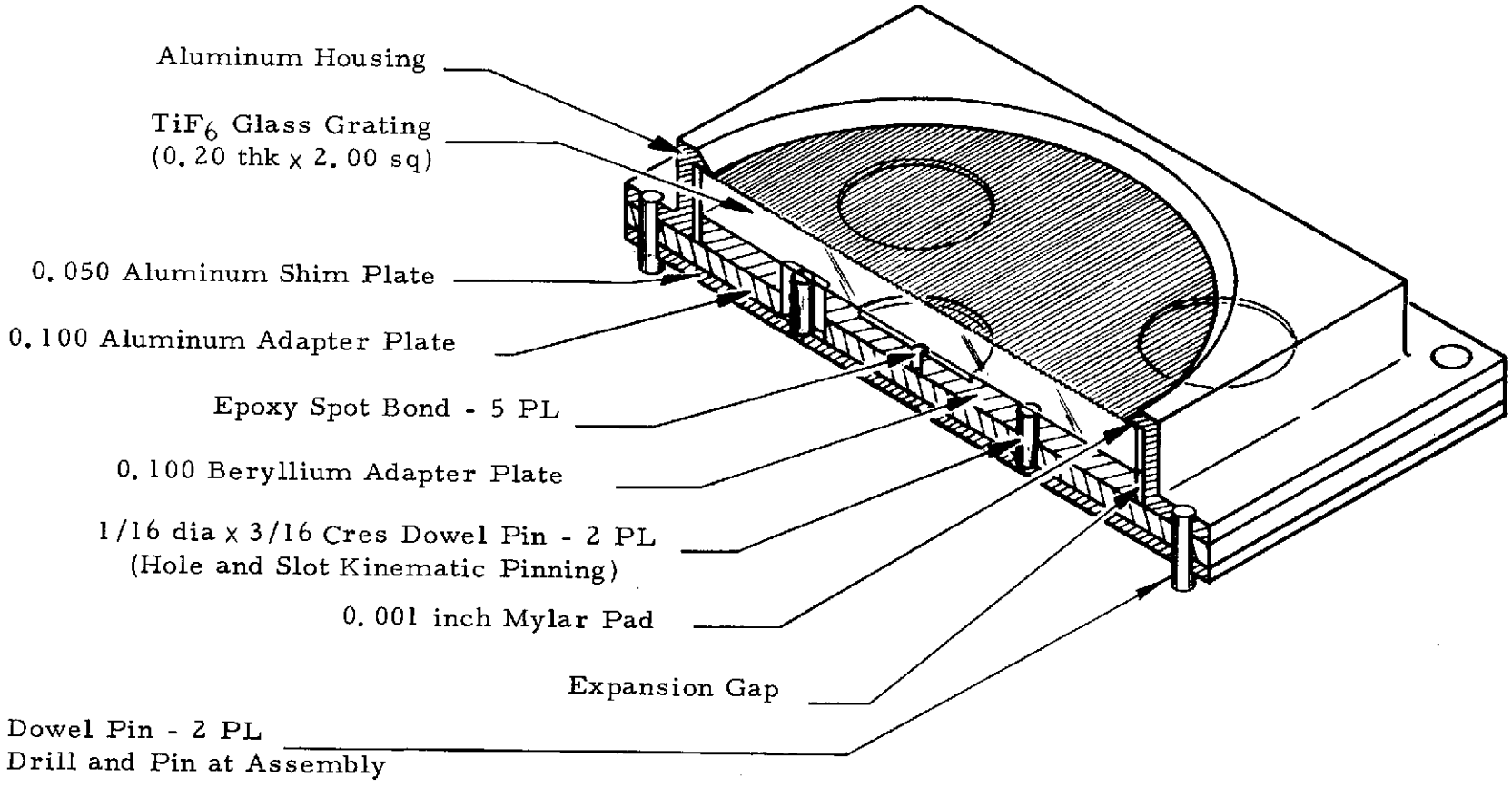

Figure 6-6. Grating Assembly

which will be mounted on the optics base plates and covered with an insulation blanket. The telescope field stop (including the entrance aperture for the grating channels) is mounted in a separable package along with two sets of reststrahlen mirrors of mutually orthogonal reflection directions and their detectors.

WEIGHT SUMMARIES

Two weight analyses were performed; one for the dual 6-inch telescope final version described in this report and one for a larger version which used a 4.6-inch telescope for the radiation cooler channels and a 12-inch telescope for the grating radiometer.

Weight Summary (Dual, 6-inch Telescope Version)

		Pounds
Main Frame Assembly		7.138
Main Frame	6.482	
Thermal Blanket	0.400	
Calibration Assembly	0.256	
Subtotal	7.138	
Continuous Filter Wedge Spectrometer*		4.33
Cooler Housing Subassembly		
Radiation Cooler	1.029	
Stepper Motor	1.03	
CV Filter Disk	0.15	
Tuning-Fork Chopper	0.15	
Cooler Housing	0.681	
Subtotal	3.04	

*The weight of the support structure for this unit is included in the main frame assembly.

		Pounds
Telescope/Aft Optics Subassembly		
Telescope (6-inch)	0.887	
Bolometric Unit	0.403	
Subtotal	1.29	
Fixed Grating Radiometer		2.447
Telescope (6-inch)	0.889	
Grating Filter Unit	1.408	
Tuning Fork Chopper	0.15	
Subtotal	2.447	
Overall Assembly Subtotal		13.915
Epoxy, paint and hardware (10%)		1.392
Wiring and interconnect (5%)		0.696
Total Weight		16.003
Electronics Weight (from Section 9)		7.51
Total System Weight		23.513 Pounds

Weight Summary (12-inch and 4.6-inch Telescopes Version)

		Pounds
Main Frame Assembly		9.877
Main Frame	8.891	
Thermal Blanket	0.73	
Calibration Assembly	0.256	
Subtotal	9.877	
Continuous Filter Wedge Spectrometer		3.504
Main Frame Subassemblies*		
Radiation Cooler	1.029	
Motor/Filter Disk Assembly	1.256	
Tuning-Fork Chopper Assembly	0.137	
Subtotal	2.458	

*The weight of the support structure for this unit is included in the main frame assembly.

			Pounds
Telescope/Aft Optics Assembly			
Telescope (4.6-inch)		0.783	
Bolometric Unit		0.263	
	Subtotal	1.046	
Fixed Grating Radiometer			4.187
Telescope (12-inch)		3.25	
Grating Filter Unit		0.937	
	Subtotal	4.187	
Overall Assembly Subtotal			17.568
Epoxy, paint and hardware (10%)			1.757
Wiring and interconnect (5%)			0.878
		Total Weight	20.203 Pounds
		Electronics Weight	7.51
		Total System Weight	27.713 Pounds

Section 7
THERMAL ANALYSIS

THERMAL MODEL

The proposed Mariner Jupiter/Saturn Spectro-Radiometer design consists of two Cassegrain telescopes mounted side by side and boresighted in a common look direction. The main housing is a bonded aluminum frame of monocoque construction utilizing integral honeycomb sandwich panels. A separate subframe structure housing the aft-optics and IR channel preamplifiers bolts to a honeycomb base plate/frame closing one end of the radiometer. Two subframes in addition support the primary optics which include the primary mirror and the secondary mirror and spider support for each telescope. The main housing is of non-circular cylindrical cross-section roughly described as that produced by wrapping two circular cylinders of 7-inch diameter together by a common skin. Aluminum honeycomb sandwich panels partition the two primary optical paths, support the radiation cooler and the CVF drive motor subassembly, located toward the aft end of the instrument (end opposite the aperture), and provide a rigid base for mounting the radiometer to the spacecraft.

When mounted to the spacecraft, the instrument will be covered with a multilayer aluminized mylar thermal blanket designed to minimize heat exchange with space and spacecraft. The principle heat transfer will occur from conduction between the radiometer and the spacecraft mounting platform through the mounting posts and by radiation to space through the two apertures.

In the preliminary thermal analysis only axial temperature gradients will be considered. This simplification is reasonable by virtue of the proposed design structural characteristics and by the apparent polarity of power dissipating and absorbing elements. Tables 7-1 and 7-2 provide summaries of projected thermal conductivities and radiation couplings, respectively, between nodes of the thermal model shown schematically in Figure 7-1. Also

Table 7-1. Thermal Model Nodal Conductivities

From Node	To Node	Conduction Path Model	Thermal Conductivity Watt-°C^{-1}
1	2	Two 4-inch long, 0.015-inch thick aluminum cylindrical sections of 7-inch diameter casing* plus equal length of six 0.015-inch thick honeycomb panel facings: two 9.5-inch width (divider panel), two 17.25-inch width (instrument casing panel) and two 8.5-inch width (radiation cooler support panel).	2.41
1	6	Conductive isolation of the casing skin with the honeycomb baseplate supporting the aft-optics and telescope structures. Value is based on a conservative estimate of epoxy bond conductance of 0.3 mw-in^{-2} °C^{-1}, a bond material thickness of 0.01-inch, and contact surface area of 10 square inches.	0.006
2	3	Same as 1-6 (due to spring cover high-resistance epoxy bond).	0.006
2	7	1) Conductive isolation of the radiometer to the mounting platform	0.00005
		2) and 3) projected bounds for spacecraft conductive interfacing (note: these values simulate mounting interface at the aft end only; see node 4-8 for additional mounting post conductivity).	0.05 0.5
3	4	1) Spring cover open. Two 4-inch long, 0.015-inch thick stainless-steel cylindrical sections of 7-inch diameter. 2) Spring cover closed. Two 2-inch long, 0.015-inch thick stainless-steel cylindrical sections of 7-inch diameter terminating in a 7-inch diameter, 0.015-inch thick disk.	0.092 0.0236
5	6	One 2-inch diameter, 3-inch long, 0.015-inch thick cylindrical baffle bonded to node 6 with silver loaded epoxy for high conductivity.	0.352
6	7	Same as 2-7.	0.00005 0.05 0.5

*The thermal model of the instrument casing skin and spring cover consists of two parallel cylinders 16 inches long divided into four axial nodes. (See Figure 7-1.)

Table 7-2. Thermal Model Radiation Conductivities

From Node	To Node	Radiation Path Model	Radiation Conductivity Watt-°C^{-4} x 10^{-9}
1	2	Internal surfaces of adjacent cylindrical sections of 7-inch diameter, 4-inch length with a view factor of 0.3, and emissivity of $\epsilon = 1$.	1.93
1	5	Internal surface of a cylindrical section of 7-inch diameter, 4-inch length to primary baffle (see Table 7-1 node 5-6) $\epsilon = 1$.	1.77
1	6	Internal surface of a cylindrical section of 7-inch diameter viewing an annulus at one base with a view factor of 0.26, and emissivity of $\epsilon = 0.05$.	0.0836
1	8	External surface of a cylindrical section of 7-inch dia and 4-inch length viewing space with $\epsilon = 0.01$ (thermal blanket).	0.0644
2	3	Same as 1-2	1.93
2	8	Same as 1-8	0.0644
3	4	Same as 1-2	1.93
3	8	1) Same as 1-8. 2) Same as 1-9 but with $\epsilon = 0.1$ (shiny surface, no thermal blanket)	0.0644 0.644
4	8	1) Spring cover open same as 1-2 plus 3-8 with $\epsilon = 0.1$. 2) Spring cover closed 7-inch diameter disk $\epsilon = 0.1$.	2.57 0.282

listed in Tables 7-1 and 7-2 are the assumptions upon which each factor is based. Not specifically included in the thermal model described in Tables 7-1 and 7-2 are the telescope secondary mirrors and supporting structures which are modeled as follows:

To a first order approximation one can determine the temperature gradient in the secondary mirror support members from predicted boundary temperatures determined by the thermal model of Figure 7-1 by making

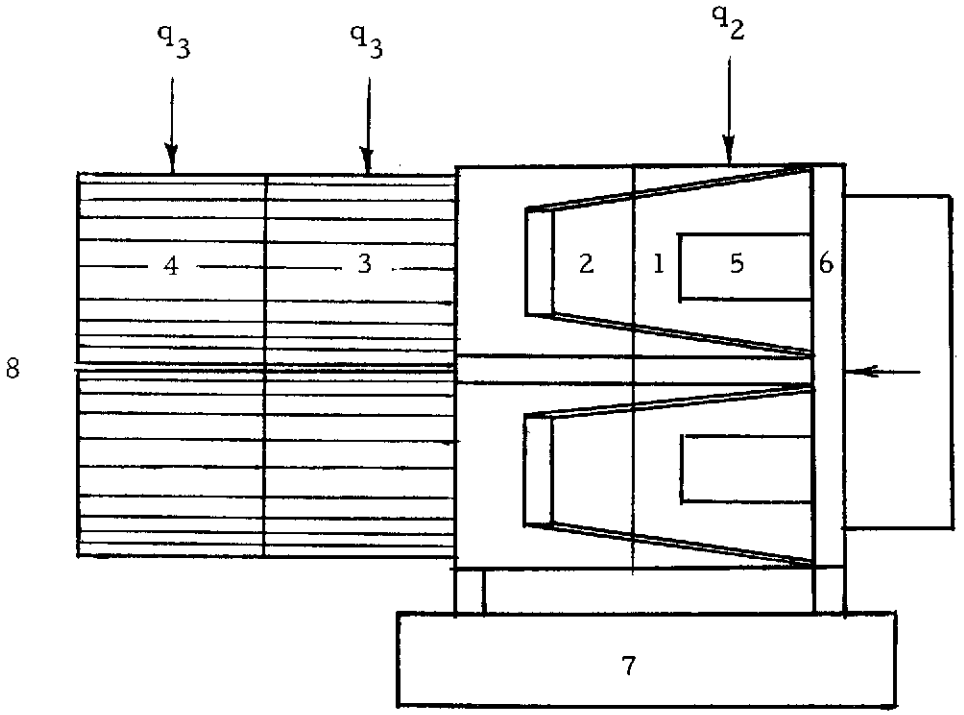

Node	Description
1, 2	Radiometer housing and frame
3, 4	Spring cover
5	Primary baffle
6	Telescope mounting plate
7	Spacecraft mounting platform
8	Cold space
Heat Inputs	**Source**
q_1	Preamplifier power dissipation
q_2	Motor power dissipation
q_3	Ambient spacecraft power flux

Figure 7-1. Thermal Model Nodal Schematic

certain assumptions regarding thermal conductivity of the support mounting bond. Assuming that a reflective coating of aluminum having $\epsilon = 0.05$ is used on the back and sides of each secondary mirror (back side facing the aperture) to decouple it from space view its equilibrium temperature will be determined primarily by the temperature gradient in the mirror support members. The thermal model of the secondary mirror and support structure consists of six rectangular cross-section aluminum support rods each divided into ten nodes of 0.2 x 0.05 inch cross section and 0.6-inch length. Each support rod is bonded at one end to the telescope mounting frame and supports the secondary mirror at the opposite end.

The surfaces of the support rods are coated black and hence are strongly radiatively coupled to the telescope cavity (node 2). It has been determined that the reflective backside of the secondary mirror 3-inch diameter disk (side facing the aperture) views space (node 8) with a view factor of 0.1, the spring cover (nodes 3 and 4) with a view factor of 0.5 and the telescope housing cavity (node 2) with a view factor of 0.4. The total emissive area of a secondary mirror is computed to be 16 square inches.

Other assumptions made relating to the thermal model are the following:

1. Temperature of cold space is -240°C.
2. Temperature of the spacecraft mounting platform will be constant at a value within the following range: -23°C (250°K) to 0°C.
3. Aluminum construction throughout with the exception of the spring cover with constant thermal conductivity of K = 5.6 watt-in^{-1}-°C^{-1} over the temperature range of from 150°K to 300°K. *
4. Stainless steel spring cover (aperture cover) with conductivity K = 0.56 watt-in^{-1}-°C^{-1} (factor of 10 less than aluminum).
5. Honeycomb core density of 0.64 gram-cm^{-3} (lb/ft^{-7}) for all honeycomb panels.

---

*A compendium of the properties of materials at low temperature (phase II), National Bureau of Standards Cryogenic Engineering Laboratory, Boulder, Colorado, Dec. 1961.

6. Joule heating from aft-optics area preamplifiers is estimated to be 1.5 watts (heat input to node 6). Dissipation from the CVF drive motor including encoder and filter wheel is 5 watts (heat input to node 1) and that from the calibration paddle actuator is negligible in the steady state.

7. Incident heat flux from the spacecraft bus and high gain antenna to the spring cover (which is not thermally blanketed but is assumed to have an emissivity of 0.1 due to its polished metal surface) is 0.6 watt per node (heat input to nodes 3 and 4 altogether is 0.12 watt).

8. Incident heat flux from the planets Jupiter and Saturn plus solar albedo effects have been calculated and were found to be negligible for heat balance considerations.

The thermal model just described allows, to a first order approximation, quantitative assessment of specific temperature related design factors such as the following:

1. Warpage of honeycomb sandwich panels due to temperature gradients across the panels.
2. Thermal elongation of optical support members.
3. Localized Joule heating
4. Cold sink contamination of primary optical components
5. Heat load to the spacecraft

The significance of these factors is discussed for steady state analysis in the following section.

THERMAL ANALYSIS

Using the configuration and assumptions outlined above, a number of steady state analyses were performed to establish a set of bounding temperature predictions for the radiometer. A summary of computed results is given in Table 7-3. First, a configuration of conductive isolation from the spacecraft mounting platform was investigated. In this case the principle heat dissipation occurs by radiation through the apertures and by radiation exchange from the outside surface of the aperture spring cover (which may or may not be thermally blanketed (see Tables 7-3 and 7-4) with spacecraft ambient flux emissions.

Table 7-3. Temperature Control Boundaries

Spacecraft Conductivity Interface (watt-°C^{-1})	Mounting Plate Temperature (°C) T_7	Cover Status	Power Status (6.5 watt)	Interface Heat Load (+) Power Conducted to Radiometer (watt)	Cover Temp (°C) T_4	Cavity Temp (°C) T_2	Axial Case Gradient (°C) $T_1 - T_2$	Telescope Mounting Plate Temp (°C) T_6
0.001	-	Off	On	-	-70.6	0.6	2.4	15.1
	-	Off	Off	-	-162.7	-141.9	0.1	-137.8
	-	On	On	-	-5.5	28.4	2.2	40.5
	-	On	Off	-	-127.7	-117.1	0.1	-114.6
0.1	-23	Off	On	-1.3	-79.8	-13.7	2.2	-5.5
	0	Off	On	-0.4	-72.2	-1.9	2.2	9.2
	-23	Off	Off	2.6	-106.8	-55.1	0.6	-41.8
	0	Off	Off	3.3	-97.4	-40.7	0.5	-25.3
	-23	On	On	-2.5	-29.1	0.8	2.0	4.0
	0	On	On	-1.4	-20.8	10.7	1.9	17.4
	-23	On	Off	1.7	-67.6	-44.3	0.3	-35.8
	0	On	Off	2.3	-54.2	-28.4	0.4	-18.2
1.0	-23	Off	On	-1.9	-85.3	-22.1	1.9	-20.0
	0	Off	On	-0.3	-72.2	-1.9	1.9	2.4
	-23	Off	Off	4.0	-90.4	-30.0	0.2	-24.0
	0	Off	Off	5.6	-77.1	-9.5	0.3	-1.6
	-23	On	On	-3.6	-46.3	-19.1	1.8	-19.5
	0	On	On	-2.4	-28.4	1.7	1.8	3.1
	-23	On	Off	2.5	-53.2	-27.2	0.1	-23.6
	0	On	Off	3.5	-35.0	-5.9	0.1	-1.0

Table 7-4. Temperature Control Boundaries, Spring Cover Thermally Blanketed (Out to Node 3)

Spacecraft Conductivity Interface (watt-°C^{-1})	Mounting Plate Temperature (°C) T_7	Cover Status	Power Status (6.5 watt)	Interface Heat Load (+) Power Conducted to Radiometer (watt)	Cover Temp (°C) T_4	Cavity Temp (°C) T_2	Axial Case Gradient (°C) $T_1 - T_2$	Telescope Mounting Plate Temp (°C) T_6
0.001	-	Off	On	-	-60.4	5.6	2.2	19.4
	-	Off	Off	-	-157.1	-137.5	0.1	-133.8
	-	On	On	-	55.4	78.3	1.8	87.7
	-	On	Off	-	-97.1	-89.9	0.1	-88.5
0.1	-23	Off	On	-1.7	-70.1	-8.7	2.1	-2.2
	0	Off	On	-0.7	-62.7	2.1	2.2	11.7
	-23	Off	Off	2.3	-99.6	-52.1	0.4	-40.2
	0	Off	Off	3.0	-89.4	-37.2	0.5	-23.3
	-23	On	On	-3.6	-4.4	13.1	1.5	12.4
	0	On	On	-2.9	9.7	28.6	1.6	30.0
	-23	On	Off	0.9	-47.5	-34.3	0.1	-30.0
	0	On	Off	1.3	-31.1	-16.2	0.2	-10.7
1.0	-23	Off	On	-2.5	-78.6	-21.1	1.9	-19.8
	0	Off	On	-1.1	-64.6	-0.5	1.8	2.7
	-23	Off	Off	3.5	-84.0	-29.1	0.2	-23.9
	0	Off	Off	4.8	-69.8	-8.2	0.3	-1.4
	-23	On	On	-5.1	-31.5	-16.7	1.8	-19.1
	0	On	On	-4.0	-12.5	4.3	1.6	3.5
	-23	On	Off	1.2	-39.1	-25.0	0.0	-23.3
	0	On	Off	1.8	-19.0	-3.0	0.1	-0.5

The following discussion in general pertains to the case in which the thermal blanket does not extend over the spring cover (worst case cold temperatures) corresponding to the data in Table 7-3. Temperature profile data for the thermally blanketed spring cover (out of node 3) is given in Table 7-4.

Assuming that 6.5 watts are internally generated by the CVF motor and preamplifiers and 1.2 watts are incident to the aperture cover (0.12 watt is actually absorbed because of the low emissivity of the cover) the steady state temperature of the cavity (taken as node 2) is 0.6°C (273.8°K), with a 2.4°C linear axial gradient along the casing between mounting posts (nodes 1 to 2). The spring cover is epoxy bonded to the instrument frame and is made of stainless steel which has a low thermal conductivity compared with aluminum, hence the temperature of the aperture spring cover can be much lower than the cavity temperature, in this case, -70.6°C (202.6°K). The telescope mounting plate is located toward the aft-end of the instrument adjacent to the principle internal power sources; its temperature is a function of the heat rejection capability of the proposed design. It is assumed in the thermal model that the method of heat rejection be by radiation to the telescope cavity from the primary baffle. This would help to reduce axial temperature gradients along the instrument casing due to power flow through the casing skin and place no special thermal requirements on bonded joints.* This method requires, however, that a good thermal conductive path exists between the preamplifiers located in the aft-optics area and the primary baffles.** Using this technique, the primary baffle must be bonded to the telescope mounting plate with a suitable filler such as silver loaded epoxy. Assuming the above model, the temperature of the telescope mounting plate during normal data taking operation of the instrument*** is computed to be 15.1°C (292.3°K). Assuming a filler is not

---

* i.e., minimum conductivity. In addition, epoxy bonded construction results in a lower heat load for the spacecraft in general than braze because of its high inherent thermal resistance.

** This requirement could also help to minimize temperature gradients in the aft-optics since the joule heating is constant.

***Aperture cover open, power on.

used to increase thermal conductance to the baffle, temperatures in the aft-optics area (including primary mirrors) could go as high as 81.2°C (354.4°K). This could produce temperature gradients in the region as high as 77°C compared with 1°C for a conductively tied baffle. Using the above boundary temperatures, the temperatures of the telescope secondary mirrors is computed to be -4.3°C (268.9°K) or -40.3°C (232.9°K) depending on the assumed thermal conductance of the epoxy bond between the mirror support members and mounting frame. Both cases of high and low conductance are of interest since the high conductance case determines the worst possible temperature gradient in the mirror support members, while the low conductance case provides the lower limit of mirror temperature. The secondary mirror, however, can get colder than the lowest temperature indicated above (which was the special case of thermal isolation of the instrument from the spacecraft) for the case where the instrument is thermally tied to the spacecraft which is at the lower limit of the assumed spacecraft temperature variation. Under these conditions, the secondary mirror boundary temperatures are reduced by heat rejection to the spacecraft through the mounting posts and the temperature of the secondary mirrors drops to -49.7°C (223.5°K). Since this last element is potentially the coldest optical element in the system, it does not appear likely that condensation of outgassing contaminants on its optical surface would be a problem as long as power was on. However, should the power be turned off during boil-off (outgassing of water and oil contaminants from insulating blankets and motors), the cavity temperature could drop as low as -142°C (131°K) risking contamination of all exposed optical surfaces. The heater power necessary to warm the telescope mounting plate to 0°C for a conductively isolated instrument is computed to be 2.6 watts with the aperture cover open and 2.3 watts with the cover closed.

This amount of joule heating would result in cavity temperatures (node 2) of -26.4°C (251.8°K) and -23.6°C (149.6°K), respectively. An alternative to heater compensation of a conductively isolated instrument to maintain acceptable operating temperature is careful design of a conductive interface

with the spacecraft mounting platform.* Table 7-3 gives a summary of casing temperature vs conductive interfacing over a practical range of conductivities typically achieved in similar applications. (Also for total isolation, i.e., C = 0.2221.) It should be pointed out that almost any desired value of conductivity within practical limits can be produced by proper selection of materials and sizing of the conductive path.** For example, consider the instrument mounting interface to be four stainless steel grommet-type fasteners consisting of a plug and sleeve section with internal, all metal, self-locking threads. The thermal conductivity is primarily determined by the contact conductance at the metal-to-metal interfacing which is a function of the contact surface area, bolt torque, bolt and bushing material and surface condition. A typical value of contact conductance for a stainless steel 1/4-inch diameter bolt is 0.025 watt-in^{-2}-°C^{-1}. Assuming a total bearing surface area of 1 square inch per bolt yields a contact conductance for four mounting posts in parallel of 0.1 watt-°C^{-1}.

Another important design consideration is warpage of honeycomb structural panels due to thermal gradients across the panels. Such warpage of the honeycomb base plate supporting the telescopes could cause boresight error. The magnitude of the temperature gradient across a honeycomb structure is a function of the core density and panel width and is proportional to the heat flow through the panel. Assuming a minimum core density of 8 lb/ft^3 and a panel thickness of 0.5 inch the conductance per square inch of panel surface can be approximated by equation 1.

$$C = \frac{K\rho_c}{T\rho_{al}} \qquad (1)$$

where C = Area conductance of honeycomb panel, watt-in^{-2}-°C^{-1}

K = Thermal conductivity of aluminum, watt-in^{-1}-°C^{-1}

---

* Provided temperature stability of the mounting platform is satisfactory and the instrument does not significantly load the spacecraft thermally.

**A specially designed thermal belt or strap is sometimes used as a controlled conductive path in lieu of the mounting posts.

ρ_c = Honeycomb core density, lb-ft^{-3}

ρ_{al} = Density of solid aluminum, lb-ft^{-3}

T = Panel thickness, inch

where K = 5.6 watt-in^{-1}-°C^{-1}

ρ_c = 8 lb-ft^{-3}

ρ_{al} = 174 lb-ft^{-3}

T = 0.5 inch

yields C = 0.5 watt-in^{-2}-°C^{-1}

The temperature gradient can be expressed as follows:

$$\Delta T = q/CA$$

where ΔT = Temperature gradient across honeycomb panel, °C

q = Heat flow through panel, watt

C = Area conductance of honeycomb panel, watt-in^{-2}-°C

A = Surface area of honeycomb facing, in^2

Enumerating equation 2 for an approximate honeycomb facing area of 70 square inches and 6.5 watts worst case power flow through the panel yields

$$\Delta T \approx 0.2°C$$

The effect of this temperature gradient on boresight error can be read from Figure 7-2 which is plotted from the results of a computer simulation of boresight error as a function of temperature gradient assuming various thicknesses of aluminum plate of honeycomb and a telescope separation of 7.0 inches. From Figure 7-2, a 0.2°C temperature gradient across a 0.5 inch thick support plate would produce less than 0.1 mrad boresight error or less than 5% of the short side of the 3 x 5.4 mrad rectangular IFOV. This estimate is conservative since the existing frame structure and support panels would help to constrain warpage.

Another important thermal design consideration is the effect of thermal expansion/contraction of structural elements. The effect of ambient temperature change on the system is ignored, since all primary structural components

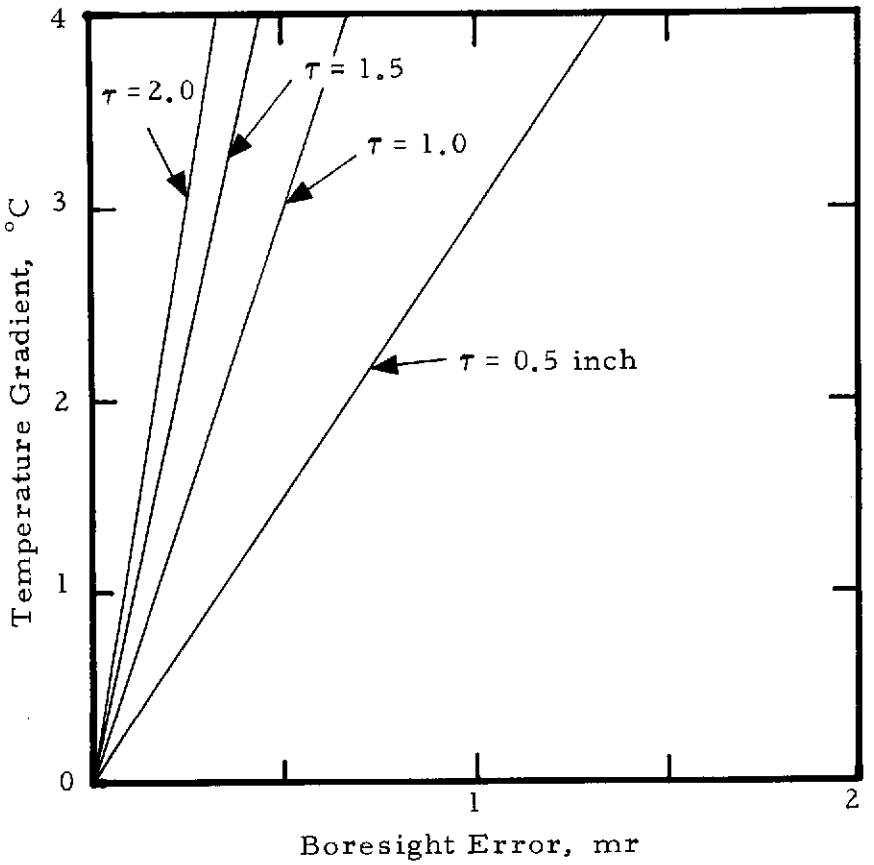

Figure 7-2. Boresight Error Versus Temperature Gradient Across a Given Honeycomb Panel Thickness

including the optical element support members are aluminum with the same coefficient of expansion, therefore all dimensions would scale linearly with temperature change. More significant from the standpoint of system performance are local temperature gradients within the system.

An axial displacement of the secondary mirror position relative to the primary mirror could cause optical defocusing of the image and potentially degrade resolution. A rule of thumb estimate to the magnitude of acceptable defocusing is the product of estimated image blur diameter with the f/No. of

the optical system. Assuming an image blur size of 0.01 inch (determined from optical ray trace data) and an f/No. of 3.5 yields a defocusing tolerance of ±0.018 inch for the two telescopes.

Figure 7-3 shows the worst case temperature distribution predicted in a single secondary mirror support assuming a six member support spider. The worst case temperature distribution occurs for complete conductive

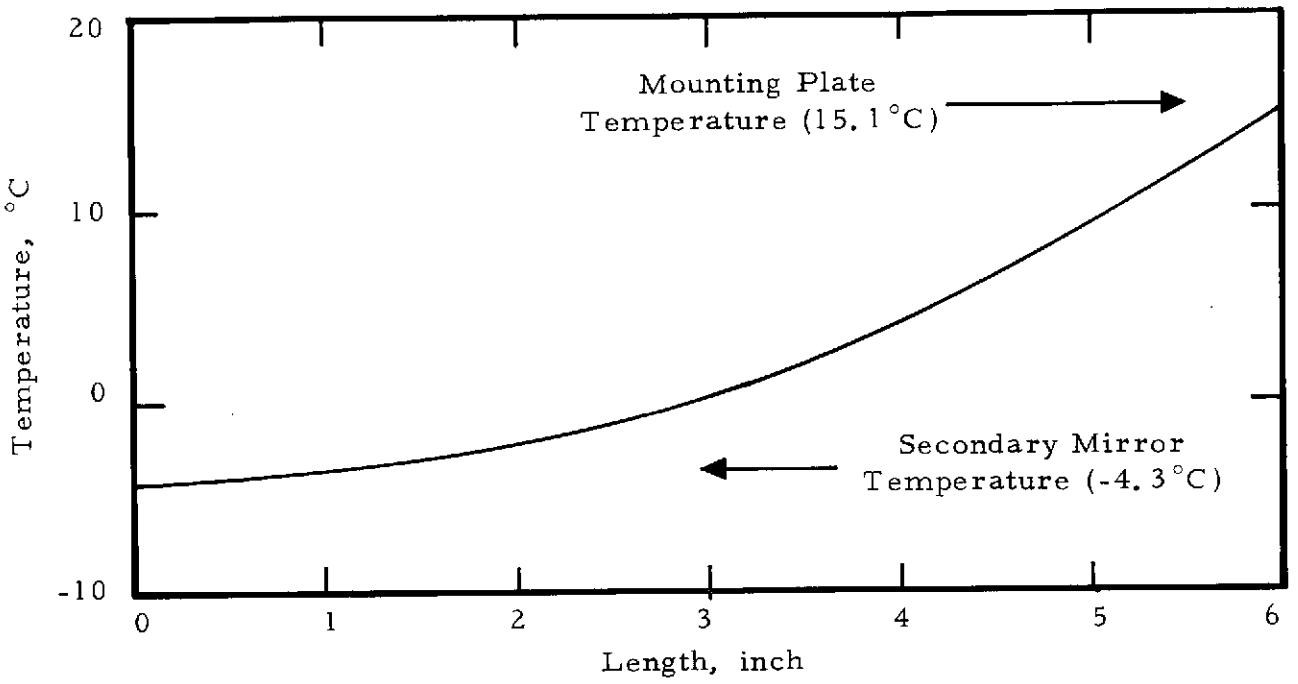

Figure 7-3. Worst Case Temperature Gradient in Secondary Mirror Support Member

isolation of the radiometer from the spacecraft and conductive epoxy bonding of the support member to the telescope mounting plate. Using the coefficient of thermal expansion of aluminum of 2.4×10^{-5} inch/inch°C and integrating elongation over the temperature distribution curve of Figure 7-3 yields a net thermal displacement of the secondary mirror of 0.0005 inch.

For small axial displacements of the secondary mirror of a Cassegrain telescope, the amount of defocusing is approximately equal to the axial dis-

placement times the magnification squared. Assuming an overall focal length of the telescopes to be 21 inches and a radius of curvature of the primary mirrors of -18 inches yields a magnification of 2.34. Squaring this value and multiplying by the support member displacement computed above (assuming it is all axial) yields 0.003 inch defocusing. This amount of defocusing is of an order of magnitude below the acceptable design tolerance variation predicted by rule of thumb above.

CONCLUSIONS

The thermal design of the radiometer has been reviewed. The results of an initial computer simulation of temperature behavior verifiys thermal feasibility of the proposed design. Preliminary quantitative analysis of potential thermal design problems shows reasonablecompatibility with system performance objectives.

It is not recommended that the radiometer be conductively isolated from the spacecraft mounting platform unless suitable measures are taken to allow continual warming of the instrument to assist venting of outgassing products. Failure to do so would be to risk contamination of primary optical elements.

In the final design special attention will be given to insure adequate heat rejection of principal power sources and electrical grounding of thermally isolated components such as the casing skin.

Operation of the radiation cooler is considered in another section of this report.

Section 8
RADIATION COOLER DESIGN

A study of requirements for detector cooling by means of a passive radiation cooler has been undertaken for the Mariner Jupiter/Saturn Spectro-Radiometer experiment. The parametric analysis was performed based on constraints that may or may not change at a later date.

The basic thermal requirement for the radiation cooler is to provide cooling $\leq 180^{\circ}K$ for detectors with joule heating of 25 mw. The basic radiation cooler design is discussed. Attention is particularly given to detector alignment, cooler degradation in space, insulation, low conductance support, and material selection for the cooler radiator. (See Figure 8-1.)

Parametric studies are made to determine approximate cooler size based on radiator thermal properties, spacecraft mounting temperature, electrical power for outgassing, and field of view of cooler radiator during Jupiter encounter. A detailed tabulation of heat inputs for a typical 5.0-inch diameter cooler is also given.

From this design study we can say that the $180^{\circ}K$ temperature can easily be attained by a 5.0-inch diameter cooler with a very comfortable margin of safety. The following conclusions can be made from the study:

1. The radiator diameter will be 5.0 inches
2. Total cooler weight will be 1.029 pounds.
3. The radiator material will be aluminized teflon or other suitable low solarabsorptance/high infrared emissivity material.
4. The cooler will be $108^{\circ}K$ when the radiator is facing the spacecraft +Y axis. (Figure 8-2.)
5. The cooler will be $162^{\circ}K$ when the radiator is facing the spacecraft -Y axis. (Figure 8-2.)
6. A heater of 0.52 watt will have to be provided to regulate the temperature at $180^{\circ}K$.

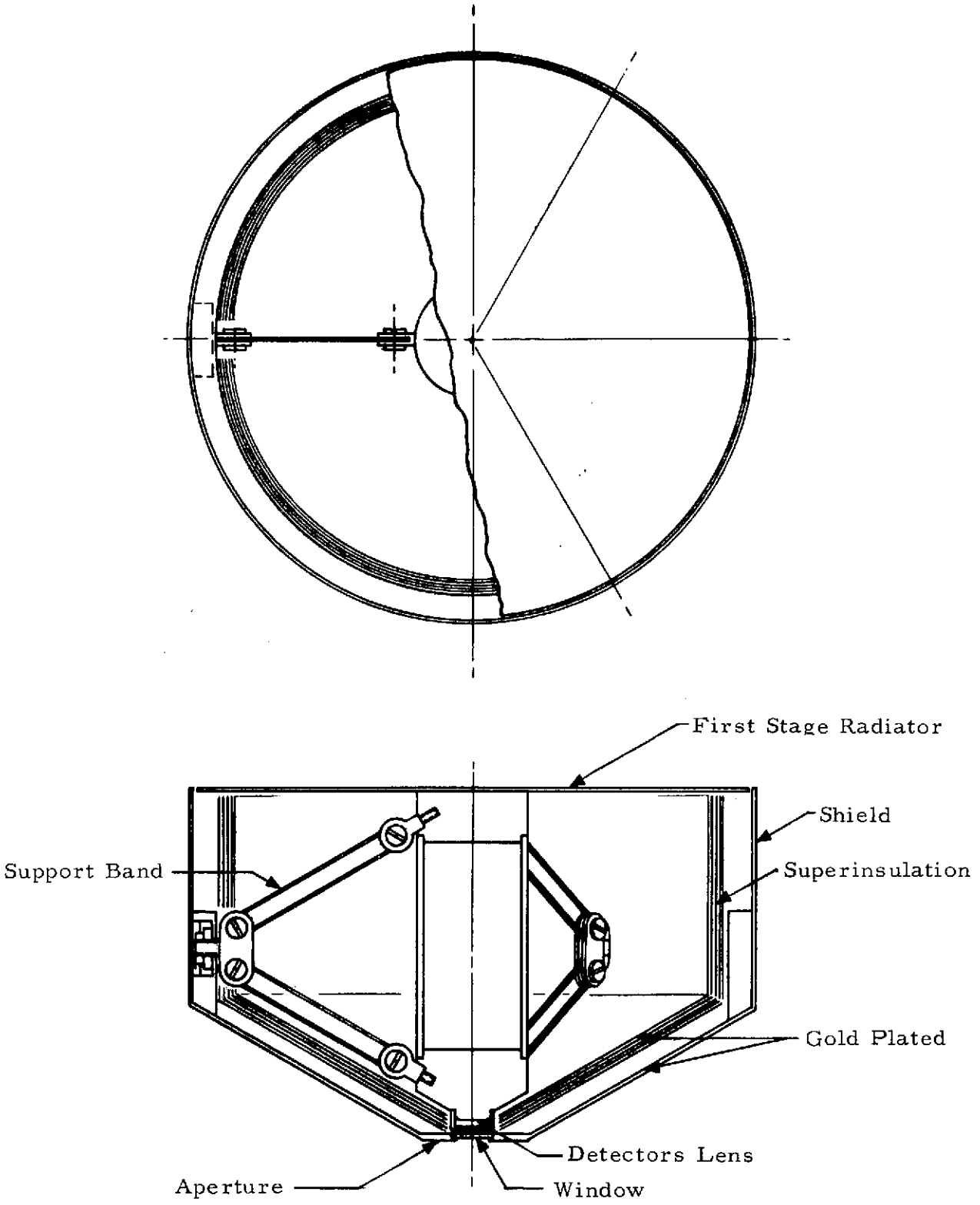

Figure 8-1. MJS Radiation Cooler

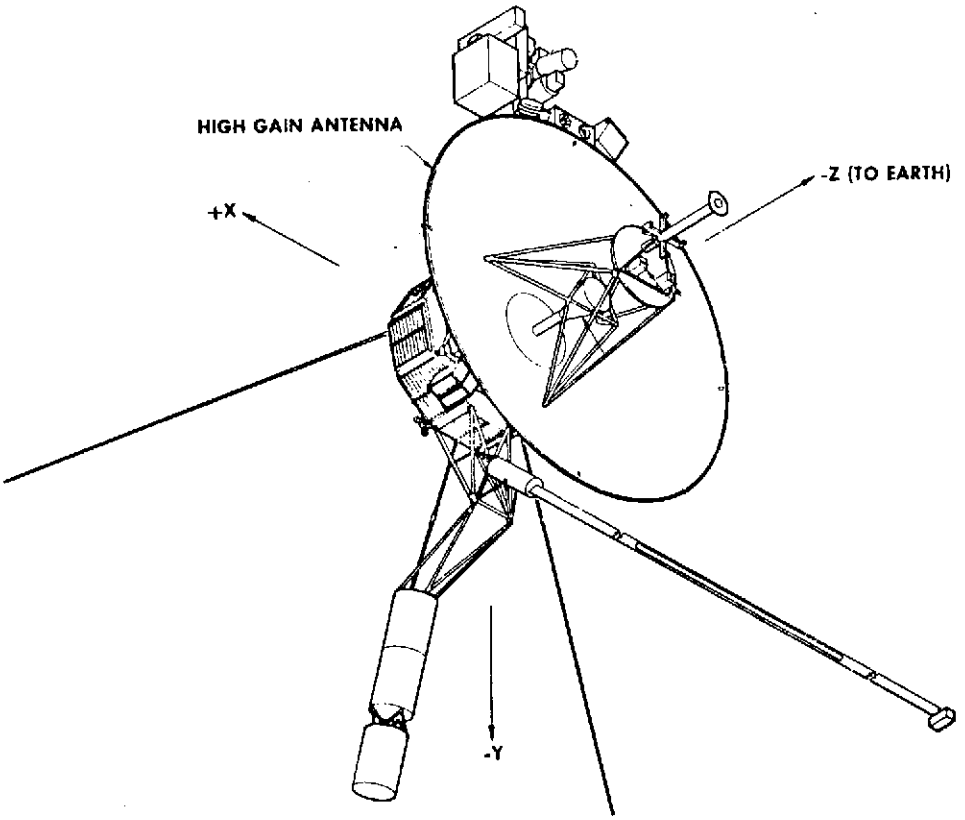

Direction of Surface Normal	Incident Flux From High Gain Antenna (milliwatts/ft^2)	Incident Flux From Spacecraft Bus (milliwatts/ft^2)
+x	0.5	104.0
-x	0.5	52.0
+y	0.0	0.0
-y	49.0	135.0
+z	0.0	78.0
-z	20.0	0.0

Figure 8-2. Radiation Emitted by High Gain Antenna and Spacecraft Bus During Near Jupiter Encounter That is Incident at Instrument Surfaces

7. A heater of 2.20 watts will be required to heat the cooler to 250°K to outgas contaminants.
8. A 6°K change in the mounting surface changes the first-stage radiator temperature by 1°K.

BASIC COOLER DESIGN

The design concept of the radiation cooler and its requirements are discussed in this section. The cooler is shown in Figure 8-1. Variations of this design are possible, but the heat transfer paths are characteristic of all radiation coolers.

The assembly consists basically of an outer shield mounted to the spacecraft via the telescope frame. The study assumed that the cooler shield temperature is the same as the telescope frame. The shield supports the cold first stage and detector by means of low-conductance fiberglass epoxy bands. The internal surface of the shield and the first stage facing the shieldare platedwith low emissivity gold. The detector and lens are mounted to one end of the first stage. On the opposite end is the first-stage radiator.

The radiator surface is of high emittance to dissipate the net power on the stage by radiation to space. Superinsulation is used between the shield and first stage to decrease the radiation energy transfer.

The addition of a heater, temperature sensor, and electrical connector produces a complete radiation cooler. The cooler will be mounted to the telescope and the thermal conductance will be such that the nominal shield temperature is maintained at 250°K.

REQUIREMENTS

The cooler requirements are as follows:

1. Cool detectors with 25 mw maximum joule heating to ≤180°K.
2. Upon alignment with the telescope the detectors must not shift more than ±0.008 inch longitudinally and ±0.008 inch radially.

3. Minimum weight.
4. 180°K detector temperature must be attained with maximum incident flux as noted in Figure 8-2.
5. Provide means of outgassing contaminants from detector lens.

STAGE SUPPORT

The 0.14-lb first stage will be supported by six glass-reinforced epoxy bands. The bands will have a cross section of 0.050 X 0.025 inch. The bands will have a tensile strength of ≥ 190,000 psi. Bands of this size and configuration have been fabricated and evaluated for a radiation cooler in another application.

The method of supporting the first stage is similar to the way the hub of a bicycle wheel is supported by its rim. Because of its symmetry, temperature change will not dislocate the detector radially.

Superinsulation

Superinsulation between the shield and first-stage provides the best reflective insulation value per pound for high-vacuum service. Its low thermal conductivity, low emissivity and effective separation of layers provide a highly effective thermal barrier. However, published values by manufacturers must be used with caution. Usually values reported are based on flat plate calorimeter tests where theoretical equations apply. Where penetrations and openings are necessary, a correction factor must always be used.

For the superinsulation to be effective, the cooler must be designed to ease the application of the insulation. The superinsulation will consist of six layers. Each layer will be made of mylar, aluminized on both sides, and a dacron net spacer.

Emittance and Absorptance of Gold Surface

Since radiation can be a major source of heat transfer in the radiation cooler, the emissivity and absorptivity of the gold-plated surfaces had to be

known. The emissivities and absorptivities of commercial gold surfaces are generally available but lack consistency and certain specifics regarding test conditions and surface preparation.

Low emissivity gold is desirable on the shield and first stage, because it decreases the need for more superinsulation. If many layers of superinsulation are properly applied, the effect of the gold becomes negligible.

To obtain first hand data, SBRC designed and built a special calorimeter specifically for this purpose under a company sponsored research program. The heat transferred by radiation was measured between surfaces at room temperature and liquid nitrogen temperature. The aluminum surfaces were gold plated by various plating vendors. From the test data, the total absorptivities of the liquid nitrogen cooled surfaces were computed.

The results of these tests indicated that gold absorptivity varies greatly with purity, process, technique, etc. The best surface tested was a matte, unbuffed, high-purity gold surface. The absorptivity at 77.3°K for radiation from a 300°K surface was about 0.0135. The extrapolated room temperature emittance of this surface would be approximately 0.0282.

It was found that absorptivities and emissivities of gold taken from text books, etc., must be used with caution, since they are often the best values attained. The best values are difficult to attain; they are dependent on plating technique, vendor, purity of solution, etc.

Seven samples were tested and absorptivities were obtained with the samples at liquid nitrogen temperature. The accuracy of the absorptivities was in the order of ±5%. The accuracy was a function of rate of heat transfer, outer surface temperature, and inner surface area.

THERMAL PROPERTY AND REQUIREMENTS OF FIRST STAGE RADIATOR

The first-stage radiator receives solar energy when the radiator is in the -Z axis direction (Figure 8-2). Reference 1,* shows the loss of reflectance over a period of one year for some thermal control coatings. The change in solar reflectance will increase the cooler temperature. To minimize the effect of solar energy on the first-stage radiator, an investigation was made to find alternate coatings for the black honeycomb radiator.

Requirements

The coating should have the following properties:

1. High infrared emissivity ($\epsilon \geq 0.80$) and low solar absorptivity ($\alpha \leq 0.25$).
2. Ease of application on radiator without degrading low-emissivity gold-plated surface.
3. Predictable thermal properties confirmed by flight tests.

Table 8-1 lists the important parameters and data concerning the coatings. The comments are from information gathered by talking to those who are considered authorities in the area of thermal control coatings and from technical literature tabulated in the list of references.

The white paints in Table 8-2 are considered unstable when exposed to UV in vacuum. However, in this application the amount of degradation will not be known until UV exposure and radiation levels become defined. The emissivity will not degrade. The expected degradation of α is due to bombardment from electrons and protons.[4]

The H-2 and Z-93 inorganic white paints are more difficult to apply than the S-13G. The S-13G requires thorough cleaning and experience in applying it. However, once applied it is very difficult to remove.

---

*A list of references pertinent to this section is given at the end of this section.

Table 8-1. Candidate Materials for Radiator

Coating Name	α	$\Delta\alpha$*	ϵ_H	Thickness (in.)	Curing Temperature Maximum (°F)	Reference
S-13G	0.23	0.05	0.89	0.009	Room	6
Z-93	0.18	0.07	0.90	0.005	Room	6
H-2	0.16	0.06	0.90	0.008	225	3, 4
Teflon, FEP Aluminized	0.14	0.02	0.82	0.005**	150	9
SI-100	0.10	0.00	0.76	0.011**	150	
MSI-100	0.05	0.00	0.76	0.011**	150	
Teflon, FEP Silvered	0.07	0.02	0.82	0.005	150	9

*Protons plus electrons
**Including adhesive

ϵ_H - Hemispherical emissivity at ~180°K

Table 8-2. Coating Materials

Coating Name	Source
S-13G, White Paint, Organic	Illinois Institute of Technology Research Institute
Z-93, White Paint, Inorganic	Illinois Institute of Technology Research Institute
H-2, White Paint, Inorganic	Hughes Aircraft
Teflon, FEP, Aluminized	Hughes Aircraft; Lockheed Palo Alto Research Laboratories
SI-100, Silvered Quartz	Optical Coating Laboratories
MSI-100, Silvered Quartz	Optical Coating Laboratories
Teflon, FEP, Silvered	Lockheed Palo Alto Research Laboratories

Cryogenic temperatures will not affect the adherence. Potassium silicate is the binder in the H-2 and Z-93 white paints. Silicon RTV-602 is the binder in the S-13G

An important difference between the H-2 and Z-93 is the curing temperature. H-2 requires a curing temperature of 225± 10°F for 25 to 30 minutes whereas the Z-93 is cured at room temperature. It may be possible to cure the H-2 at room temperature but would require development time. Since one side of the radiator is gold plated, it must be masked for each coat of paint sprayed. The mask or protective coating must also be able to withstand elevated curing temperatures without leaving a residue.

The aluminized teflon and second surface mirrors (SI-100, and MSI-100) have very stable thermal properties in the space environment. The aluminized teflon and silvered film is easier to apply than the second surface mirror. The SI-100 and MSI-100 have very low α but this is not absolutely required for this application. The application of the second surface mirror is a very tough task. A cooler at HAC utilized the MSI-100 on a flat aluminized plate.[5] Many problems were encountered on that program.

Conclusion

The metalized teflon film (alumnized or silvered) should be used for this application:

1. Metalized teflon films have been temperature cycled to 77°K with no failure at the bondline. The substrate was an aluminum alloy.[9]
2. It is easier to apply than second surface mirror.
3. It is more stable (α) than the white paints in the space environment.
4. Metalized teflon films have been used on the Mariner 5, OGO-6, ATS-4, and SAS-4 spacecraft.

Outgassing - Degradation of Radiation Cooler

During long exposure to the space environment, the cold surfaces of the second stage can collect volatiles and other materials from within the cooler. Since outgassing of volatiles within the cooler can be detrimental

to the cooler performance, high outgassing materials like flux residue, certain plastics, paints, etc., must not be used. In addition to the small amount of outgassing from the cooler a certain degree of outgassing will exist from the remaining spacecraft experiments and from the spacecraft itself that must be considered. These contaminants can overcoat critical surfaces and parts and destroy the experiment. Cooler degradation did occur in two radiation coolers flown in space.[10,11]

A NASA committee was formed to investigate the cooler degradation problem.[12] To overcome the problem the following must be incorporated in the cooler:

1. Decrease outgassing by proper material selection and processing.
2. Place a high transmittance (in the wavelength of interest) window on the warm shield to prevent contaminants from entering through the aperture.
3. A heater must be mounted on the first stage. When an above-normal first-stage temperature becomes evident (from temperature telemetry information) the first-stage heater can be commanded ON to heat the stage to a temperature of approximately 250°K. Therefore, all volatiles previously collected on the first stage will be outgassed and the cooler first stage will be returned to a condition for proper detector operation.

THERMAL ANALYSIS

Energy Balance of First Stage

The energy absorbed by the first stage is equal to that radiated to space by the radiator. The following expression is used for the first-stage energy balance.

$$W_1 = Q_1 + Q_2 + Q_3 + Q_4 + Q_5 + Q_6 + Q_7 \qquad \text{(I)}$$

where W_1 = Energy radiated to space by first-stage radiator

Q_1 = Radiation from spacecraft appendages

Q_2 = Detector joule heating

Q_3 = Conduction through structural bands

Q_4 = Conduction by heater leads

Q_5 = Radiation through superinsulation

Q_6 = Solar energy incident on radiator

Q_7 = Conduction through detector and temperature sensor leads.

Energy Radiated To Space by Radiator. - The 5.0-inch diameter radiator has an area of 19.6 in^2. The aluminized teflon film has an infrared emissivity of 0.80. From $W_1 = \sigma \times A_1 \times \epsilon_1 \times T_1^4$

σ = Stefan Boltzmann's constant

A_1 = Radiator area

ϵ_1 = Radiator emissivity

T_1 = Temperature of first stage radiator

Radiation from Spacecraft Appendages. - The radiant flux from the spacecraft appendages varies according to the position of the radiator with respect to the spacecraft axis. In the worst case, the radiant flux will be 9.74 mw/in^2 (-Y axis). In the +Y axis there is no spacecraft radiant flux incident on the radiator.

$$Q_1 = A_1 \times \epsilon_1 \times W_2$$

where W_2 = Radiant flux from spacecraft appendages. (Figure 8-2.)

Detector Joule Heating. - The detector joule heating and radiation through the aperture was assumed not to exceed 0.025 watt (Q_2).

Conduction through Structural Bands. - Six structural bands support the first stage from the shield. The bands are in the shape of rubber bands but fabricated out of unidirectional wound glass and impregnated with epoxy. Tensile strengths in the order of 180,000 lb/in^2 have been attained in a similar application. The thermal conductivity is 0.019 watt/in°K. For this study, a band 0.050 inch wide and 0.025 inch thick was used. The length of the band is dependent on the cooler size.

$$Q_3 = N_1 \times A_2 \times K_1 \times (T_S - T_1)/L_1$$

where N_1 = Number of bands (12)

A_2 = Cross-sectional area of band

K_1 = Thermal conductivity

T_S = Shield temperature

L_1 = Band length

Conduction by Heater Leads. - The manganin heater wires for outgassing are 0.0126 inch diameter. Manganin has a thermal conductivity of 0.558 watt/in°K. It will have an overcoat of kapton to prevent electrical shorts. The length varies as the cooler diameter changes.

$$Q_4 = N_2 \times A_3 \times K_2 \times (T_S - T_1)/L_2$$

where N_2 = Number of wires (2)

A_3 = Cross-sectional area

K_2 = Thermal conductivity

L_2 = Heater wire length

Radiation Through Superinsulation. - Prediction of energy through the superinsulation is difficult due to the effect of conduction, radiation, penetrations, installation methods, etc. Published data are generally based on ideal calorimeter tests. The equation below is unusual for superinsulation heat leak, but it is a conservative one for this application. The equation is for a body enclosed within another. The energy radiated from the outside to the inner is then halved for energy through the superinsulation. The parts are electro-deposited gold and six layers of superinsulation are placed between the first stage and shield.

$$Q_5 = \left[T \times A_4 \times \epsilon_2 \times (T_S^4 - T_1^4)\right] \times 0.5$$

where A_4 = Area across which heat is transferred (60 in^2)

$\epsilon_2 \cong (\epsilon_3 \times \epsilon_4)/(\epsilon_3 + \epsilon_4)$

and ϵ_3 = Emissivity of first-stage gold.

ϵ_4 = Emissivity of shield gold.

The emissivity of the gold is temperature dependent.

Solar Energy Incident on Radiator. - The energy from the sun, absorbed by the radiator can be expressed as follows:

$$Q_6 = S \times A_1 \times \alpha \times \text{Cos } \theta$$

where S = Solar constant (0.0335 watt/in^2 worst case)

α = Solar absorptivity of aluminized teflon film (0.15)

θ = Angle between radiator normal and between cooler center to sun (worst case 0°)

Conduction through Detector and Temperature Sensor Leads. - The manganin wires are 0.005-inch diameter and their length changes for each cooler diameter. Each wire will be coated with kapton to prevent electrical shorts. There is a total of six wires, four for two detectors, and two for the temperature sensor.

$$Q_7 = N_3 \times A_5 \times K_2 \times (T_S - T_1)/L_3$$

where N_3 = Number of wires

A_5 = Cross-sectional area

L_3 = Wire length

Knowing the cooler geometry and thermal parameters, temperature of the first stage can be determined from equation (I).

Parametric Analysis

Radiator Temperature Versus Cooler Diameter Versus Radiator Material. - Figure 8-3 gives the theoretical radiator temperature for different radiator diameters. It shows temperature for a black honeycomb radiator and an aluminized teflon radiator. The black honeycomb radiator is the ideal material if no solar energy is incident on the radiator. (+Y axis in Figure 8-2.) However, when solar energy strikes the radiator (-Z axis), the temperature of the radiator is about 180°K. Note that the aluminized teflon radiator attains a much colder temperature (140°K) than the black honeycomb radiator when solar energy is incident on the radiator

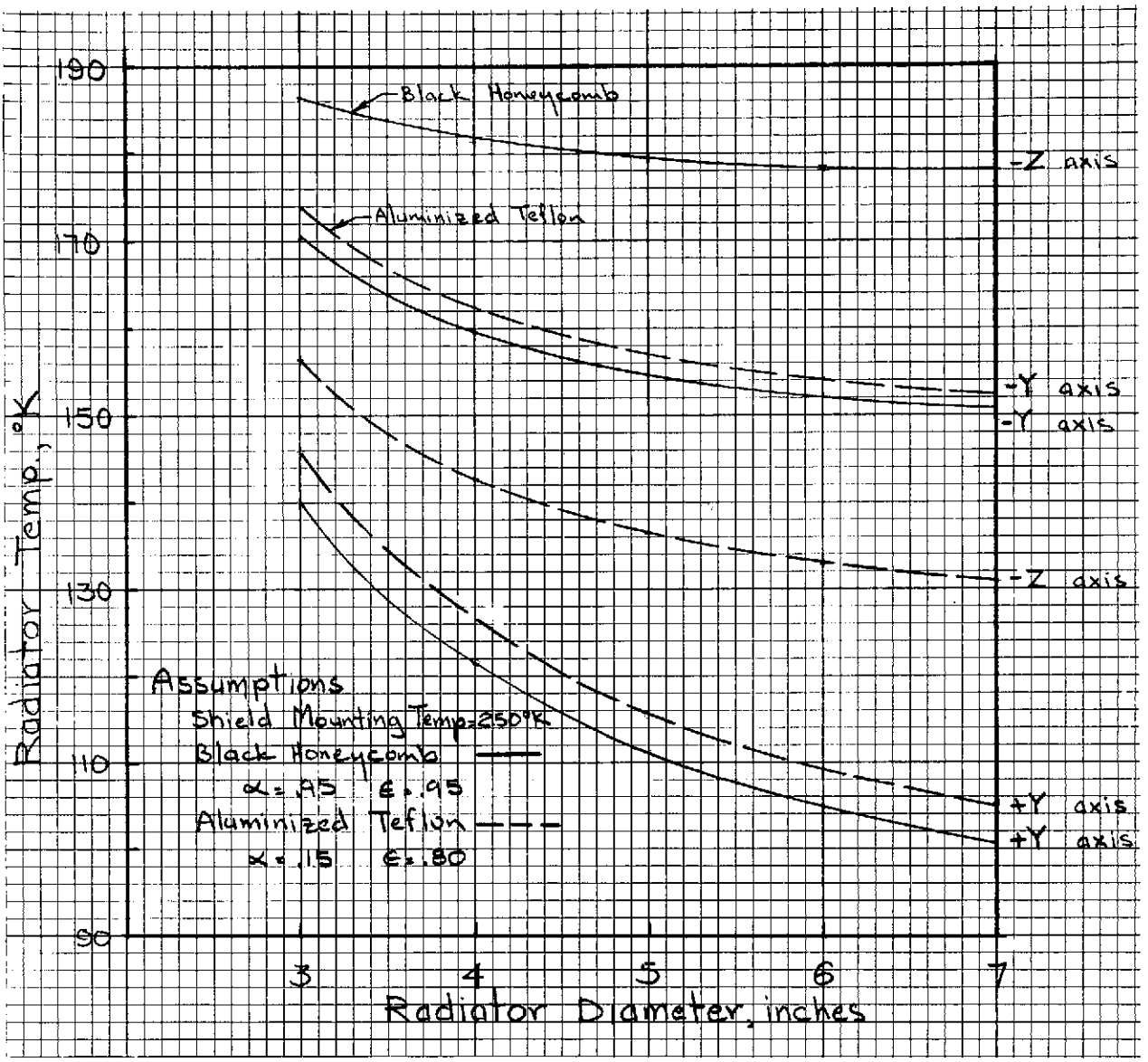

Figure 8-3. Radiator Temperature Versus Cooler Diameter Versus Radiator Material

(-Z axis). This is because the aluminized teflon film has a solar absorptivity of 0.15 whereas the black honeycomb radiator has a solar absorptivity of 0.95. When the radiator receives maximum energy from the spacecraft (-Y axis), the temperature for the black honeycomb radiator would be slightly less (3°K) than the aluminized teflon radiator.

From Figure 8-3 it can be concluded that the black honeycomb radiator will not meet the 180°K requirement when solar energy is incident

on the radiator. The aluminized teflon film will give a maximum temperature of 157°K and a minimum temperature of 116°K for a 5-inch diameter cooler.

Radiator Temperature Versus Cooler Diameter Versus Mounting Temperature. - Figure 8-4 shows how radiator temperature changes for different shield mounting temperature. The nominal shield mounting

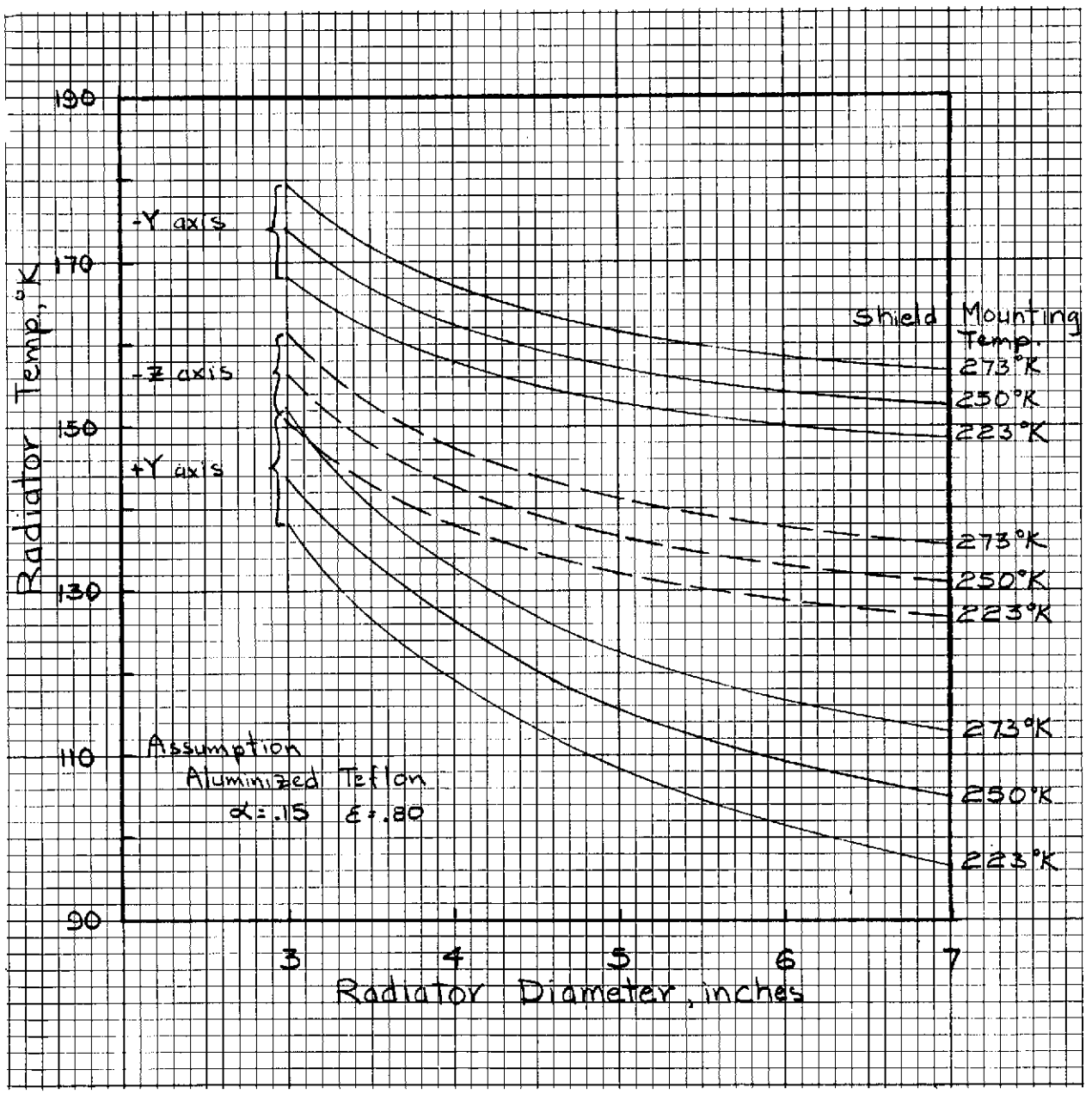

Figure 8-4. Radiator Temperature Versus Cooler Diameter Versus Mounting Temperature

temperature will be 250°K. The maximum could be 273°K and the minimum could be 223°K. The analysis shows that the radiator temperature changes 1°K for every 6°K change in the shield mounting temperature (-Y axis).

The maximum temperature for a 5-inch radiator diameter cooler will be 162°K. This is 18°K below the allowable maximum of 180°K. Note that Figure 8-4 is based on an aluminized teflon film radiator thermal coating. The minimum temperature can be as low as 108°K for a 5-inch diameter radiator cooler when the shield mounting temperature is 223°K. This occurs when the radiator views the +Y axis of the spacecraft. In this axis no solar or spacecraft energy is incident on the radiator.

Aluminized Teflon Film Versus Second Surface Mirror Radiator. - Figure 8-5 shows radiator temperature for two radiator thermal coatings. The aluminized teflon film and second surface mirrors have been thoroughly discussed under Thermal Property and Requirements of First-Stage Radiator. The curves in Figure 8-5 are based on a shield temperature of 250°K. The -Y axis signifies the condition when the radiator receives solar energy and the -Z axis is the condition when no solar or spacecraft energy is incident on the radiator.

The temperature differences are very small. Aluminized teflon film will be less expensive and easier to bond than the second surface mirror. If the space environment affects the aluminized teflon film, then the second surface mirror can be used with no thermal penalty.

Electrical Power for Outgassing Versus Radiator Diameter. - Normally it is desirable to get the coldest operating temperature cooler for added margin of safety. However, due to problems of cooler degradation and the necessity of an electrical heater, the power requirements for outgassing must be determined.

Figure 8-6 shows the electrical power requirement for various cooler diameters. Note that two curves are shown. One is for a radiator heated to 250°K and the other for 273°K. The type of volatiles and condensibles must

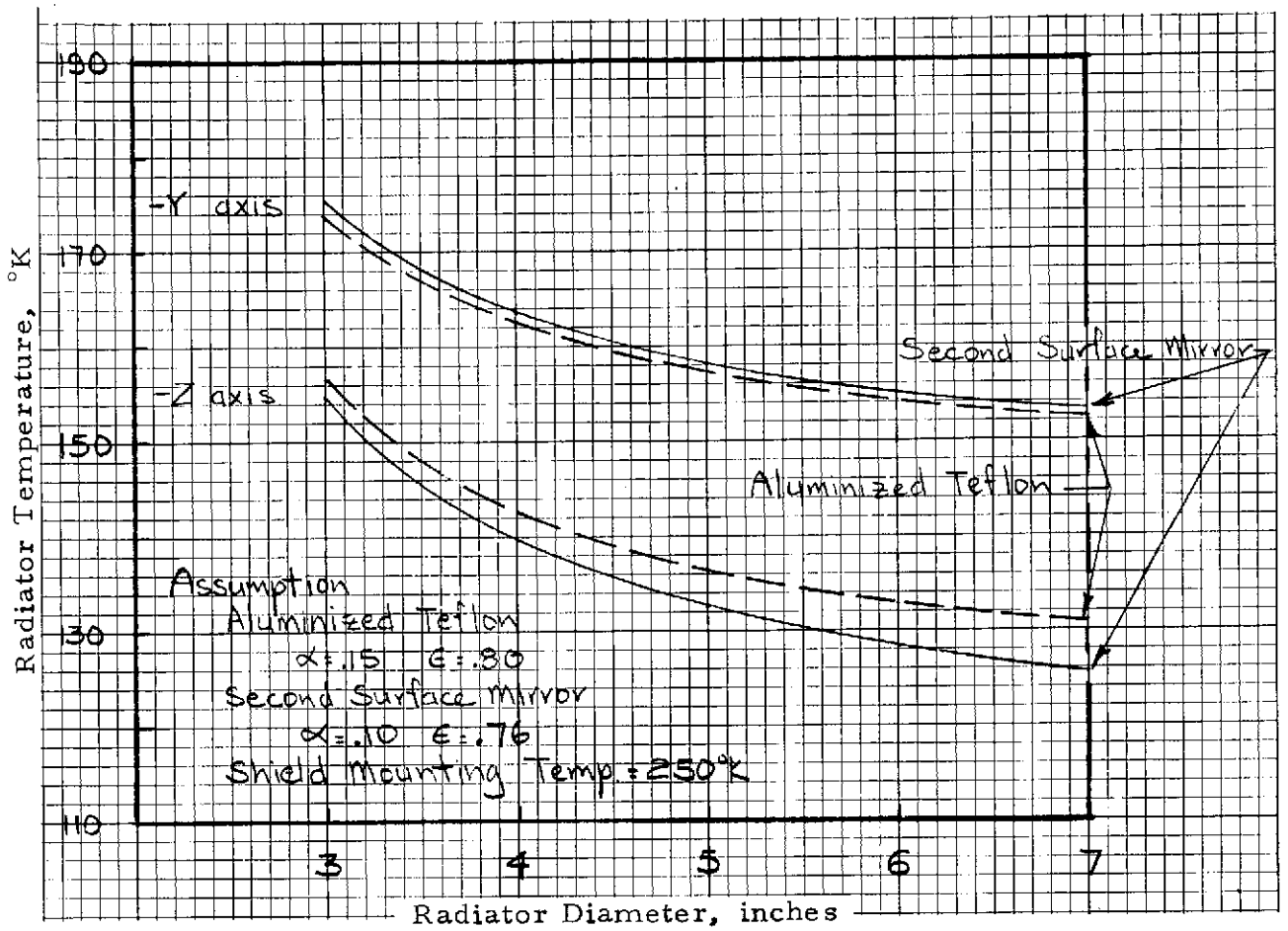

Figure 8-5. Aluminized Teflon Film Versus Second Surface Mirror Radiator

be first determined before the required temperature can be determined. In general, it is best to heat the first stage to as high as possible without degrading parts and components.

For example, Figure 8-6 shows that a 5-inch diameter radiator cooler will require 2.25 watts to heat the first stage to 250°K. It will require 3.20 watts to heat the first stage to 273°K.

MJS Cooler - Typical Thermal Loads

Table 8-3 summarizes the thermal heat loads of the cooler when the radiator is oriented perpendicular to the -Z axis, -Y axis, and +Y axis (see Figure 8-2). These axes were selected because they gave the extremes of

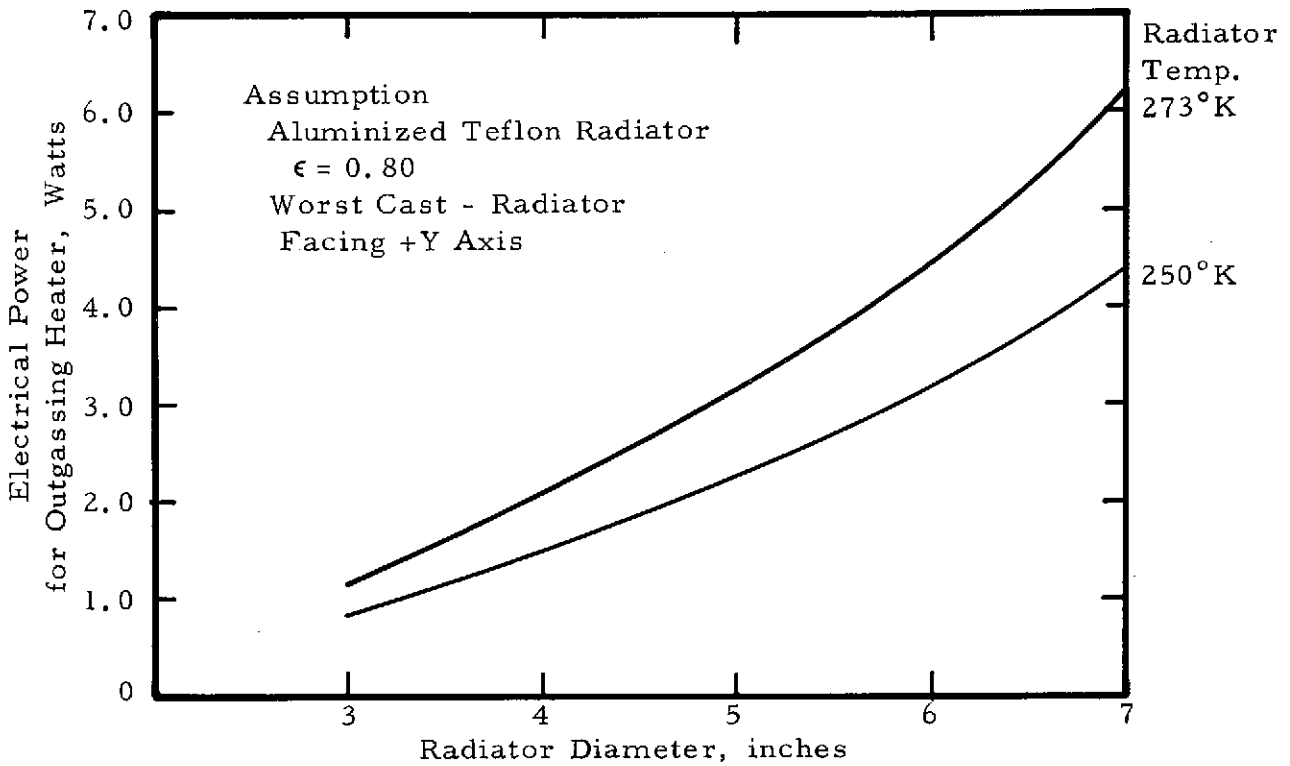

Figure 8-6. Electrical Power Versus Radiator Diameter

thermal loading. In the -Z axis the solar flux is greatest, in the -Y axis the spacecraft flux is greatest, and in the +Y axis no solar or spacecraft flux is incident on the radiator. Table 8-3 is based on a shield mounting temperature of 250°K and 5-inch diameter cooler.

Table 8-3. Thermal Summary

	Radiator Perpendicular to		
	+Y Axis	-Y Axis	-Z Axis
Shield Temperature	250°K	250°K	250°K
First-Stage Radiator Temperature	115°K	157°K	136°K
Radiation from spacecraft appendages	0.0000 watt	0.1529 watt	0.0022 watt
Joule heating	0.0250	0.0250	0.0250
Conduction through structural bands	0.0194	0.0134	0.0164
Conduction by heater leads	0.0063	0.0044	0.0053
Radiator through superinsulation	0.0488	0.0466	0.0485
Solar radiation	0.0000	0.0000	0.0986
Conduction through detector and temperature sensor leads	0.0035	0.0024	0.0029
	0.1030 watt	0.2447 watt	0.1989 watt

REFERENCES

1. J. B. Heaney, NASA GSFC; "Results From The ATS-3 Reflectometer Experiment"; AIAA 4th Thermophysics Conference; June 1969; AIAA No. 69-644.

2. E. R. Streed, Ames Research Center; "Passive Thermal Control By Second Surface Mirror"; Space and Aeronautics, Feb. 1969.

3. Telecon with Paul M. Blair, Jr. of Hughes Aircraft.

4. Paul M. Blair, Jr.; R. J. Andres; E. C. Smith; "Particulate Radiation Effects Simulating Synchronous Altitude on the Solar Absorptance of Several Spacecraft Thermal Control Surfaces"; AIAA 6th Thermophysics Conference; April 1971; AIAA No. 71-453.

5. Telecon with Joe Orth of Hughes Aircraft.

6. John Gilligan/G. A. Zerlant
Illinois Institute of Technology Research Institute
Polymer Chemistry Section

7. VISSR for SMS; SBRC VISSR/SMS Technical Staff; Quarterly Report for Period Ending 28 February 1971.

8. J. P. Millard; NASA Ames; "Results From The Thermal Control Coating Experiment on OSO-III"; AIAA 3rd Thermophysics Conference; June 1968.

9. Telecon with S. A. Greenberg; Lockheed Palo Alto Research Labs.

10. R. Shapiro, NASA GSFC; Nimbus II Flight Evaluation and Engineering Report.; NASA TND-4881.

11. Spaceborn Passive Radiator For Detector Cooling (Unpublished); Arthur D. Little Inc.

12. Degradation of the Radiant Cooler Of The Nimbus III High Resolution Infrared Radiometer HRIR - Report of the Committee; Unpublished; NASA GSFC.

Section 9
ELECTRONICS PACKAGING AND PARTS COUNT

As part of this study a brief analysis was made of the number of electronic components of various types in the total system. The block diagram (Figure 2-6) shows by a dotted line that a portion of the electronics, namely, preamplifiers, bias supplies and certain other circuits, arecontained within the optical head on the spacecraft scan platform. The remaining electronics are located in the spacecraft bus and are connected to the optical head by a cable which must pass through the bearings on the spacecraft scan platform. The number of wires which must be carried in this cable is shown in the block diagram.

The parts count was based on the block diagram and use was made of existing Viking IRTM technology and existing electronic circuit part counts which were already in existence in other SBRC programs. No attempt was made to design circuits but merely a scaling was made from existing systems. Results of this analysis are shown in Table 9-1 which shows the number of integrated circuits, transistors, diodes, resistors, capacitors, and other special components such as hybrid circuits which are used in the preamplifiers. Total parts count for this system is something over 1700 components (probably a round number of 1800 could be used).

REPAIRABLE CORDWOOD CONCEPT

To achieve the total system weight of 24 pounds, extremely lightweight electronic packaging concepts will be needed. Among these is a SBRC developed technique currently being used in the Viking IRTM consisting of two printed circuit boards separated by rigid foam as shown in Figure 9-1. The assembly is fabricated by first bonding the machined foam core between the two printed circuit boards. A hole is drilled from one side through the board and the foam through which axial leaded components are inserted. Each axial component, therefore, has a small hole large enough to admit the lead on one

Table 9-1. Mariner Jupiter/Saturn Parts Count

Block	Quantity-Units	IC	Trans/Diodes	Res	Caps	Other	Total Per System
Chopper P. A.	1 (for 12 ch)	14	4	46	6		70
AC Gain	12	1	1	2	2	1	84
Synch Demod	12	2		8	1		132
DC Diff Amp	12	1		2	1		48
DC Amp	12	1	1	4	2		96
Integ DC Mem & Rest.	12	4	8	18	6		432
Gain Change	12		1	2			36
Multiplexer	1	12	11	24	15	Hybrid 3	65
Chop/Demod Driver	1	1		2			3
Temp. Mon. Proc.	8	1		9	2		96
Pre-Amp	2	1	1	6	2		20
AC Gain	2	1		2	2	1	12
Bias Reg.	1	2	4	4	2	2	14
AC Diff Amp	2	1		2	1		8
Demod & LPF	2		4	7	4		30
Phase Comp.	2		2	2	2		12
Chop Driver	1	4	5	20	10		39
Demod Driver	1	1		2			3
Bias Supply	1	2	3	8	3		16
Mode, Cal & Restore & CVF Drive Logic	1	31	44	84	1		160
Rad. Cooler Temp Control	1	2	3	8	3	1	17
Motor Driver & Encoder Buffer	1		50	34	15	EM 13	112
Led Driver	1		4	3	1		8
CAL Lamp Driver	1	1	4	4	2		11
Cal Shutter Driver	1		5	4	1	1	11
Power Supply	1	4	33	13	29	5	85
Interface Filterface Ckts	1	6	33	55	12		106
		93	221	375	125	27	1726

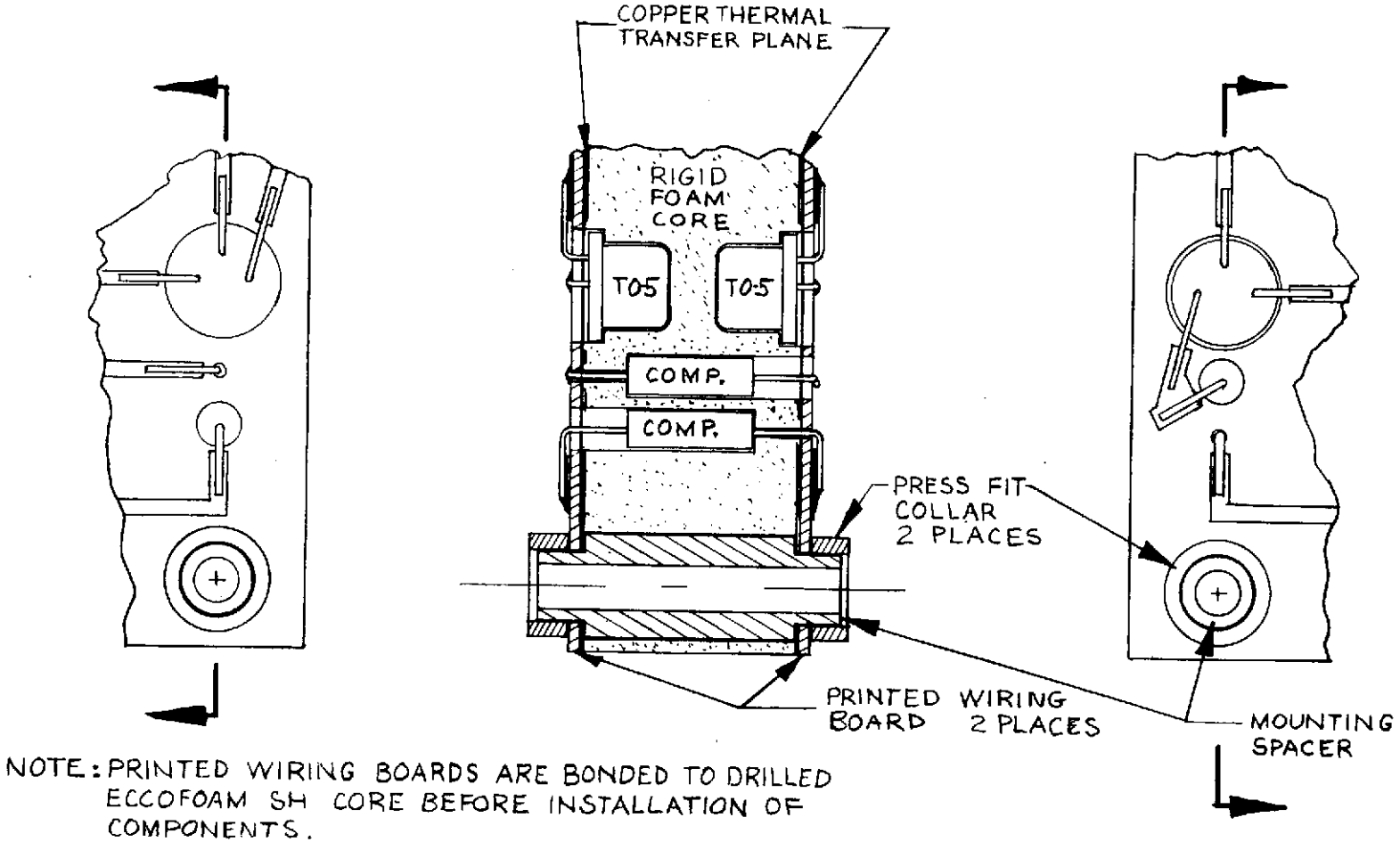

NOTE: PRINTED WIRING BOARDS ARE BONDED TO DRILLED ECCOFOAM SH CORE BEFORE INSTALLATION OF COMPONENTS.

Figure 9-1. Repairable Cordwood Construction

side but a hole large enough on the other side to withdraw the part if it becomes necessary. The leads for both ends of the component are bent over and soldered to the PC lands on the outside of the printed circuit board. The hole in the foam is made slightly smaller than the component so as to support it. The large and small holes are alternated on adjacent components so that when viewing one side, only half of the components are visible. Transistors are mounted in a similar manner. The can is supported by the hole in the foam core, the leads are bent over and soldered to the circuit pads, unlike welded cordwood modules which tend to be small because they are nonrepairable, this construction can be made virtually any size. The density of the packaging can be higher than welded cordwood modules because a mother board is not used and there is no wasted space between the modules. The component density of the repairable cordwood concept is equal to or higher than that of the welded cordwood modules, and a density of between 15 and 20 components per cubic inch has been demonstrated.

Because it is a relatively new concept, particularly for Viking, it is being environmentally qualified for that program. One problem area currently under study for the IRTM is a way to conduct the heat away from the package. The drawing of Figure 9-1 shows a copper heat conducting sheet on the inner side of each printed circuit board. In general, this technique will be used for low-level analog circuitry; power supplies and high-power dissipating circuits will be fabricated in the normal manner.

WEIGHT ANALYSIS

The component density for the repairable cordwood assembly including mounting pads averages 20 components/$(\text{in.})^3$. It is assumed that all the circuitry except the preamplifiers and the power supply and motor driver will be packaged using the cordwood technique. The power supply and motor driver circuits will be packaged on conventional single-sided printed circuit board; the preamplifiers will be hybrid circuits mounted near the detector assembly.

Therefore, the total number of cordwood components is 1529, at a density of 0.034 lb/(in.)^3. The weight would be

$$1529 \cdot \frac{1}{20} \times 0.034 = 2.6 \text{ lb}$$

Power and motor driver circuitry, assuming a density for single-sided PC construction of 10 components/(in.)^3, will weigh

$$\frac{200}{10} \times 0.034 = 0.68 \text{ lb}$$

Preamplifier and assemblies in optical head will weigh about 0.65 lb based on Viking IRTM calculations.

The bus electronics housing will weigh approximately 1.8 lb assuming an average wall thickness of 0.125 in.

Summarizing the electronics weight, then:

Repairable Cordwood Assemblies	2.6 lb
Power Supply and Motor Drivers	0.68
Preamplifiers	0.65
Bus electronics housing	1.80
Conformal coating	0.28
Miscellaneous hardware	0.5
Wire	1.00
Total Weight	7.51 lb

Section 10

CALIBRATION TECHNIQUES

FIELD-OF-VIEW CALIBRATION OBJECTIVES

Near Field Measurements

The objective of the field of view (FOV) for calibration is to determine the polar response diagram of each of the individual fields of view in relation to the instrument mounting axes.

Assumptions

1. Thermal effects will not cause significant shifts in the individual FOVs.
2. The effect of atmospheric absorption will be small enough to allow the test to be accomplished in air or in a nitrogen purged atmosphere.

Description. - A collimator larger than the instrument aperture which contains an autocollimation capability as well as individual source types and sizes is used. The collimator is placed in front of each telescope in turn and the shape of the geometric response function is plotted for each channel as shown in Figures 10-1 and 10-2.

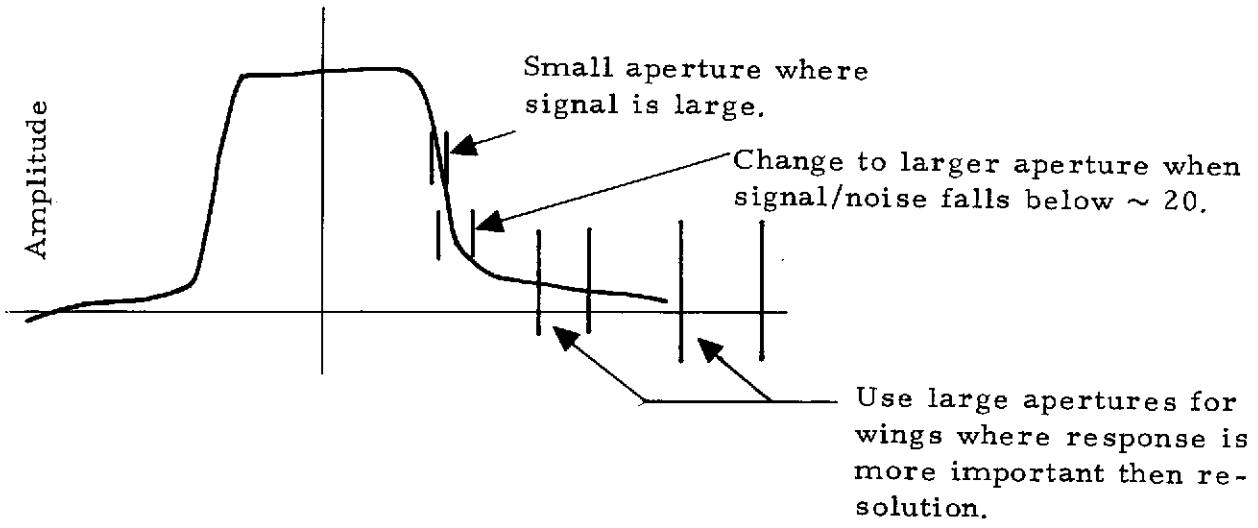

Figure 10-1. Field-of-View Response

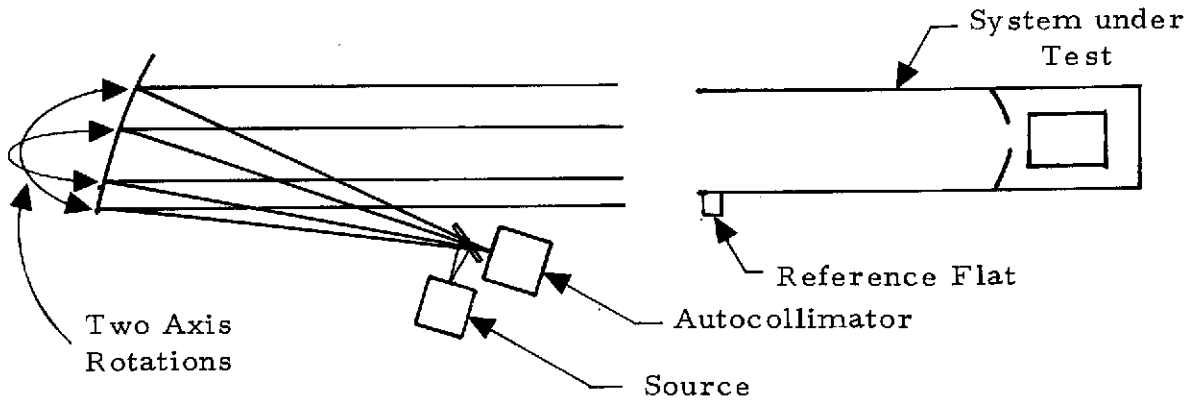

Figure 10-2. Field-of-View Test Setup

Far Field Measurements

The telescope is focused at a given distance, and a series of hot circular discs is centered on the optical axis and the contribution from each is plotted. The discs are increased in size from the size roughly corresponding to the angular subtense of the FOV to the size corresponding to perhaps 10 to 15 or more FOVs. The setup for this test is shown in Figure 10-3.

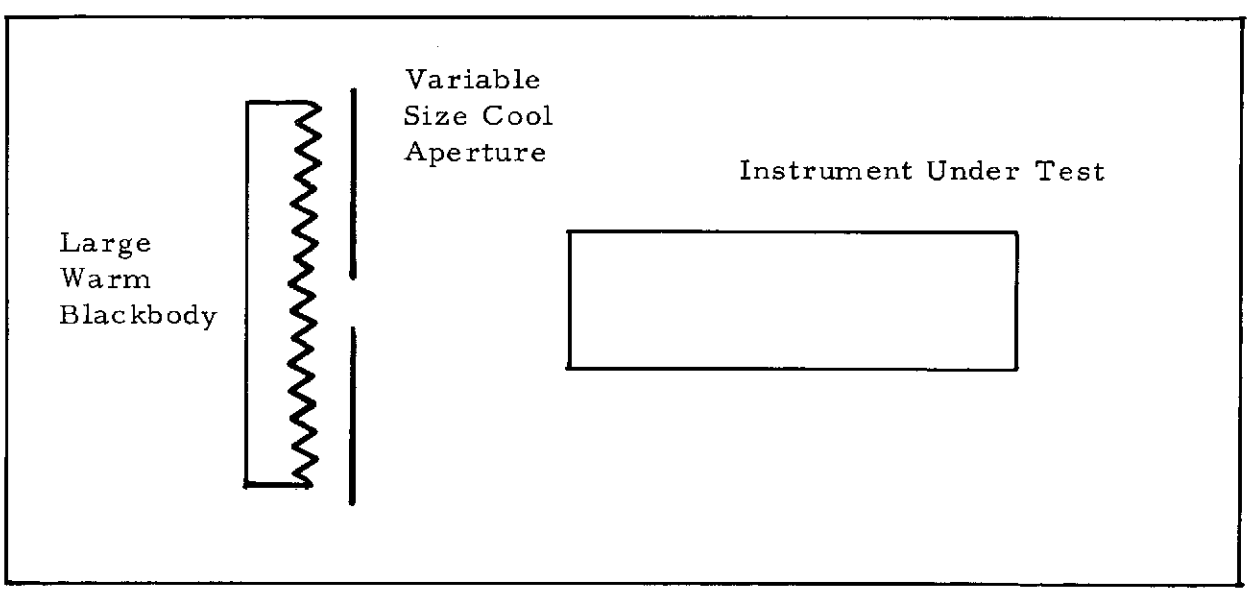

Figure 10-3. Far Field Test Setup

Assumptions

1. Thermal effects will not cause significant shifts in the individual FOVs.
2. Effects of atmospheric absorption must be removed (especially if the distance of the targets is varied to change the apparent angular subtense).

ABSOLUTE WAVELENGTH CALIBRATION

Filter Spectrometer and Fixed 4.25- to 4.75-μm Channel

The short-wavelength calibration is designed to determine the wavelength response and wavelength resolution as a function of instrument operating parameters such as temperature, temperature gradients, wheel position, etc.

Assumptions

1. Thermal effects will cause significant changes in parameters and must be calibrated.
2. Atmospheric absorption must be removed during the test.
3. A window can be used between the instrument and the source monochromator.
4. The resolution of the source monochromator should be less than 0.2% of wavelength.
5. The source monochromator must overfill the FOV and aperture of the instrument.

Description. - The test setup, shown in Figure 10-4, consists of a source monochromator in a nitrogen purged box feeding a telescope. The output from the telescope passes through a window in the side of the thermal-vacuum chamber to the instrument under test. The monochromator is set to a wavelength and instrument takes data in its normal fashion. The monochromator is then set to a new wavelength and the process is repeated until a curve of instrument output versus wavelength is provided for each instrument temperature.

Grating Spectrometer 10 to 40 μm

The long-wavelength calibration will determine the wavelength response of the grating spectrometer portion of the instrument. An accurate

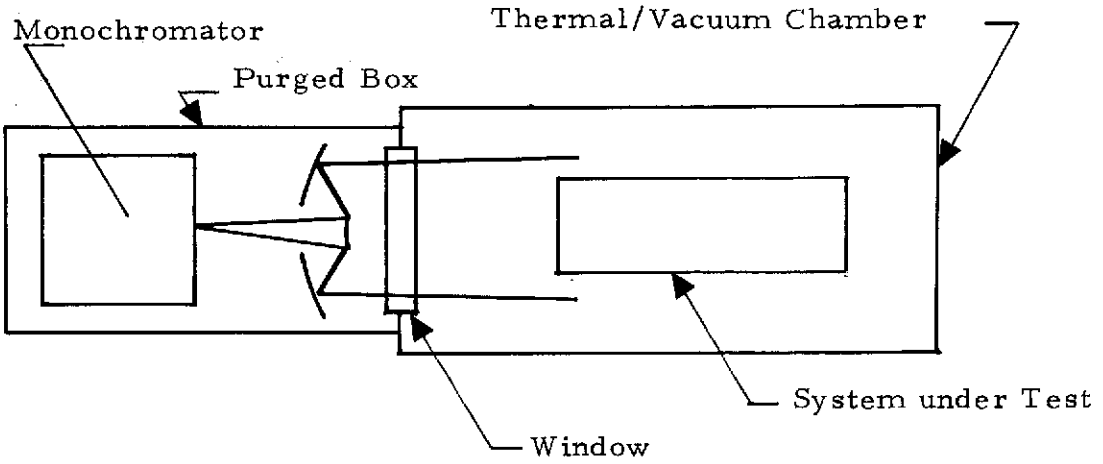

Figure 10-4. Short-Wavelength Spectral Response Measurement Setup

measurement of the spectral response for each channel is required to assist in the proper interpretation of the measured data.

Assumptions

1. Assumptions 1, 2 and 5 of Part 1 apply to this part.
2. A window cannot be used between the source and the instrument.
3. The resolution of the source monochromator is 3 cm^{-1} and covers the frequency region of 1000 to 250 cm^{-1}.
4. The aperture and FOV of the grating radiometer must be filled.

Description. - The arrangement of the test is shown schematically in Figure 10-5. A source/interferometer/beam expander combination provides the input to the telescope and thence to the two field stops of the grating spectro-radiometer portion of the instrument. The flux from the infrared source is modified by the Michelson interferometer and the output matched with a beam expander so that both the aperture and the two FOVs are over-filled.

The Michelson interferometer will be operated in a step/record fashion. Each sample point will be taken by holding the movable end-mirror of the interferometer in the next path difference position during the data readout. The eight parallel outputs of the instrument are collected at each path

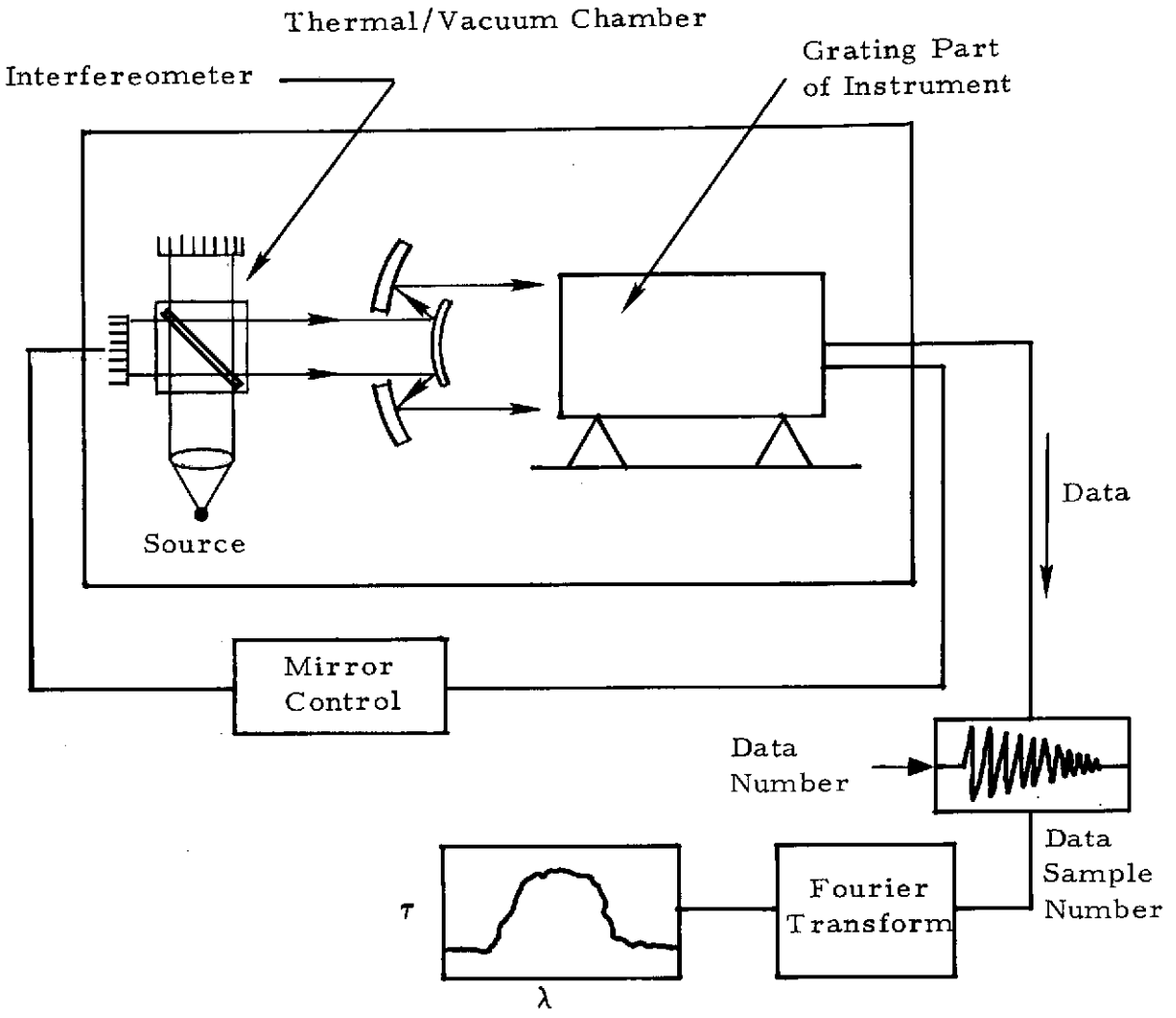

Figure 10-5. Long-Wavelength Spectral Response Measurement Setup

difference position, thus they generate an interferogram for each spectral channel. These digital outputs will then be Fourier transformed on a digital computer (with a fast Fourier transform algorithm) to provide the spectral or instrumental response function for each channel as modified by the calibration source spectrum (source, interferometer, and beam expander). This latter effect can be removed by recording an interferogram with a detector of known spectral response.

To achieve a resolution $\Delta\nu$ (apodized) of 3 cm^{-1} a maximum path difference of about $\overline{X}$ = 0.33 cm will be required of the interferometer. If the wavenumber of the highest frequency component detected is ν_m, then an interferogram sampling interval of $\Delta x = (2\nu_m)^{-1}$ is sufficient to avoid aliasing or overlapping in the computed spectra. Taking ν_m = 1000 cm^{-1} and assuming that a full two-sided interferogram is recorded, then a total of $N = \overline{X}/\Delta x + 1 \simeq 1330$ interferogram points would be taken during the measurement. This could be reduced by nearly a factor of two if only a one-sided (cosine) transform with enough additional points were taken to establish the phase.

The angular subtense of the two field stops for the grating portion of the instrument is somewhat less than 15 mr. The maximum resolving power $R = \nu_m/\Delta\nu$ required for the calibration is about 333. The usable angular diameter for the Michelson interferometer (with a modulation of 0.64 at maximum path difference $\overline{X}$ for $\nu = \nu_m$) is $= 2/\sqrt{R} \simeq 110$ mr. Thus, to overfill both the field and aperture of the instrument for the grating channels, an interferometer aperture diameter somewhat less than 1 inch is perfectly adequate when used in conjunction with a beam expander.

To make optimum use of the dynamic range provided by the 10-bit quantization provided in the instrument, provision will be made for setting the gain at the zero path difference position to give near full-scale channel outputs. With these conditions, the digitizing noise can be kept to less than 1% of the inband signal for all channels with the possible exception of the 14- to 24-μm channel. If the digitizing error for the short-wavelength band is deemed excessive, the use of different (lower) gain for the highest peaks of the interferogram can be used to decrease the digitizing noise of the transformed spectrum.

ABSOLUTE RADIANCE CALIBRATION

Long Wavelength

The purposes of the long wavelength calibration are to measure the in- and out-of-wavelength band radiometric characteristics of the channels

in the 6- to 100-μm region and measure the characteristics of the inflight calibration paddles.

Assumptions

1. The instrument must be at its operating temperature and have the same type of temperature gradients as it will have in flight.
2. The instrument must be fully assembled and all parts of the system in use.
3. No windows can be used between the collimator and the instrument.

Description. - The instrument is placed in a thermal-vacuum chamber which sets the instrument's temperature and temperature gradients to those expected in flight. In the chamber is a collimator with a cold (LNe) blackbody, a temperature controlled warm blackbody, an intense short-wavelength source, and a remotely controlled mirror to switch the collimator between the sources. See Figure 10-6.

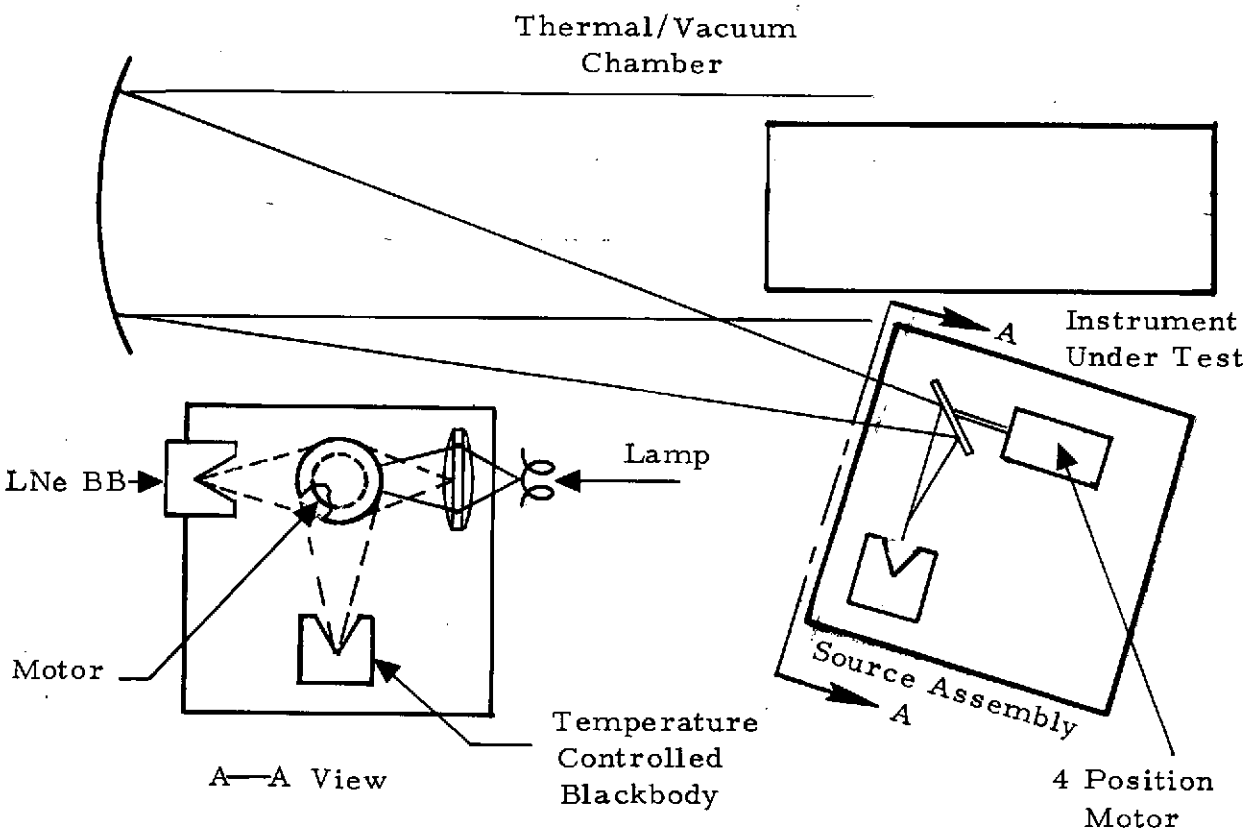

Figure 10-6. Long-Wavelength Radiance Calibration Setup

When the mirror is in the cold blackbody position the emitted and scattered energy from the two collimator mirrors and the instrument telescope is measured. When the mirror is in the warm blackbody position the instrumental transfer function and the constants for the calibration paddles are obtained. With the mirror in the short-wavelength source position the out-of-wavelength band response of the instrument can be evaluated.

Short Wavelength

The purpose of the short-wavelength calibration is to determine the characteristics of the sun calibration paddle, and to adjust the gains of the channels in the 0.4- to 5-μm region.

Assumptions

1. The absolute calibration of the filter spectrometer and the 4.25- to 4.75-μm channels depends on the inflight sun calibration and not the ground calibration.
2. The characteristics of the sun calibration paddle do not change throughout the mission.
3. The instrument must be at the proper temperature and the effects of atmospheric transmission eliminated during this test.
4. The solar irradiance falling on the paddle can be calculated to the required accuracy at Jupiter and Saturn.

Description. - The end result of this test is to obtain a transfer constant which when multiplied times the output from the instrument during sun calibration gives instrument responsivity.

Since the characteristics of the sun calibration paddle's effect on the instrument are not totally calculable a direct measurement must be made. The measurement is performed by comparing the output of the instrument when looking at a known diffuse reflector such as ground aluminum and the output when the sun port is illuminated. The same source and collimator with a wavelength-defining narrow-band filter is used to illuminate the diffuse reflector and the sun port. See Figure 10-7.

By using a series of filters the wavelength dependence of the transfer constant can be measured.

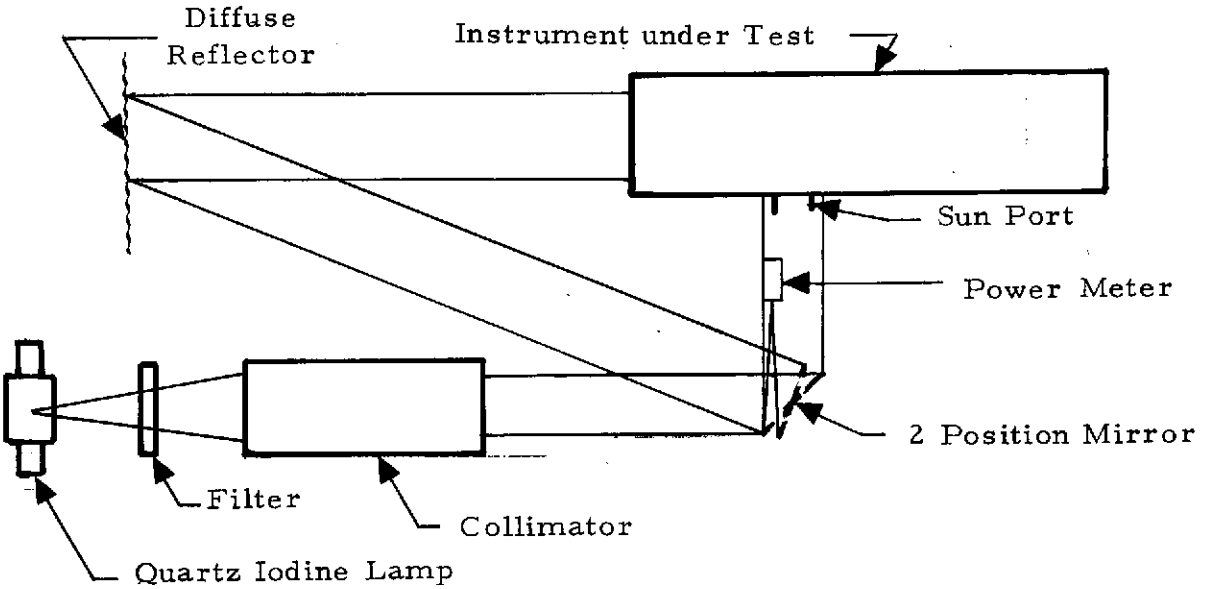

Figure 10-7. Short-Wavelength Radiance Calibration Setup

The gains of the various channels can be set by measuring the absolute amount of power entering the instrument with the power meter and setting the gains accordingly.

Section 11

ERROR ANALYSIS

The sources of error which contribute to the uncertainty in the radiometric data obtained with the instrument can be grouped in the following categories:

1. Errors Introduced into the Radiometric Spectrometer During Initial Calibration. - Error sources originate in both the instrument and the calibration equipment, but insofar as the resulting uncertainty is concerned, they are indistinguishable.
2. Errors Associated With Data Retrieval. - Errors in data taken during calibration can be minimized by various methods such as integrating, and averaging. However, during flight, the full effect of system noise, etc., must be taken into account. Also, errors associated with the in-flight calibration technique must be considered.

INITIAL CALIBRATION

The sources of error shown in Table 11-1 were considered in determining the magnitude of uncertainty that would exist in the initial calibration of the radiometric spectrometer. These errors are indicated as absolute and relative. Also indicated for each source is the magnitude (2σ value) of the error. The uncertainty in the system calibration as a result of these errors is summarized in Table 11-2.

Table 11-1 Item Descriptions

The following items describe the entries in Table 11-1.

1. Digitization Errors. - These can be minimized during calibration by extracting the data prior to digitization.
2. System Noise. - This can be minimized by increasing the number of independent readings made at each data point and averaging the results. Ten readings per sample are assumed in the table.
3. Restore Voltage Drifts. - First order drifts in the restore voltage are assumed to be temperature effects considered in item 6. Second order restore voltage drifts are assumed to be random.
4. Restore Noise. - During calibration it can be minimized or eliminated by increasing the restore period.

Table 11-1. Sources of Error Occurring During Initial Calibration

Error Source	Error Parameter	Error Contribution (%) of Full Scale					
		Absolute			Relative		
		CVF ** Spect.	Grating *** Channel	Albedo and Bolo.	CVF Spect.	Grating Channel	Albedo and Bolo.
Instrument							
1. Digitization	±0.1%	nil	nil	nil	nil	nil	nil
2. System Noise $\frac{J}{S}$	Error per reading* is $\sim\frac{3\text{-}4}{SNR}$ %	$\frac{0.47}{1.0}$	$\frac{0.2}{0.57}$	$\frac{0.1}{0.3}$	$\frac{0.47}{1.5}$	$\frac{0.2}{0.57}$	$\frac{0.1}{0.3}$
3. Restore Voltage Drifts	nil	nil	nil	nil	nil	nil	nil
4. Restore Noise	$\frac{1}{5}$ of 2 above	n/a	0.16	nil	n/a	0.16	nil
5. Cross Talk	60-db isolation	nil	nil	nil	nil	nil	nil
6. Temperature of Instrument	±1°K	0.2	0.2	0.2	0.2	0.2	0.2
7. Spectral Measurement Errors							
Grating Interference Filters Reststrahlens Coatings Mirrors Detectors	±1% Total	nil	nil	nil	nil	nil	nil
8. CVF Position Errors	20% of Step Size	0.2	n/a	n/a	0.2	n/a	n/a
9. Input Voltage Variation	±1%	nil	nil	nil	nil	nil	nil
Calibration							
10. Blackbody Temperature $\frac{J}{S}$	±0.1°C	n/a	$\frac{0.4}{1.0}$	$\frac{0.2}{0.4}$	n/a	nil	nil
11. Blackbody Emissivity	±0.1%	n/a	0.1	0.1	n/a	nil	nil
12. Blackbody Reflectance	0.05%	n/a	nil	n/a	n/a	nil	n/a
13. Optical Transmittance	±1% per optical element	1.4	1.4	1.4	nil	nil	n/a
14. Calibrator-Radiometer Interaction (View Factor)	nil	nil	nil	nil	nil	nil	nil
15. Non-Uniformity of Blackbody Temperature	nil	nil	nil	nil	nil	nil	nil
16. Lamp Emittance	n/a	nil	n/a	n/a	nil	n/a	n/a
17. Diffuser Geometry	±1%	1.0	n/a	1.0	1.0	n/a	1.0
18. Monochromator Errors	±0.5%	0.5	n/a	n/a	nil	n/a	n/a
19. Interferometer Amplitude Variation	1-2%	n/a	nil	n/a	n/a	nil	n/a

* 10 readings per sample assumed
** For channel having lowest SNR
***14- to 24-μm channel shown

Table 11-2. Major Error Sources - Initial Calibration

Band	SNR		System Noise[2] Error (% of Full Scale)		Calibration Error[3] (% of Full Scale)		2σ Error	
(μm)	Jupiter	Saturn	Jupiter	Saturn	Jupiter	Saturn	Jupiter	Saturn
14-24	5900	1050	0.017	0.095	1.45	1.7	2.9	3.4
25-27.8	875	250	0.114	0.40	1.43	1.53	2.86	3.16
30.8-34.4	677	234	0.147	0.427	1.4	1.48	2.8	3.1
35.7-38.4	443	175	0.226	0.57	1.4	1.46	2.84	3.14
17-35	11,500	845	0.009	0.118	1.42	2.61	2.84	5.2
40-55	1520	625	0.066	0.16	1.4	1.58	2.8	3.16
0.8-1.3[1]	2040	670	0.049	0.15	1.8	1.8	3.6	3.6
1.25-2.45	1680	557	0.06	0.18	1.8	1.8	3.6	3.6
2.35-3.0	1680	470	0.06	0.212	1.8	1.8	3.6	3.6
2.9-3.5	240	76	0.416	1.32	1.8	1.8	3.7	3.6
3.4-6.0	213	67	0.47	1.50	1.8	1.5	3.72	4.28
4.25-4.75	1070	355	0.094	0.38	1.8	1.4	3.6	2.9
0.4-4.0	2900	925	0.034	0.108	1.8	1.4	3.58	2.8
6-100	966	330	0.103	0.30	1.42	1.5	2.84	3.04

[1]SNRs for CVF channels are averaged over the band.

[2]Channels having 10-sec dwell times are sampled 10 times per data point and the results averaged.

[3]RSS of all sources of calibration error.

5. Cross Talk. - Cross talk between channels is assumed to be nil.

6. Temperature of the Instrument. - It was assumed that the instrument temperature can be maintained within 1°K of the desired calibration temperature, and that the slope change of the responsivity/temperature transfer function will not exceed ±5% over the 50°C operating temperature range.

7. Spectral Measurement Errors. - A Perkin-Elmer Model 112 or 16U spectrometer will be used for all reflectance and transmittance measurements. The stated repeatability accuracy of the instrument is ±1%, but at wavelengths beyond 20 μm the lack of available signal reduces the accuracy. Relative response measurements are sufficient for mirrors and optical elements in the radiometer because only a determinable scale factor is involved. This stated uncertainty applies directly to optics within the calibrator, however, which is considered below. An error of ±1% is assigned to the combined spectral measurements of the filter and the detector array, but only errors in wavelength calibration are considered.

8. CVF Position Errors. - If 10-bit position encoding is used for the CVF wheel, then an error of approximately 22% in each step position will be seen. The amplitude uncertainty assigned to this cause is 0.2%.

9. Input Voltage Variation. - It was assumed that the input voltage could be maintained within ±1% of the nominal voltage during calibration; therefore, its contribution to the calibration uncertainty will be nil.

10. Calibration Blackbody Temperature. - An uncertainty of ±0.1°C was assumed at a blackbody temperature of 130°K.

11. Blackbody Emissivity. - An uncertainty of ±0.1% was assumed.

12. Blackbody Reflectance. - A value of 0.05% with a 300°K background temperature was assumed. The planet and space blackbody geometry is made identical to eliminate this effect. Otherwise this could be the source of large error.

13. Optical Transmittance. - The error owing to uncertainties in transmittance or reflectance measurements of the optical elements in the calibrator can be given by the expression: $\epsilon_c = \pm\sqrt{n\Delta^2\rho} \cong 1.4$, $n = 2$, $\Delta = 1\%$, $\rho = 0.95$.

14. Calibrator-Radiometer Interaction. - Interaction between the calibrator and the radiometer which might produce temperature gradients within the instrument is assumed to be negligible.

15. Non-Uniformity. - Non-uniformity of blackbody temperature is assumed to be negligible.

16. Lamp Emittance. - Lamps are not used for absolute calibration, but only for determining scale factors.

17. Diffuser Geometry.- Diffuser geometry determined the scale factor for solar calibration. The error in determining the scale factor is assumed to be ±1%.

18. Monochromator Errors. - Errors in determining spectral bandpass of short-wavelength channels are assumed to produce an error of ±0.5%.

Table 11-1 clearly shows that the major sources of error are the system noise and uncertainties in the temperature and emissivity of the long-wavelength blackbody calibration. In the case of the system noise it is assumed that ten readings per sample will be taken. This means that each data point will require 100 seconds during calibration. Requirements on blackbody calibration are extremely stringent. The absolute temperature must be known to ±0.1°C which at temperatures of 130°K is probably on the limits of the state of the art. Also, the properties of the blackbody must be very well controlled to reduce the error from this source. This implies that the calibration system is limited to one using a collimator in which the blackbody itself can be quite small. The direct approach of using a large blackbody to fill the aperture would not be practical in this case because errors in the blackbody reflectance, primarily, could cause large errors.

Table 11-2 shows the 2σ error from major error sources for each channel. The errors are expressed as a percentage of the full scale radiance for each channel.

Data Retrieval Errors

Errors originating in the system or the data link are given in Table 11-3.

Inflight Calibration

In the event there is cause to believe that the initial calibration has changed since launch, the sources of error leading to uncertainty in radiometric data shown in Table 11-3 would be used.

Table 11-3. Sources of Error Affecting In-Flight Data Retrieval

Error Source	Error Parameter	Error Contribution (%)					
		Absolute			Relative		
		CVF Spect.	Grating Channel	Albedo and Bolo.	CVF Spect.	Grating Channel	Albedo and Bolo.
Instrument							
1. Digitization	10 bits, ±0.1%	0.1	0.1	0.1	0.1	0.1	0.1
2. System Noise $\frac{J}{S}$	Error per reading is ~3-4/SNR%	$\frac{7.2}{2.5}$	$\frac{1.2}{2.4}$	$\frac{0.3}{0.9}$	$\frac{7.2}{2.5}$	$\frac{1.2}{2.4}$	$\frac{0.3}{0.9}$
3. Restore Voltage Drifts	±0.5%	n/a	0.5	0.5	n/a	0.5	0.5
4. Restore Noise $\frac{J}{S}$	1/5 of 3 above	n/a	$\frac{0.24}{0.48}$	$\frac{0.06}{0.18}$	n/a	$\frac{0.24}{0.48}$	$\frac{0.06}{0.18}$
5. Cross Talk	60-db isolation	nil	nil	nil	nil	nil	nil
6. Instrument Temperature	±1°K	0.2	0.2	0.2	0.2	0.2	0.2
7. Channel Linearity	≤0.1% Full Scale	0.1	0.1	0.1	nil	nil	nil
8. Spectral Bandpass	±1%	1.0	1.0	1.0	nil	nil	nil
9. CVF Position Errors	20% of Step Size	0.2	n/a	n/a	0.2	n/a	n/a
10. Input Voltage Variation	±5% Voltage Variation	0.1	0.1	0.1	0.1	0.1	0.1
In-Flight Calibration							
11. Blackbody Plate Temperature	±0.5°C	n/a	1.0	1.0	n/a	nil	nil
12. Blackbody Plate Emissivity	±1%	n/a	1.0	1.0	n/a	nil	nil
13. Blackbody Plate Reflectance	±1%	n/a	nil	nil	n/a	nil	nil
14. Optical Transmittance Non-Uniformities	±0.5%	0.1	0.1	0.1	nil	nil	nil
15. Detector Response Non-Uniformities	±3% PbS	3.0	nil	nil	nil	nil	nil
16. Diffuser Plate Surface Degradation	-2%	2.0	n/a	2.0	nil	n/a	nil
17. Lamp Emittance Changes	nil	nil	nil	nil	nil	nil	nil
Data Link							
18. Bit Error Rate	10-4	nil	nil	nil	nil	nil	nil

*Worst case signal-to-noise ratios are assumed.

Table 11-3 Item Descriptions

The following items describe the entries in Table 11-3.

1. Digitization. - During data retrieval it is assumed that the above error sources apply to each data sample. Therefore the errors associated with items 1, 2, 3, 4 have to be evaluated for their full effect; no averaging can be done since the error applies to each data sample.

2. System Noise. - The SNR is stated as peak signal to rms noise. Therefore, for a given data sample the reading is corrupted by the peak-to-peak value of the noise. The error per reading is equal to approximately 3 divided by the SNR and is expressed as a percentage.

4. Restore Noise. - For those channels using dc restoration, the dc restore noise is approximately 1/5 of the channel noise.

10. Input Voltage Variation. - A ±5% variation of the spacecraft power supplies is assumed which gives a 0.1% uncertainty in system gain.

11. These items have to do with the inflight calibration paddles. We
12. are concerned only with changes which may have occurred to these
13. paddles since the time the instrument was calibrated in the laboratory and the inflight calibration was compared with the laboratory calibration. The paddles are assumed to be at the instrument temperature.

14. Optical Transmittance. - This error applies to uncertainties in measuring the optical transmittance of optical elements within the calibrator.

15. Detector Response. - Because PbS detectors typically exhibit 30% variation in sensitivity across their dimensions, an error of 3% was assigned to changes in this profile during the mission. This is a factor since the inflight calibrator does not illuminate the entire detector area.

18. Bit Error Rate. - A factor of one error in 10,000 is assigned to the data link.

Table 11-3 shows sources of error affecting inflight data retrieval. The errors due to system noise are for the worst case SNRs, and in that case predominate as the largest source of error. However, in Table 11-4 the major error sources for each individual channel are combined to give the 2σ error. These two major sources are system noise and calibration errors.

Table 11-3 is intended to show the magnitude of all of the noise sources; however, Table 11-4 is more useful since the errors are evaluated on a

Table 11-4. Major Error Sources, In-Flight Data Retrieval

Band	SNR		System Noise Error (% Full Scale)		Calibration Error (% Full Scale)		2σ Error	
(μm)	Jupiter	Saturn	Jupiter	Saturn	Jupiter	Saturn	Jupiter	Saturn
14-24	5900	1050	0.051	0.285	1.4	1.4	1.96	2.86
25-27.8	875	250	0.342	1.2	1.4	1.4	2.87	3.7
30.8-34.4	677	234	0.44	1.28	1.4	1.4	2.93	3.8
35.7-38.4	443	175	0.68	1.71	1.4	1.4	3.1	4.4
17-35	11,500	845	0.027	0.35	1.4	1.4	1.96	2.9
40-55	1520	625	0.198	0.48	1.4	1.4	2.0	2.95
0.8-1.3	2040	670	0.147	0.45	3.74	3.74	7.48	7.5
1.25-2.45	1680	557	0.18	0.54	3.74	3.74	7.48	7.5
2.35-3.0	1680	470	0.18	0.635	3.74	3.74	7.48	7.6
2.9-3.5	240	76	1.25	3.96	3.74	3.74	7.9	10.9
3.4-6.0	213	67	1.41	4.5	3.16	3.16	6.9	10.9
4.25-4.75	1070	355	0.282	1.14	3.16	3.16	6.3	6.7
0.4-4.0	2900	925	0.10	0.324	3.74	3.74	7.48	7.48
6-100	966	330	0.31	0.90	3.16	3.16	6.3	6.58

per channel basis. The errors quoted in Table 11-4 are 2σ errors; that is, 95% of the time the error will be less than the stated value. If half of this value were used it would imply that 68% of the time the error would be less than 1σ value.

Section 12

HISTORICAL DEVELOPMENT OF THE MJ/S RADIOMETRIC SPECTROMETER

SCIENCE TEAM ACTIVITIES

The first instrument concepts were developed during the time the science team was operating to formulate the science requirements. Results of this activity were summarized in the Infrared Experiments Team Report, published January 1971.[1] In this report the first concept of the instrument is described. The instrument consisted of two separate telescope systems. The first, a 12.5-cm diameter Cassegrainian telescope, was used for five broad thermopile spectral bands none of which were spatially coincident. Each band had a FOV of 2 mr x 2 mr. A 45° mirror was used to perform the function of optical chopping by viewing space, the scene, and an internal reference surface.* The second system was a 25-cm diameter Cassegrainian telescope used for the filter wedge spectrometer having five bands ranging from 1 to 18 μm. Spectral resolution was 1%. Cooling for the detectors was assumed to be 77°K using PbS, PbSe, and HgCdTe.

The performance of these two systems is summarized in Tables 12-1 and 12-2.

Significant features for comparison of this early concept with later ones are as follows: 1) spectral bands were much wider than those considered later in the study; 2) a narrower FOV was considered for this early concept; 3) the system lacked spatial simultaneity; and 4) even for this design the SNRs at Saturn were not uniformly greater than 100. In the filter wheel spectrometer, the detector cooling temperature of 77°K is somewhat impractical owing to weight and size constraints, and contamination problems. Also, the 1% spectral resolution is difficult to achieve in practical filter wheels. In effect

*Spectral filtering was accomplished by means of reststrahlen materials and scatter filters.

Table 12-1. Performance of Radiometric Channels, Thermopile Radiometer

Spectral Bands (μm)	Filter Type	Field Lens	Optical Trans (%)	Jupiter (134°K) SNR	Jupiter (134°K) NEDT (°K)	Saturn (98°K) SNR	Saturn (98°K) NEDT (°K)	Uranus (64°K) SNR	Uranus (64°K) NEDT (°K)	Neptune (55°K) SNR	Neptune (55°K) NEDT (°K)	Dyn Range
20-100	3 Reflect $BaTiO_3$ + Yamada Filter	Diamond	30	817	0.045	250	0.09	24	0.37	14	0.42	58
14-26	3 Reflect MgO + IR-6 Lens	IR-6	50	645	0.038	93	0.15	1.3	4.3	0.16	25	4×10^3
20-30	2 Reflect $BaTiO_3$ 1 Reflect CaF_2 IR-6 Lens	IR-6	30	332	0.091	67	0.25	1.76	3.7	0.28	16	1.2×10^3
32-55	3 Reflect BaF_2 + Si Lens	Silicon Lens	35	405	0.115	147	0.18	15.7	0.68	5.1	1.47	72
60-100	3 Reflect Thallium Cloride	Diamond	40	157	0.45	82	0.52	21	0.86	11	1.2	14

Telescope: 5-in dia f/5 Cassegrainian, 20% obscured by secondary mirror, $A_o = 10^2$ $(cm)^2$, FOV = 2 x 2 mr.

Detector: Evaporated thermopile, 18 junctions, resistance = 3500 ohms, responsivity = 140 volts/watt (ν), time constant = 50 msec

Dwell Time: 1 sec, $\Delta f = 0.3$ Hz

Table 12-2. Performance Summary for Filter Wheel Spectrometer

Channel (μm)	Spectral Resolution $\frac{(\%)}{\Delta\nu\ (cm^{-1})}$	Detector Type	Detector Cooling Temp (°K)	D* cm $Hz^{\frac{1}{2}}W^{-1}$	SNR (Jupiter) Short λ	SNR (Jupiter) Long λ	Spectral Elements per Scan	Time per Scan (sec)	Optical Efficiency (%)
1.0-2.0	$\frac{1.5}{150 \text{ to } 75}$	PbS	77	$2\text{-}5 \times 10^{11}$	5460	3530	66	66	15
1.7-3.4	$\frac{1.5}{90 \text{ to } 44}$	PbS	77	$1\text{-}2 \times 10^{11}$	1350	410	66	66	20
3.0-6.0	$\frac{1.5}{50 \text{ to } 25}$	$\frac{\text{HgCdTe}}{\text{PbSe}}$	$\frac{120}{77}$	$\frac{2 \times 10^{10}}{9 \times 10^{10}}$	$\frac{133}{66}$	$\frac{23}{17}$	66	66	40
5.0-10.0	$\frac{1.5}{30 \text{ to } 15}$	HgCdTe	77	$1\text{-}4 \times 10^{10}$	22	970	66	66	40
9.0-18.0	$\frac{3}{33 \text{ to } 16.6}$	HgCdTe	77	$2\text{-}1 \times 10^{9}$	18	165	33	33	40

Telescope Data

Aperture: 10-in. dia f/10 20% obscured by secondary mirror. Field lens f/1. Detector size (0.05 x 0.05 cm)

FOV: 2 x 2 mr

Dwell Time: 1 sec: $\Delta f = 0.3$ Hz

this cooling constraint makes the SNR performance marginal beyond 5 or 6 μm in the practical case. In addition to the radiometric and spectrometric channels, eight photometric channels used silicon photodiodes. The weight for the total system was estimated to be 20 pounds and the power consumption 12 watts.

It is of interest that the design has come full circle from the early concept. The design started from a concept using two separate telescopes, went through several iterations involving scanned telescopes, scan mirrors, large aperture single telescopes with multiple functions, and finally returned to the original two-telescope scheme.

A later team report[2] describes a different instrument concept (Figure 12-1). A single 10-inch Cassegrainian telescope is shared between the long-wavelength radiometric and the short-wavelength spectrometric channels by means of a rotating 45° mirror behind the telescope. The long-wavelength spectral bands are the same as before and the filter wheel spectrometer now covers the range of 1 to 12 μm with 2% spectral resolution rather than the original value of 1%. A cooling capability of 100°K is now assumed. The weight of the total instrument at this point was assumed to be 29 pounds and the power dissipation 15 watts.

This system, as described in the report, lacked spatial simultaneity among the long-wavelength channels and also the short-wavelength channels. In addition, the two systems did not take data simultaneously. Spectral filtering for the long-wavelength channels was assumed to be either interference filters or reststrahlen filters in combination with intrinsic absorption properties of certain crystal materials.

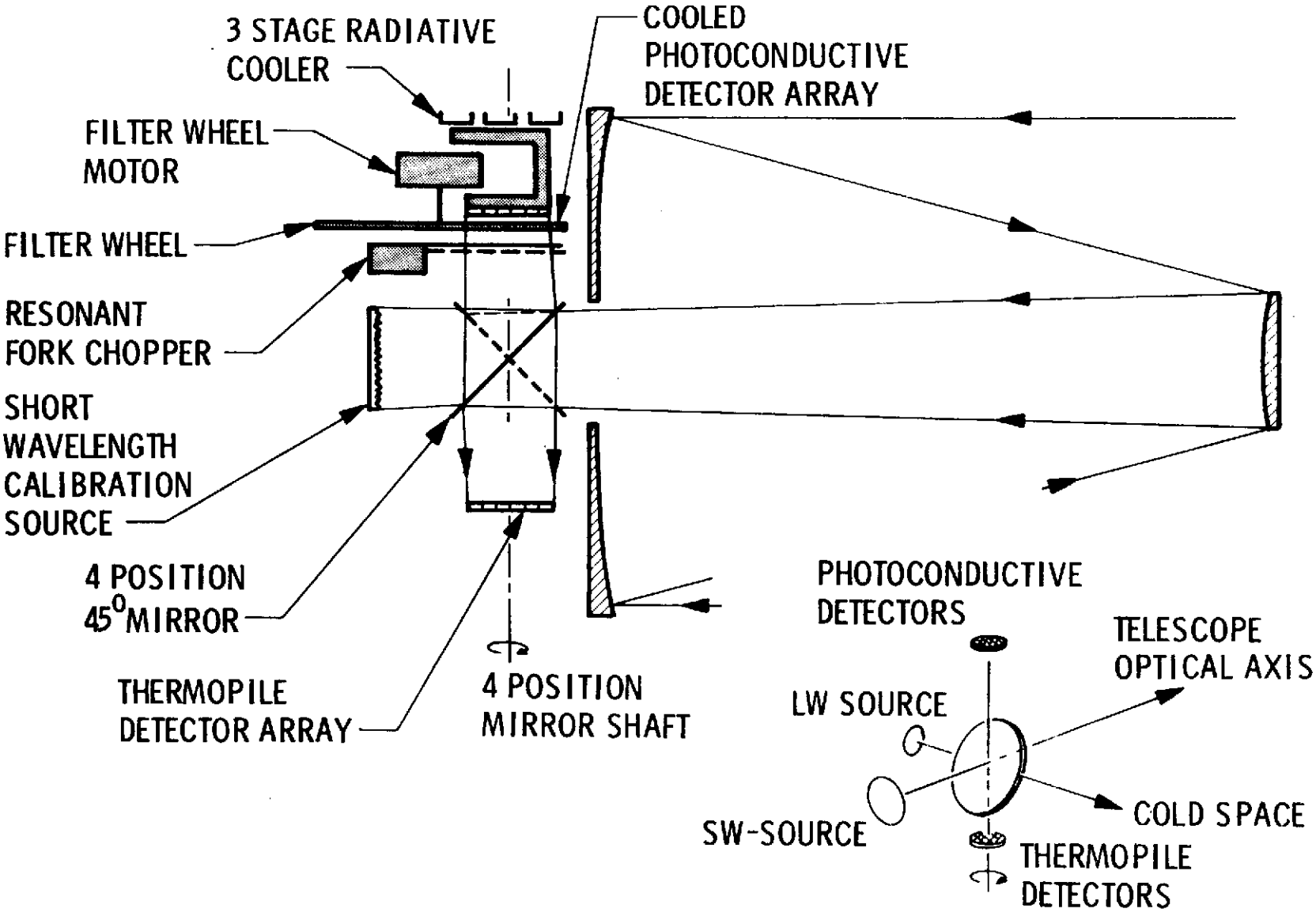

Figure 12-1. Instrument Conceptual Drawing OPGT Mission Design Phase

STUDY CONTRACT

While the science team activities were in progress, SBRC and JPL were negotiating a contract to perform a study of the concept and critical components of the radiometric spectrometer. The original SBRC proposal for this study was submitted on 8 October 1971; a revised proposal was submitted on 10 November 1971; and an official JPL go-ahead was given on 21 January 1972 although actual work did not start until 1 February 1972. At that time two contract work orders involving project management and conceptual design were opened.

The concept studied during this period was a single telescope which was scanned to view planet, space, and a reference surface. This was considered to be a lighter weight approach than using a telescope and an additional 45° scan mirror. The optical beam was brought out through the hollow trunnion bearing by means of a fixed 45° mirror mounted on the primary mirror (see Figure 12-2).

The system depended on separating the two instrument functions by means of a dichromatic mirror which would reflect the long wavelengths ($\lambda > 10$ μm) and transmit the short wavelengths ($\lambda < 5.8$ μm). This arrangement would allow simultaneous viewing of coincidence spatial areas for all channels except the long-wavelength radiometric channels which at this point were still using separate filters.

Long-wavelength filtering techniques were also being actively investigated during this time; it was determined that of four types of filters, three were unsuitable. These were interference bandpass filters which were not practical beyond 30 μm, reststrahlen filters which were not applicable for the specific spectral bands required, and metal mesh filters which were not practical at wavelengths shorter than 50 μm because of the mechanical tolerances required. Therefore, it was determined that a fixed grating spectrometer was the most feasible and that a single grating operating in

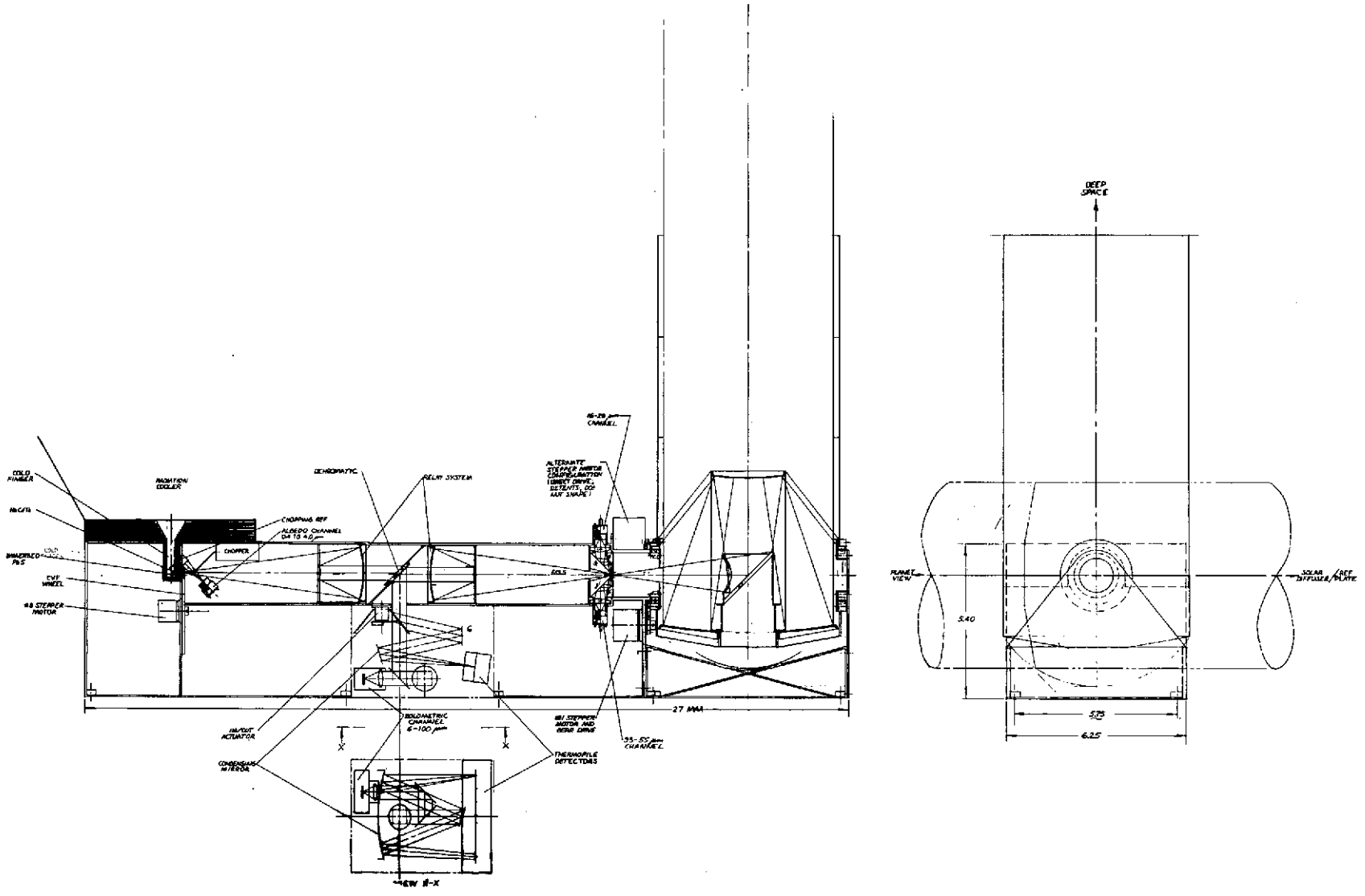

Figure 12-2. Mariner Jupiter/Saturn Opto-Mechanical Concept

SBRC

the first order would be used together with reststrahlen order separation filters and thermopile detectors. This had the advantage that all the wavelength channels now would be spatially coincident.

During that time also considerable effort was spent coordinating with Dick Parker of JPL the effects of radiation on materials. Parker arranged for proton and electron irradiation of samples of optical materials and detectors which were supplied to him and were later measured and evaluated at SBRC.

During the latter part of March the system aperture was reduced to 6 inches and replicated optics were actively being investigated; several samples of the GE Pioneer experiment telescope had been examined and evaluated. Also a fixed grating spectrometer approach was determined and the design effort in this area was proceeding. At that point the requirement still existed for long-wavelength coverage from 13.7 to 50 μm in six separate bands. These bands were spectrally narrower than those planned originally; hence, the SNRs obtained were quite low. By the end of March, the first design results indicated unsatisfactory performance. Performance of the system at that point is summarized in Table 12-3.

About that time a series of iterations began to improve the performance to an acceptable level. In some channels the SNR was over a factor of 100 too low. Other significant disadvantages were the lack of spatial coincidence between the 0.4 to 4.0 μm and 6 to 100 μm channels and the long baffle (9 inches) that would be required for the telescope. A number of factors were considered to improve the performance:

1. Immersed PbS was used for the filter wheel wavelengths shorter than 3 μm giving improvement factors of up to 40.
2. The above change allowed the lens for the HgCdTe detector to be optimized eliminating chromatic aberration. Improvement factor was 1.5.
3. An optimized low-pass filter was used in the long-wavelength channels instead of a true integrator. The improvement factor here was 1.57.

4. The preamplifier noise factor was eliminated for the short-wavelength channels since the system was detector noise limited. The improvement factor was 1.5.

5. Thermopile responsivity values used in the previous calculations were found to be wrong. Correct value of NEP is 1.6×10^{-10} w/$\sqrt{\text{Hz}}$.

Table 12-3. SNR Performance, 6-inch Telescope System

	Band (μm)	SNR			
		Jupiter		Saturn	
		Short End	Long End	Short End	Long End
CVF Spectrometer	0.8-1.3	28.6	26.8	9.25	9.0
	1.25-2.45	26.0	14.6	18.7	5.2
	2.35-4.6	37.6	10.7	10.0	3.7
	4.4-5.8	12.5	9.2	5.2	3.0
Thermopile Grating Radiometer	13.7-14.3	2.3		0.21	
	19.42-20.62	12.0		2.32	
	25.0-27.8	29.6		8.5	
	30.77-33.9	19.7		7.0	
	33.9-37.7	18.2		7.15	
	48.78-50	1.96		0.93	
Fixed Channels	16-30	115.0		22.2	
	30-60	66.5		28.5	
	6-100	89.8		30.7	
	0.4-4.0	505.0		160.6	

1 sec integration time
2 x 2 mr FOV
6-inch diameter aperture
1.5 preamplifier noise factor - should apply only to thermopile channels

These factors improved performance. However, without changes to the FOV, aperture size, spectral bandpass, or dwell time, the required SNRs of 100 would not be achieved. Furthermore, mechanical considerations essentially ruled out scanning telescopes larger than 6-inch diameter.

At a meeting at JPL on 10 April all these factors were reviewed, and the following recommendations were made:

1. Delete the 3.5- to 5.8-μm filter wheel band. The SNR in this range was probably too low to salvage anyway. The 4.25- to 4.75-μm fixed channel was retained. Note that the 3.5- to 6.0-μm band was later reinstated.
2. Delete the 13.7- to 14.3-μm, 19.4- to 26.2-μm, and 48.78- to 50-μm grating channels; replace these with one channel from 14 to 24 μm.
3. Increase telescope aperture from 6 to 12 inches diameter and increase the FOV from 2 x 2 to 4 x 4 mr.

A configuration satisfying the foregoing requirements is shown in Figure 12-3 and the performance of the system at this point is summarized in Table 12-4.

About that time the idea for inflight calibration involving the rotating paddles inside the telescope was developed. The method to shorten the overall length of the telescope by combining a baffle with a flower petal arrangement to close off the telescope aperture was developed. However, it was still intended to calibrate the short-wavelength channels by means of a 6-inch solar diffuser mounted on the high gain antenna.

A calculation was made to determine why the system performance was lower than that originally proposed in the team report. It was determined that so far as the long-wavelength channels were concerned, the difference in spectral bandpass was a significant factor. In the case of the grating spectrometer a number of other factors was involved. One was a factor of 1.5 for preamplifier noise degradation that was used in the later calculation that does not apply. There was a factor of 1.3 to account for the difference in equivalent noise bandpass between the true integrator and the pass filter,

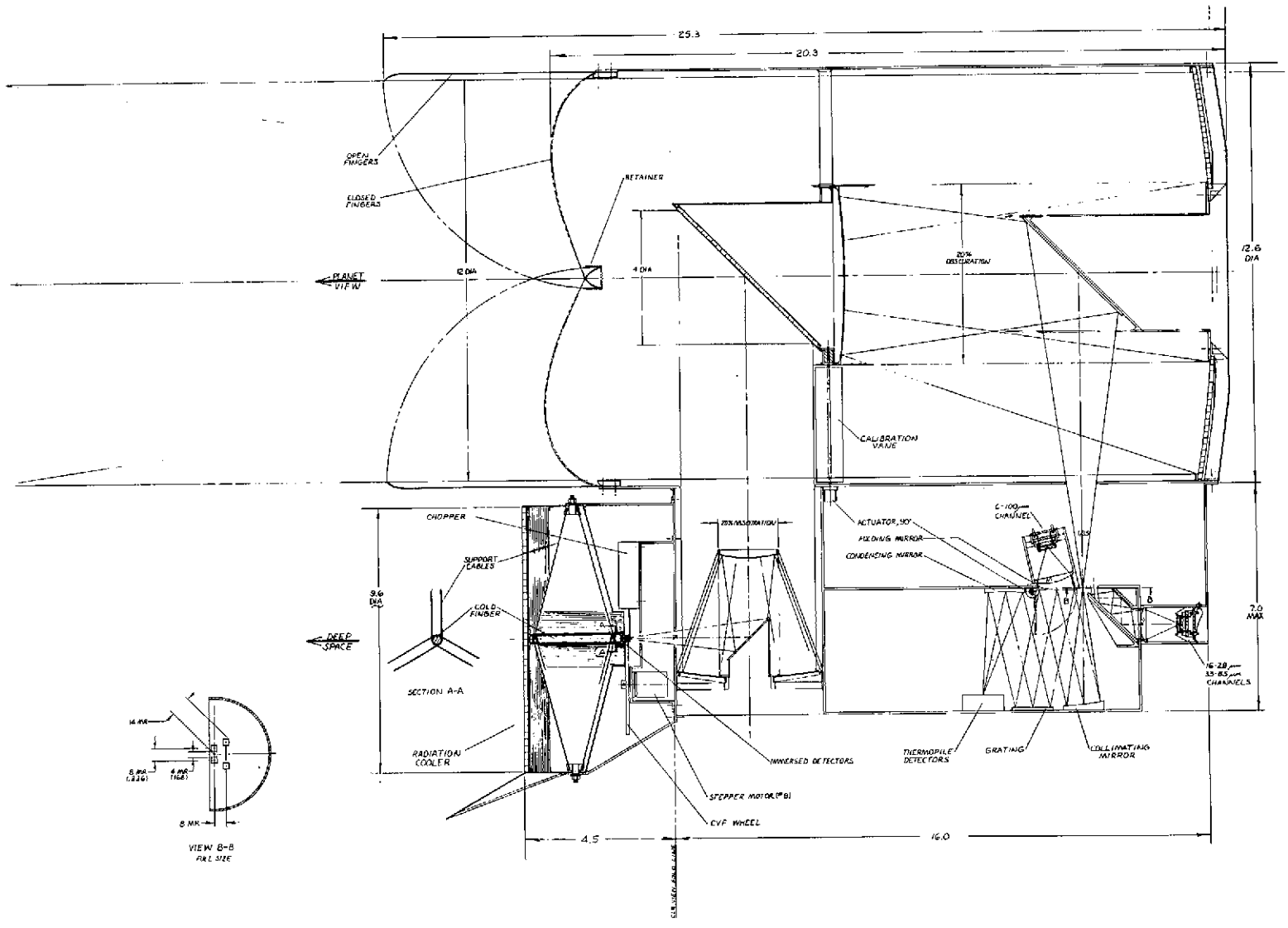

Figure 12-3. Optical Schematic, 12-Inch Folded System

and a factor of 1.5 to account for chromatic aberration in the field optics. These factors brought the recent system performance within a factor of two of the originally proposed system. Efforts were also made to obtain FOV coincidence of the 0.4- to 4-μm and 6- to 100-μm channels by means of a flipper actuator in the 4-inch system.

Table 12-4. SNR Performance 12-inch Telescope System

	Band (μm)	SNR			
		Jupiter		Saturn	
		Short End	Long End	Short End	Long End
CVF Spectrometer	0.8-1.3	4800	2920	1570	980
	1.25-2.45	4900	1480	1600	500
	2.35-3.0	4100	2260	1090	695
	2.9-3.5	53	38	16.3	12.4
	4.25-4.75	20Z		67.2	
Thermopile Grating Radiometer	14.0-24.0	337		60.2	
	25.0-27.8	94		26.8	
	30.8-34.4	60		20.6	
	35.7-38.4	32		12.7	
Fixed Channels	16.0-30.0	1200		230	
	30.0-60.0	708		303	
	6.0-100.0	1680		573	
	0.4-4.0	5500		1750	

Considerable work was performed on this 12-inch system, a cutaway isometric drawing of which is shown in Figure 12-4. A layout drawing of this system is shown in Figure 12-5. The 4.6-inch telescope was later made separate from the 12-inch system and the two were boresighted together. Two spectrometer designs were worked during this period, one for the 4 x 4 mr FOV and the other for 10 x 10 mr FOV.

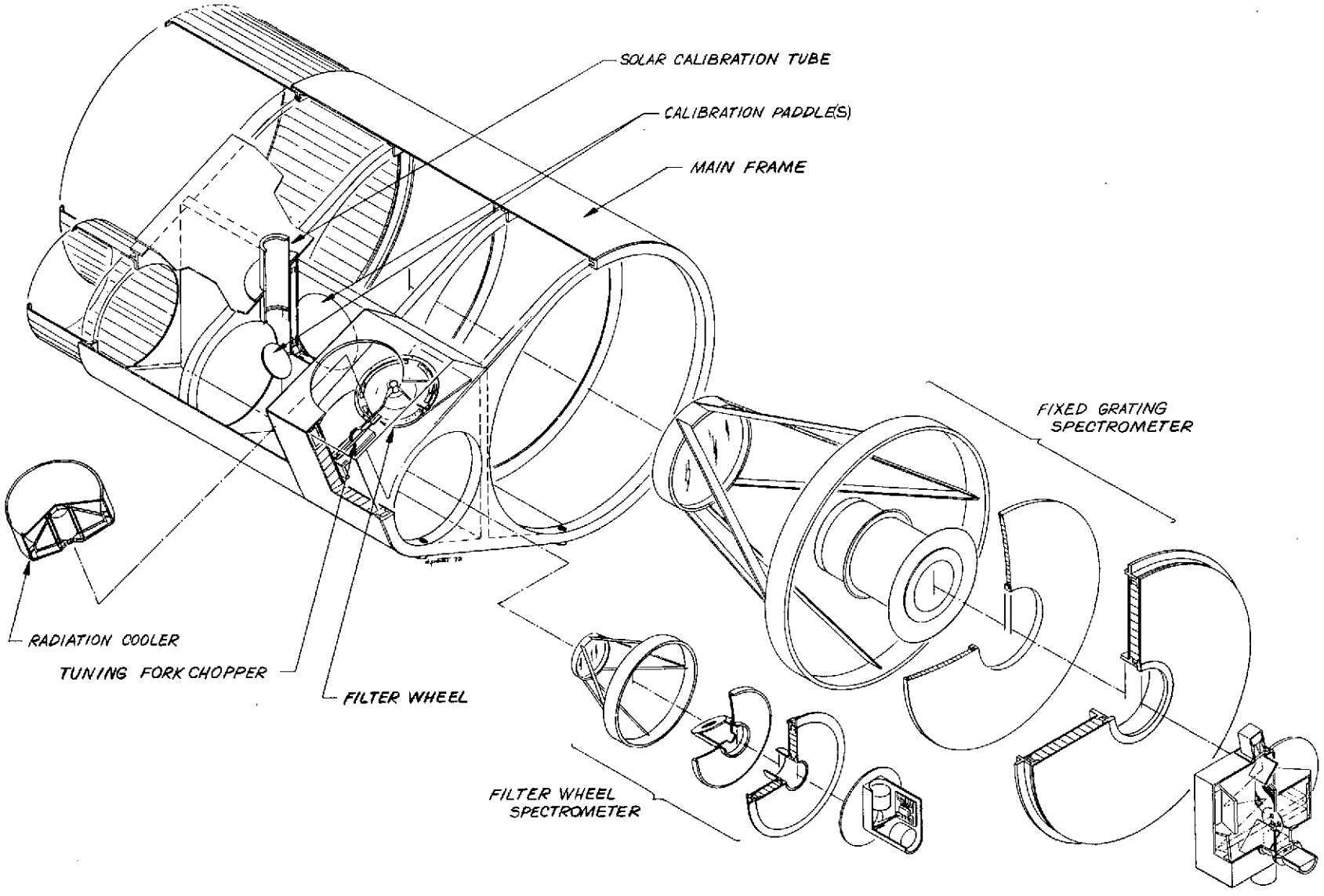

Figure 12-4. Cutaway Isometric, 12-Inch System

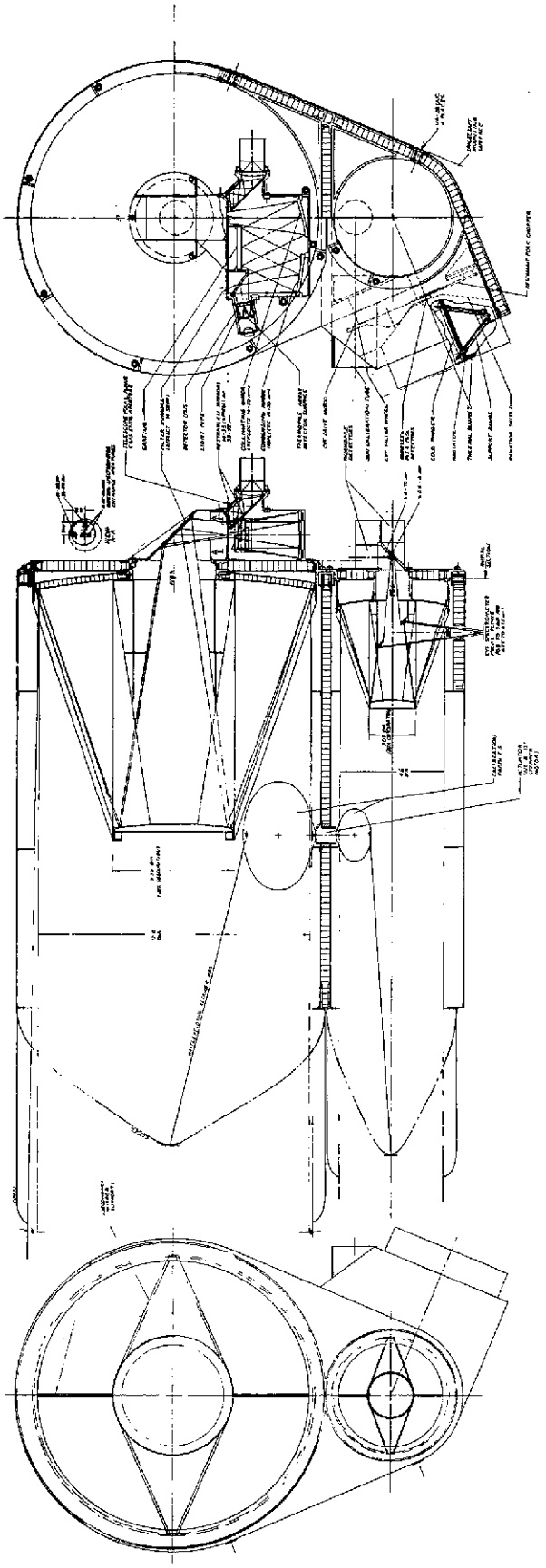

Figure 12-5. System Layout Drawing

At that time the subtleties of the spectrometer design were becoming understood. A performance summary, dated 4 May 1972, was generated for distribution at a Cal-Tech Science Team Meeting. Results of the analysis indicated that the performance of the system was still unsatisfactory. In addition, the weight analysis showed that the system as described would weigh 28 lb (4 lb overweight).

SBRC became aware of the performance increases that had been achieved with pyroelectric detectors during the past year and a half. A brief calculation had been made earlier in the program with TGS detectors in mind, but the anticipated performance increase of about a factor of two was felt not to be worth the additional complications of a chopper that would be required. It appeared, however, that the detectivity of TGS detectors was a factor of approximately 10 higher than for thermopiles. Therefore, in spite of mechanical complexities and the chopping losses of the chopper, the TGS detectors would provide more than a factor of 3 improvement.

New calculations were performed which showed that is was possible to reduce the FOV back to 4 x 4 mr and to reduce the 12-inch aperture down to a 6-inch diameter. These changes would give about the same performance that would have been possible with the 12-inch diameter system with a 10-mr view and thermopile detectors. At the same time it was decided to make both telescopes the same; namely, 6-inch diameter to simplify the design and reduce fabrication costs.

The most recent changes to the system were the result of a detailed design of the spectrometer. With thermopiles, the spectrometer required two short-wavelength rejection coatings on the mirror to reduce the out-of-band response to solar reflected energy. But the in-band loss of these coatings was a factor of 2. With the use of pyroelectric detectors these coatings can be eliminated since a selective chopper made of barium fluoride could be used. An analysis of the grating design indicated that the grating efficiency fell off markedly at the extreme ends of the spectral region.

Attempts were made to optimize the grating to minimize the effect by changing the blaze wavelength and by double blazing the grating to flatten the efficiency. However, neither of these techniques was particularly successful. Therefore, the 14- to 24-μm channel was removed from the grating, and was operated as a separate channel from the reflecting back surface of the chopper. Filtering was accomplished by multiple reflections of MgO. The grating efficiency was then optimized for the remaining three channels and an SNR improvement of roughly a factor of three was obtained in the longest wavelength channel. A large improvement in the 14- to 24-μm channel was obtained by this procedure because the detector could be square rather than rectangular. This reduction in detector size gave an additional factor of 3 in performance. Some of the latest efforts involved recalculating the weight for the new system and redoing the thermoanalysis for the two 6-inch systems.

REFERENCES

1. Proposal for Participation in Mission Definition for Grand Tour Missions to the Outer Solar System, Jet Propulsion Laboratory, Pasadena, California, January 1971.

2. Outer Planets Grand Tour Mission Definition Phase, Report of the Infrared Science Team, dated February 1972, Jet Propulsion Laboratory, Pasadena, California.

Section 13

CONCLUSIONS AND RECOMMENDATIONS

CONCLUSIONS

Major conclusions drawn from the study are as follows:

1. Adequate signal to noise ratios have been achieved for all channels except for the 6-μm end of the CVF spectrometer.
2. All channels operate simultaneously.
3. Spatial simultaneity is achieved for the grating radiometer channels and the CVF spectrometer channels.
4. Weight and power requirements have been met.
5. The size and form factor for the experiment is compatible with the MJS spacecraft.
6. For the most part, no extensive research or development will be required to design and build the instrument. Most techniques and processes are either taken from existing programs or are extensions from these programs.

SBRC feels that a viable instrument concept has been demonstrated and that the results of the study should go far in determining the final configuration of the infrared science experiments for the MJS mission. Furthermore, these results should prove valuable in determining the nature and mix of other experiments for the mission.

RECOMMENDATIONS

SBRC feels that additional efforts should be spent in the following areas before hardware development is initiated:

1. Dichromatic filter - the Coherent Radiation Laboratories have been under contract with SBRC to develop the filter which separates the albedo and bolometric channels. The results so far indicate that the technique will work, but additional measurements should be made at SBRC to confirm the properties of this device.
2. Diffraction grating - it would be valuable to obtain a grating of the design established in the study to determine efficiency and possible deleterious effects of Wood's anomalies.

3. The dynamic properties of the reflective low-frequency chopper described in the study should be investigated.

4. Alternatives to the method of in-flight calibration described in the study should be investigated since the technique described has several shortcomings.

5. The techniques of laboratory calibration should be analyzed in detail to determine the impact on cost and schedule.

6. There appear to be several new pyroelectric detector materials which only recently have been investigated. These materials offer improvements in performance beyond that currently available with TGS. It is suggested that a continuing study be made of these materials as they become available.